Development of Circulation Controlled Blade Pitching Laws for Low-Velocity Darrieus Turbine

Jagan Mohan Rao Gorle

THESE

Pour l'obtention du Grade de
DOCTEUR DE L'ECOLE NATIONALE SUPERIEURE DE MECANIQUE ET D'AEROTECHNIQUE
(Diplôme National – Arrêté du 7 août 2006)

Ecole Doctorale :
Sciences et Ingénierie en Matériaux, Mécanique, Energétique et Aéronautique

Secteur de Recherche :
Axe Hydrodynamique et Écoulements Environnementaux (HydÉE)
Département Fluides, Thermique et Combustion

Présentée par :

Jagan Mohan Rao GORLE

****

Development of Circulation Controlled Blade Pitching Laws for Low-Velocity Darrieus Turbine

****

Directeur de thèse :
Malick BA, Professeur, ISAE-ENSMA

Co-encadrants :
Ludovic CHATELLIER, Maître de Conférences, Université de Poitiers
Frédéric PONS, Maître de Conférences, ISAE-ENSMA

****

Soutenue le 18 Novembre 2015

devant la Commission d'Examen

****

JURY

Laurent DAVID	Professeur, Univ-Poitiers	Président du jury
Jean-Marc LAURENS	Enseignant-Chercheur (HDR), ENSTA	Rapporteur
Peter RUTHSCHMANN	Professeur, T- U München	Rapporteur
Thierry MAITRE	Maître de conférences (HDR), INP Grenoble	Examinateur
Malick BA	Professeur, ISAE-ENSMA	Examinateur
Ludovic CHATELLIER	Maître de conférences, Univ-Poitiers	Examinateur

"To raise new questions, new possibilities, to regard old problems from a new angle, requires creative imagination and marks real advance in science."

Albert Einstein

"I don't think you can impose limits on science because the very nature of homo sapiens is that he - she - is an inquisitive species. You can't control science. You have to control the effects of science."

Robert Winston

"The true laboratory is the mind, where behind illusions we uncover the laws of truth."

Jagadish Chandra Bose

Abstract

With key applications in marine renewable energy, the vertical axis water turbine can use current or tidal energy in an eco-friendly manner. However, it is difficult to reconcile optimal performance of hydrokinetic turbines and compliance with the aquatic environment as the main drawback of the turbines is the formation of non-linear flow structures caused by the unsteady movement of the blades. Eddies in the flow are advected and can interact with other blades, which leads to a reduction in power output. To limit this phenomenon, the turbines operate at high speeds, which are likely to reduce the shaft power. High speeds of rotation also forbid the passage of aquatic animals, and are the cause of a suction effect on the sediments.

The objective of this thesis work is twofold. First, it aims to develop a blade pitch control to get the flow adjusted around the blade profile at any given flow configuration by incorporating the profile's motion with respect to incident flow. Such a system intends to achieve the objective of operating at reduced speeds without vortical releases, which should allow achieving a high torque without causing damage to the environment.

This thesis work is mainly carried out in three phases. In the first phase, the irrotational flow over an arbitrary profile is formulated using conformal mapping. Prospective potential flow application on the basis of Couchet theory (1976) is involved in the development of a control law that decides the blade pitching in a constant circulation framework. In the second phase, a numerical validation of the developed analytical work is presented using CFD to examine how the theoretical formulation can be effectively applied to Darrieus turbines. In the final phase, two prototypes are developed- one is classical Darrieus turbine with fixed blades, and other is the turbine with pitching blades for experimental measurements of performance as well as flow fields in order to validate the computational results.

Acknowledgement

I would like to express my sincere appreciation to the Institute PPRIME at the Department of Fluids, Thermal & Combustion. I would firstly like to express my deep gratitude to Prof Malick Ba, my thesis director, who was leading this research accurately and advising me which allowed me to advance in this project. My sincere thanks to Dr Frederic Pons and Dr Ludovic Chatellier, who acted as co-supervisors throughout the tenure. Their utmost scientific and human qualities along with regular availability enabled me to perform in the best working conditions. Their interest in listening to my suggestions was providing immense motivation time-to-time and contributed to the success of this work. Their openness allowed me think diversely and gently directed the project in new research avenues within the planned schedule.

I would like to thank Prof Laurent David, Head of HydEE (Hydrodynamics and Environmental Flows) team at the Institute PPRIME who welcomed me in their team. Special thanks to the technical team of the laboratory, Patrice Allary, Romain Bellanger and Jean-Marc Mougenot, who have always been supportive by providing the solutions and solving the issues in technical arrangements. Patrice's involvement in arranging the computational resources and the role of Romain and Jean-Marc in my experimental campaigns is invaluable.

Being an international researcher, I cannot forget the administrative support of Jocelyne Bardeau, Melanie Ferret and Héba Riad who rendered their services from day one beyond the satisfactory level.

Since the laboratory is not only a workplace but also a place of life and exchange, I was interacting with the post-docs, PhD students and interns (Balkrishna, Clement, Aurelien, Zaynab, Diego, Faisal, Pierre, Allassane, Moez, Carlos and Sachin) whose enthusiasm and good humour ensured a happy and friendly atmosphere in the laboratory. The cultural mix and scientific conversations were rich and instructive. I appreciate the assistance of Mr Ravi Purohit for proof-reading several papers and for providing helpful suggestions to improve this manuscript.

I acknowledge the support and encouragement from my family members, whose genuine concern always kept my morale high. I specially thank my wife, Akhila. Her unwavering love and support have been undeniably the bedrock upon which my success is built. I am greatly indebted to my dad who has been my strength and courage, not just during my thesis work, but throughout my life. Finally, I thank all of my teachers, right from day one at elementary school, as they made me who I am today. May god grant all our wishes so we can be happier ever.

Contents

List of Figures

List of Tables

Nomenclature

Reference frames

T_0	Fixed reference frame
T_0'	Reference frame of free-stream
T_1	Reference related to the connecting rod that connects the rotor and the blade
T	Reference frame of blade

Design and functional parameters

a	Radius of the circle (m)
$L(=2a)$	Chord length of the profile (m)
R	Radius of the rotor (m)
L/R	Chord-to-Radius ratio
N	Number of blades
h	Height of the rotor (m)
A_T	Turbine's swept area (m^2)
A	Cross-sectional area of the channel
b	Blockage ratio
σ	Solidity

Flow and profile kinematics

V_0	Free-stream velocity (m/s)
P_0	Free-stream pressure (Pa)
W	Relative velocity (m/s)
Re	Reynolds number
M	Mach number
St	Stokes number
P	Power output (W)
ω	Turbine's rotational velocity (rad/s)
λ	Tip-speed ratio
λ_{opt}	Optimum tip-speed ratio
α	Blade azimuth position $(^o)$

Ψ	Global azimuth position of the turbine (^{o})
γ	Effective blade incidence (^{o})
θ	Blade orientation with respect to its tangent (^{o})
β	Equivalent static profile incidence with respect to attack velocity (^{o})
E	Eccentricity of the profile from the velocity field curvature
ϕ	Potential function of the flow related to the reference frame T_0' (m^2/s)
ψ	Stream function of the flow related to the reference frame T_0' (m^2/s)
f	Complex potential of the flow in $z-$plane (m^2/s)
F	Complex potential of the flow in $Z-$plane (m^2/s)
F_c	Couchet potential to the circulation Γ
$l(t),\ m(t)$	Tangential and normal velocity components of the free-stream with respect to the profile in translational reference (m/s)
$u,\ v$	x and y velocity components of the free-stream in the reference frame T_0' (m/s)
Γ	Circulation around the profile (m^2/s)

Torsor

$F_t,\ F_n$	Tangential and normal force components acting on the blade (N)
$F_l,\ F_d$	Lift and drag forces of the blade (N)
$X,\ Y$	Scaled tangential and normal components of the resultant force $(kg.m/s^2.m)$
$X',\ Y'$	Non-dimensional quantities of scaled tangential and normal components of the resultant force
M_0	Moment due to hydrodynamic forces about the blade centre $(kg.m/s^2)$
M_0'	Non-dimensional moment due to hydrodynamic forces about the blade centre $(kg.m/s^2)$
M_{00}	Moment due to hydrodynamic forces about the rotor $(kg.m/s^2)$
M_{00}'	Non-dimensional moment due to hydrodynamic forces about the rotor

Numerical modeling

ρ	Fluid density (kg/m^3)
μ	Dynamic viscosity of the fluid (kg/ms)
ν	Kinematic viscosity (m^2/s)

P	Pressure (Pa)
ζ	Transport scalar variable
$\bar{\zeta},\ \zeta'$	Mean and fluctuating components of ζ
$\mathbf{v}$	Arbitrary control volume
$\vec{u}$	Velocity vector
$\vec{A}$	Surface area vector for the volume $\mathbf{v}$
Γ	Diffusion coefficient
$\mathcal{V}$	Cell volume
S	Source per unit volume
N_{faces}	Number of cell faces
U_{ref}	Reference velocity (m/s)
$u',\ v',\ w'$	Fluctuating velocity components of the reference velocity U_{ref}
μ_t	Turbulent viscosity
k	Turbulence kinetic energy
ϵ	Dissipation rate of turbulence kinetic energy k
ω	Specific dissipation rate of turbulence kinetic energy k
Tu	Turbulence intensity (%)
δt	Time interval (s)
∇^2	Laplace operator
$u_i'\bar{u}_j'$	Reynolds stress tensor
τ_{ij}	Shear stress tensor
$G,\ Y$	Generation and destruction terms of turbulent viscosity μ_t
$\bar{\mu}$	Mean
$\bar{\sigma}$	Variance

Abbreviations

IPCC	Intergovernmental Panel on Climate Change
EMEC	European Marine Energy Centre
UNEP	United Nations Environment Programme
GFDRR	Global Facility for Disaster Reduction and Recovery
VAWT	Vertical Axis Wind/Water Turbine
HAWT	Horizontal Axis Wind/Water Turbine
NACA	National Advisory Committee for Aeronautics
RPM	Rotations per minute

COP	Coefficient of Power
FVM	Finite Volume Method
CFD	Computational Fluid Dynamics
FOU	First Order Upwind
SOU	Second Order Upwind
SIMPLE	Semi-Implicit Method for Pressure-Linked Equations
RANS	Reynolds Averaged Navier-Stokes
URANS	Unsteady RANS
SST	Shear Stress Transport
RNG	Re-Normalization Group
LES	Large Eddy Simulation
DES	Detached Eddy Simulation
PIV	Particle Image Velocimetry
PMMA	Polymethylmethacrylate
BVI	Blade-Vortex Interaction

CHAPTER 1

INTRODUCTION

Contents

1.1 Introduction

Anthropogenic climate change is a global issue that motivates and persuades the search for sustainable energy sources. The Intergovernmental Panel on Climate Change (IPCC, 2007) highlighted the environmental issues due to the use of fossil fuels which account for more than 80% of the energy needs across the world (IEA, 2008). Pacala and Socolow (2004) suggested a list of solutions to such environmental issues through green energy systems. This research project mainly focuses on the development of an efficient tidal energy system to produce electricity at low water velocities.

In order to build a rapport with the reader, this chapter introduces the research project with background information on the research theme. With the greatest conviction, the motivation and purpose of this research is presented following the statement of the research problem. It is then persevered with research objectives, scope and limitations of the project with an intention of providing everything that

the reader has to know before gearing up for the next phase of the report. This chapter ends with a description of the structure of dissertation.

1.2 Marine systems: A platform for renewable energy

1.2.1 Tidal energy

In the context of a continuous search for alternative energy sources, tidal currents is regarded as strong renewable energy source to replace fossil fuels. Since their emergence, European Marine Energy Centre (EMEC) has encouraged both academics and industrial partners to exploit different systems for extracting energy from water currents. Marine energy can be either extracted from tidal impoundment or by rotating a water turbine. The studies of Miguel and Aydin (2011), and Couch and Bryden (2004) details these two methods. Figure 1.1 summarizes the available methods and technologies to accomplish the energy extraction.

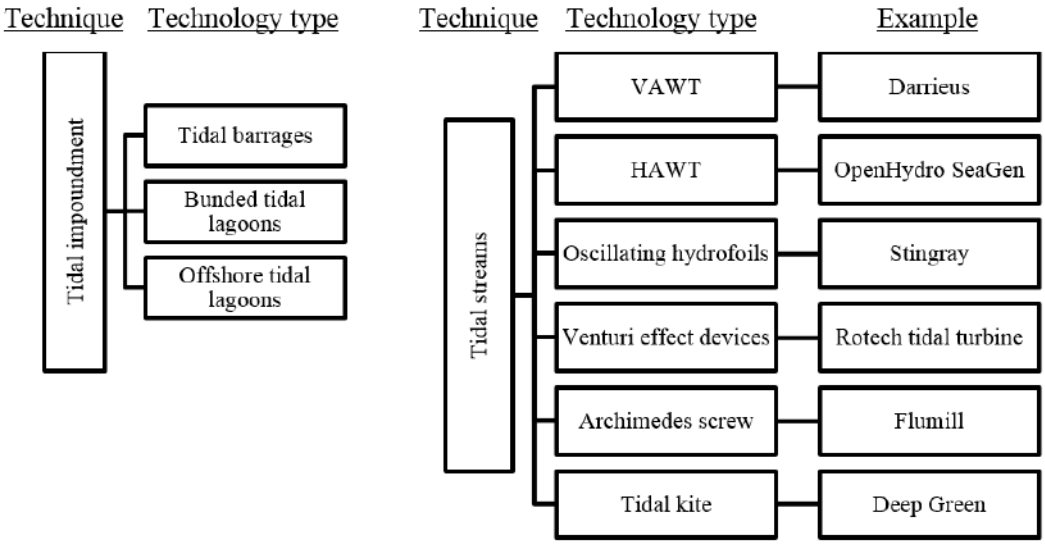

Figure 1.1: Energy extraction techniques

In the process of tidal impoundment, electricity is produced through the conversion of the potential energy of fluid flow as it leaves the barrage. Although the operations of barrage energy extraction units were initiated long ago, tidal energy devices such as turbines have dominated them with strong focus on research and development activities in recent times (Pahl, 2007).

In spite of a relatively low energy density, it is possible to extract the energy from tidal currents under certain flow conditions where the flow speed is higher than 2 m/s or so. The advantage of marine energy systems over other renewable energy sources is that the tidal flow conditions are easily and accurately predictable.

Furthermore, the availability of tidal energy sources like rivers and oceans significantly proposes them as effective energy sources. European Commission (1996) approximated that the majority of tidal energy producing sites in Europe and UK would generate a power of 50 TWh/year. According to Carbon Trust (2011), the coastal water currents in the UK are capable of producing 21 TWh/year which would meet more than 5% of country's energy demand.

1.2.2 Tidal turbine

A water turbine, also called as tidal or marine turbine comprises a set of blades that have specific airfoil sections, attached to a rotor. The system is allowed to pass the water flow through the device whilst the blades rotate about the rotor to generate the power. Despite the fact that the marine energy industry can somewhat expand on experience picked up by the wind turbine industry, and although some tidal turbine plans are fundamentally based on wind turbines, there is a significant distinction between the development of these two devices. Whilst the wind energy is a fast-growing business with a genuinely uniform outline methodology adapted by the manufacturers such as three blades, axis positioning, pitch control etc.., marine current vitality is still in its outset. Various ideas are under scrutiny to find better solutions in the area of marine power extraction.

Organization	Device name	Type	Min/Max speed	No. of turbines per unit	Power output
Thropton Energy Services (UK)	Water Current Turbine	HAWT	0.5 m/s size dependent	1	2 kW
Eclectic Energy Ltd. (UK)	DuoGen	HAWT	0.6 m/s no limit	1	-
Energy Alliance (Russia)	Submerged Hydro Unit	HAWT	Min 3 m/s	1	1-5 kW
Tidal Energy Pty. Ltd. (Australia)	TBD	VAWT	-	1	Velocity and size dependent
Seabell Int. Co., Ltd. (Japan)	STREAM	VAWT	0.6 m/s no limit	2	-
New Energy (Canada)	EnCurrent	VAWT	0.5 3m/s	1	5 kW
Alternative Hydro Solutions Ltd (Canada)	Freestream Darrieus	VAWT	0.5 m/s size dependent	1	2-3 kW
Lucid Energy Technologies (USA)	Gorlov Helical Turbine	Both	No limit for VAWT, 1.1m/s for HAWT	1 or more	20 kW

Table 1.1: Hydroturbine manufacturers and technology summary

UK, Canada and Australia along with European countries including France, Germany and Norway are likely to lead the marine turbine industry and research with several manufacturers and research facilities for device innovations. To the manufacturing end, there are over 100 active developers across the world. Marine Current Turbines Ltd., Alstom Hydro, Voith Hydro, OpenHydro, Sabella, Ocean Renewable Power Company are some of the major players in the industrial sector that are pursuing diverse turbine concepts. Table 1.1 shows some marine turbine manufacturers and their products including technical specifications. In addition to such industrial development programs, several universities have been performing

prospective research in this field (Achard and Maitre, 2006; Amet et al., 2009; Paillard et al., 2013).

1.2.3 Horizontal vs Vertical axis turbine

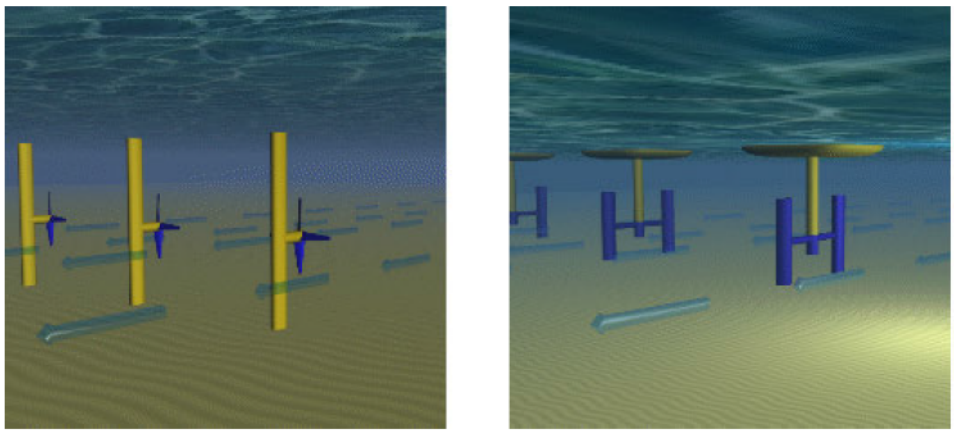

Figure 1.2: Horizontal and vertical axis tidal turbines (©2008 Aquaret)

Although the capitalization of tidal currents seems to be a dependable way of meeting the increasing energy demands, the concern is on how it is done. The popularly known rotor arrangements are horizontal and vertical axis systems, which are shown in Figure 1.2. Horizontal axis water/wind turbines (HAWT) are definitely more classical in usage than vertical axis water/wind turbines (VAWT). A detailed comparison is made in the following points.

- A vertical axis turbine usually require fewer parts than a typical horizontal turbine. Generally, a HAWT should be properly oriented in free-stream flow before the operation to ensure right placement of the device. Unlike this, a VAWT doesn't need a specific orientation since the blade can equally catch the flow in any direction. This is more advantageous when the flow is inclement.

- A conventional HAWT has better performance than a VAWT in terms of power output. According to Malcolm (2003), HAWT systems are 45% - 50% efficient whereas the maximum possible efficiency of VAWTs vary between 35% - 40%. After understanding the technological aspects and flow complexities, Maydew and Klimas (1981) proved that it is possible to produce better efficient VAWT than a similar sized HAWT.

- From the view point of fluid mechanics, the blade's operation in case of a VAWT is azimuth dependent because of continuous change in its effective

incidence with respect to the free-stream flow. In addition, there is a serious concern about blade-vortex interaction. These complexities make the numerical modeling of VAWTs more difficult and therefore the prediction of their ability in power generation is subject to corrections. On the other hand, HAWTs are simple since the blade's performance is theoretically independent of its azimuth position. Also, the blade-wake interaction is limited. This is one of the reasons why HAWTs have enjoyed rapid growth compared to VAWTs.

- From the view point of structural mechanics, the fluid force on HAWT is axial which act on the blades in perpendicular direction which is an azimuth depending action. A constant bending moment is applied on the blades when the turbine operates in a uniform flow. The constant inertial forces act in the direction of blade's axis. In contrast, the fluid dynamic forces acting on the blades of a VAWT promptly vary in cyclic manner. As identified by McLaren et al. (2012), such variations in the forces impose serious structural problems such as vibrations in VAWTs. Another major structural problem with VAWTs relatively more than with HAWTs, as noted by Ashwill et al. (1990), is fatigue because of the continuous cycle of external forces. Since the structural design of the turbine is not within the scope of this project, further consideration on this topic is not made.

- While explaining the possibilities and benefits of pitching blades, Gipe (2009) noted that small HAWTs can achieve 25%-40% improvement in their power output. A straight and fixed bladed VAWT doesn't compromise with the improvement of flow dynamics. This needs a special treatment, which is the major objective of the present research work.

- Often times, the measurements of any wind or tidal turbine are made in uniform flow conditions. When there are directional changes and turbulence in the flow, the assumption of uniformity is no longer valid. When the axis of HAWT rotor is aligned with the flow direction, Loland (2011) explained that these unsteady, non-uniform and turbulent flow conditions disturb the optimal operation and thus reduce the power production. This causes the capacity factor of a HAWT, as defined by the ratio of actual output to potential output over a given period of time, also drops. The VAWTs do not encounter such performance issues due to their omnidirectional operation.

- In a given set of operating conditions, better fluid dynamic performance can be achieved with a HAWT with twisted blades than that with straight blades. Obviously, twisted blades are difficult to manufacture. But, VAWT with straight blades provides a solution to operate in optimal flow speeds. Much

better performance can be achieved by regularizing the torque characteristics by incorporating the helical blades (Priegue et al., 2015; Armstrong, 2011).

- The installation process is another feature that differentiates both systems. The geometry of the VAWTs is so simple that it offers the feasibility to get installed in arrays without disturbing each other. These turbines can be installed more densely without any operational issues in getting higher output. But, HAWTs interfere with each other when there is not enough space between the successive turbines.

This above discussion reveals the fact that VAWTs are not as much optimized and exploited as they could have been, due to the complexity associated with its flow dynamics. VAWT is surely an effective green energy source in terms of production, installation and operation. With new developments in design and technology, VAWTs can be used in much better way to extract the power in optimum conditions. More research projects and development programs in this area can bring commercial success to these machines.

1.3 Problem statement

Energy demands are ever-increasing phenomena across the world. With boosting technological applications and human interest in realizing more sophisticated life, 21st century is characterized by rigorous needs for energy as never before. Coal was the prime and only energy source in early 20th century. This raw material was competed by oil and gas after Second World War and there was a drastic shift from carbon to hydrocarbon based energy sources due to their higher energy density. Robelius (2007) noted that fossil fuels supply 40% of total energy for global needs, and also supplied various estimations of the depletion of oil & gas and cost predictions of traditional energy supply.

Apart from the concern about energy resources and availability, the sensitive issue lies in the environmental impact created by the consumption of hydrocarbon fuels. Several global organizations such as Division of Early Warning and Assessment of UNEP-France, World Meteorological Organization-Switzerland, Global Facility for Disaster Reduction and Recovery, International Water Association-London, United Nations Framework Convention on Climate Change-Germany, Arctic Monitoring and Assessment Program, Norway have been adequately addressing the climate change issues and greenhouse effect. Richardson et al. (2009) identified that there was a drastic increase in greenhouse emissions in past half century all over the world. Their study noted how climate indicators including mean surface temperature, sea level rise, ocean temperatures, ocean acidification etc... are already showing abnormal variations. On one hand, these implications pose serious problem to the energy world. On the other hand, more energy is

sought to meet increasing needs. Renewable energy sources in this context are free and inexhaustible which are available in abundance.

The Darrieus type is the most common vertical axis turbine model used in tidal and wind energy industry. A typical Darrieus rotor is simple in construction and generally consists of 2 to 4 blades. The system rotates at higher speeds than the incoming flow for better power characteristics so that the tip-speed ratio is maintained more than 1. Although Darrieus turbines require no blade pitch control for synchronous applications (Singhal et al., 2009), an efficient pitch control of the blade, as it travels through azimuth, can increase the torque characteristics (Cheng et al., 2012; Lazaukas, 1992).

1.4 Research objectives

The development of advanced methods to enhance the performance of a conventional energy device such as a Darrieus tidal turbine requires a base for constructing the techniques. A deeper knowledge of the local flow field around the blades is necessary to apply these techniques in real flow conditions. Taking this into consideration, this thesis sets out the following objectives.

- Development of blade pitch control laws for preventing the vortex formation based on ideal flow concepts and analytical calculation of torsor effects.
- Numerical evaluation of flow fields and turbine's performance with fixed and pitching blades for comparing the real flow conditions with ideal ones.
- Identification of feasible blade pitching regimes for performance optimization.
- Experimental validation of computational results using torque and velocity measurements.

1.5 Scope and limitations

This study presents a comprehensive investigation of a vertical axis water turbine of Darrieus type with straight and fixed/pitching blades. A concrete base for developing the pitch control laws was constructed with a focus on improving the power characteristics of the turbine and controlling the vortex shedding from the blades. This analytical work is based on the potential flow framework and supported by CFD analysis. An experimental investigation completes these analyses to provide all facets of an effective research on developing a hydroturbine. The design parameters concerned in this study cover free-stream velocity (V_0), tip-speed ratio (λ) and solidity of the turbine (σ). For pitching blade studies, various pitching regimes were tested. The relationship between the turbine's performance and various flow

variables required numerous parametric studies, which led to acquire the optimum operating and design conditions.

In this research, only NACA 0015 blades were considered for the sake of simplicity. In developing the turbine models, 100% manufacturing accuracy with allowable tolerance were assumed. During the experimental studies, power transmission losses from motor to turbine were neglected. Uncertainties in the motor's operation as well as the carriage's linear motion were found in the order of $\pm 1\%$, which were specially treated to assess their propagation in the solution domain.

Another critical limitation of this study is the confinement of the computational and experimental analysis to 2D hydrofoil under constant flow and turbine's rotational velocities. Such investigations have reduced the computational cost, laboratory efforts and time. Therefore, more sophisticated models may be required to examine complex physics such as dynamic stall, vortex formation and dispersion, blade-vortex interaction etc... in 3D analysis.

1.6 Structure of the dissertation

This dissertation is divided into 7 chapters; Figure 1.3 shows the coherent process by linking all chapters which the project has followed during the course of time.

Presenting the background of the current project topic, Chapter 1 - *INTRODUCTION* establishes the research platform by discussing the need for green energy sources, rationale for the project, objectives, scope and limitations of the research. Chapter 2 - *LITERATURE REVIEW* consists of a survey of scholar and industrial works related to the project. It also presents the evolution of researches in Darrieus turbine design with fixed and pitching blades with an emphasis on analytical models, computational analysis and experimental studies with an equal importance of design parameters. Such a review of existing sources of information can justify the need for the present research by identifying the gaps and therefore lay a path to build an efficient methodology to proceed with the project.

Chapter 3 - *COUCHET POTENTIAL & PITCH CONTROL LAW* portrays the analytical framework with complete hydrodynamic analysis and the development of a pitching blade control law, which is based on the potential flow concepts. The objective of preventing the vortex formation from the blades is achieved by imposing a constant circulation around the moving blades. A complete demonstration of the pitch control methodology through mathematical exertion is presented alongside the identification of effective pitch control regimes.

This theoretical work leads to the evaluation of conventional Darrieus turbine both numerically and experimentally. Chapter 4 - *FIXED BLADE MODEL: COMPUTATIONAL ANALYSIS* starts with the fundamental understanding of CFD applications followed by the computational methodology in detail. Computational analysis for benchmarking was performed using a commercial CFD solver,

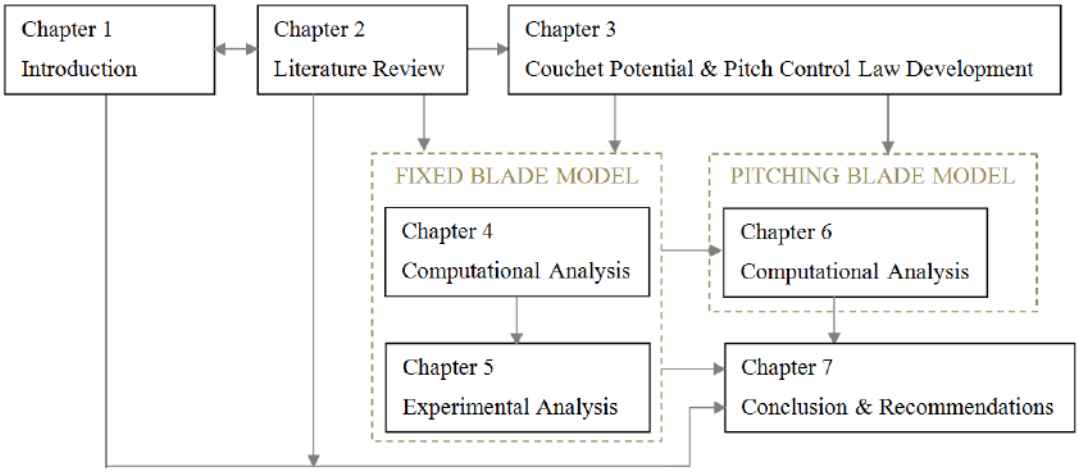

Figure 1.3: Information flow chart of the dissertation

Star CCM+ where overset meshes were used to incorporate superposing body motions. Pre-processing, processing and post-processing steps are described and the need for result validation is explained. A full range of CFD results are presented and analyzed.

Understanding the importance of validating the computational results, Chapter 5 - *FIXED BLADE MODEL: EXPERIMENTAL ANALYSIS* describes the laboratory methodology adapted in this research. A digital Particle Image Velocimetry (PIV) system, fully synchronized with torque acquisition set-up is used. The torque and PIV results are used to validate the CFD findings. The effect of tip-speed ratio λ, solidity σ and free-stream velocity V_0 was calculated. Quantitative results mainly comprise the torque measurements and power coefficient evolution, while a qualitative analysis is based on flow field structures around the blade (local) as well as turbine (global).

The effectiveness of the constant circulation applied to the blades is explained and analyzed in Chapter 6 - *PITCHING BLADE MODEL: COMPUTATIONAL ANALYSIS*. While exploring the pros and cons of this framework, a variable circulation imparted to the blades is examined and its performance is tested against that of the classical turbine and constant circulation schemes. Corresponding pressure, velocity and vorticity fields, and power characteristics are presented, leaving the concluding remarks to the next chapter.

Chapter 7 - *CONCLUSION AND RECOMMENDATIONS* summarizes the key revelations of the analytical, numerical and experimental analysis of Darrieus turbine's hydrodynamics with fixed and pitching blades, in order to prove that not only the research objectives have been fulfilled but also contribute to present day research activities in fluid mechanics. This report ends with constructive recommendations to build a forward path for future research.

CHAPTER 2
LITERATURE REVIEW

Contents

2.1 Introduction

In Chapter 1, the introduction for research project was provided where the tidal energy sources were identified as effective alternatives to hydrocarbon fuels for increasing energy demands across the world. The motivation to reduce the carbon footprint and hence the risks associated with global warming constitutes the key driving force to develop the renewable energy technologies. This chapter presents detailed information of a vertical axis tidal turbine including the terminology used in developing a device, its working principle and salient studies conducted to test

such a device computationally and in laboratory. However, the delated information supplied by numerous scholars pertained to the present research topic is likely to throw the reader into a turmoil state. This chapter therefore reviews the existing literature in 5 sections. Starting with the discussion of Darrieus turbine operation, the design parameters and their influence on the turbine's performance is explained. In the next section, the investigation methods usually employed to investigate the performance of a Darrieus turbine are clarified. The difference between the ideal Betz limit and the performance of a turbine in a confined flow is explained. Finally, relevant scholastic studies on the performance improvement techniques and their results are demonstrated. The whole structure of literature review assists the researcher in preparing a suitable methodology. Such a wider, but not exhaustive, literature review helps to find the gaps in the existing scientific sources.

2.2 Operation of Darrieus turbine

A Darrieus machine can be either a wind turbine or water turbine whose axis is positioned in transverse direction to the fluid flow. The principle of operation was patented by the French engineer, Darrieus in France and USA in 1925 and 1931 respectively. Patent details are available in the references. Irrespective of the application, all of Darrieus models work on the same principle as shown in Figure 2.1. When an aerodynamic or hydrodynamic profile rotates in a flow transverse to the axis of rotation, force is generated whose tangential component leads to the thrust. Before presenting the principle of operation in detail, characteristic parameters related to the Darrieus machine design are discussed.

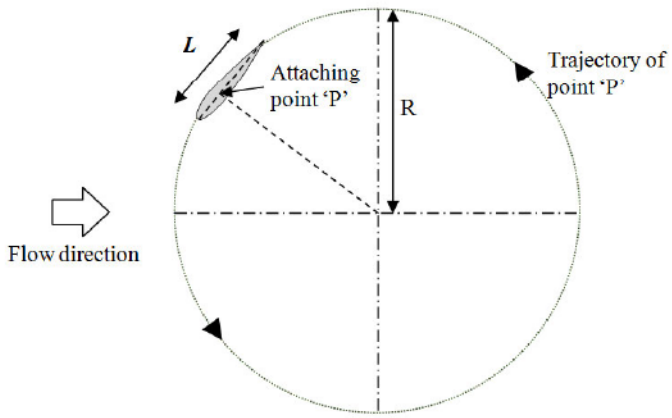

Figure 2.1: Sectional view of Darrieus turbine operation

2.2.1 Design parameters

Referring to Figure 2.1, consider a Darrieus model with N number of blades of symmetrical profiles whose chord length is L and rotate at a distance of R from the rotor's centre. The point P makes the joint between the blade and connecting rod of the rotor. The swept area of the turbine A is useful in comparing different turbines is defined for a straight bladed device as

$$A = 2Rh \tag{2.1}$$

where h is the height of the rotor.

With this information, the geometry of the turbine is characterized by means of some dimensionless quantities. One such parameter is the solidity σ which defines the degree of blockage offered by the turbine to the flow. Mathematically, solidity σ is defined by

$$\sigma = \frac{NLh}{A} = \frac{NL}{2R} \tag{2.2}$$

The solidity of the blade or the chord-to-radius ratio L/R is now defined as the ratio of blade chord to the rotor's radius.

2.2.2 Functional parameters

Apart from the design factors, there are external conditions, called functional parameters which have major impact on the turbine's performance. Two such parameters are the free-stream velocity V_0 and rotor's rotational velocity ω. A dimensionless quantity is deduced from these two parameters, called the reduced velocity or tip-speed ratio λ which is defined by

$$\lambda = \frac{R\omega}{V_0} \tag{2.3}$$

Tip-speed ratio λ strongly influences the fluid dynamics across the turbine and therefore the turbine's overall performance. The flow regime is characterized by the Reynolds number Re, which is the ratio of inertial force to viscous force. Reynolds number is expressed as

$$Re = \frac{R\omega L}{\nu} = \frac{\lambda V_0 L}{\nu} \tag{2.4}$$

Here, the blade positioning has no effect on Re during the studies of the local flow around the blade because the rotational velocity is used in the definition of Re. Another dimensionless parameter, Mach number M, compares the flow velocity with the acoustic speed a in order to characterize the compressibility of the flow. This is defined as

$$M = \frac{R\omega}{a} = \frac{\lambda V_0}{a} \tag{2.5}$$

For hydroturbines, the flows are usually considered as incompressible since $M << 0.3$.

2.2.3 Hydrodynamic analysis of Darrieus turbine

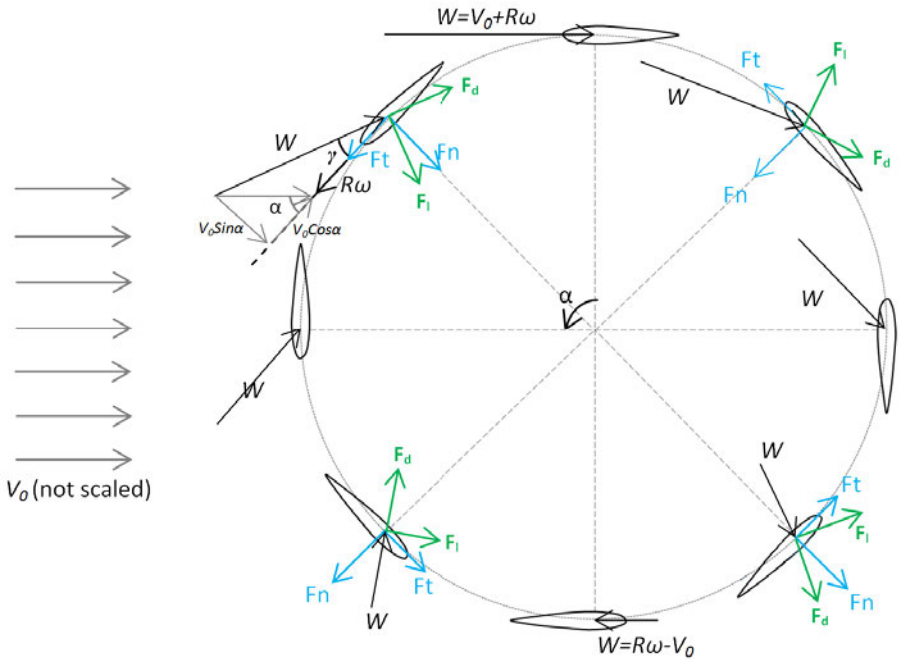

Figure 2.2: Velocity and force vectors acting on the blade at various azimuth positions

Figure 2.2 shows the velocity vectors and force components around the Darrieus turbine blade as it travels through the complete azimuth. Effective angle of attack of the blade γ changes with the azimuth angle α and the tip-speed ratio λ as the blade completes a cycle. Equation 2.6 defines this variation of γ which can affect the blade stall phenomenon in a cycle.

$$\gamma = \tan^{-1}\left(\frac{\sin\alpha}{\lambda + \cos\alpha}\right) \tag{2.6}$$

The azimuthal variation of the angle of attack γ affects the relative velocity W of the blade. Refer to Figure 2.2, the blade relative velocity W is defined as,

$$W = \sqrt{(V_0 \sin\alpha)^2 + (V_0 \cos\alpha + R\omega)^2} \tag{2.7}$$

Equations 2.6 and 2.7 have the graphical representation in Figures 2.3 (a) and 2.3 (b) respectively, where the blade incidence γ and relative velocity W are plotted as functions of azimuth angle α.

The analysis of effective angle of attack γ of the blade and relative velocity W as a function of tip-speed ratio λ forms the platform for the present research.

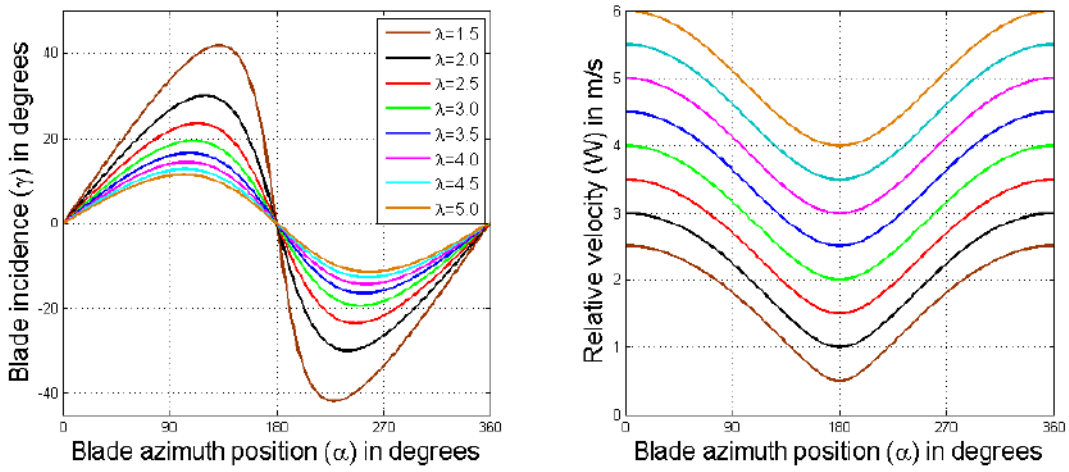

(a) (b)

Figure 2.3: Azimuthal variation of blade incidence γ and relative velocity W for different tip-speed ratios λ

Upcoming chapters will discuss these relations extensively for the computational analysis. During the blade's motion along the azimuth, the blade's incidence plays an important role in creating the hydrodynamic forces. Therefore, the thrust and normal forces also vary with the blade's travel and also with the tip-speed ratio λ. Structural investigation of these forces leads to the analysis of turbine's performance. Tangential component of the force F_t is of paramount interest in this research because the assessment of kinetics and their effect on the power characteristics mainly depends on the tangential force. Figure 2.2 assists to find the relationship between the tangential and normal components of the force (F_t and F_n), and lift and drag forces (F_l and F_d), which are defined as

$$F_n = F_l \cos\gamma + F_d \sin\gamma \tag{2.8}$$

$$F_t = F_l \sin\gamma - F_d \cos\gamma \tag{2.9}$$

Finally, the performance of the turbine is mainly calculated in terms of the power output P of the turbine, which is defined as

$$P = F_t R\omega \tag{2.10}$$

The dimensionless power factor, called coefficient of power COP is the key parameter used in this study to measure and compare the device's performance under various conditions. Equation 2.11 defines the COP.

$$COP = \frac{P}{0.5\rho A V_0^3} \tag{2.11}$$

2.3 Darrieus turbine performance evaluation

2.3.1 Blade thickness and camber

Before discussing the turbine's design parameters, it is necessary to understand the suitability of available blade profiles for Darrieus turbine applications. Jacobs and Sherman (1937) supplied the information of the NACA sections and their performance for varying Reynolds number Re, which persuades to select the symmetrical sections for current research. The computational studies of Danao et al. (2012) presented the effects of blade thickness and camber on the performance of small scale Darrieus turbine. Thinner profiles experience higher pressure coefficient and extract more energy from the fluid flow. Therefore, thinner profiles are better in performance than the thicker profiles. This study also noted that the profiles with a smaller camber like LS0421 yield better performance for Darrieus turbines when compared to those with higher camber. This is supported by Healy (1978a), where it is noted that slightly cambered airfoils can provide better performance, with a proper control on the excessive rotational velocities of the turbine. In the study of Beri and Yao (2011) about self-starting VAWTs, cambered profiles were proven to deliver the best performance at optimum flow velocities.

The studies of Healy (1978b) on the examination of symmetrical airfoils using multiple-stream tube model on a wide range of Reynolds numbers revealed that thicker sections perform better than the thinner sections at low Re. This is due to the fact that the thicker profiles can resist stall phenomenon better than the thinner ones. The disagreement between these results, and those of Danao et al. (2012), and Beri and Yao (2011) is mainly because of the differences in the respective numerical methodologies. This type of analysis on the effect of blade camber on the performance capabilities as well as starting torque has the genesis in early studies of Baker (1983) and Kirke (1998). The findings of these two studies consolidated that camber has a positive impact on the starting characteristics as well as power extraction from the fluid flow during the upwind part of cycle which would cause a considerable improvement in the overall turbine performance.

McIntosh (2009) through the parametric studies identified that the maximum power coefficients attained by thinner blade profiles are higher than those by thicker profiles. In addition, profile thickness was found to be an important parameter in defining the power curve slope; thicker the profile, steeper the power curve. The optimum tip-speed ratio λ_{opt} for thinner airfoils is higher than that for thicker profiles which reveals that the performance of thicker blade sections is superior to thinner sections when the tip-speed ratio λ rapidly changes during the operation.

The scope of the present research work does neither comprise the self-starting capabilities of Darrieus turbine nor the consideration of rapid changes in tip-speed

ratio λ. The choice of blade profile is therefore limited to the simplest design. Also, the structural stability under hydrodynamic loading is a key consideration for the blade fabrication during the prototype development. NACA 0015 is the thinnest usable profile for our experimental model. Based on this argument, NACA 0015 is chosen for CFD studies as well as in prototyping.

2.3.2 Solidity σ

For rotating machines, solidity σ is one of the major influencing design parameters as the device performance is concerned. From the definition of solidity σ given by Equation 2.2, it is clear that σ is solely a function that decides on the turbine's geometry. Due to its importance in influencing the device performance, numerous articles were published on its effects in turbomachines. The actuator disc theory (Glauert, 1948) examines theoretical influence of solidity on the overall performance. Based on this, Templin (1974) developed a computational model for single streamtube application which considered σ ranging from 0.05 to 0.5. This assumed a constant velocity induction factor a, which is defined as the free-stream velocity flow through the actuator disc i.e., $(V_1 - V_2)/V_1$. From the results obtained by Healy (1978b) shown in Figure 2.4, it is noted that the maximum power increases with increasing solidity until it reaches a certain value, beyond which the peak falls down at a quicker pace. Also, the optimum operating range identified from COP-λ curves is wider for the turbines with lower solidity. However, there is a danger of increasing centrifugal stresses in case of low solidity models due to their higher optimal tip-speed ratio. These studies considered static airfoil data and neglected blade-wake interactions, which resulted in extremely higher and unrealistic COP values.

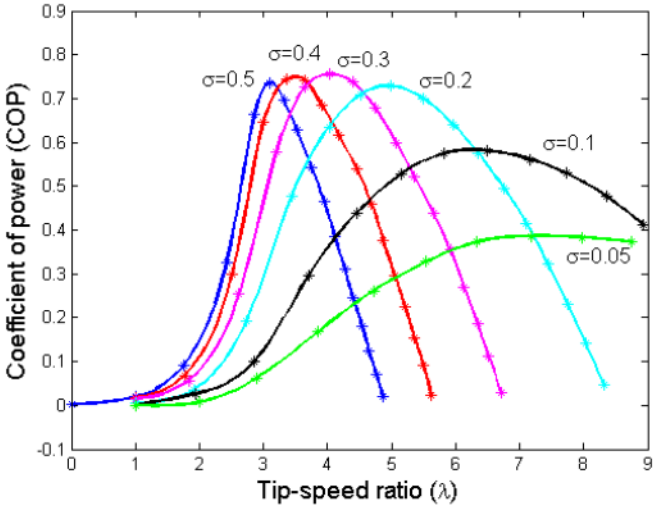

Figure 2.4: Effect of solidity σ on COP curve (Healy, 1978b)

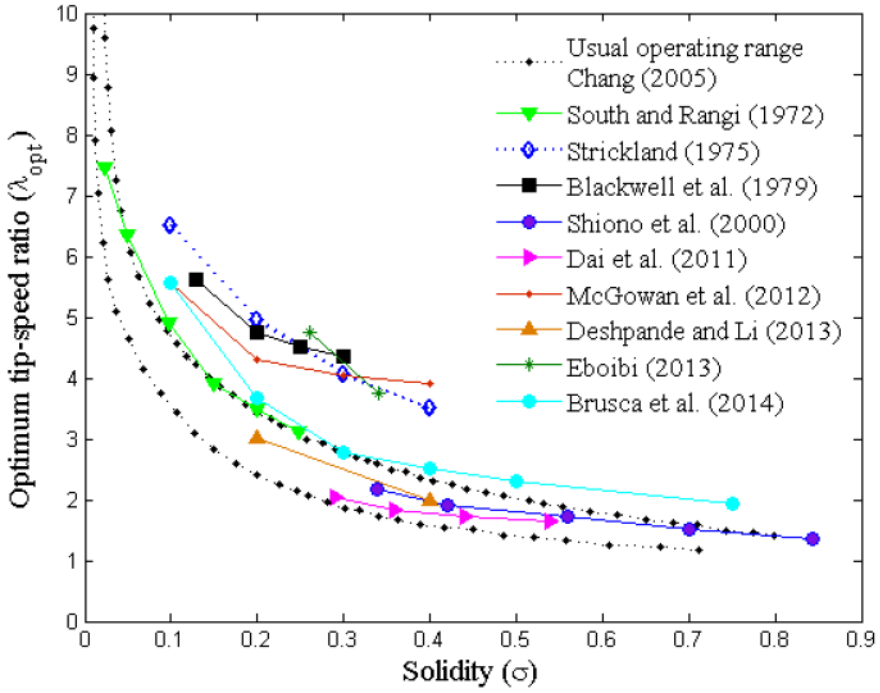

Figure 2.5: Effect of solidity σ on the optimum tip-speed ratio λ_{opt} from literature survey

The primary effect of solidity σ on the turbine's operation is to create the blockage effect to the incoming flow. The blockage is not merely limited to the free-stream, but extends to wake. This means that the presence of a solid body causes the flow to deviate around the turbine as well as create a velocity deficit. This is because of the recovery of kinetic energy which causes a portion of the fluid to flow on either side of the rotor to balance the mass budget. Larger solidities result in greater expansion of the streamtube passing through the rotor and lower flow velocity within the rotor.

Another key feature is the reduced blade incidence due to the velocity deficit inside the rotor. At lower values of λ, this phenomenon leads to stall. Consul et al. (2009) explained how the turbine with higher solidity prevents the drop and rise in the performance. At higher tip-speed ratio λ, the blades operate at lower incidence which results in a loss of efficiency. Chang (2005) identified the usual range of optimum tip-speed ratio λ_{opt} for a wide range of solidity. A collection of published results from research articles for the optimum tip-speed ratio λ_{opt} for the corresponding model solidity is plotted in Figure 2.5. Most of the results are consistent with the Chang's usual operating range.

As the solidity of the turbine increases, the maximum COP drops and attains lower operating regions of λ. Such turbine models exhibit sharply sloped COP

curves, compared to low solidity designs. These points are explained by Figure 2.6, where the effects of solidity σ on the turbine's power coefficient is illustrated. This figure compares the turbine with 0.75 solidity σ, which was analyzed using momentum model by Mays and Holmes (1979), with four different models with lower solidity, examined by Templin (1974). Higher solidities result in peaky COP curve with narrow operating range. The maximum COP becomes less sensitive to the changes in tip-speed ratio until λ reaches approximately 5. These studies accounted for the sensitivity parameter, based on the upper and lower limits of λ for acceptable performance output. The overall trends of the models shown in Figure 2.6 complement each other.

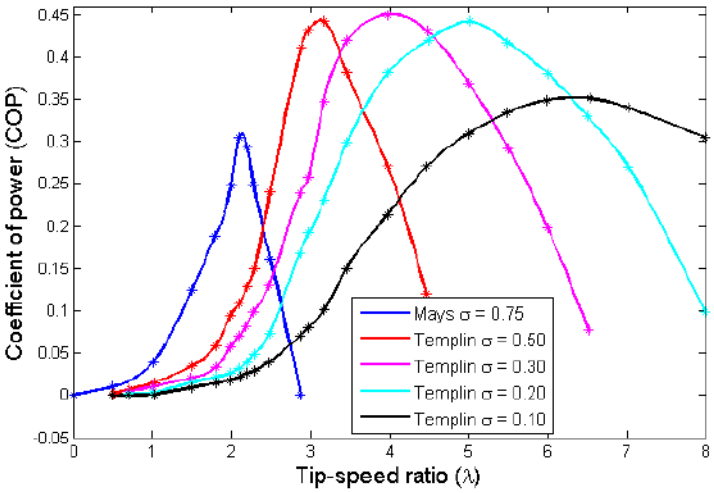

Figure 2.6: Effect of solidity σ on the turbine's performance (Kirke, 1998)

Further understanding about the effects of solidity σ is available from the study of Eboibi et al. (2013) where a three-bladed VAWT model with three different solidities, $\sigma = 0.2$, 0.6 and 0.98 were computationally investigated. Symmetrical NACA blades with 12% and 22% thickness distributions were used and compared for performance and visualization results. As shown in Figure 2.7, the NACA0012 profile was found to have better maximum COP at all of the tip-speed ratios. Both the sections attained the same optimal tip-speed ratio λ_{opt} of 4.5, 2.5 and 2 for the chosen solidities respectively. All of the solidity models with NACA0022 blades provided better power features at λ less than 3. This result was also supported by Templin (1974) which stated that the thicker profiles yield better performance at lower values of λ.

This notes on the solidity effects on the overall turbine's output throws light on the consideration of σ as a key design parameter. In this research, four models with different solidity σ were considered. The solidity σ is altered based on the rotor's diameter. These models were computationally studied for the performance measurements as well as flow visualizations and critical analysis is carried out.

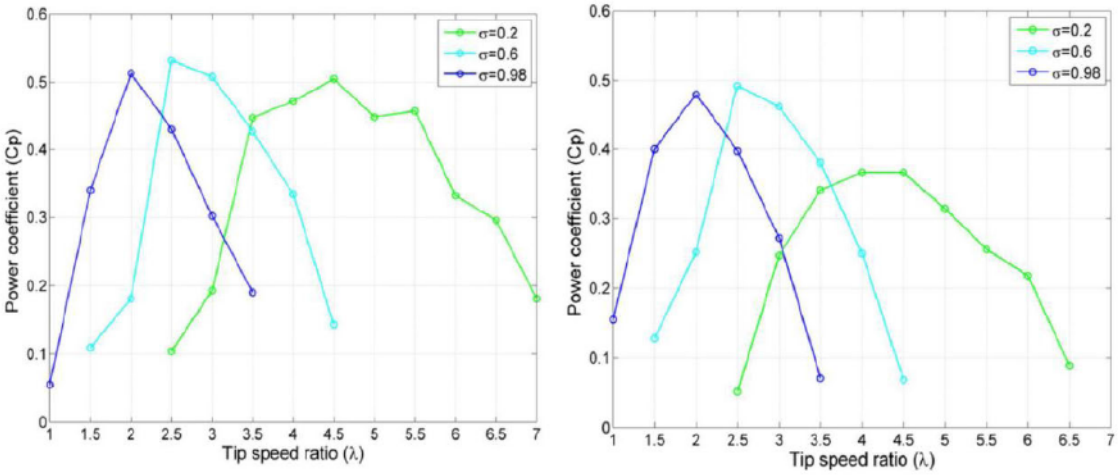

(a) NACA0012 (b) NACA0022

Figure 2.7: Effect of solidity by varying the blade section (Eboibi et al., 2013)

The experimental validation is however conducted only for the base model with $\sigma = 0.533$.

2.4 Darrieus turbine investigation methods

There are various methods available to investigate the flow and performance of any low Reynolds number turbomachine. Broadly, these are classified into computational and experimental methods. Although both the methods are quite effective in assessing the VAWT, they have their own advantages and disadvantages from the stand point of present research. Table 2.1 provides specific knowledge about the pros and cons of these two methods. The complete validation of numerical results with experimental process is described in Chapter 4. In this section, we present the methods of computational and experimental analysis employed by various scholars in their studies of VAWT.

2.4.1 Numerical studies

The development and application of numerical methodologies for finite volume methods for the studies of flow problems such as VAWT increase the accuracy, when compared to vortex or momentum modeling methods. Advanced hardware capabilities have enabled the application of CFD to complex flow problems at adequate resource deployment. The end results of a typical CFD study are not only limited to visualization of flow field across the virtual prototype and measurement of scalar parameters, but can be extended to more advanced purposes such as uncertainty analysis and shape/property/process optimization, which may not be feasible with experimental techniques. Flexibility in modeling the solid body is

another advantage in CFD studies. The numerical studies do not rely on the external data since CFD can calculate the flow induced forces on the turbine model autonomously. Therefore, this research has chosen CFD as an investigation method for VAWT analysis. This section presents a survey of CFD studies that were conducted by scholars for VAWT test cases.

2.4.1.1 Fluid dynamics and performance

In the examination of 20 airfoils of both symmetric and non-symmetric type for the efficiency improvement, Mohamed (2012) noted that no specific profile shape has been found till now for VAWT application. This study identified the supremacy of S-1046 section over NACA symmetrical sections for low solidity applications. In spite of its technical data and relevance to modern VAWT research, this study suffered from methodological drawbacks such as insufficient mesh resolution particularly at leading and trailing edges. With reference to experimental data, this resulted in prediction inaccuracy.

The relationship between the tip-speed ratio λ and flow physics is subject to a number of investigations. One such study was performed by McLaren et al. (2012) which considered the 3-bladed Darrieus turbine model with NACA0012 profiles for CFD studies using SST $k-\omega$ viscous model. The resulting force coefficients were validated against experimental results. These results are consistent with the studies on the low solidity and high solidity models by Templin (1974), and Mays and Holmes (1979) respectively. This shows that VAWT has experienced a high fidelity analysis long time ago.

An interesting study on the 2-bladed Darrieus turbine model for dynamic stall analysis using 2D CFD computations was conducted by Amet et al. (2009) and the results are in agreement with the experimental data provided by Laneville and Vittecoq (1986). This study used a refined $k-\omega$ viscous model, developed by Kok (1999) and analyzed the effect of extreme operating conditions at $\lambda = 2$ and $\lambda = 7$. Stalling behaviour was scrutinized as a key difference between the operation of wind and hydro VAWTs. The largest amount of vortex shedding during the cycle is associated with undesirable performance of the turbine.

When the self-starting capabilities of a small scale 3-bladed VAWT model was tested by Untaroiu et al. (2011) using standard $k-\epsilon$ turbulence model for both 2D and 3D CFD cases and validated against the laboratory results supplied by Hill et al. (2008), over-prediction by 2D simulations and under-prediction by 3D simulations were observed. The validated results in this study are in comparison with the findings of Howell et al. (2010). However, the incapacity of $k-\epsilon$ model to capture transition at low Reynolds numbers resulted in a limited accuracy. More accurate near-wall modeling and application of blended turbulence models might be necessary to capture the transitional effects.

Computational methods	Experimental methods
Main features	
Wide and flexible solid modelling capabilities Wide range of turbulence models and applicability to different media Capable of simulating the complex phenomenon (dynamic stall, vortex shedding, BVI etc ...) Multiple solvers and turbulence models (RANS, LES, DES etc ...) are available Strongly rely on the assumptions made Excellent post-processing capabilities User-oriented interface and support facilities which make 'user-friendly'	Physical reproduction of the flow Limited number of designs and geometry Divided into laboratory and field testing procedures Practical conditions can be realized in the laboratory experiments Standardization of the procedure allows the repetition wide range of kinematic parameters Uncontrolled structural parameters
Speed and accuracy	
Moderate/slow processing depending on the solver settings and flow complexities More accuracy can be accomplished with additional time resources	Time consuming for the best accuracy with the deployment of appropriate skills Almost instantaneous raw measurements Heavy post processing on advanced measurements
Cost	
High to very high	Huge financial resources are required. Also, materials, skills and human efforts are highly needed
Limitations	
Fair knowledge and expertise is needed Large and precise input information is required Standard procedure to solve the conservation equations is time consuming Proper validation against experimental data is required	Higher cost propositions cause to assess a low number of parameters Errors from environmental factors are possible which cannot be controlled The size of experimental facility such as towing tank are limited which can pose serious limitations like blockage effect Measured performance may not be realized in real applications

Table 2.1: Comparison of VAWT investigation methods

For the transient analysis of the flow across a 3-bladed Darrieus turbine with NACA0018 sections, Iida et al. (2007) carried out Large Eddy Simulation, which revealed an inverse relationship of flow divergence and dynamic stall phenomenon

with the tip-speed ratio λ. The study however lacked the verification and validation of the numerical results.

Based on the above discussions, CFD creates an obvious platform for flexible and acceptable solutions for the VAWT analysis, although the reliability of the results is always subjective. Higher computational costs that are usually tied up with the VAWT studies using CFD pose a serious limitation for intensive numerical analysis. The accuracy of computational studies can be improved with appropriate definition of boundary conditions and implementation of right methodology. The credibility of the CFD work is still in need of verification and validation, which is discussed in the following.

2.4.1.2 Verification and validation

Verification and validation provides a quantitative evaluation of CFD models to ascertain the trustworthiness of computational results. This involves the comparison of numerical findings with experimental results which are considered standard and more accurate. With sufficient insight and careful practice, the verification and validation process can reduce, or sometimes avoid, the level of conflict between the observations of numerical and experimental tests, and bring consistency with the secondary data sources. An inspection on how scholars have validated their CFD models in their studies on VAWT was performed and the details are presented in this section.

The studies of Castelli et al. (2010, 2011) included the validation of CFD models applied for VAWT studies against wind tunnel experimental results. Since the purpose of these studies was confined to compare the quality of the results, the performance of the turbine in terms of COP was only taken into account, but no flow physics. Such studies have voids in the process of verification and validation as they could not make a decision of choosing the right CFD model.

The experimental studies on a VAWT model with symmetrical airfoils were conducted by Howell et al. (2010), taking into account the surface roughness of the blade and solidity of the model under a range of operating conditions. Figure 2.8 shows the comparison of numerical and experimental COP. Unlike other studies mentioned earlier, this study delivered different fashioned COP curves where 2D CFD model was over-predicting the experimental results and 3D CFD model was under-predicting at higher values of λ. Though a clear knowledge about the performance of VAWT is acquired by establishing a constructive relationship between the operating conditions and tested parameters, this study could not develop the scientific base for adopting the RNG $k-\epsilon$ turbulence model.

Extending to further comments, the studies of Castelli et al. (2010, 2011) are revisited here. Their parametric studies in a low turbulence wind tunnel were used to validate the 2D numerical results which used realizable $k-\epsilon$ turbulence model

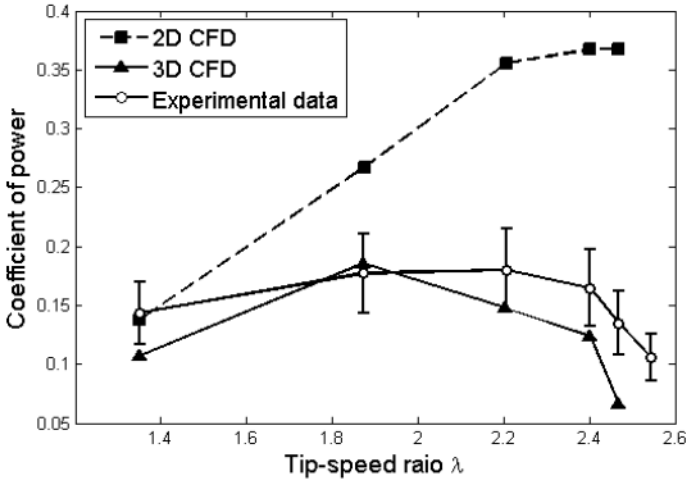

Figure 2.8: Verification and validation of 2D and 3D CFD models (Howell et al., 2010)

with enhanced wall treatment. The selection of the viscous solver was based on the commercial software documentation.

In the context of over-predicting 2D CFD studies, and concerning the complexities and computational resources associated with 3D computational analysis, the study of Ferreira et al. (2007) is worth noting. In this study, flow field visualization was used to verify and validate the 2D numerical modeling for a Darrieus turbine case. Some of the results for non-dimensional vorticity are shown in Figure 2.9. At a tip-speed ratio $\lambda = 2$, both laminar and turbulent solvers were used to capture the dynamic stall phenomenon and compared with PIV data available from the investigations of Ferreira et al. (2007). The following two points are concluded from these studies.

1. Spalart-Almaras model was not successful in predicting the dynamic stall of a 2D VAWT at lower values of λ.

2. $k - \epsilon$, LES and DES models exhibited approximately same trends in the force evolutions for the first half of turbine cycle, but provided dissimilar vorticity fields. Therefore, mere comparison of global power characteristics of the turbine is not sufficient for verification and validation.

As an answer to the shortcomings of the studies of Ferreira et al. (2007), a comprehensive verification and validation of CFD modeling was done by Edwards et al. (2012). Using the CFD information about pitching airfoil behaviour under laboratory testing conditions, provided by Lee and Gerontakos (2004), this study compared both quantitative and qualitative numerical measurements with the experimental data. This study noted that SST $k - \omega$ turbulence model is the best

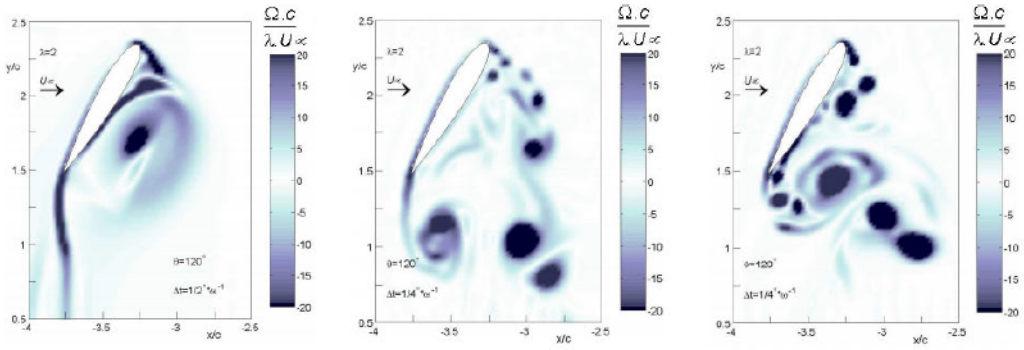

(a) $k-\epsilon$ model (b) LES model (c) DES model

Figure 2.9: Comparison of various turbulence models in capturing the non-dimensional vorticity (Ferreira et al., 2007).

suitable for measuring the force coefficients as well as predicting the flow physics across the Darrieus turbine. There is a close match between the numerical and experimental calculations of power curves, but there is a 10^o phase lag with CFD field representation compared to PIV results. It is therefore noted that uncertainties in the phase angle for comparison purpose is very difficult to avoid and an order of millidegrees for every phase measurement of 10^o may be acceptable. Although there are some concerns about the low Reynolds number transition effects in the CFD studies, the overall performance of SST $k-\omega$ model was satisfactory. Figure 2.10 shows some of these validation results. A number of scholars (McLaren et al., 2012; Danao et al., 2012; Amet et al., 2009) have adopted SST $k-\omega$ for VAWT studies. Thus, in the present research, SST $k-\omega$ is used for the turbulence modeling of the flow across a Darrieus turbine. The rationale for adopting this model, its fidelity and adequacy for VAWT CFD studies is discussed in Chapter 4.

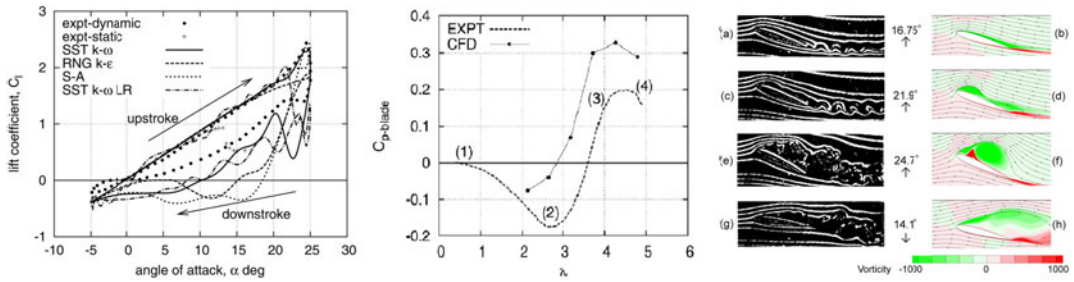

(a) Lift coefficient (b) COP curves (c) Flow pattern

Figure 2.10: Verification and validation in the case of pitching airfoil (Edwards et al., 2012)

Considering the unsteadiness and complexity in the operation of Darrieus

turbine, a suitable verification and validation process is definitely necessary for performing a reliable analysis. The computational studies performed during the present research are therefore complemented by the experimental results.

2.4.2 Experimental studies

Experimental investigation of any flow problem is considered as the most reliable technique since it tends to replicate realistic operating conditions within the test facility. There are however some serious limitations including huge costs, requirement of numerous technical competences such as manufacturing, data acquisition, time concerns and many other factors related to equipment and environment.

Sandia National Laboratories carried out the field tests on 5m, 17m and 2m curved bladed Darrieus wind turbine in 1974 to determine various design elements and measure machine's performance. The experiments focus mainly on the effect of number of blades, 2 and 3, on the turbine's performance, influence of blade camber and the design processes such as mounting the accelerometer, drag brake, welding etc... Such field tests experience the inability to control environmental conditions and flow parameters, which encourage the laboratory investigations. This section presents experimental studies performed by various researchers to analyze the flow across a Darrieus turbine.

2.4.2.1 Particle Image Velocimetry (PIV)

Particle Image Velocimetry (PIV) has been broadly used to measure and analyze the flow fields. For the flows across the Darrieus turbine, numerous studies were performed and some of them are referred in this section.

Fujisawa and Shibuya (2000) conducted a PIV campaign for the analysis of a small scale vertical axis water turbine of Darrieus type with a focus on dynamic stall in stationary and rotating reference frames. The transient dynamics of stalling process and shedding of small vortices in pairs were clearly captured when the velocity vector distributions were used to reconstruct the field. This study pointed out that the tip-speed ratio λ has little effect on the characteristics of the dynamic stall phenomenon but stall appearance and its growth rate are influenced by the changes in λ. While their experimental study was performed at a Reynolds number Re=3000, the PIV experiments of Ferreira et al. (2007) took place at a Reynolds number Re=50000 and 70000 to validate the 2D CFD results of flow past a single-bladed turbine model at a fixed tip-speed ratio $\lambda = 2$.

In recognition of above mentioned studies, the PIV experiments performed by Edwards et al. (2012) and Danao (2012) considered the flow across a Darrieus turbine with a solidity σ of 34% at different tip-speed ratios. These studies attempted to visualize the flow field around the blade at specific azimuth positions throughout the cycle at a regular phase difference of 10^o. Figure 2.11 shows the

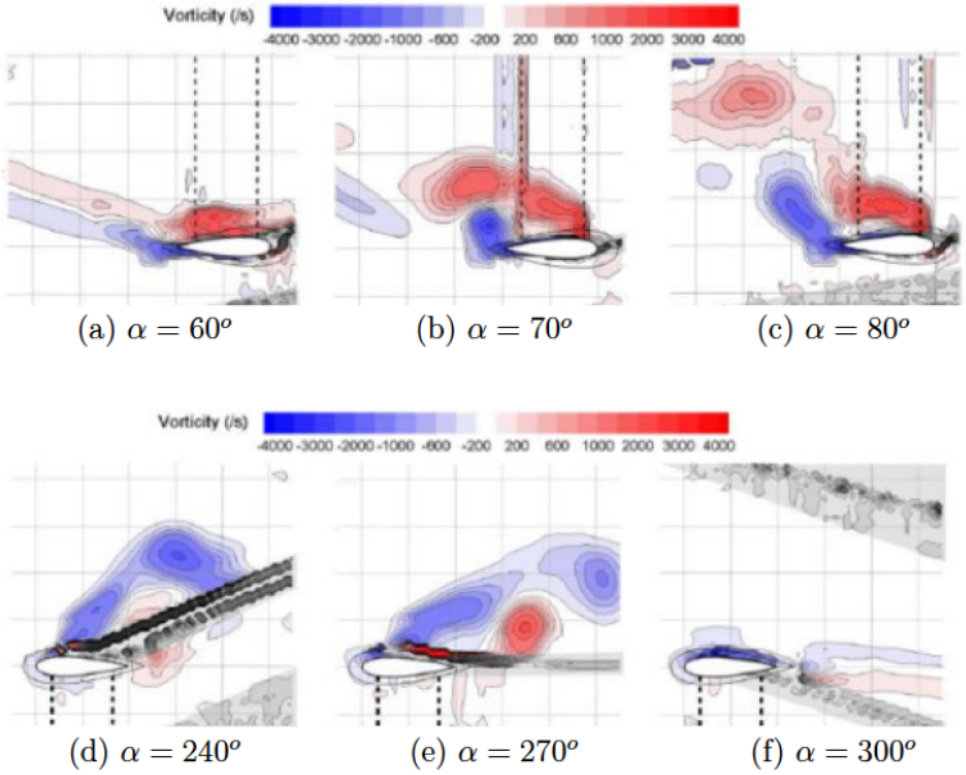

(a) $\alpha = 60^o$ (b) $\alpha = 70^o$ (c) $\alpha = 80^o$

(d) $\alpha = 240^o$ (e) $\alpha = 270^o$ (f) $\alpha = 300^o$

Figure 2.11: PIV visualization of blade stalling at specific azimuth position α (Edwards et al., 2011)

instantaneous flow patterns of blade stalling for every 10^o azimuth position of the blade. However, some of the azimuth positions could not be covered due to viewing difficulties. This led to a motivation in PIV studies for present research to acquire the detailed information about the flow patterns around the blade at every 10^o of azimuth position.

In addition to these references, other studies on PIV studies of hydroturbines such as flow analysis across underwater tidal power by Doroshenko and Doroshenko (2014), experimental analysis of flow through a small scale axial water turbine by Johnson et al. (2013), wake zone modeling for a tidal turbine by Good et al. (2011) etc ... aimed primarily at PIV measurements and flow visualization for specific understanding of fundamental flow characteristics of turbines. Following this insight into the PIV applications for low speed turbine analysis, digital PIV system which is fully synchronized with other technical systems like torque acquisition is used in this research to explain the Darrieus water turbine performance and changes in flow fields with respect to the operating conditions.

2.5 Power extracted by a turbine

The flow diversion around the turbine due to the restriction offered by the device to uniform flow makes the power calculation complex. Precise examination of this flow diversion needs the consideration of various length scales associated with the turbine geometry, wake size etc... The work of Consul et al. (2013) is worth considering here, which developed the numerical models to account for most of these scales.

2.5.1 Lanchester-Betz theory

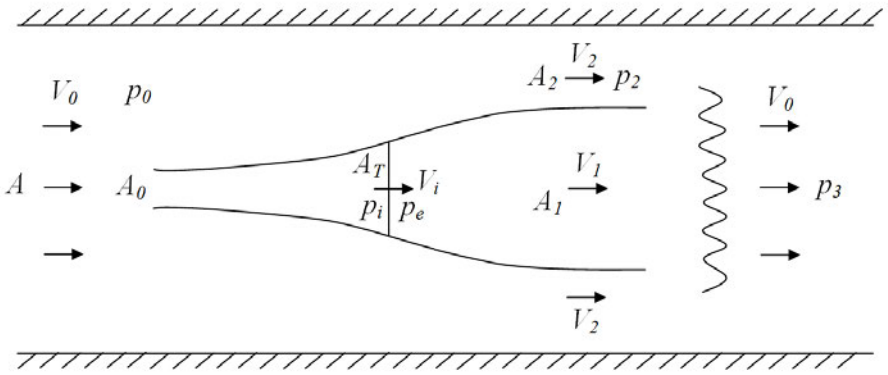

Figure 2.12: Schematic of a turbine in a confined channel flow (Garret and Cummins, 2007)

Consider a turbine stage as shown in Figure 2.12, which has a swept area A_T, placed in a uniform channel of velocity V_0 and cross-section A. The assumption of constant channel area A is valid for low Froude number flows in open-channels, which is usual in case of tidal turbines. The sectional size of the streamtube going through the turbine varies from A_0 far upstream to A_1 far downstream with A_T at the turbine's location. The flow field development studies consider the pressure as a sum of static and hydrostatic components. The variation of pressure between the extremes of streamtube account for the difference of upstream pressure p_0 and downstream pressure p_3. The immediate upstream and downstream of the turbine are subjected to the pressure conditions p_i and p_e respectively. The mean flow velocity across the turbine is V_T. The expansion of the streamtube is defined by the increase in its sectional area from A_0 to A_1 with a flow velocity V_1. Beyond the wake zone, the flow through the area A_2 is characterized by the velocity V_2 and pressure p_2. This type of uniform flow configuration with no swirling components is analogous to Lanchester Betz formulation. This means, as $A \to \infty$, $p_2 = p_0$ and $V_2 = V_0$. A mixing action is assumed at the downstream section to get the flow returned to uniform velocity V_0 with a pressure p_3.

From the mass conservation principle applied to an incompressible flow,

$$A_0 V_0 = A_T V_T = A_1 V_1 \tag{2.12}$$

$$(A - A_1)V_2 + A_1 V_1 = A V_0 \tag{2.13}$$

Equation 2.13 can be written as

$$A(V_2 - V_0) = A_1(V_2 - V_1) \tag{2.14}$$

From the momentum conservation principle with incompressible flow assumption, the force on the turbine F is calculated from

$$F = \rho A V_0^2 - \rho(A - A_1)V_2^2 - \rho A_1 V_1^2 + (p_0 - p_2)A \tag{2.15}$$

Bernoulli's equation for the flow outside the streamtube is given by

$$p_0 - p_2 = \frac{1}{2}\rho(V_2^2 - V_0^2) \tag{2.16}$$

From Equations 2.14 and 2.16,

$$F = \frac{1}{2}\rho A_1(V_2 - V_1)(V_2 + 2V_1 - V_0) \tag{2.17}$$

When Bernoulli's equation for upstream and downstream conditions of the turbine is combined with Equation 2.16 with uniform pressure outside the streamtube, it gives

$$p_i - p_e = \frac{1}{2}\rho(V_2^2 - V_1^2) \tag{2.18}$$

which defines the force on the turbine as

$$F = (p_i - p_e)A_T = \frac{1}{2}\rho A_T(V_2^2 - V_1^2) \tag{2.19}$$

Equating the Equations 2.17 and 2.19, we get

$$V_T = \frac{V_1(V_2 + V_1)}{V_2 + 2V_1 - V_0} \tag{2.20}$$

Neglecting the internal losses, the turbine power P is calculated from

$$P = F V_T = \frac{1}{2}A_T \frac{V_1(V_2 + V_1)(V_2^2 - V_1^2)}{V_2 + 2V_1 - V_0} \tag{2.21}$$

In the limiting case, as $A \to \infty$ which implies $V_2 = V_0$, Equation 2.20 becomes

$$V_T = \frac{1}{2}(V_0 + V_1) \tag{2.22}$$

This is known as Lanchester-Betz result, which reduces the Equation 2.21 to

$$P_{LB} = \frac{1}{4}A_T(V_0 + V_1)(V_0^2 - V_1^2) = \frac{1}{2}(1 + \eta)(1 - \eta^2)\left(\frac{1}{2}A_T V_0^3\right) \tag{2.23}$$

where $\eta = \frac{V_1}{V_0}$. The power produced by the turbine is maximum of 0.59 when η

is 1/3. This is the classical Betz limit. Power output of the turbine is however subject to the flow confinement which is detailed in the next section.

2.5.2 Turbine performance in a confined flow

When the turbine occupies the entire channel section, the blockage effects are prominent which increase the streamwise velocity across the turbine. At lower values of λ, the coefficient of power COP is controlled by the blade stalling, which results in power reduction. At higher values of λ, predominant blockage effect increases the blade incidence which results in increased power output. The study on Consul and Willden (2010) on the operation of Darrieus turbine in a confined flow revealed that the Betz limit was exceeded by 100% in the case of maximum blockage effect. In the present study, the CFD studies are performed using the 2D Darrieus models while the experiments are conducted on the 3D turbine model, whose blockage effects are different from each other for a given channel width. In order to eliminate the resulting differences in the performance calculations, this section revisits the analysis of Garrett and Cummins (2007) on the turbine's operation in a confined flow. When the turbine occupies the entire channel section, the power (reference) is obtained from

$$P_{ref} = AV_0(p_0 - p_3) \tag{2.24}$$

Here, p_3 is the downstream pressure where low-velocity wake merges with the high velocity stream. This reference pressure P_{ref} is always greater than P due to the energy loss in the merging action (Garret and Cummins, 2004). Comparing the momentum terms between the wake region and far downstream,

$$(A - A_1)(p_2 + V_2^2) + A_1(p_2 + V_1^2) = A(p_3 + V_0^2) \tag{2.25}$$

From Equations 2.14 and 2.16,

$$p_0 - p_3 = \frac{1}{2}\rho(V_2 - V_0)(V_2 + 2V_1 - V_0) \tag{2.26}$$

From Equations 2.24 and 2.26,

$$P_{ref} = \rho AV_0\frac{1}{2}(V_2 - V_0)(V_2 + 2V_1 - V_0) \tag{2.27}$$

Introducing the Equations 2.14 and 2.17 in Equation 2.27, we get

$$P_{ref} = FV_0 \tag{2.28}$$

and

$$\frac{P}{P_{ref}} = \frac{V_T}{V_0} \tag{2.29}$$

From Equations 2.16 and 2.26,

$$p_3 - p_2 = \rho(V_2 - V_0)(V_0 - V_1) \tag{2.30}$$

Introducing the blockage ratio b as the ratio of turbine sweep area A_T to the channel sectional area A, then from Equations 2.12 and 2.13,

$$V_1(V_2 - V_0) = bV_T(V_2 - V_1) \tag{2.31}$$

With lower blockage effect (say $b << 1$), using Lanchester-Betz results as shown in Equation 2.29, we have

$$\frac{P}{P_{ref}} = \frac{V_0 + V_1}{2V_0} \tag{2.32}$$

Two observations are made here. Mathematically, turbine's operation is most effective when $V_1 = u_0$. However, the power output becomes zero in this condition. When maximum power condition is considered by assuming $V_1 = V_0/3$, then $P = 2P_{ref}/3$. This means that only one third of power is lost to the fluid flow. On the other hand, when the turbine's geometry offers significant blockage effect (say $1 - b << 1$), then

$$V_2 \simeq 2(1 - b)^{-1}(V_0 - V_1) \tag{2.33}$$

with $V_T \simeq V_1$ and

$$P = 2(1 - b)^{-2}A_T V_1(V_0 - V_1)^2 \tag{2.34}$$

This is consistent with the maximum power condition when $V_1 = V_0/3$, which gives

$$P_{max} = \frac{16}{27}(1 - b)^{-2}\frac{1}{2}A_T V_0^3 \tag{2.35}$$

Therefore, a factor of $(1 - b)^{-2}$ distinguishes the power output from the turbine in case of flow confinement from that of an isolated turbine i.e., Lanchester-Betz limit. The power production will still increase as blockage ratio b increases.

2.6 Circulation-based analysis

Several studies on flow analysis of vertical axis wind turbines and hydroturbines emphasized on the importance of the wake zone in the calculation of forces with efforts being made to investigate the circulation around the blades as a function of two periodic variables : the instantaneous angle of attack and relative velocity of the blades. According to Kelvin's theorem, in the perfect fluid case, the circulation of velocity field around a fluid field is constant in time. On considering a fluid field of great extension around the blades, Kelvin's theorem requires that a change of circulation around the blade is compensated by the shedding of opposite circulation vortices. These vortices are then convected downstream, forming a wake. The method of singularities can model this type of flow, to calculate the contribution

of the wake on the flow around the profile (Zanon et al., 2013; Ferreira, 2009) to derive the forces on the blades. However, the dependency of the discretized equations in the trailing edge region leads to smaller trailing edge angles which would finally result in inaccurate solutions.

2.7 Performance improvement

The enhancement of the fluid dynamic efficiency of a rotating machine depends on the blade design as well as the flow structure around the profile. While discussing the flow control mechanisms for vertical axis turbine's performance improvement, Samsonov and Baklushin (1992) classified these two approaches into five different ways, out of which the first four deal with the airfoil's shape alteration and the final one constitutes the active flow control. Several scholars worked on the structural optimization of profiles using the shape sensitivity and topology optimization methods. Carrigan et al. (2012) used differential evolution algorithm coupled with the geometry modeler, mesher and CFD solver to develop an automated process of airfoil shape optimization to maximize the power output. Optimization of a Darrieus turbine through blade element momentum theory was performed by Bedon et al. (2013) who used polynomial interpolations of existing symmetrical airfoil data to increase the energy production while emphasizing on the consistent performance of evolutionary algorithms. A similar optimization technique was employed by Bavanish and Thyagarajan (2013) for an horizontal axis wind turbine to improve the power coefficient of the device. Nevertheless, there are several quibbles about the existing shape optimization techniques including possible unknown design issues during the objective function optimization with design constraints being imposed. The infeasibility of having larger operating samples for increased geometric degrees of freedom was identified as a problem of localized optimization (Huyse and Michael, 2001). Furthermore, Drela (1998) noted the need for a posteriori smoothing of noisy optimized shapes. Also, due to the severe dependency of performance improvement on the location of sampled conditions, the performance of the optimized shapes away from the sampled conditions is disappointing.

Out of numerous research articles and reports available about the Darrieus turbine, most of them are pertinent to wind energy applications. Very few of them are found related to tidal energy. Belhache et al. (2014) studied computationally the wake characteristics in the context of deploying multiple marine turbines. There is a strong influence on the downstream turbine's performance due to its interaction with the wake released from the upstream ones. Hyun et al. (2010) studied the performance of Darrieus turbine using a two-equation turbulence model and compared the results with experimental data. Also, a parametric study for solidity and camber was performed to optimize the model's performance. The numerical simulations conducted by Goude (2012) using two-dimensional vortex method

revealed the relationship between the channel size and the solution convergence in terms of required number of turbine rotations. This study also analyzed how channel boundaries could alter the performance of the turbine.

The wake area is characterized by a velocity deficit which results in shear zones within the flow field. Another source of unsteady vortices is the blockage effect, which depends on the turbine's solidity σ, which is a key parameter in terms of performance. Increasing the number of blades, to a feasible extent, significantly increases the power output and also alters characteristics of the power curve (Shiono et al., 2000; Consul et al., 2009). The parametric studies of Gosselin et al. (2013) using URANS models revealed that blockage effects are associated with power extraction characteristics: the performance coefficient increases with the turbine's solidity up to a certain optimal value beyond which the turbine's performance deteriorates. The phenomenon of dynamic stall with critical motion of leading edge vortex over the suction surface is detrimental to the blade's power characteristics (Wang et al., 2012; Ferreira et al., 2009).

One of the solutions to improve the turbine's performance is to equip the turbine with a diffuser to increase the downstream flow section and thus increasing the incident fluid velocity (Mehmood et al., 2012; Mehmood et al., 2011). Another way to limit the flow bypass in order to enhance the performance coefficient is to stack the turbines one on another and juxtaposing them, facing the tidal flow (Antheaume et al., 2008). The fluid is then accelerated between the turbines thereby increasing the power output.

Several scholars have performed aerodynamic and hydrodynamic studies of Darrieus turbines with H-shaped blades to enhance the efficiency of the device. Results of Hwang et al. (2009) and Paillard et al. (2013) with pitching blades and Antheaume et al. (2008) with fixed blades suggested the adverse influence of blade wake and dynamic stall on the turbine's overall performance due to the unsteady forces exerted on the blades. Without taking vortex triggering into account, these types of turbines are subject to wake interactions over a large part of the rotation, which can result in cyclic disturbances related to each blade. The importance of vortex formation during the fluid dynamic analysis was identified by the studies of Khalid et al. (2013), Ahmadi et al. (2009), Paraschivoiu et al. (2009) and Wang et al. (2007) applied the potential flow concept for analysing the vertical axis tidal turbine. Single and two-bladed vertical axis turbines with cavities to ensnare the vortices, aiming at vortex shedding control were studied by Zannetti et al. (2007). In this work, the blade profiles were created analytically using conformal mapping and unsteady flow computations were performed using vortex method. Figure 2.13 shows the respective vorticity control.

From the perspective of improving the efficiency of vertical axis wind turbines, other work has been done on controlling the rotation of the blades. The objective of these studies was to maximize the power obtained on the axis of rotation by

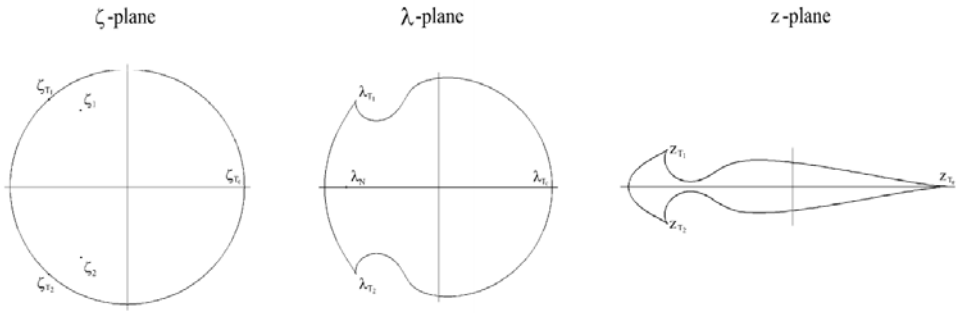

(a) Conformal mapping sequence of a one-bladed turbine model.

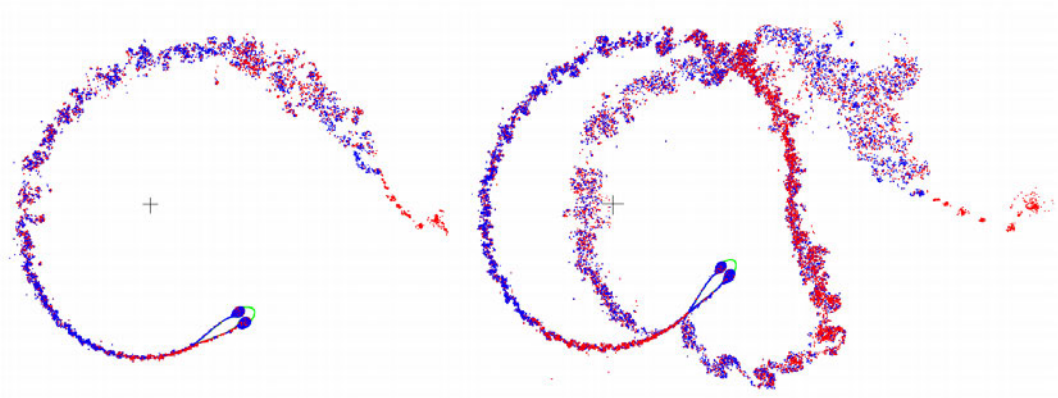

(b) Vortex shedding visualization
Blue dots: clockwise circulations; Red dots: counter-clockwise circulations.

Figure 2.13: Vortex control through analytical modeling (Zannetti et al., 2007)

controlling the angle of attack of the blades to avoid stall. A torque controlling the rotation of the profile on its axis can be obtained by the inertia of eccentric weights on the profile and the restoring force of connecting rods that join the centre of the turbine and blades (Lazauskas, 1992). Various masses and lengths of connections were tested using a model of multiple tube current for empirically optimizing the parameter values collected on the power shaft.

With a deeper insight into the flow characteristics around the profile, adjusting the profile motion in order to achieve the desired physical patterns around the profile can improve the dynamic efficiency of the blade. One of the ways to accomplish this is to control the circulation around the blade to avoid eddy formation due to the rotational motion of the turbine (Duraisamy and Lakshminarayan, 2014). A critical concern here is how and how much circulation is to be imparted to the blade. Following the research speculations on the designing aspects such as flap deployment, trailing edge shape etc. to control the circulation around the profile, focus has shifted to analysis-based ventures. Shires and Kourkoulis (2013) applied

a tangential fluid jet to control the blade circulation for a Darrieus turbine. Although there is a certain increase in the overall torque output, this method suffered from additional drag due to the increased trailing edge thickness. Another viable technique, implemented by Wilhelm et al. (2010), was to apply an appropriate pitching to the profile during the device operation which could control the fluid dynamic forces experienced by the blade thereby compensating for the unsteady flow patterns to maximize the turbine's torque output. But the feasibility of enabling sudden pitch change associated with larger angular acceleration/deceleration at specific flow velocities corners this choice. Such control techniques originate from the fact that the profile is subject to instantaneous angular motion throughout its azimuthal travel.

The complexity in analysing the performance of a variable pitch Darrieus turbine was identified by Lazauskas (1992). In this study, load characteristics attributed to optimum geometry were considered along with usual design variables of a vertical axis wind turbine in order to achieve high starting torque, high peak efficiency and broad operating range. Variable pitching mechanisms achieved by suitable cam devices were found to be the best solutions to achieve these objectives. While self-acting pitch control systems seem to produce better low speed torque than the forced pitch device, their performance in real flow conditions was not described in this study.

Hwang et al. (2006) achieved 30% increment in output power by optimizing the blade's pitching angle of a lift-based vertical axis cycloidal wind turbine. Pitching was controlled by an active control system that ensured the maximum instantaneous tangential force of each blade. Paraschivoiu et al. (2009) achieved better performance of a 7 kW wind turbine model of Darrieus type through an optimized blade pitch control, where the pitching angle was modeled with an analytical function whose coefficients are used as variables in the optimization process. Two pitching models were considered in this study : one was the simple sinusoidal variation and the other was more general, relating closely the blades' pitch to the local flow conditions along their circular path. A gain of almost 30% in the annual energy production was obtained with the polynomial optimal pitch control.

Some analytical work was performed by Rathi (2012) to enhance the power produced by a vertical axis wind turbine, where a dynamic model for free-pitching blades was also devised and analyzed. His double-multiple streamtube model based on Blade Element Momentum theory, with additional modifications was developed to predict the power generated by a straight bladed, or H-Type Darrieus, wind turbine with blades of varying pitch. The concept of active blade pitch control was also examined, with a focus on continuously varying blade pitch to maximize the blades' aerodynamic force coefficient driving a rotor at all tip-speed ratios of operational interest. Performance was greatly improved at lower tip-speed ratio compared to a rotor with fixed-pitch blades, allowing more power to be generated

at lower wind speeds.

Sumantraa et al. (2014) and Benedict et al. (2013) investigated the performance of a small scale vertical axis turbine utilizing dynamic blade pitching. As shown in Figure 2.14 (a), the model's pitch mechanism to instantaneously change the blade pitch phasing enables the device to adapt itself to changes in wind direction thereby maximizing power extraction. A CFD model was developed and the model predictions correlated extremely well with test data. The validated CFD model was used to develop a fundamental understanding of the physics of power extraction of such a turbine. Both experimental and CFD studies showed that the turbine efficiency is a strong function of the blade pitching amplitude. The optimal tip-speed ratio λ_{opt} depends on the blade pitch kinematics, and it decreased with increasing pitch amplitude for the symmetric blade pitching case. CFD analysis showed that the blade extracts all the power in the frontal half of the circular trajectory, however, it loses power into the flow in the rear half. Fixed-pitch turbine showed lower efficiency compared to the variable pitch turbines owing to the massive blade stall in the rear half, caused by the large angle of attack and high reverse camber. The maximum achievable COP of the turbine increases with higher Reynolds numbers, however, the fundamental flow physics remains mainly identical irrespective of the operating Reynolds number. Similar dynamic pitch control mechanism was used by Chougule and Nielsen (2014) for the vertical axis turbine model with 3 blades, as shown in Figure 2.14 (b), to achieve improved performance.

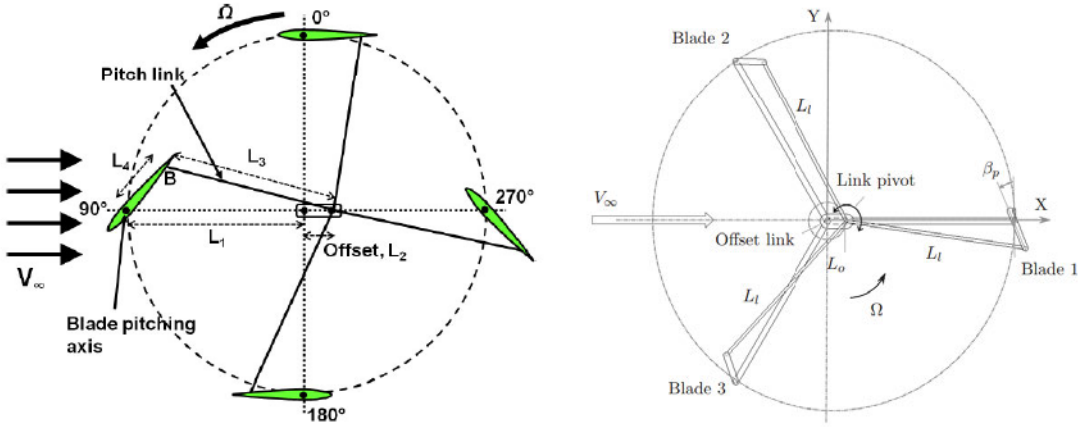

(a) (b)

Figure 2.14: Schematic diagrams of dynamic blade pitch control mechanisms, used by (a) Benedict et al. (2013), and (b) Chougule and Nielsen (2014)

Bhatta et al. (2008) achieved the pitch control by rotating each individual blade about its vertical axis, while camber control is realized using a trailing edge

flap on each blade. Using camber and pitch controls help in creating a greater force differential across the turbine than using pitch control alone. Table 2.2 consolidates the gain achieved by different pitch control mechanisms, studied by various scholars to realize the improved performance.

Reference	Analysis method	Pitching mechanism	Max COP rise
Chougule and Nielsen (2014)	Multi-body simulation	Sinusoidal	12%
Miau et al. (2012)	Double-multiple streamtube & CFD	$-10 < \theta(\alpha) < 10$ $-70 < \theta(\alpha) < 70$	22% 22%
Paraschivoiu et al. (2009)	Double-Multiple Streamtube model	Genetic algorithm based optimization strategy	11%
Lazauskas (1992)	Double-Multiple Streamtube model	Sinusoidal Self-acting stabilized Aeropitch	2% 11% 13%
Soraghan et al. (2013)	Double-Multiple Streamtube model	Analytical model	10%
Li-xun et al. (2014)	CFD	Analytical model	19.3%
Erickson et al. (2011)	Experimental and CFD	Sinusoidal	34%
Gazzano et al. (2010)	Wake-vortex model	Sinusoidal Optimized pitching	15% 29%

Table 2.2: Literature summary of the studies on blade pitching mechanisms and their effectiveness in increasing the performance

2.8 Conclusion

With an introduction to the fundamentals of Darrieus turbine and flow across it, this chapter provided the information about the influence of various design parameters on the performance of a vertical axis turbine. This discussion along with the information supplied by various scholars conferred the rationale for chosen design criteria to model and develop the turbine model for current research. The investigation methods used in the studies of VAWT were presented and the details were summarized in Table 2.1. The effect of flow confinement, where the blockage effects are no longer negligible, was discussed, which is useful in correcting the turbine's performance in the present research. Handful literature exists on the turbine's design with pitching blades and their performance analysis. The effectiveness of these blade pitching techniques was quantified and presented in Table 2.2. The overall review of state-of-the-art allowed finding the gaps in existing literature. In this regard, the current research intends to fulfil the following:

1. A very limited information is available about the influence of design parameters on the performance of high solidity turbine models ($\sigma > 0.4$). Even

these studies were mostly dedicated to the COP curve evolution without detailed information about the flow field development. This thesis undertakes the flow physics in the operation of high solidity turbine models in order to illustrate the performance characteristics as well as to analyze the flow dynamics around the blade and across the turbine.

2. Majority of the research studies were performed using either computational or experimental method. A very few studies employed both the techniques which were however limited to the fundamental analysis of the turbine models. The detailed investigation about the flow across a turbine is therefore seeking a complete verification and validation. In the present work, computational fluid dynamics (CFD) was used for the evaluation of turbine's performance. These numerical results are validated using experimental analysis for power curves as well as flow field variables. Both the techniques are compared for different flow parameters to institute the validity of individual methods. While the computational examination remains the key investigation method, the experiments are conducted to complement the numerical analysis.

3. The vortex control and performance improvement of the turbine constitute the central objective of the present research. Various scholars experimented the blade pitching techniques which were mostly based on either sinusoidal motion or crank-type mechanism. This project develops dynamic pitch control laws based on potential flow concepts. Such motion control of the blade about its hydrodynamic centre is based on a mathematical framework that creates a scientific base for vortex control and, at the same time, performance improvement.

CHAPTER 3

COUCHET POTENTIAL & PITCH CONTROL LAW

Contents

3.1 Introduction

The theoretical framework of Couchet (1976) supplies the concept of the imposition of constant circulation to the profile motion within a fluid flow. With the application of conformal transformation and generalization of the Kutta-Joukowsky condition, Couchet developed the analytical formulations for the velocity, pressure and torsor fields for an airfoil in an irrotational flow. When the circulation is subject to change, vortices behind the airfoil must be considered and corresponding hypothetical formulation of airfoil motion in the existence of vortex sheet enables the calculation of pressure and force fields through the method of singularities. This chapter details the analytical formulation developed by Couchet and its extension to hydrofoil motion in order to develop the pitch control law to arrest the vortex shedding. Following this, thorough investigation on the influence of various design parameters on the blade's performance is presented.

3.2 Conformal transformation and Schwartz-Villat theorem

Conformal transform with inclusion of Laurent expansion can be found in numerous applications. Works of Prosnak (1987) and Klonowska and Prosnak (1996) used the Laurent series in the transform to map the multiply connected domains. Deglaire et al. (2008) used the same transform to map the circles onto specific wing profiles for fast vortex particle simulations.

The usual practice of calculating the velocity potential around a cylinder first, and then extending it to more complex shapes using conformal transformation $Z \to H(z)$ is illustrated in Figure 3.1, showing the transformation of the cylinder interior $|Z| \leq a$ into a wing profile.

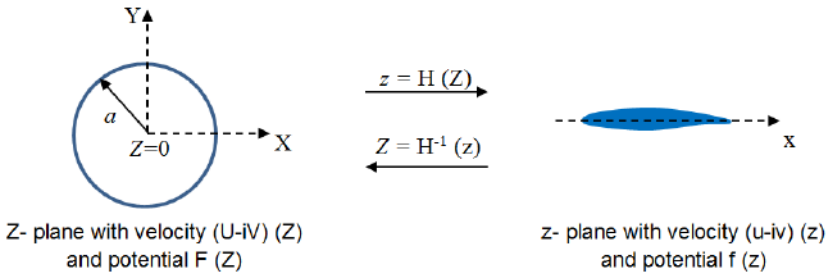

Figure 3.1: Transformation of cylinder into an airfoil

A general form of the conformal transformation for a profile with its centre at $Z = 0$ is

$$H(Z) = Z + \frac{a_1}{Z} + ... + \frac{a_n}{Z^n} + ... \tag{3.1}$$

Defining the velocity potential associated to the flow over a cylinder as $F(Z,t)$ and that after the transformation as $f(z,t)$ so that

$$\int_{circle} \frac{dF}{dZ} dZ = \int_{profile} \frac{df}{dz} dz. \tag{3.2}$$

When applied to a circle of radius a to map into a flat plate of length $4a$, the Joukowsky transformation function is given by

$$H(Z) = Z + \frac{a^2}{Z} \tag{3.3}$$

with $Z = ae^{i\alpha}, \alpha \in [0, 2\pi]$. Then $z = H(ae^{i\alpha}) = 2a\cos\alpha$

$H'(Z) = 0 \Leftrightarrow 1 - \frac{a^2}{z^2} = 0$. This represents two points $Z = a$ and $-a$ on the circle and which correspond to the end points of the flat plate, $z = -2a$ and $2a$.

In addition, the Schwartz-Villat theorem calculates the function at all external points of a circle if the imaginary part of a complex function is known on the circle. If a function $G(Z,t)$ is expressed using Laurent series as $G(Z,t) = a_0 + \sum_{k=1}^{\infty} \frac{a_k}{z^k}$, then $\forall Z$ with $|Z| > a$,

$$G(Z,t) = -\frac{1}{\pi}\int_{C+}\frac{\psi(Z')}{Z'-Z}dZ' + a_0 \tag{3.4}$$

where $C = \{Z, |Z| = a\}$ and $\psi = Im(G)$.

3.2.1 Couchet theory

Under ideal conditions, the flow is free from variations and turbulence, and therefore treated as irrotational. The work of Couchet (1976) is considered from hereafter to develop the motion laws for a profile.

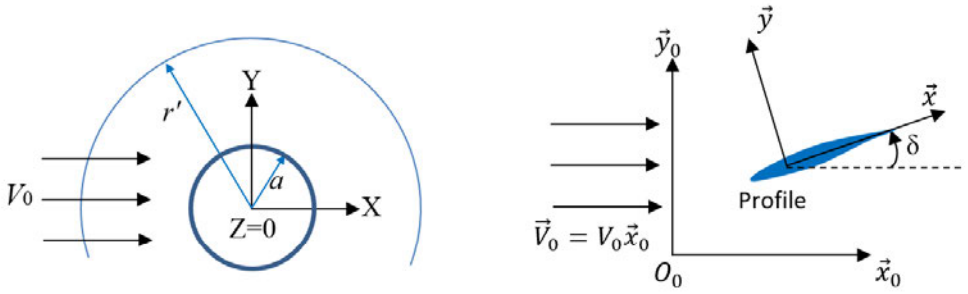

Figure 3.2: Schematic of flow around the cylinder (left) and its transformed map for profile motion (right)

For an ideal fluid flow around a circular profile, represented by $|Z| = a$ in a complex plane, the velocity potential $F(Z,t)$ associated with the flow is obtained from the velocity components U and $-V$, which satisfy the Cauchy equations so that

$$\left.\begin{aligned}\frac{\partial U}{\partial X} &= \frac{\partial(-V)}{\partial Y} \quad ...Incompressible flow\\ \frac{\partial U}{\partial Y} &= -\frac{\partial(-V)}{\partial X} \quad ...Irrotational flow\end{aligned}\right\} \tag{3.5}$$

The velocity around the cylinder is holomorphic and follows the Laurent series as

$$U - iV = \sum_{n=1}^{\infty} A_n Z^n + A_0 + \sum_{n=1}^{\infty}\frac{A_{-n}}{Z^n} \tag{3.6}$$

According to residue theorem to determine the coefficient A_{-1},

$$\left.\begin{aligned}\int_{C+} U - iV dz &= 2i\pi A_{-1}\\ \int_{C+} U - iV dz &= \Gamma\end{aligned}\right\} \Rightarrow A_{-1} = -i\frac{\Gamma}{2\pi} \tag{3.7}$$

Here, C^+ is the contour traced in anticlockwise direction around the cylinder and Γ is the circulation of the velocity field on C^+. The velocity at infinity is bounded and the coefficients $A_i = 0$, $\forall i \geq 1$ and $A_0 = V_\infty$. Therefore, velocity potential $F(Z,t)$ associated with the flow is obtained from

$$F(Z,t) = V_\infty Z + \frac{\Gamma}{2i\pi}\ln\frac{Z}{a} + G(Z,t) \tag{3.8}$$

where $G(Z,t) = B_0 + \sum_{k=1}^{\infty}\frac{B_k}{z^k}$ and Γ is circulation around the circle.

It is now required to define the boundary conditions associated to the profile motion before determining the function $G(Z,t)$ and the free stream velocity. Consider the profile with centre O and zero lift axis $(O,\vec{x})$ obtained by conformal transformation of the circle $|Z| = a$ as shown in Figure 3.2. The profile is set at an incidence of $\delta = (\vec{x}_0,\vec{x})$ in $T_0 : (O_0, \vec{x}_0, \vec{y}_0, \vec{z}_0)$ and the fluid at infinity is in the reference frame of $T_0' : (O_0', \vec{x}_0, \vec{y}_0, \vec{z}_0)$ which is the uniform translation of T_0. $T : (O, \vec{x}, \vec{y}, \vec{z}_0)$ is related to the profile. The velocity at infinity is zero in T_0' and therefore the velocity potential now takes the form

$$F(Z,t) = \frac{\Gamma}{2i\pi}\ln\left(\frac{Z}{a}\right) + G(Z,t) \tag{3.9}$$

The velocity components u and v, relative to T_0', are expressed in the system of profile axis such that

$$\vec{V}_{fluid/T_0'} = u\vec{x} + v\vec{y} \tag{3.10}$$

And, the complex potential associated with this velocity is $f(z,t)$ so that

$$\frac{df}{dz} = u - iv \tag{3.11}$$

If $l(t)$ and $m(t)$ are the velocity components of O in the reference frame T, then the speed of the profile centre O in the translated reference frame is

$$\vec{V}_{O/T_0'} = l(t)\vec{x} + m(t)\vec{y} \tag{3.12}$$

The relative velocity on the profile in complex vector form is therefore given by

$$\vec{V}_{fluid/T} = \overline{\left(\frac{df}{dz}\right)} - \left(l + im + i\dot{\delta}z\right) \tag{3.13}$$

Slip condition subjects the profile contour to $\vec{V}_{fluid/T}\cdot\vec{n} = 0$, where $\vec{n}$ is the normal to the contour. This can also be written as $\mathrm{Im}\left(\overline{V}_{fluid/T}dz\right) = 0$ on the profile contour. Defining $\psi = Im(f)$, the boundary condition is expressed as

$$d\psi = -mdx + ldy - \dot{\delta}\left(xdx + ydy\right)$$

$$\psi = ly - mx - \frac{\dot{\delta}}{2}\left(x^2 + y^2\right) + C(t) \tag{3.14}$$

The function $G(Z,t)$ can be determined from the imaginary part of the potential function. Referring to Equation 3.9, $\ln\left(\frac{Z}{a}\right) = i\alpha, \forall\ Z \in C$. Thus,

$Im[G(Z,t)] = Im[F(Z,t)]$ on the circle, which can be written as

$$\begin{aligned}\operatorname{Im}\left[F\left(Z \in circle, t\right)\right] &= \operatorname{Im}\left[f\left(z \in \text{profile}, t\right)\right] \\ &= \psi\left(z \in \text{profile}, t\right) = ly - mx - \frac{\dot{\delta}}{2}(x^2 + y^2) \quad (3.15)\end{aligned}$$

Since the imaginary part of the function $G(Z,t)$ is known on the circle, the function at all points outside of the circle can be known according to Schwartz-Villat theorem, given by Equation 3.4. Thus,

$$G(Z,t) = -\frac{1}{\pi}\int_{C^+} \frac{ly' - mx' - \frac{\dot{\delta}}{2}\left(x'^2 + y'^2\right)}{Z' - Z} dZ' = l(t)G^1(Z) + m(t)G^2(Z) + \dot{\delta}G^3(Z) \quad (3.16)$$

where $x' + iy' = H\left(Z'\right)$ is a point on the profile and C^+ is the circle with $|Z| = a$. The differential expressions G^1, G^2 and G^3 mentioned in Equation 3.16 are defined in Table 3.1.

G-term	**Definition**	**Circle with $\|Z\| = a$**	**Flat plate [-2a, 2a]**
$G^1\left(Z\right)$	$-\frac{1}{\pi}\int_{C^+} \frac{y'}{Z'-Z} dZ'$	$H\left(Z\right) - Z - \frac{a^2}{Z}$	0
$G^2\left(Z\right)$	$\frac{1}{\pi}\int_{C^+} \frac{x'}{Z'-Z} dZ'$	$i\left(Z - H\left(Z\right) - \frac{a^2}{Z}\right)$	$-2i\frac{a^2}{Z}$
$G^3\left(Z\right)$	$\frac{1}{2\pi}\int_{C^+} \frac{x'^2+y'^2}{Z'-Z} dZ'$	$\frac{1}{2\pi}\int_{C^+} \frac{H(Z')H(Z')}{Z'-Z} dZ'$	$-i\frac{a^4}{Z^2}$

Table 3.1: G-terms for circle and flat plate

The resulting Couchet potential, as a function of circulation Γ, takes the form

$$F_C = \frac{\Gamma}{2i\pi}\ln\left(\frac{Z}{a}\right) + l\left(t\right)G^1\left(Z\right) + m\left(t\right)G^2\left(Z\right) + \dot{\delta}G^3\left(Z\right) \quad (3.17)$$

The velocity field in the translated reference frame T_0' around the profile is obtained by differentiating the velocity potential with respect to z. Since the complex potential $F(Z,t)$ is known, the flow velocity components can be determined by

$$\begin{aligned}\left(u - iv\right)\left(z,t\right) &= \frac{df\left(z,t\right)}{dz} = \frac{dF\left(Z,t\right)}{dz} \\ &= \frac{1}{H'\left(Z\right)}\frac{dF\left(Z,t\right)}{dZ} = \frac{1}{H'\left(Z\right)}\left(\frac{dG}{dZ}\left(Z,t\right) - i\frac{\Gamma}{2\pi Z}\right) \quad (3.18)\end{aligned}$$

From the definition of G in Table 3.1 and Equation 3.18,

$$\begin{aligned}\left(u - iv\right)\left(z,t\right) &= \left(1 - \frac{1}{H'\left(Z\right)}\right)\left(l - im\right) + \\ &\frac{1}{H'\left(Z\right)}\left(\left(l + im\right)\frac{a^2}{Z^2} + \frac{\dot{\delta}}{2\pi}\frac{d}{dZ}\int_{c^+}\frac{x'^2 + y'^2}{Z' - Z}dZ' - i\frac{\Gamma}{2\pi Z}\right) \quad (3.19)\end{aligned}$$

In the case of a flat plate, $H'(Z) = 1 - \frac{a^2}{Z^2}$ and the velocity field in the translated reference frame is

$$(u - iv)(z,t) = i\left[\frac{2a^2\left(m + \dot{\delta}\frac{a^2}{Z}\right) - \frac{\Gamma Z}{2\pi}}{Z^2 - a^2}\right] \tag{3.20}$$

The Kutta-Joukowsky condition is satisfied when the velocity at tip $H(a) = Z_0$ is finite and the necessary condition, referring to Equation 3.18, is

$$\frac{dG}{dZ}(Z_0) - i\frac{\Gamma}{2\pi Z_0} = 0 \tag{3.21}$$

Noting the cusp of trailing edge as $H(a)$, then

$$i\frac{\Gamma}{2\pi a} = l\frac{dG^1}{dZ}(a) + m\frac{dG^2}{dZ}(a) + \dot{\delta}\lim_{Z\to a}\frac{dG^3}{dZ}(Z) \tag{3.22}$$

For the original flow geometry of circle $|Z| = a$, this results in

$$\left.\begin{aligned} \frac{dG^1}{dZ}(a) &= 0 \\ \frac{dG^2}{dZ}(a) &= 2i \\ \frac{dG^3}{dZ} \underset{Z\to a}{\longrightarrow} 2i\underbrace{\left(-i\frac{1}{4\pi}\lim_{Z\to a}\frac{d}{dZ}\int_{C+}\frac{x^2+y^2}{Z'-Z}dZ'\right)}_{\Omega} \end{aligned}\right\} \tag{3.23}$$

The necessary condition for a finite velocity at the tip is obtained from Equations 3.22 and 3.23 as

$$\Gamma = 4\pi a\left(m + \dot{\delta}\Omega\right) \tag{3.24}$$

For example, in the case of a flat plate, $\Omega = \frac{1}{2i}\frac{dG^3}{dZ}(a)$ with $G^3(Z) = -i\frac{a^4}{Z^2}$, which results in the following condition of finite velocity at the trailing edge

$$\Gamma = 4\pi a(m + \dot{\delta}a) \tag{3.25}$$

Note: In the stationary case, $\dot{\delta} = 0$, and $m = -V_0\sin\delta$. Then the condition of finite velocity at the trailing edge becomes,

$$\begin{aligned} i\frac{\Gamma}{2\pi a} &= -2iV_0\sin(\delta) \\ \Gamma &= 4\pi a V_0\sin(\delta) \end{aligned} \tag{3.26}$$

On the other hand, as the circulation Γ in Equation 3.25 is constant, and according to Kelvin theorem, the flow is characterised as irrotational. The condition of finite velocity at the trailing edge imposes a constant velocity projection of abscissa point $x = a$ over $\vec{y}$ in the reference frame T_0' as shown in Figure 3.3. The irrotationality and the concept of potential flow applied in a constant circulation framework in this condition is fulfilled.

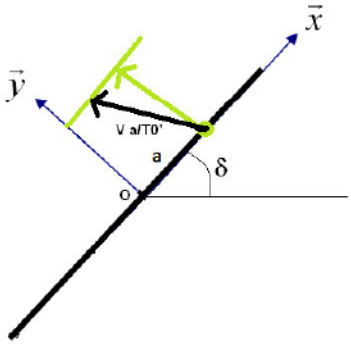

Figure 3.3: Velocity of point $x = a$ must remain constant along $\vec{y}$ to satisfy the finite velocity condition at the trailing edge

3.2.2 Calculation of forces on the profile

3.2.2.1 Pressure on the profile

Having obtained the analytical expression of the velocity field around the profile, the objective now is to determine the expression of the pressure field to calculate the torsor efforts of the fluid on the blade. In the Galilean reference T_0', the Euler equation can be written as

$$\rho \left[\frac{\partial \vec{V}_{fluid/T_0'}}{\partial t} + \overrightarrow{grad} \left(\frac{\left\| \vec{V}_{fluid/T_0'} \right\|^2}{2} \right) + \overrightarrow{rot} \vec{V}_{fluid/T_0'} \times \vec{V}_{fluid/T_0'} \right] = -\overrightarrow{grad}\, p \quad (3.27)$$

where p is the pressure and $\vec{V}_{fluid/T_0'} = u\vec{x} + v\vec{y}$. The flow is assumed to be potential and the velocity field relative to the reference T_0' is derived from the potential, denoted by $\varphi_0(x_0, y_0, t)$, such that

$$\left.\begin{aligned} \overrightarrow{V}_{fluid/T_0'} = -\overrightarrow{grad}\varphi_0 = u_0\vec{x}_0 + v_0\vec{y}_0 = u\vec{x} + v\vec{y} \\ u_0 = \frac{\partial \varphi_0}{\partial x_0}, v_0 = \frac{\partial \varphi_0}{\partial y_0} \end{aligned}\right\} \quad (3.28)$$

The Euler equation is then reduced to $\overrightarrow{grad}\left(\rho\frac{\partial\varphi_0}{\partial t} + \rho\frac{u^2+v^2}{2} + p\right) = 0$, and provides the Bernoulli equation for unsteady potential flow as

$$p + \frac{1}{2}\rho\left(u^2 + v^2\right) + \rho\frac{\partial \varphi_0}{\partial t} = C(t) \quad (3.29)$$

The velocity potential φ(x,y,t) is defined by $u = \frac{\partial\varphi}{\partial x}$, $v = \frac{\partial\varphi}{\partial y}$. A fixed point $A(x, y)$ in the reference frame T is identified by the reference frame T_0' by

$$\left.\overrightarrow{O_0'A}\right| \begin{array}{l} x_0\,(x, y, t) \\ y_0\,(x, y, t) \end{array}$$

Since $\vec{V}_{fluid\ in\ A/T_0'} = \overrightarrow{grad}\varphi_0 = \overrightarrow{grad}\varphi$, at all points i.e.

$$A(x,y) = (x_0(x,y,t), y_0(x,y,t)), \varphi(x,y,t) = \varphi_0(x_0(x,y,t), y_0(x,y,t), t)$$

Thus,

$$\frac{\partial\varphi}{\partial t} = \frac{\partial\varphi_0}{\partial x_0}\frac{\partial x_0}{\partial t} + \frac{\partial\varphi_0}{\partial y_0}\frac{\partial y_0}{\partial t} + \frac{\partial\varphi_0}{\partial t}$$

where $\frac{\partial x_0}{\partial t}$ and $\frac{\partial y_0}{\partial t}$ are the velocity components of the point A in the reference frame T_0'. Therefore,

$$\frac{\partial\varphi}{\partial t} = \overrightarrow{grad}\varphi_0 \cdot \vec{V}_{A/T_0'} + \frac{\partial\varphi_0}{\partial t} = \vec{V}_{fluid\ in\ A/T_0'} \cdot \vec{V}_{A/T_0'} + \frac{\partial\varphi_0}{\partial t} \tag{3.30}$$

The velocity of the point A is a function of that of the point O by the relation:

$$\vec{V}_{A/T_0'} = \vec{V}_{O/T_0'} + \dot{\delta}\vec{z}_0 \times (x\vec{x} + y\vec{y}) = \left(l(t) - \dot{\delta}y\right)\vec{x} + \left(m(t) + \dot{\delta}x\right)\vec{y} \tag{3.31}$$

From Equations 3.30 and 3.31,

$$\frac{\partial\varphi}{\partial t} = u\left(l(t) - \dot{\delta}y\right) + v\left(m(t) + \dot{\delta}x\right) + \frac{\partial\varphi_0}{\partial t}. \tag{3.32}$$

The Bernoulli equation therefore becomes:

$$p = -\frac{1}{2}\rho\left(u^2 + v^2\right) + \rho\left(u\left(l - \dot{\delta}y\right) + v\left(m + \dot{\delta}x\right)\right) - \rho\frac{\partial\varphi}{\partial t}. \tag{3.33}$$

3.2.2.2 Resultant forces exerted by the fluid flow

If X and Y are the force components of $\vec{F}_{fluid\to profile}$ expressed in the system of profile frame T,

$$X + iY = \int_{c^+} ipdz \tag{3.34}$$

Since Bernoulli equation is used to express the pressure as a function of the velocity potential,

$$f = \varphi + i\psi$$

$$X + iY = -\frac{i\rho}{2}\underbrace{\int_{c^+}\left(\overline{\frac{df}{dz}}\right)^2\overline{dz}}_{(1)} + i\rho\underbrace{\int_{c^+}\left(l + im + i\dot{\delta}z\right)d\varphi}_{(2)} - i\rho\underbrace{\int_{c^+}\frac{\partial\varphi}{\partial t}dz}_{(3)} \tag{3.35}$$

Using the residue theorem, the first integral in the Equation 3.35 yields zero. $l + im$ and $\dot{\delta}$ in the second integral do not depend on φ. Therefore, $\int_{c^+} d\varphi = \int_{c^+}\frac{\partial\varphi}{\partial x}dx + \frac{\partial\varphi}{\partial y}dy$ which is equal to $\int_{c^+}\overrightarrow{V}_{fluid/T_0'} \cdot \vec{t}ds = \Gamma$.

Since $\varphi = Re\left(G(Z,t) - \frac{i\Gamma}{2\pi}\ln\left(\frac{Z}{a}\right)\right)$, then

$$zd\varphi = zdRe\left(G(Z,t)\right) + zd\left(-\frac{i\Gamma}{2\pi}\ln\left(\frac{Z}{a}\right)\right) = d\left(z\mathrm{Re}\left(G\right)\right) - \mathrm{Re}\left(G\right)dz - \frac{i\Gamma}{2\pi}\frac{z}{Z}dZ$$

On integrating this expression over the profile contour gives:

$$\int_{c^+} z d\varphi = \underbrace{\int_{c^+} d\left(zRe\left(G\right)\right)}_{=0(c^+ is\ a\ closed\ contour)} - \int_{c^+} Re\left(G\right) dz - \underbrace{\int_{c^+} \frac{i\Gamma}{2\pi}\frac{z}{Z} dZ}_{=0(using\ residue\ theorem)} .$$

Therefore, the second integral becomes $(l + im)\,\Gamma - i\dot{\delta}I$ where $I = \int_{c^+} Re(G)dz$. Looking at the third integral,

$$\begin{aligned}\int_{c^+} \frac{\partial Re\left(F\left(Z,t\right)\right)}{\partial t} dz &= \int_{c^+} \frac{\partial Re\left(G\left(Z,t\right)\right)}{\partial t} dz + \int_{c^+} \frac{\partial}{\partial t} Re\left(-\frac{i\Gamma}{2\pi}\ln\left(\frac{Z}{a}\right)\right) dz \\ &= \int_{c^+} \frac{\partial Re\left(G\left(Z,t\right)\right)}{\partial t} dz + \underbrace{\int_{\alpha=0}^{2\pi} \frac{\partial}{\partial t}\left(\frac{\Gamma}{2\pi}\alpha\right) d\alpha}_{=0} .\end{aligned}$$

Therefore, Equation 3.35 becomes

$$X + iY = i\rho\left(l + im\right)\Gamma + \rho\dot{\delta}I - i\rho\frac{dI}{dt} \tag{3.36}$$

where $I = \int_{c^+} Re(G)dz$. For example, in case of a flat plate with a length of $4a$,

$$I = 4\pi a^2 m(t) \tag{3.37}$$

3.2.2.3 Moment about the centre

Let $A(x(s), y(s))$ be a point on the profile contour, then the moment about point O is:

$$\overrightarrow{M_O^{fluid\to profile}} = \int_{c^+} \overrightarrow{OA} \times \overrightarrow{dF^{fluid\to profile}}. \tag{3.38}$$

Since the flow is planar, $M_O = \overrightarrow{M_O^{fluid\to profile}} \cdot \vec{z}$ such that

$$M_O = \int_{c^+} pxdx + pydy = Re\left[\int_{c^+} pz\overline{dz}\right]. \tag{3.39}$$

Using the boundary condition $d\psi = -mdx + ldy - \dot{\delta}\left(xdx + ydy\right)$,

$$M_O = Re\left[\int_{c^+} -\frac{1}{2}\rho z\left(\frac{df}{dz}\right)^2 dz + \rho z\left(l\left(t\right) - im\left(t\right) - i\dot{\delta}\overline{z}\right) d\varphi - \rho z\frac{\partial\varphi}{\partial t}\overline{dz}\right]. \tag{3.40}$$

Since $\int_{c^+} z\left(\frac{df}{dz}\right)^2 dz = \int_{c^+} z(u - iv)^2 dz = \int_{c^+} z\left(\frac{\Gamma}{2i\pi z} + \frac{b_2}{z^2} + \frac{b_3}{z^3} + \ldots\right)^2 dz$ and $i\int_{c^+} z\bar{z}d\varphi$ in Equation 3.40 yield pure imaginary results, its contribution to M_0 is zero. Recalling $\int_{c^+} zd\varphi = -I$ and defining $J = \frac{1}{2}\int_{c^+} Re\left(G\left(Z,t\right)\right) d\left(r^2\right)$, M_O is calculated from

$$M_O = -\rho Re\left[\left(l\left(t\right) - im\left(t\right)\right) I + \frac{dJ}{dt}\right]. \tag{3.41}$$

For example, in case of a flat plate of length $4a$, $\int_{c^+} G^3\left(Z\right) d\left(r^2\right) = -i\int_{c^+} \frac{a^4}{Z^2} d\left(r^2\right) =$

$4\pi a^4$. Therefore, J in this case becomes,

$$J = 2\pi a^4 \dot{\delta}. \tag{3.42}$$

3.3 Application of Couchet theory to Darrieus turbine

3.3.1 Profile in angular motion

With an intention to apply the compatibility condition obtained in section 3.2.1 to the blades of a vertical axis water turbine, the finite velocity condition at the trailing edge is translated into a pitch control law for the profile. The flow is thus presumed to be irrotational as the profile rotation and its control are compatible with potential flow.

For the sake of simplicity, a single blade profile is considered, which is placed in a uniform flow of velocity $\vec{V}_0 = V_0\vec{x}_0$. The influence of other blades is neglected. Let the axis of rotation be $(O_0, \overrightarrow{z}_0)$ and its rotational velocity $\omega\overrightarrow{z}_0$. The profile chord length is $2L(= 4a)$, having its centre at O, and axis of zero lift $(O, \vec{x})$ is related by the connection to a branch of pivot axis $(P, \overrightarrow{z}_0)$ so that $\overrightarrow{O_0P} = R\overrightarrow{y}_1$. Azimuthal position of the blade is denoted by the angle α, which is subtended by $\overrightarrow{x}_0$ and $\overrightarrow{x}_1$ or $\overrightarrow{y}_0$ and $\overrightarrow{y}_1$. Angular velocity of the profile is the time rate of change of α. In order to satisfy the finite velocity condition at the trailing edge of the profile, the angle $\theta\,(\overrightarrow{x}_1, \overrightarrow{x})$ subtended by the blade with the tangent of its trajectory at P should be controlled. The vector $\overrightarrow{OP} = kL\overrightarrow{x}$, with $k \in [-1, 0.5]$ is fixed between the centre of the profile O and its axis of control in rotation. $T_0 : (O_0, \overrightarrow{x}_0, \overrightarrow{y}_0, \overrightarrow{z}_0)$ is the fixed coordinate system, $T_0' : (O_0', \overrightarrow{x}_0, \overrightarrow{y}_0, \overrightarrow{z}_0)$ is the free-stream reference frame and $T : (O, \overrightarrow{x}, \overrightarrow{y}, \overrightarrow{z}_0)$ is the frame related to the profile. Details are presented in Figure 3.4.

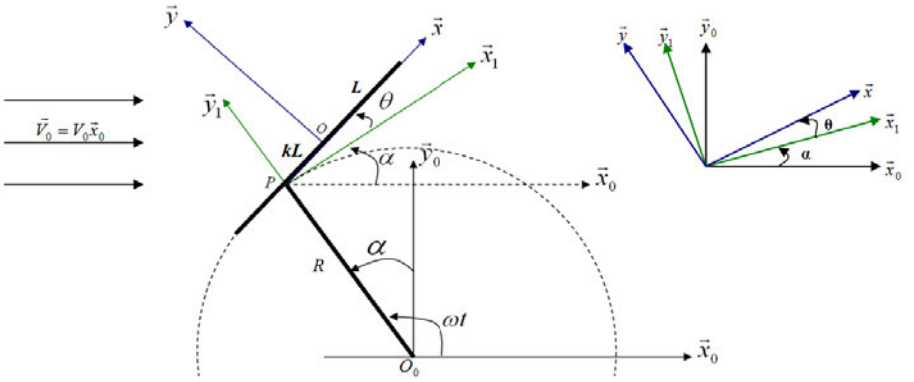

Figure 3.4: Kinematics of a pitching blade attached to the Darrieus rotor

On the profile, the velocity of point O with respect to T_0' is denoted by

$$\overrightarrow{V}_{O/T_0'} = l(t)\,\vec{x} + m(t)\,\vec{y} \tag{3.43}$$

By changing the reference frame,

$$\overrightarrow{V}_{O/T_0'} = \overrightarrow{V}_{O/T_0} - \overrightarrow{V}_{O\in T_0'/T_0}$$

where $\overrightarrow{V}_{O/T_0} = \overrightarrow{V}_{P/T_0} + \overrightarrow{OP} \times \vec{\Omega}_{T/T_0} = -R\omega\vec{x}_1 - kL\left(\omega + \dot{\theta}\right)\vec{y}$ and $\overrightarrow{V}_{O\in T_0'/T_0} = V_0\vec{x}_0$. Therefore, the velocity components in Equation 3.43 become,

$$l(t) = -\left(R\omega\cos(\theta) + V_0\cos(\alpha+\theta)\right) \tag{3.44}$$

$$m(t) = R\omega\sin(\theta) + V_0\sin(\alpha+\theta) - \mathrm{k}L\left(\omega + \dot{\theta}\right) \tag{3.45}$$

Equation 3.25 delivered the necessary condition for the profile to obtain a potential flow without vortex shedding. In case of a flat plate of length $2L = 4a$, its rotational speed relative to the reference frame T_0' is $\dot{\delta}\vec{z}_0 = \left(\omega + \dot{\theta}\right)\vec{z}_0$. The condition for finite velocity at the trailing edge can be written as

$$\Gamma = 2\pi L\left(m(t) + \left(\omega + \dot{\theta}\right)\frac{L}{2}\right) \tag{3.46}$$

From Equations 3.44 - 3.46, the condition for finite velocity at the trailing edge is

$$\Gamma = 2\pi L\left(R\omega\sin(\theta) + V_0\sin(\alpha+\theta) + (1-2\mathrm{k})\left(\omega + \dot{\theta}\right)\frac{L}{2}\right) \tag{3.47}$$

Defining the tip-speed ratio (λ) as $R\omega/V_0$ and the influencing parameter (E) as $(1-2k)L/R$, the constant circulation Γ imposed on the profile can be formulated as

$$\Gamma = 2\pi L(V_0 + R\omega)sin\beta \tag{3.48}$$

where β is the equivalent static profile incidence with respect to the relative velocity $W(= V_0 + R\omega)$. Noticing that $\frac{d}{dt} = \omega\frac{d}{d\alpha}$, the compatibility between the profile's motion and the potential flow is expressed by the equation

$$\frac{d\theta}{d\alpha} = \frac{2}{E}\left(1 + \frac{1}{\lambda}\right)\sin\beta - 1 - \frac{2}{E}\sin\theta - \frac{2}{\lambda E}\sin(\theta+\alpha) \tag{3.49}$$

The velocity field around the profile can be analytically expressed using Equations 3.20 and 3.45,

$$(u - iv)(z,t) = i\frac{2a^2\left(R\omega\sin(\theta) + V_0\sin(\alpha+\theta) - \mathrm{k}L\left(\omega + \dot{\theta}\right) + \left(\omega + \dot{\theta}\right)\frac{a^2}{Z}\right) - \frac{\Gamma Z}{2\pi}}{Z^2 - a^2}$$

For non-dimensionalizing, let $u' = \frac{u}{V_0}$, $v' = \frac{v}{V_0}$, $Z' = \frac{Z}{2a} = \frac{Z}{L}$ and $z' = \frac{z}{L}$. After decomposition of the rational fraction into simple elements and replacing $\frac{d\theta}{d\alpha}$ by the second member of the differential equation, the velocity field can be written

as

$$u' - iv'(z',t) = \frac{2i\left(\frac{1}{1-2k}\left((1+\lambda)\sin\beta\ -\lambda\sin\theta\ -\sin(\theta+\alpha)\ \right)-(1+\lambda)\sin\beta\ \right)}{2Z'+1}+$$
$$\frac{i\frac{1}{1-2k}\left(\lambda\sin\theta\ +\sin(\theta+\alpha)\ -(1+\lambda)\sin\beta\ \right)}{Z'}$$
$$=\frac{2i\left(\frac{\lambda E}{2}\left(1+\frac{d\theta}{d\alpha}\right)-(1+\lambda)\sin\beta\ \right)}{2Z'+1}-\frac{i\frac{\lambda E}{2}\left(1+\frac{d\theta}{d\alpha}\right)}{Z'} \tag{3.50}$$

where $z' = H(Z') = Z' + \frac{1}{4Z'}$. The velocity field is described by two vortices in the Z-plane. The vortex centre at origin in this plane has a potential varying between $1/\left(z' \pm \sqrt{z'^2-1}\right)$ with $Z = \left|z' \pm \sqrt{z'^2-1}\right| > 1$ in the plane of the profile. The velocity associated with this potential is finite when $z' \to 0$, and decreases in $1/z'$ for $|z'| \gg 1$. The vortex centre at z'=0.5 is located on the leading edge, where the speed is infinite. For a profile whose radius of curvature at the leading edge is non-zero, the velocity is finite in $z' = -1$. The condition for the finite velocity at the trailing edge is therefore translated into the motion compatibility with the potential flow assumption.

With the idea of Equations 3.36 and 3.41, keeping the same notations, the hydrodynamic torsor on the point O on unit profile scale can be expressed as,

$$\{fluid \to profile\} = \begin{cases} \overrightarrow{F}^{fluid\to profile} = \rho\left(\dot{\delta}I - m(t)\,\Gamma\right)\overrightarrow{x} + \rho\left(l(t)\,\Gamma - 4\pi a^2\frac{dm}{dt}\right)\overrightarrow{y} \\ \overrightarrow{M}_O{}^{fluid\to profile} = -\rho\left(l(t)\,I + 2\pi a^4\frac{d\dot{\delta}}{dt}\right)\overrightarrow{z} \end{cases}$$

The kinematics of turbine blade are such that

$$\left.\begin{aligned} \delta &= \theta+\alpha \\ l(t) &= -\left(R\omega\cos(\theta)\ +V_0\cos(\alpha+\theta)\ \right) \\ m(t) &= R\omega\sin(\theta)\ +V_0\sin(\alpha+\theta)\ -\mathrm{k}L\left(\omega+\dot{\theta}\right) \end{aligned}\right\} \tag{3.51}$$

where θ is the solution of the differential Equation 3.49. The dimensionless components of the torsor of the fluid on the profile are noted as,

$$\left.\begin{aligned} X' &= \frac{\overrightarrow{F}^{fluid\to profile}\cdot\overrightarrow{x}}{\rho V_0^2 L} \\ Y' &= \frac{\overrightarrow{F}^{fluid\to profile}\cdot\overrightarrow{y}}{\rho V_0^2 L} \\ M'_O &= \frac{\overrightarrow{M}_O{}^{fluid\to profile}\cdot\overrightarrow{z}}{\rho V_0^2 L^2} \end{aligned}\right\} \tag{3.52}$$

According to Equations 3.36, 3.37, 3.41 and 3.42, and further assuming a constant

rotational velocity ω for the turbine, then Equation 3.52 becomes

$$X' = -2\pi\left(\frac{1}{1-2k}\left(\lambda\sin\theta\ + \sin\left(\theta+\alpha\right)\ \right) - \frac{2k}{1-2k}\left(1+\lambda\right)\sin\beta\ \right)^2$$

$$Y' = -2\pi\left(\lambda\cos\theta\ + \cos\left(\theta+\alpha\right)\ \right)\left(\kappa(1+\lambda)\sin\beta\right) + \frac{\pi E\lambda^2}{1-2k}\cos\theta$$

$$M'_O = \pi(\lambda\cos\theta + \cos(\theta+\alpha))\left(\lambda\sin\theta + \sin(\theta+\alpha) + \frac{8k^2-4k+1}{2}\kappa\right) - \frac{\pi E\lambda^2}{4(1-2k)}\cos\theta$$

where $\kappa = \frac{1}{(1-2k)^2}[(1+\lambda)\sin\beta\ - \lambda\sin\theta\ - \sin\left(\theta+\alpha\right)\ ]$.

To evaluate the torque available for power generation, the moment due to fluid action at O_o needs to be calculated. For this, the system is decomposed into two elements, one is the combination of the shaft $O_0\vec{z}_0$ and the link O_0P and second is the turbine blade. The torsor of the fluid on second element and that of the second on first element are expressed as,

$$\left.\begin{aligned}\{fluid \to 2\} &= \left\{\begin{array}{cc} X & 0 \\ Y & 0 \\ 0 & M_O \end{array}\right\}_{O,(\vec{x},\vec{y},\vec{z})} \\ \{2 \to 1\} &= \left\{\begin{array}{cc} X_{21} & 0 \\ Y_{21} & 0 \\ 0 & M_{21P} \end{array}\right\}_{P,(\vec{x},\vec{y},\vec{z})}\end{aligned}\right\} \tag{3.53}$$

Applying the fundamental principle of dynamics at the point P in the second element while neglecting the mass of the blade,

$$\begin{array}{lll} X + X_{12} = 0 & & X_{21} = X \\ Y + Y_{12} = 0 & \text{therefore} & Y_{21} = Y \quad \text{with } M_P = M_O - kLY \\ M_P + M_{12P} = 0 & & M_{21P} = M_{21} \end{array} \tag{3.54}$$

The action of the fluid on the blade is therefore equal to the action of the blade on first element. The moment on the shaft per unit scale is $M_{O_0} = M_P + R\sin\theta\ Y - R\cos\theta\ X$. Dimensionless moment about Oo by $\rho V_0^2 l^2$ is denoted by M'_{O_0}which is equal to

$$M'_{O_0} = M'_O + \left(\frac{\sin\theta}{E} - k\right)Y' - \frac{\cos\theta}{E}X' \tag{3.55}$$

Here, the torque transmission from second to first element requires a motor and

therefore the connection between these two elements is not modelled.

3.3.2 Study of control law in a uniform flow

Figure 3.5 shows the solution for Equation 3.49 which is of nonlinear-first-order type using the Runge-Kutta method of order 4. Although initially there is a short transient behaviour, the solution converges quickly to a single 2π-periodic solution for $\theta \geq \frac{\pi}{2}$ approximately.

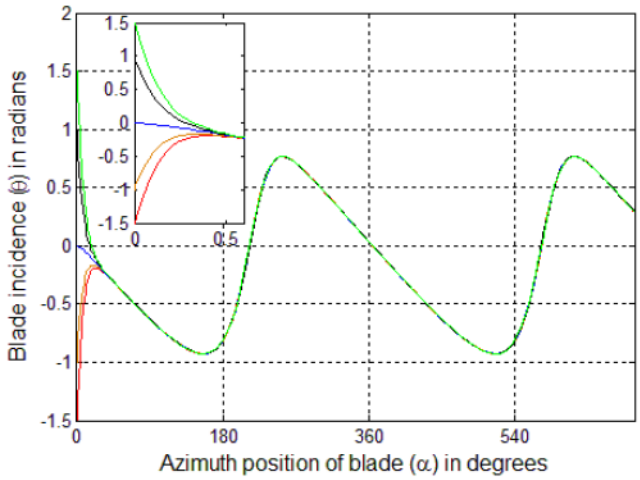

Figure 3.5: θ (α) for E=0.2 and $\lambda = 1.25$ with no circulation for different initial conditions. Solutions rapidly converge to the same periodic law. This solution stability with respect to the initial conditions is true for other values of the parameters E, λ and β for values of $|\theta(0)|$lower than $\pi/2$.

3.3.2.1 Effect of λ

The physical interpretation of the device performance is attributed to limits of λ. For simple cases, the control law defined by Equation 3.49 can be expressed analytically whereas the solution must be consistent with numerical results for limiting cases. Figure 3.6 shows the positioning of the blade under various operating conditions while Figure 3.7 presents the blade's positioning for different values of λ for a given circulation corresponding to $\beta = 0.1$ rad.

For λ close to zero, the velocity of point P on the blade is negligible compared with the flow velocity. If the incidence of the plate $\theta + \alpha$ is constant, the steady flow over the fixed plate is the solution for ideal fluid flow. For λ tending to infinity, Equation 3.49 results in $\frac{d\theta}{d\alpha} = \frac{2}{E}\sin\beta \ - 1 - \frac{2}{E}\sin\theta$. When $\lambda >> 1$, the average value of θ is approximately equal to $\sin^{-1}(\sin\beta \ - E/2)$.

For $\lambda = 0.5$, a periodic oscillation of the solution around the straight line $\theta = \beta - \alpha$ is observed. The shape of the solution is unchanged up to a certain value of tip speed ratio λ_0, beyond which the solution acquires a new shape. This

critical value of λ_0 is a function of β. For $\beta = 0.1$ rad, λ_0 is approximately equal to 0.895. The amplitude of the oscillations decreases as λ increases.

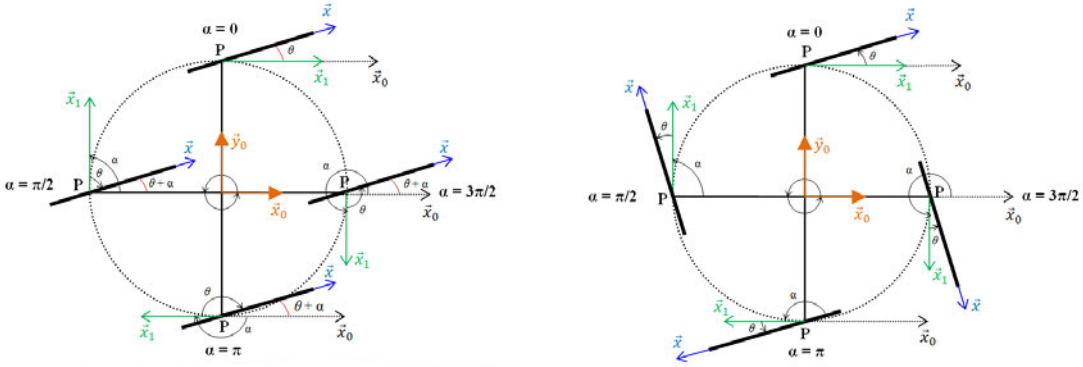

(a) (b)

Turbine blade controlled at low ω with constant $\theta + \alpha$ (left) and high ω with constant θ (right) for $\lambda \to \infty$

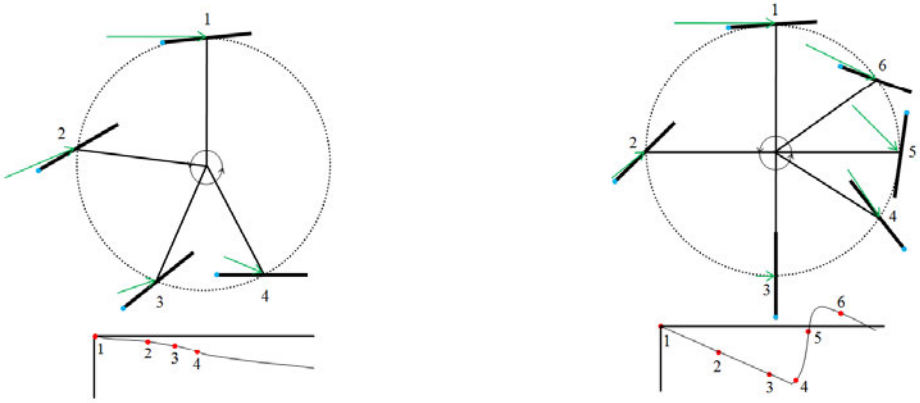

(c) (d)

Profile position controlled by the law $\theta(\alpha)$ for λ= 0.5 (left) and λ=0.9 (right). Apparent velocity is shown by green arrows and the leading edge of the profile is marked by a blue dot

Figure 3.6: Influence of operating conditions on blade position that follows pitch control law

Figure 3.8 shows the plot of profile's orientation θ with apparent velocity and that at leading edge for various values of λ. The variations of apparent velocity are compensated by the angular variations so that the circulation around the plate is kept constant. The necessary condition of compatibility of profile's motion with a potential flow is thus verified. From Equation 3.36, the components of torsor of

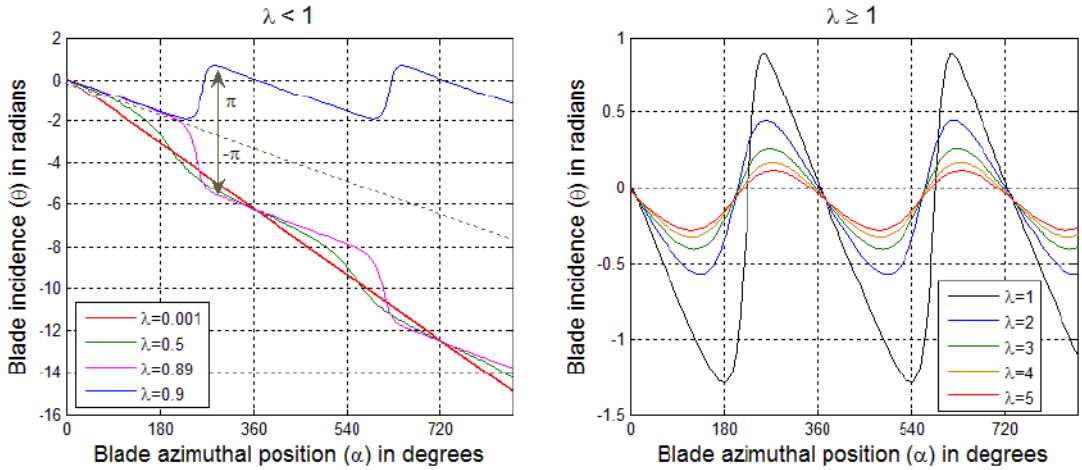

Figure 3.7: Solution for the control law of $\theta(\alpha)$ using forth order Runge-Kutta method for β=0.1 and E=0.4

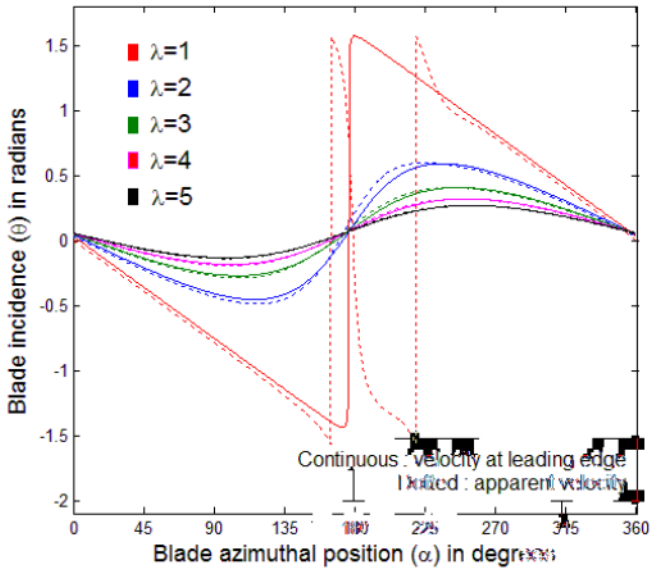

Figure 3.8: Control law for $\theta(\alpha)$ for tip-speed ratio $\lambda > 1$. Curvature effects are not negligible at high rotational velocities as they decrease here the angle θ about 0.2 radians relative to a straight apparent flow.

the fluid on the profile in the reference frame $\left(O,\ \vec{x},\ \vec{y}\right)$ are

$$\left.\begin{aligned} X &= \underbrace{-\rho m \Gamma}_{steady} + \underbrace{\pi \rho l^2 m \left(\omega + \dot{\theta}\right)}_{unsteady} \\ Y &= \underbrace{\rho l \Gamma}_{steady} - \underbrace{\pi \rho l^2 \dot{m}}_{unsteady} \\ M_O &= \underbrace{-\pi \rho l m}_{steady} - \underbrace{\frac{\pi}{8} \rho l^4 \ddot{\theta}}_{unsteady} \end{aligned}\right\} \tag{3.56}$$

where each force component is expressed as the sum of steady and unsteady terms. Figure 3.9 shows the evolution of the steady and unsteady components of force and moment for different values of tip-speed ratio λ. It is seen that the oscillations in the unsteady component in X-force increase with tip-speed ratio λ up to the critical value of about 0.9. Later, it tends to retain a stable evolution. The unsteady component however exhibits increased oscillations as λ increases. The unsteady component of Y-force and moment are almost equal to zero irrespective of the tip-speed ratio. Also, the oscillatory structures of these two parameters increase in amplitude with increasing λ. For λ close to its critical value, a local disturbance in the evolution curves of torsor elements is noticed soon after every half rotation.

3.3.2.2 Effect of parameters E and β

According to the definition of the parameter E in section 3.3.1, moving the axis of rotation from $(P, \vec{z}_0)$ to the leading edge of the profile is equivalent to the calculation of the control law by lengthening the chord or shortening the distance R between the profile and axis of turbine. As seen in Figure 3.10, the solution is very sensitive to the parameter E due to the effect of curvature of the velocity field in the reference frame T_1 for the larger rotational velocities. For lower positive values of E so that $|\sin\beta - E/2| \leq 1$, the solution oscillates around a constant value of θ, equal to $\sin^{-1}(\sin\beta - E/2)$. The curvature of the velocity field results in an increase (or a decrease if $k > 0.5$) of the angle between the apparent velocity, carried by the tangent to the trajectory of the point P, and the profile. If the parameter E is too high to impart sufficient effects on the profile to compensate for the curvature of the velocity field, the case of $|\sin\beta - E/2| > 1$ leads to such a control that the profile is rotated about its axis $(P, \vec{z}_0)$ at high velocity. As a result, unsteady rotational effects maintain the circulation around the profile. On the other hand, smaller values of E, say 0.4, increase the effect of profile sufficiently to compensate for the curvature of velocity field where the flow can be considered as quasi-stationary in the reference frame T_1.

As per the definition of the circulation given by Equation 3.48, the parameter β conditions the circulation Γ imposed on the profile. As shown in Equation 3.56, the steady terms of the force expressions are explicit functions of the imposed circulation Γ, therefore β is an influential parameter in the hydrodynamic analysis. In addition, this plays an important role in the calculation of unsteady force and moment terms. The critical tip-speed ratio λ_0 inversely varies with β. Higher values of β increase the circulation around the blade. In order to conserve the circulation, the blade must be subject to higher rotational speed about point P which increases the unsteady effects.

When $\lambda << 1$, the flow is set around the profile which is at a constant incidence

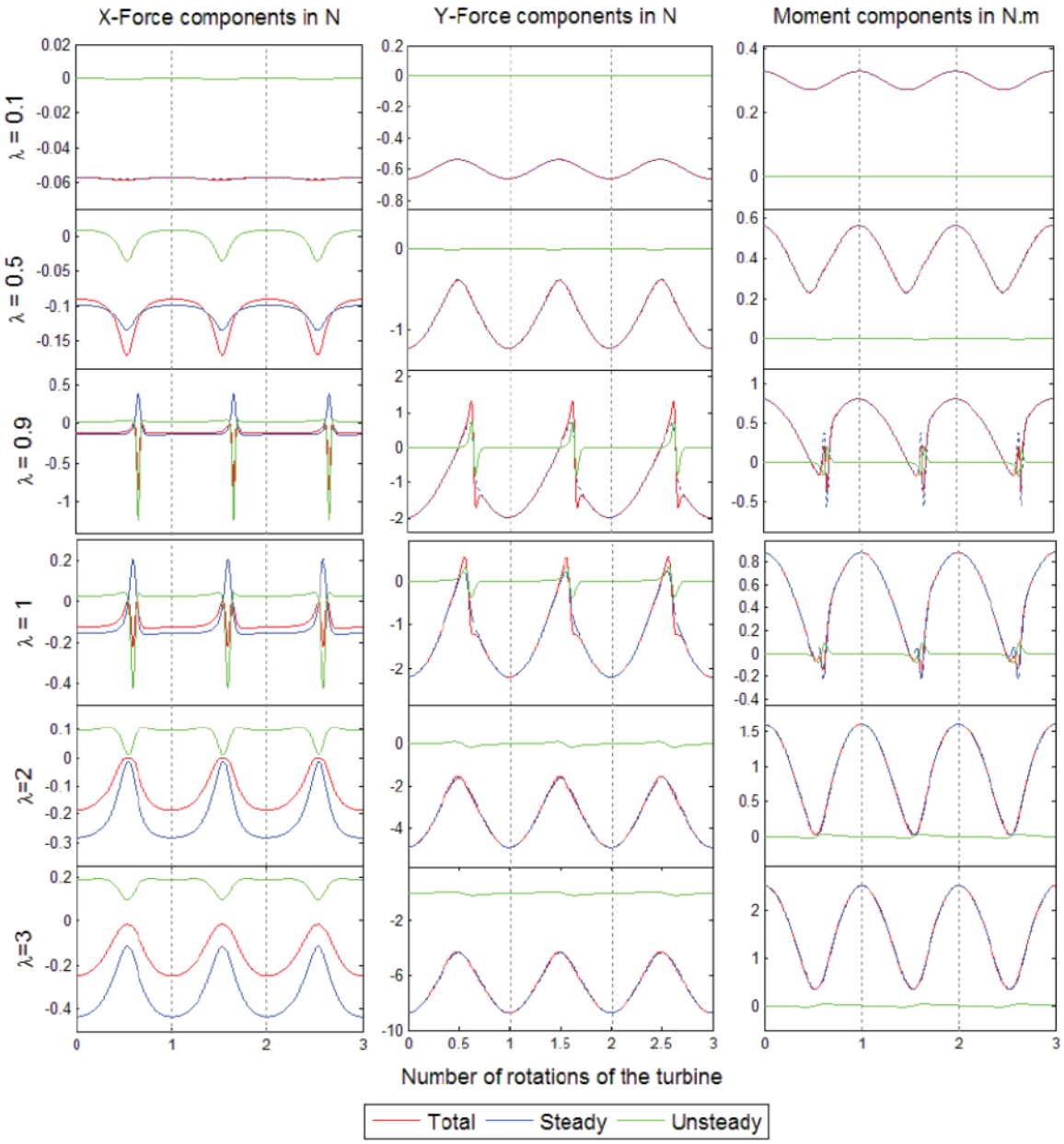

Figure 3.9: History of steady and unsteady components of force and moment through three turbine rotations for different values of tip-speed ratio λ. These calculations are based on a free-stream velocity $V_0 = 1$ m/s, constant imposed circulation corresponding to $\beta = +5^o$ and $k = -0.5$ for rotor radius of 0.3 m.

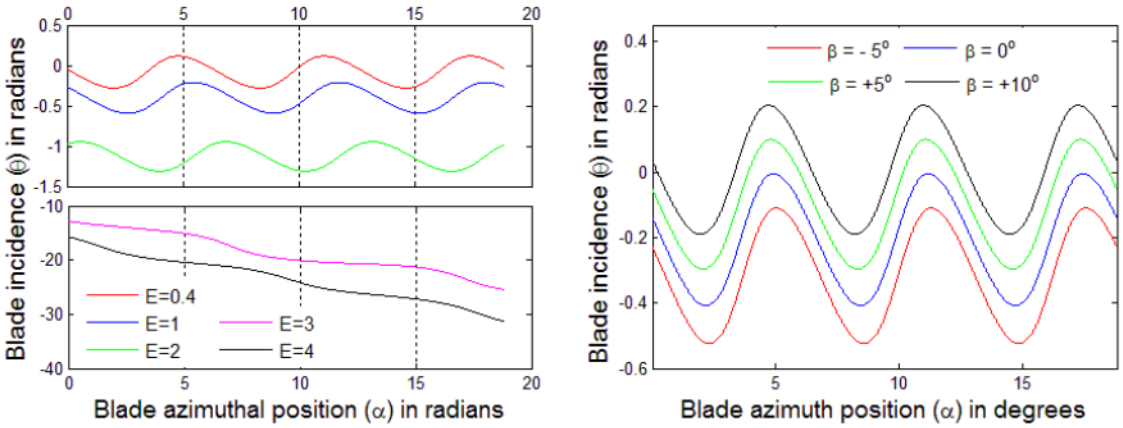

Figure 3.10: Control law as a function of E for β=0.1 and λ=5 (left), and as a function of β for E=0.4 and λ=5 (right) in reference T_1

$(\theta + \alpha)$. The resultant force is approximately $-\rho V_0 \Gamma \vec{y}_0$. For tip-speed ratio λ close to the critical value λ_0, both steady and unsteady terms are involved in the force calculations with the later dominating at specific azimuthal locations. Figure 3.11 (a) shows the plot of moments per blade for two cycles for $\lambda = 0.9$, in which the jumps are noticed at α about 200^o. However, the evolution of the moment is much smoother for $\lambda > 1$. Figure 3.11 (b) shows the resultant moment at the turbine's centre for different values of the circulation imposed around the blades for $\lambda = 2$.

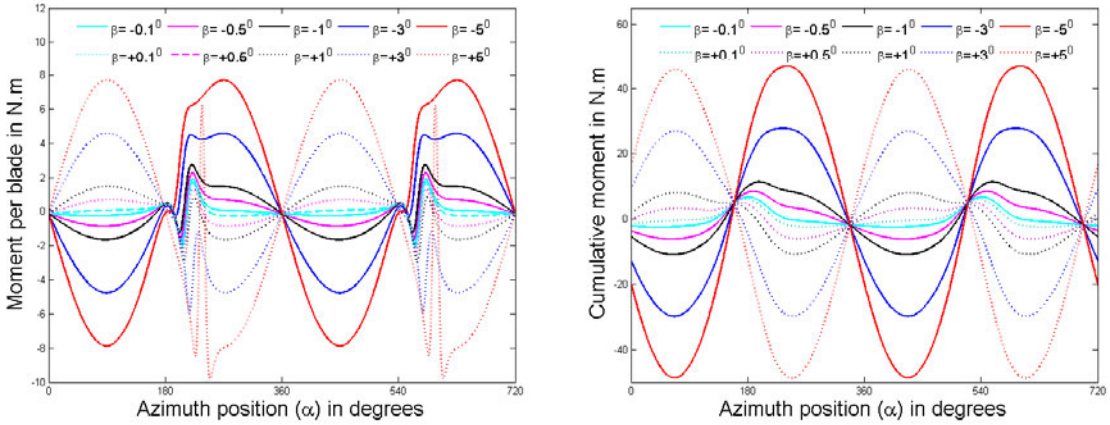

(a) (b)

Figure 3.11: Torque evolution as a function of imparted circulation to the blades for $V_0 = 1$ m/s. (a) Moment of a single blade at the centre of the turbine at $\lambda_0 = 0.9$, and (b) Resultant moment of 4 blades at $\lambda = 2$

3.4 Conclusion

The objective of this chapter was to examine whether potential flow conditions could be applied to real flow situations in order to gain the advantage on ideal flow behaviour with constant circulation. The irrotational flow over an arbitrary profile was formulated using conformal mapping. A prospective potential flow application on the basis of Couchet theory is involved in the development of a control law that decides the blade pitching. Such a reduction of the flow problem comprised the generalization of the Kutta-Joukowski condition for the profile's motion. In this chapter, the hydrodynamic forces and moment acting on the profile in ideal flow conditions were calculated. In addition, the effect of tip-speed ratio λ and design parameters E and β on the blade's performance was quantified. The application of pitch control law in the real flow conditions is however limited due to viscous losses and rotational effects, which are presented in Chapter 6. Before examining the effectiveness of this blade pitch control using CFD studies, benchmarking analysis of a classical Darrieus turbine with fixed blades is necessary. Chapter 4 and 5 will therefore present the numerical and experimental investigations of fixed blade model respectively.

CHAPTER 4

FIXED BLADE MODEL: CFD ANALYSIS

Contents

4.1 Introduction

The process of modeling a physical problem, creating an appropriate mesh and solving the governing equations for an accurate solution is usually not straightforward. The computational solution is always the result of many assumptions and compromises, involving the concepts of designing, discretization, fluid dynamics, turbulence modeling etc... The hydrodynamic flow across a Darrieus turbine is one such complex problem to solve and analyze since the flow phenomenon includes unsteadiness and turbulence. A comprehensive investigation of the device performance and a substantial enhancement in its power characteristics can be realized with a good understanding of the exact flow mechanism. Apart from analytical and experimental approaches, CFD has been an effective tool to predict the flow physics in both research and industrial applications. Table 4.1 shows the list, not exhaustive, of CFD studies performed by various researchers on flow analysis of vertical axis water/wind turbine of Darrieus type. The purpose of this chapter is to present a suitable CFD implementation methodology by splitting the process into the three key themes: pre-processing, processing and post-processing.

4.2 Pre-processing

Pre-processing activities consists of creating the geometrical representation of Darrieus hydroturbine and an appropriate spatial discretization for turbulence modeling. Since the turbine model has straight blades, only 2D computations are targeted by neglecting the three-dimensional relieving effects.

4.2.1 CAD model

The replication of real-time physics in the computational setting and quality of numerical results fundamentally depend on the development of right CAD model and mesh generation. The vertical axis turbine model for numerical simulations consists of a four-blade rotor system with NACA 0015 profiles. Before developing the CAD model, the hydrofoil shape study was performed which was important to understand the hydrodynamic forces around the blade during the turbine's rotation. NACA 0015 profile is given by the NACA 4-digit equations reported in Jacobs et al. (1933). Table 4.2 provides the basic design specifications of the turbine model for numerical studies.

The solidity of the turbine σ, as defined by the Equation 2.2, is equal to 0.533 for the base model. The size of the computational domain is in consistent with the towing tank dimensions, which is used for the experiments. Also, the domain size ensured the complete flow development with no flow reversal during the simulations.

Table 4.1: Summary of CFD studies on VAWT from literature survey

Reference	Model configuration	Mesh type	Viscous model(s)
Vertical Axis Water Turbine studies			
Asim et al. (2013)	4-4, 4-8, 4-12, 8-4, 8-8, 8-12, 12-4, 12-8, 12-12*	Sliding mesh	SST $k-\omega$
Hyun et al. (2010)	3, 4 and 6 bladed models with NACA634-021, NACA653-018 profiles	Sliding mesh	SST $k-\omega$
Fleisinger et al. (2014)	3 bladed model with modified Naca 633018 profiles	Transient sliding mesh for FSI analysis	SST $k-\omega$
Marsh et al. (2012)	3 bladed model with modified Naca 634221 profiles	Rotating mesh with unstructured tetrahedral cells	SST $k-\omega$
Wenlong et al. (2013)	3 bladed model with Naca 0015 profiles	Rotating mesh, unstructured triangular cells in core and near wall refinement with rectangular cells	Standard $k-\epsilon$
Klaptocz et al. (2007)	3 bladed model with Naca 634021 profiles	Rotating mesh	Spalart-Allmaras
QinetiQ (2004)	3- & 6-bladed models with NACA 0012 profiles	Unstructured rotating mesh	$k-\epsilon$
Meneses et al. (2014)	3 bladed model with NACA 0025 profiles	Rotating mesh, structured rectangular cells in stationary region and triangular cells in the sliding zone	SST $k-\omega$
Gupta and Biswas (2013)	3 straight and twisted blade models	Unstructured moving mesh	Standard $k-\epsilon$
Lain and Osorio (2010)	3 bladed model with NACA0025 profiles	Sliding mesh for blade trajectory over steady zone for fluid field	SST $k-\omega$
Vertical Axis Wind Turbine studies			
Almohammadi et al. (2015)	3 bladed model with NACA 0015 profiles	Rotating mesh with quadrilateral cells	SST $k-\omega$ and RNG $k-\epsilon$
Ferreira et al. (2007)	Single blade with NACA 0015 section	Quadrilateral structured mesh with moving sub-grids	S-A, $k-\epsilon$, DES, LES
Horiuchi et al. (2005)	3-bladed model with TWT11251 profile	Moving mesh	DES
Vassberg et al. (2005)	1-bladed model with NACA0015 & WARP0015-RC8 profiles	Structured quadrilateral moving mesh	Baldwin-Lomax
Hansen and Sørensen (2001)	1-bladed model with NACA 0015 profile	Moving mesh	$k-\epsilon$ and non-linear $k-\epsilon$
Consul et al. (2009)	2-bladed model with NACA 0015 profile	Circular rotating mesh	SST $k-\omega$ and Spalart-Allmaras
Shires and Kourkoulis (2013)	1-bladed model with NACA0018, CC-E0020EJ & TE-ELLIPSE profiles	2D Octree hexahedral mesh	SST $k-\omega$
Benedict et al. (2013)	4-bladed model with NACA 0015 profile	Overset structured mesh	$k-\epsilon$ and non-linear $k-\epsilon$
Carrigan et al. (2012)	3-bladed model with NACA 0015 profile	Moving hybrid grid	Spalart-Allmaras

Parameter	Specification
Blade section	NACA 0015
Chord length (L)	0.08 m
Number of blades (N)	4
Rotor diameter (D)	0.6 m

Table 4.2: Design specifications for Darrieus turbine

4.2.2 Meshing

The flexibility of the computational mesh structure is associated with the adaptability and accuracy of the flow analysis system in order to evaluate the level of geometrical complexity it can handle and the degree of control it offers over the resolution of flow features (Baker et al., 2007). The primary function of the computational grid is to fit the solution domain and decompose its volume into sub-domains, called control volumes or cells, where the conservation equations are solved. The continuous flow problem is thus discretized into numerous small problems. Anderson (1995) gave more details on the numerical implementation behind the mesh generation.

4.2.2.1 Finite volume method

Star CCM+ uses finite volume method (FVM) where the numerical solver employs a cell-centred finite volume method to evaluate the partial differential equations based on control volume integration to compute the flow variables at cell-centroid (Versteeg and Malalasekera, 1995). Though this process looks similar to finite difference method, FVM works well with both structured and unstructured meshes. The FVM uses Gauss divergence theorem to convert the volume integrals into surface integrals and hence the value from cell faces into cell surfaces. The discretization of conservation equations can be described by considering a transport scalar variable ζ whose unsteady conservation equation for an arbitrary control volume v is given in an integral form:

$$\int_{\mathrm{v}} \frac{\partial \rho \zeta}{\partial t} d\mathrm{v} + \oint \rho \zeta \vec{u}.d\vec{A} = \oint \Gamma_{\zeta} \nabla \zeta.d\vec{A} + \int_{\mathrm{v}} S_{\zeta}.d\mathrm{v} \tag{4.1}$$

where ρ, $\vec{u}$, $\vec{A}$, Γ_{ζ} and S_{ζ} represent the fluid density, velocity vector, surface area vector for the volume v, diffusion coefficient for ζ and source of ζ per unit volume respectively. When applied Equation 4.1 to a finite cell whose volume is $\mathcal{V}$ with number of enclosing faces N_{faces}, the discretized form of conservation equation becomes

$$\frac{\partial \rho \zeta}{\partial t}\mathcal{V} + \sum_{f}^{N_{faces}} \rho_f \zeta_f \vec{u}_f.\vec{A}_f = \sum_{f}^{N_{faces}} \Gamma_{\zeta} \nabla \zeta_f.\vec{A}_f + S_{\zeta}\mathcal{V} \tag{4.2}$$

where ζ_f is the amount of ζ convected through the face f, $\rho_f \zeta_f \vec{u}_f . \vec{A}_f$ is the mass flux through the face f. Here $\vec{A}_f = |\vec{A}_f| \vec{n}_f$ where $|\vec{A}_f|$ is the face area and $\vec{n}_f$ represents the unit normal vector ejecting outwards of the face f. While the values of scalar property ζ are stored at the cell centroid, Equation 4.2 required the face centred values ζ_f, which necessitates the interpolation of ζ from cell centre to faces. These can be done by using 1st order scheme or 2nd order scheme. In First Order Upwind (FOU) the values at cell faces are the averaged values with adjacent cell centres and in Second Order Upwind (SOU), the values are the averaged with next two cells. However, FOU method produces numerical diffusion as the discretized equations are more diffused than the original equations and even more diffusion for large gradients, while the SOU method gives a smooth solution with less numerical diffusion with more time as it requires more cells in numerical calculations. Tu et al. (2008) explained that FOU method converges faster than the SOU method, but this analysis requires more accurate prediction of secondary flow and boundary layer flow structures, where SOU is more useful. This will help to predict correct flow properties in flow analysis for retrieving a solution.

4.2.2.2 Mesh structure

Mesh representations are classified as structured and unstructured grids depending on the regularity in cell connections. Simple and regular geometries can have structured mesh while complex models have unstructured ones. Structured meshes usually have the quadrilateral and hexahedral cells for 2D and 3D geometries respectively, while triangular and tetrahedral cells are present in unstructured 2D and 3D meshes. The structured meshes are usually space efficient and provide quicker solution convergence and better resolution. On the other hand, the unstructured meshes are space inefficient due to the need for an explicit storage of neighbourhood connectivity. Another type is the 'hybrid meshing' which comprises the combination of structured and unstructured grid portions. Thompson et al. (1997) discussed in detail the grids types in CFD applications. In the present project, structured meshes are preferred due to relative simplicity in the geometry and anticipated CPU effort for a large number of computations. Figure 4.1 shows the typical structured mesh around the hydrofoil. The Chimera technique used for mesh motion however makes the grid unstructured at the interface. Next subsection provides more details on overset meshing.

4.2.2.3 Overset meshing

To incorporate the different geometrical features and their own particular motion in the computational domain, meshing was performed using Chimera technique. This is regarded as a part of Schwartz decomposition methods (Saad, 1996) as a compound finite-volume grid which offers the regions overlapping and sliding over

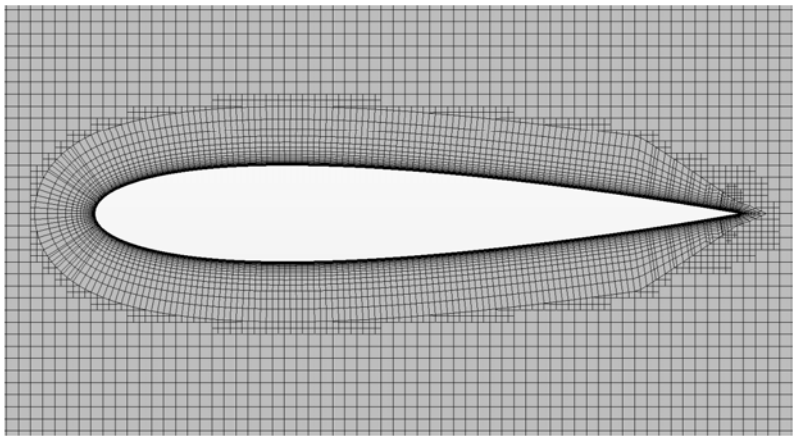

Figure 4.1: Structured mesh around the hydrofoil

each other within a common computational domain. Such technique uses Chimera interpolation (Steger et al., 1983) and simplifies the simulation strategy to handle relative motions between different regions, and flow over complex geometries with dynamic motions. Ease in dealing with complex motions using Chimera technique can thus enable the system optimization process. Hadzic (2005) detailed the overset meshing schemes used in Star CCM+.

A recent literature is available on the CFD analysis of Darrieus turbines using Chimera meshes. The parametric studies of NREL Phase VI turbine by Li et al. (2012) and Zahle et al. (2009), using overset meshes for incompressible RANS solvers Ship-Iowa and EllipSys3D, revealed the three-dimensional aerodynamic effects. These results were in close comparison with the experimental ones. In the study of Chow and Dam (2011), overset meshes were used to characterize the geometric modifications of turbine blade and analyze the corresponding aerodynamics. Several scholars (Zhang et al., 2007; Noack and Boger, 2009; Quon and Smith, 2015; Houzeaux et al., 2014 and Rolland et al., 2013) used Chimera meshes to study the relative motions between the regions within the same flow domain. In this study, O-type Chimera meshes m1, m2, m3 and m4 around respective blade profiles were created to apply individual superposed motion to the blades in order to simulate both the rotation of the turbine and blade-pitching within the computational domain. The mesh representation is shown in Figure 4.2. Each of the meshes around the hydrofoils was structurally meshed with 40x40 diametrical grid points. The background rectangular mesh m5 consists of 575x375 cells in x- and y-directions with a refined cylindrical zone that accommodates the four meshes, m1 - m4. The cell connectivity information between overset and background meshes was obtained by implicit hole cutting scheme. Works of Chan et al. (2012), and Lakshminarayan and Baeder (2010) provide more details on this.

When Chimera meshing is performed, one or more overset regions with individual mesh specifications are created over the background region. An interface is

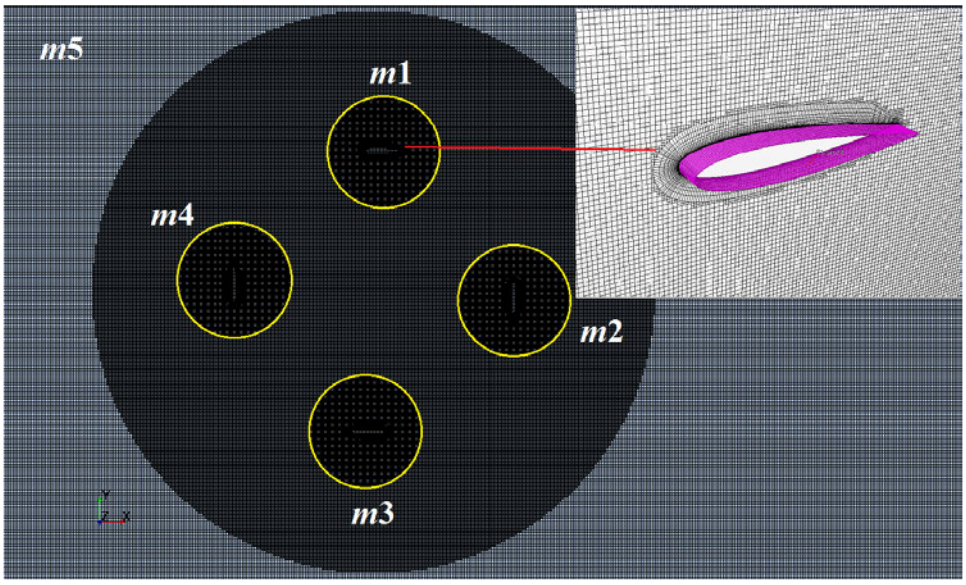

Figure 4.2: Mesh visualization and sub-zones of computational domain. Near wall modeling is shown in inset

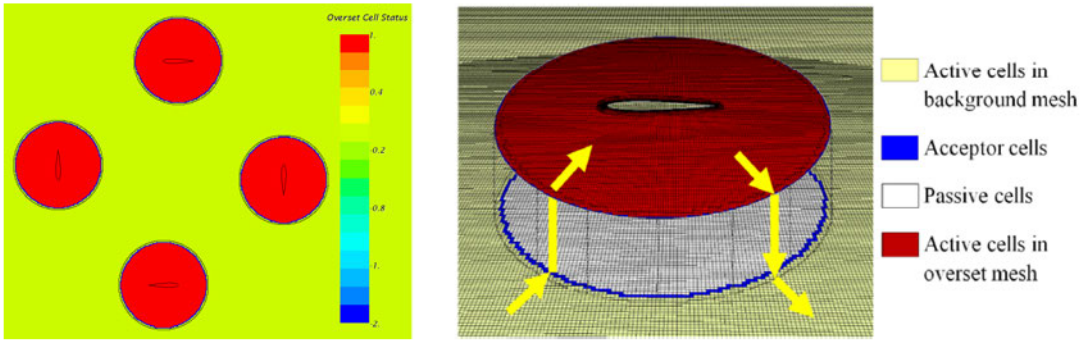

Figure 4.3: Overset cell status (left) and mesh workflow (right)

generally used to connect tightly these two regions to pass the numerical information from each other during the computations with a negligible level of iteration errors. When the simulations are run, the equations are solved only in the active cells in the background and overset regions and the data is transferred to and fro through acceptor cells at the interface by means of distance weighted interpolation. Conservation equations are solved within the acceptor cells and passive cells remain inactive except when the overset mesh moves (Tran et al., 2014; Swidan, 2013). The flux between the active and acceptor cells is computed the same way as between two active cells. This entire scheme is identical to a single continuous mesh, which prevents prolonged convergence duration for complex motion analysis. Figure 4.3 shows the overset cell status and mesh work flow design.

4.2.2.4 Basic validation

The meshing strategy implemented in current study is aimed to avoid bottlenecks of conventional meshing processes around the moving bodies. At the same time, it is important to profess that current meshing process is 'fit-for purpose'. Therefore, a basic mesh validation is performed for the pressure coefficient plot around the blade. Figure 4.4 shows the Cp-plot produced by overset and continuous meshes at various angles of attack. It is clear that the overset meshes are as effective as continuous mesh for the same near-wall resolution. This reveals the tightest coupling between the background and moving regions through acceptor cells.

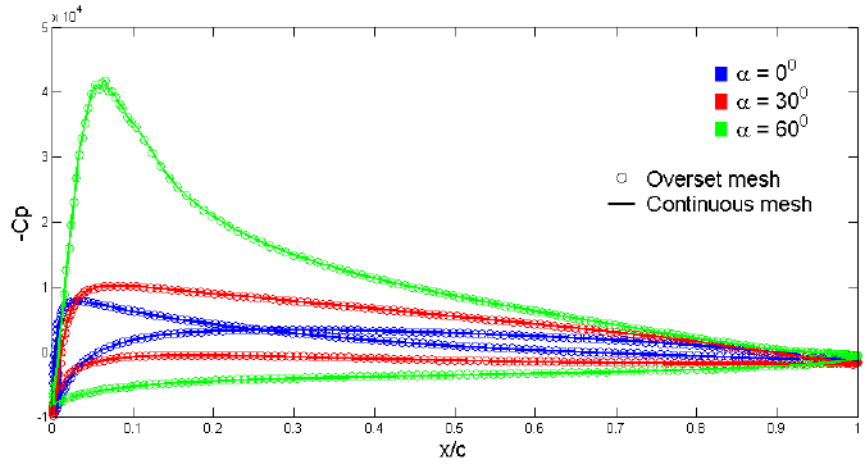

Figure 4.4: Preliminary validation of overset mesh for pressure coefficient distribution over the blade at three different azimuth positions

4.2.3 Boundary conditions

The boundary conditions for two-dimensional unsteady incompressible hydrodynamic flow are similar to those applied by Biadgo et al. (2013). The set of coordinate systems and boundary conditions are shown in Figure 4.5. In order to achieve a unique solution, velocity inlet and static pressure outlet conditions are specified for all of the computations presented in the next chapters. The inlet boundary condition specification includes the velocity components and turbulence parameters such as turbulence intensity Tu and eddy viscosity ratio μ_t/μ, which are used to calculate the kinetic energy k and its specific dissipation rate ω when two-equation turbulence models are used. A symmetry boundary condition is applied to top and bottom faces of the computational domain which create a mirror effect for the flow. These two faces are thus constrained with no velocity and scalar quantity gradients normal to the boundary. Wall specification is given to the blades where no-slip condition prevails at all times to ensure the real flow

across the rotor. Furthermore, a set of realistic backflow conditions is also specified to minimize the convergence difficulties in order to increase the robustness of calculation and prevent the back flow which does destabilize the computational code.

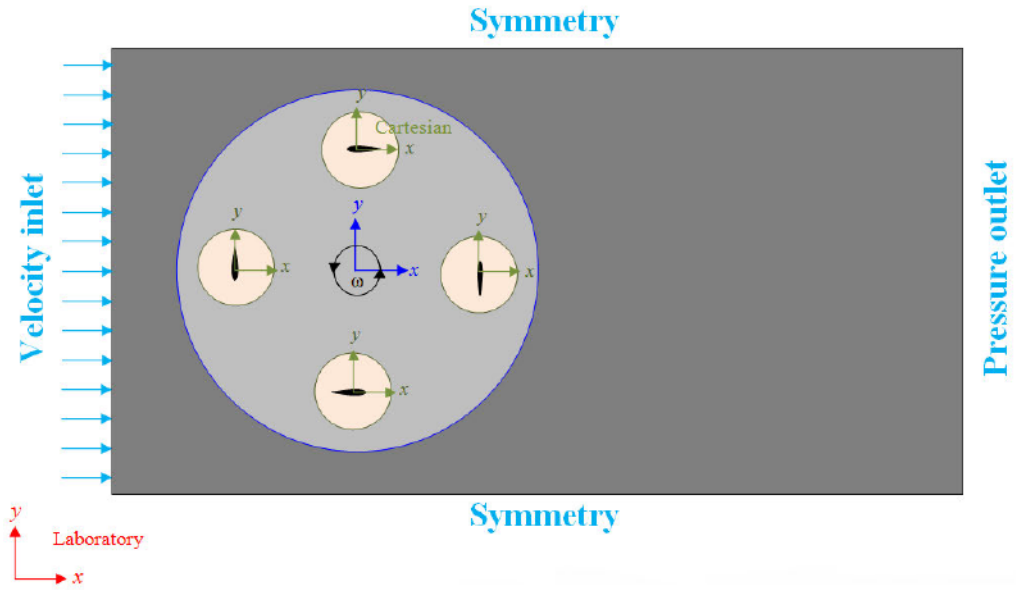

Figure 4.5: Schematic of boundary conditions and coordinate systems

4.3 Processing

4.3.1 Solver algorithm

The set of equations solved in this study are the mass and momentum conservation equations. No energy equation is considered since there is no heat transfer involved. All simulations are performed with unsteady state segregated, implicit solver formulation. This formulation employs a pressure correction scheme, whereby the momentum equations are solved sequentially for the velocity components using the best available estimate for the pressure distribution. Subsequently, the pressure correction is calculated from a derived Poisson equation and the process is repeated until the continuity equation is satisfied. The pressure correction scheme uses SIMPLE (Semi-Implicit Method for Pressure-Linked Equations) algorithm for the simulations. This algorithm provides necessary coupling between the calculated velocity field and the pressure field for segregated solution of the conservation equations. In addition, the bounded-central scheme employed by Star CCM+ solver is adapted in computations using polyhedral meshes.

4.3.2 Turbulence modeling and closure

Turbulence is inherently a three-dimensional phenomenon, characterized by random fluctuations of flow parameters, unsteadiness, unpredictability, coherent structures called 'eddies', and broad spectrum of length and velocity scales. These scales, which describe the dissipation of the turbulent kinetic energy k, play an important role in distinguishing the turbulence intensity Tu in the flow. These two parameters are defined as

$$k = \frac{1}{2}(\overline{u'^2} + \overline{v'^2} + \overline{w'^2}) \tag{4.3}$$

$$Tu = \frac{(\frac{2}{3}k)^{1/2}}{U_{ref}} \tag{4.4}$$

where u', v' and w' are the fluctuating velocity components and U_{ref} is the reference velocity. The assumption of isotropic turbulence implies $\overline{u'^2} = \overline{v'^2} = \overline{w'^2}$ so that

$$Tu_{iso} = \frac{\sqrt{\overline{u'^2}}}{U_{ref}} \tag{4.5}$$

which is identical to the RMS value of a fluctuating velocity component.

The transfer of kinetic energy from the mean flow to turbulent structures is primarily associated with these scales of eddies. This energy transfer is directed towards the smallest scales, called 'Kolmogorov microscales', where the Reynolds number is unity that causes viscous dissipation of the turbulent kinetic energy.

Turbulent flow analysis of marine energy systems is not a new problem. Masters et al. (2012) coupled blade element momentum with $k - \epsilon$ turbulence model to assess the marine turbine's performance under various operating conditions. Shives and Crawford (2014) attempted to predict the wake characteristics and power output more accurately in case of marine turbine farms by limiting the eddy-viscosity in close proximity to the turbine rotor to reduce the initial mixing rate. They also added a turbulence source terms while modeling the near-wake region. As compared with the experimental analysis, this additional modification caused an under-prediction of turbulence when the vortices break-down. Gant and Stallard (2008) studied the wake behaviour of marine turbines using URANS models and compared the device performance with the steady flow conditions.

4.3.2.1 Mathematical background

On a general note, the mathematical illustration of turbulence modeling commences with the notion of Reynolds decomposition, which defines any instantaneous flow variable ζ as

$$\zeta = \bar{\zeta} + \zeta' \tag{4.6}$$

where $\bar{\zeta}$ and ζ' are the mean and fluctuating components respectively. The mean component is obtained from

$$\bar{\zeta} = \frac{1}{\Delta t}\int_0^{\Delta t} \zeta(t)dt \tag{4.7}$$

The importance of choosing the right time interval Δt is worth noting. Theoretical idea of $\Delta t \to \infty$ is not possible in practice. For steady flows, accurate results can be obtained with Δt_{st} greater than the time scales of largest eddies. However, unsteady flows require Δt_{ust} smaller than the time scales associated with the transient behaviour of the mean flow. Sengupta (2012) and Wilcox (1998) noted the difference between the magnitudes of Δt_{st} and Δt_{ust} as of several orders.

When the Equations 4.6 and 4.7 are invoked in the time-averaged conservation equations, the Reynolds Averaged Navier-Stokes (RANS) equations are obtained which are defined as

$$\left.\begin{aligned} \nabla.U = 0 \\ \rho\frac{DU}{Dt} + \rho\frac{\partial}{\partial x_j}(\overline{u_i'u_j'}) = -\nabla P + \mu\nabla^2 U \end{aligned}\right\} \tag{4.8}$$

Compared to general conservation equations, Equation 4.8 introduces a new stress tensor $\overline{u_i'u_j'}$, called Reynolds stresses. This distinguishes the turbulence modeling from mean flow formulation. Rewriting the momentum equation as

$$\rho\frac{DU}{Dt} = -\nabla P + \nabla.\tau_{ij} \tag{4.9}$$

where

$$\tau_{ij} = \mu(\frac{\partial U_i}{\partial x_j} + \frac{\partial U_j}{\partial x_i}) - \rho\overline{u_i'u_j'} \tag{4.10}$$

This means that any real fluid flow experiences 6 additional stress components. Three of them are shear stresses, given by

$$\tau'_{xy} = \tau'_{yx} = -\rho\overline{u'v'} \qquad \tau'_{xz} = \tau'_{zx} = -\rho\overline{u'w'} \qquad \tau'_{yz} = \tau'_{zy} = -\rho\overline{v'w'} \tag{4.11}$$

and remaining are normal components, defined as

$$\tau'_{xx} = -\rho\overline{u'^2} \qquad \tau'_{yy} = -\rho\overline{v'^2} \qquad \tau'_{zz} = -\rho\overline{w'^2} \tag{4.12}$$

Since the shear stresses in Equation 4.11 depend on the correlation between two perpendicular components, they may be zero when the velocity fluctuations are independent. The normal components in Equation 4.12 have however non-zero values as they are the functions of squared velocity fluctuations. Turbulent flows typically have the turbulent shear stresses greater than viscous stresses due to coherent structure of turbulent eddies.

The RANS formulation used for modeling the turbulent flows complexifies the Navier-Stokes equations due to six additional unknown quantities, which exhibit

the concern about closure problem. New governing equations for the Reynolds stresses can be framed in order to close the problem. Another approach is to use eddy viscosity models, which is related to flow gradients. Based on these two methods, numerous turbulence models are available in CFD engineering. Although the fundamental governing equations are identical for all the models, additional variables appear due to the presence of turbulence that can be modeled with various models. Out of numerous turbulence models provided by Star CCM+, one-equation and two-equation models which are basically eddy viscosity models, are tried to choose the best suitable for low Reynolds number water turbine modeling. Following sections describe these turbulence models in detail.

4.3.2.2 Spalart-Allmaras model

This is a simple one equation model which solves the modeled transport equation for the turbulent viscosity μ_t. It does not require the calculation of length scale related to local shear layer thickness. The transport equation for the Spalart-Allmaras model for the transport variable ζ , is given by

$$\frac{\partial}{\partial t}(\rho\zeta) + \frac{\partial}{\partial x_i}(\rho\zeta u_i) = G_\zeta + \frac{1}{\sigma_\zeta}\left[\frac{\partial}{\partial x_j}\left\{(\mu+\rho\zeta)\frac{\partial\zeta}{\partial x_j}\right\} + C_{b2}\left(\frac{\partial\zeta}{\partial x_j}\right)^2\right] - Y_\zeta + S_\zeta \tag{4.13}$$

where G_ζ and Y_ζ are the generation and destruction terms of turbulent viscosity respectively due to wall blocking and viscous damping. S_ζ is the user-defined source term. The default model constants are given by

$$C_{b1} = 0.1355, C_{b2} = 0.622, \sigma_\zeta = 2/3, C_{v1} = 7.1$$
$$C_{w1} = \frac{C_{b1}}{\kappa^2} + \frac{1+C_{b2}}{\sigma_\zeta}, C_{w2} = 0.3, C_{w3} = 2.0$$

The turbulent viscosity μ_t is computed from the equation

$$\mu_t = \rho\zeta f_{v1} \tag{4.14}$$

where f_{v1} is the viscous damping function.

4.3.2.3 Standard $k-\epsilon$ model

This is a semi-empirical model and known for robustness, reasonable accuracy and economy. Standard $k-\epsilon$ model solves the following transport equations for the variables turbulent kinetic energy k and its dissipation rate ϵ.

$$\frac{\partial}{\partial t}(\rho k) + \frac{\partial}{\partial x_i}(\rho k u_i) = \frac{\partial}{\partial x_j}\left[\left(\mu + \frac{\mu_t}{\sigma_k}\right)\frac{\partial k}{\partial x_j}\right] + G_k + G_b - \rho\epsilon - Y_M + S_k \tag{4.15}$$

$$\frac{\partial}{\partial t}(\rho\epsilon) + \frac{\partial}{\partial x_i}(\rho\epsilon u_i) = \frac{\partial}{\partial x_j}\left[\left(\mu + \frac{\mu_t}{\sigma_\epsilon}\right)\frac{\partial \epsilon}{\partial x_j}\right] + C_{1\epsilon}\frac{\epsilon}{k}(G_k + C_{3\epsilon}G_b) - C_{2\epsilon\rho}\rho\frac{\epsilon^2}{k} + S_\epsilon \tag{4.16}$$

where G_k and G_b represent the generation of turbulent kinetic energy due to mean velocity gradients and buoyancy respectively. Y_M is the contribution of fluctuating dilatation in compressible turbulence to the overall dissipation rate. The eddy viscosity μ_t is computed from

$$\mu_t = \rho C_\mu \frac{k^2}{\epsilon} \tag{4.17}$$

Here, C_μ is a model constant whose value is 0.09 by default. Other model constants are

$$C_{1\epsilon} = 1.44, C_{2\epsilon} = 1.92, \sigma_k = 1.0, \sigma_\epsilon = 1.3$$

S_k and S_ϵ are the user defined source terms.

4.3.2.4 Wilcox $k-\omega$ model

While using the two-equation turbulence models, first equation uses the turbulent kinetic energy k as a variable, but there is a huge variety in selecting a variable for the second equation (Kolmogorov, 1942; Prandtl, 1945). After the use of dissipation rate of turbulent kinetic energy ϵ, the next widely-used variable is the specific dissipation rate of k, denoted by ω. This model introduced by Wilcox (1988, 1993) incorporates the modifications for low Reynolds number effects and shear flow spreading. This feature makes the $k-\omega$ model suitable for wall-bounded flows and free-shear flows.

4.3.2.5 BSL $k-\omega$ model

After the evaluation of complementary strengths and weaknesses of different two-equation models, Menter (1993, 1994) came up with a practical hybrid model. This uses Wilcox's $k-\omega$ model within the boundary layer and a transformation of the $k-\epsilon$ model into a $k-\omega$ model, characterized by $\epsilon = \beta x k\omega$ outside of the boundary layer. Apart from the dissimilar model constants, the major difference between the conventional Wilcox and hybrid models is the inclusion of additional cross-diffusion term in the later for ω formulation. The new model equations for k and ω are derived by adding the Wilcox $k-\omega$ equations times a function F_1 and the transformed $k-\epsilon$ times $1-F_1$. The function F_1 is one in the viscous sub-layer and zero outside of the boundary layer. The blending takes place in the wake region of the boundary layer.

4.3.2.6 Shear Stress Transport (SST) $k-\omega$ model

The shear stress transport (SST) model incorporates the BSL turbulence model with the addition of a function to limit the turbulent shear stress (Menter, 1994).

The transport equations for SST $k-\omega$ model are

$$\frac{\partial}{\partial t}(\rho k)+\frac{\partial}{\partial x_i}(\rho k u_i)=\frac{\partial}{\partial x_j}\left(\Gamma_k\frac{\partial k}{\partial x_j}\right)+G_k-Y_k+S_k \tag{4.18}$$

$$\frac{\partial}{\partial t}(\rho \omega)+\frac{\partial}{\partial x_i}(\rho \omega u_i)=\frac{\partial}{\partial x_j}\left(\Gamma_\omega\frac{\partial \omega}{\partial x_j}\right)+G_\omega-Y_\omega+D_\omega+S_\omega \tag{4.19}$$

where G_k and G_ω are the generation terms of turbulent kinetic energy and its specific dissipation rate respectively. Γ_k and Γ_ω are the effective diffusivity of k and ω, and Y_k and Y_ω are the respective dissipation terms of k and ω due to turbulence. D_ω is the cross-diffusive term, and the user-defined sources are denoted by S_k and S_ω.

The origins of this model lie in the observation that when applied to boundary layer problems, one of the major differences between eddy-viscosity and full Reynolds stress models is that the latter account for the effect of the transport of the principal turbulent shear stress $\tau'_{xy}=-\rho\bar{u'v'}$. The importance of modelling such an effect has been demonstrated by the success of the Johnson-King (JK) model. The JK model is a transport equation for the turbulent shear stress that is based on Bradshaw's assumption that the shear stress in a boundary layer is proportional to the turbulent kinetic energy

$$\tau'_{x_i x_j}=\rho a_1 k \tag{4.20}$$

where a_1 is a constant. By comparison, in two-equation models, the shear stress is calculated from the Boussinesq assumption

$$\tau'_{x_i x_j}=\mu_t\frac{\partial u_i}{\partial x_j} \tag{4.21}$$

As described by Menter (1992), this can be written as

$$\tau'_{x_i x_j}=\rho\sqrt{\frac{production_k}{dissipation_k}}a_1 k \tag{4.22}$$

where

$$production_k=2\mu_t S_{ij}.S_{ij}=\mu_t\left(\frac{\partial u_i}{\partial x_j}\right)^2 \tag{4.23}$$

As noted by Driver (cited by Menter, 1994), the production term is much greater than the dissipation term in the boundary layer flows with adverse pressure gradients. Therefore, Equation 4.21 overpredicts τ compared to Equation 4.20. When the production is equal to dissipation, these two equation become similar if $a_1=\sqrt{C_\mu}=0.3$.

4.3.3 Solution methods

Throughout the project, 2nd order upwind scheme was used to calculate fluid flow properties. Moreover the 2nd order upwind scheme is also used to evaluate the turbulent values of kinetic energy and dissipation rate. In the first order upwind technique, scalar properties at current cell faces are derived from the upstream cell values from the previous iteration.

Upwind Scheme is a technique which uses upstream values to calculate the current cell values. Similarly second order upwinding method uses the cell values of two adjacent cells to compute the face value of current cell.

4.3.4 Solution controls

Numerical methods used to solve the governing equations for the fluid flow most often employ one or more iteration procedures. By their nature, iterative solution methods require a convergence criterion that is used to decide when the iterations can be terminated. In many cases, iteration methods are supplemented with relaxation techniques. The criteria depend on specifications of the problem being solved and may change during the evolution of problem.

The selected criteria also depend on the numerical formulation. Star CCM+ solver has the under relaxation factors to control the effect of previous iteration on current iteration. The relationship between the under-relaxation factor χ, the scalar value ζ and resulting change in the scalar value $\Delta\zeta$ is given by

$$\zeta = \zeta_{old} + \chi\Delta\zeta \tag{4.24}$$

Table 4.3 shows the list of under-relaxation factors by default. Since no divergence issues arose, these default values were left unchanged throughout the computational work.

Parameter	Under-relaxation factor
Velocity	0.8
Pressure	0.2
Turbulence intensity	0.8
Turbulence viscosity	1

Table 4.3: Under-relaxation factors used in the computations

4.3.5 Temporal disretization

Any flow problem can be solved in steady or unsteady formulations. A steady condition can be applied when the flow structures remain constant in time. In unsteady conditions, flow variables change temporally which requires a special treatment while solving the problem computationally. Due to the unsteady nature

of the flow patterns around the Darrieus hydroturbine, only transient simulations are performed throughout the project.

In transient computations, the conservation equations are discretized in both space and time. The temporal discretization involves the integration of each term in the differential equations over a given time-step Δt.

The time evolution of a variable ζ is given by

$$\frac{\partial \zeta}{\partial t} = F(\zeta) \tag{4.25}$$

where the function F incorporates any spatial discretization. Using forward differences, the first and second-order accurate temporal discretization are given as

$$\frac{\zeta^{n+1} - \zeta^{n}}{\Delta t} = F(\zeta^{n+1}) \tag{4.26}$$

and

$$\frac{3\zeta^{n+1} - 4\zeta^{n} + \zeta^{n-1}}{2\Delta t} = F(\zeta^{n+1}) \tag{4.27}$$

where n is the value at the current time level (t), $n+1$ the value at the next time level $(t + \Delta t)$, and $n-1$ the value at the previous time level $(t - \Delta t)$. Depending on which level of accuracy is chosen, the Equation 4.26 or 4.27 is solved iteratively at each time level for ζ^{n+1} which is called implicit time integration.

The time-step, Δt, applied for the time-marching is the determining parameter of stability and convergence of the solution. The Courant-Friedrichs-Levy CFL criterion states the following stability condition

$$CFL = \Delta t \sum_{i=i}^{n} \frac{u_{x_i}}{\Delta x_i} \leq 1 \tag{4.28}$$

where CFL is the Courant number, Δx_i the length interval (eg. of the cell), and u_{x_i} the velocity in x_i-direction. While the CFL condition is a requirement for explicit schemes, this is not the case for implicit schemes. However, it provides a suitable first estimate for the time-step. Equation 4.28 states that $\Delta t \leq \Delta x_i / u_{x_i}$. As the local flow velocities in flowfield are not known a priori, a range of time-steps need to be employed in order to find the appropriate value in terms of convergence and computational efficiency.

In implicit formulation, there is no criterion for the solution stability for determining the time-step size Δt. In order to predict the time-dependent flow processes accurately, it is however important to set a suitable value for Δt. In the present computations, Δt is chosen such that the number of inner iterations per time step would ensure solution convergence as the flow time proceeds. A typical transient flow problem has a quicker start-up which rapidly decays further. A smaller Δt is therefore chosen initially which can gradually be increased for further flow time steps. Convective cell Courant number within the solution domain is a measure

to check if the time-step size is appropriate or not. Figure 4.6 shows that the cell Courant number is less than 1 for major portion of the domain while it is less than 10 in more sensitive regions around the blades which is acceptable (Vahdati et al., 1992).

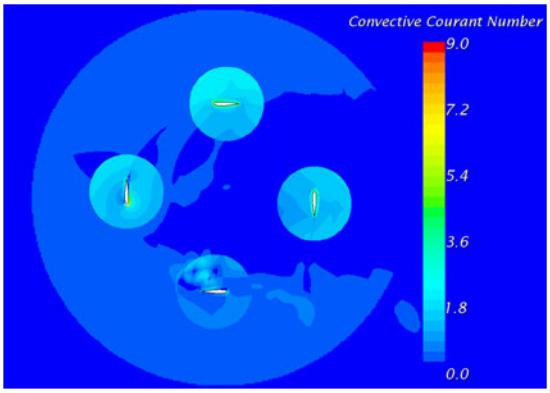

Figure 4.6: Cell convective Courant number

4.3.6 Computational considerations

The complexity of the physics involved in the simulation and size of the computational domain invoked the use of the Windows based 5 eight-core cluster located at Institut PPRIME in ENSMA. This cluster was operated from a local system which has an 8GB system memory and 3GHz processing speed. Each computation was performed on a specific server. Due to the expected transient behaviour of the CFD solution within the first half of the turbine's rotation, the solution for the first rotation cycle was not taken into consideration. Following the significant differences in the flow fields, transition to the complete flow development was identified after the first rotation cycle is completed. Although these differences in the flow field development were found negligible during the second rotation of the turbine, only the flow solution corresponding to the third rotation cycle is considered for all of the cases to ensure sufficient development of the wake zone downstream of the turbine.

4.4 Post-processing

During the solution process, the residuals of computation and the evolution of the flow parameters such as blade loading with respect to iteration / flow time are plotted to assess the convergence behaviour. Once the solution is converged, the last data set consisting of the information about the velocity and pressure at each mesh node is stored as the final solution. In order to interpret the computational findings, the entire data must be reduced to an intelligible size, which enables critical analyzes of different simulations and comparison with external data. Following

types of post-processing are used along the turbine's cycle during the computational studies.

- Solution file of last computation to resume the process if necessary
- Hydrodynamic loading on the blades
- Pressure distribution on the blades
- Contour plots (pressure, velocity, vorticity etc ...)
- Vector plots
- Streamline plots
- Composed scenes that show more than one of the above in a single figure

In addition to direct retrieval of various vector and contour plots, and force data from the solver output for standard visualization, additional post-processing techniques are required to present the performance data and visualization of advanced flow parameters. The calculation of turbine's performance parameters such as torque and coefficient of power (COP) are calculated from the hydrodynamic load distribution over the blades for one complete cycle. The calculated COP values, as key indicator of performance and design improvement, are further used to develop response surfaces for different models and operating conditions.

In spite of strong capabilities of any commercial CFD package in processing and presenting the output data in a customized manner, it is generally necessary to extract the field data of different flow variables from the solution domain using an external post-processing tool. This is particularly important in calculating advanced parameters to have an enhanced physical understanding. One such parameter is Q-criterion which identifies coherent vortical structures within the flow field. Tecplot is used as a common visualization platform for both computational and experimental results. Also, additional images and plots were obtained using Matlab for comparing the results of theoretical, numerical and experimental data.

4.5 Fidelity and adequacy of numerical models

Existence of several numerical models and their adaptable suitability to a specific flow problem opens the doors for uncertain or sometimes wrong results. It is therefore necessary to examine the selected models, particularly mesh type and turbulence model, based on their fidelity and adequacy. As discussed in section 4.2, Chimera technique is a realistic option for spatial discretization in order to incorporate multiple motions in the domain. While alleviating the drawbacks of sliding interface for simulating the relative motion between different regions, Chimera grids offer its suitability for high fidelity moving mesh computations (Zagaris et

al., 2010; Gerolymo et al., 2002). However there is a functional requirement for efficient inter-grid connectivity between the moving and non-moving regions, which considerably increases the simulation memory as well as computational cost. Also, weak interface causes solution instabilities.

While the availability of numerous grid schemes to discretize the flow domain create a wider scope for meshing possibilities, this also leads to a little confusion in choosing the right mesh topology. A critical evaluation of solver's capabilities and sensitivities is therefore necessary for selecting the best suitable mesh type. Baker (2005) provided a basic understanding of different mesh types for their ease of use and viscous accuracy. From Figure 4.7, it is clear that better accuracy in viscous flow modeling demands increasing efforts in handling the mesh. The structured multiblock grids are known to produce the most accurate results at higher difficulty while the case is reverse with simple Cartesian grids. On a compromise, the structured overset meshes bring a acceptable accuracy at manageable grid complexity which is a key trait in simulating the large flow domains.

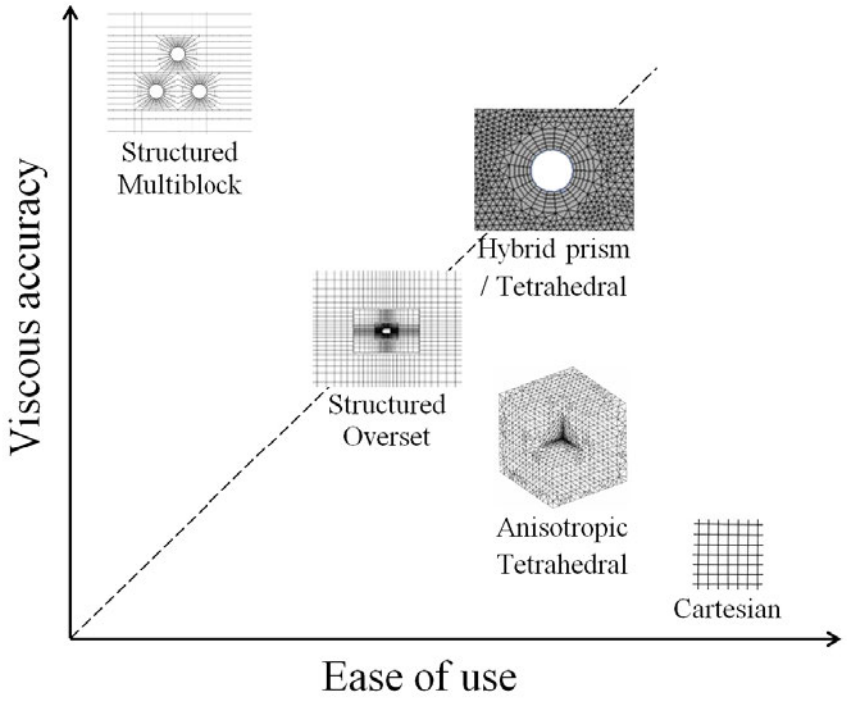

Figure 4.7: Dependence of computational effort on the mesh type (Baker, 2005)

Misconceptions about discretization such as fine meshes with coarse time steps or coarse meshes with fine time steps, were avoided to prevent poor quality results. Numerical errors due to iterative procedures, spatial and temporal discretization etc ... were properly handled and uncertainty analysis was taken into consideration.

Complexity in the physics of achieving specific objectives such as vortex shedding from the blades raises more concern about the definition of boundary condi-

tions and the selection of right solver. This is evident from the work of Schmidt and Thiele (2002) in which the performance of various turbulence models were assessed to simulate the flow over wall-mounted cubes. Several scholars described the unsatisfactory performance of RANS modeling due to number of options available that would go wrong unless they are properly managed. The capabilities of SST $k-\omega$ were deeply understood by the author in efficiently analysing partially separated flows. To my experience, there is a dramatic difference between $k-\epsilon$ and $k-\omega$ models in predicting the effective viscosity distributions, which is one of the key parameters in this project. Although this might not influence the overall analysis to a larger extent, one may lose the confidence in the adapted methodology.

The reason why $k-\omega$ model is considered superior to $k-\epsilon$ model is that the former doesn't need wall damping functions when it is applied throughout the boundary layer. Wilcox (1998) noted the advantage of implementing $k-\omega$ model over $k-\epsilon$ in case of wall bounded flows where adverse pressure gradients prevail. However, a precise specification of the specific dissipation rate of turbulent kinetic energy for the free-stream flow is necessary for $k-\omega$ model. Although an arbitrary value can be assumed for ω, there is a serious dependency of solution accuracy on the input value of ω (Menter, 1992).

One of the major contributions of SST $k-\omega$ model to increase the trust on the computational results, particularly for low Reynolds number flows, is that the model with the best near wall treatment can reflexively switch from wall function approach to low-Reynolds number scheme depending on the grid spacing which usually provides improved performance compared to other RANS models. Although some scholars (Lutum and Cottier, 2011; Ravi et al., 2013) argued that SST $k-\omega$ tends to predict excessive and early transition, the model is more suitable for complex boundary layer flows with flow separation under adverse pressure gradient. To the end of numerical stability, shear stress transport model is better than others as it does employ viscous damping functions but straightforward Dirichlet boundary conditions. All these considerations made SST $k-\omega$ model a workhorse for the present project. In Chapter 5, the strengths and drawbacks of these numerical models will be visually described through the validation, which will make firm comments on their applicability and limitations in real problems.

4.6 Mesh independence study

In order to establish better accuracy in computations, mesh dependency is investigated for specifics of solution domain such as instantaneous torque value and the number of cells in each flow region. As the size of computational domain is concerned, the focus is primarily directed to the number of cells and nodes. To examine the mesh independence issues, the simulation results of torque evolution

for one blade for one complete cycle are considered. Figure 4.8 compares the performance of three different meshes, whose statistics are furnished in Table 4.4. The results obtained from all of the three meshes are similar for azimuth position $\alpha \in [0^o, 110^o]$. There is a vortex shedding from the blade as the blade is about to commence its second quadrant of rotation and blade-vortex interaction during its travel in the third quadrant. These physical phenomena are reflected in the mesh independence study for $\alpha \in [110^o, 300^o]$. The coarser resolution (Mesh 1) has failed in capturing the vortex shedding while Mesh 2 and 3 have successfully resolved this. With due consideration of CPU effort needed for highly refined meshes, this study continued with the 'fine' mesh (Mesh 2).

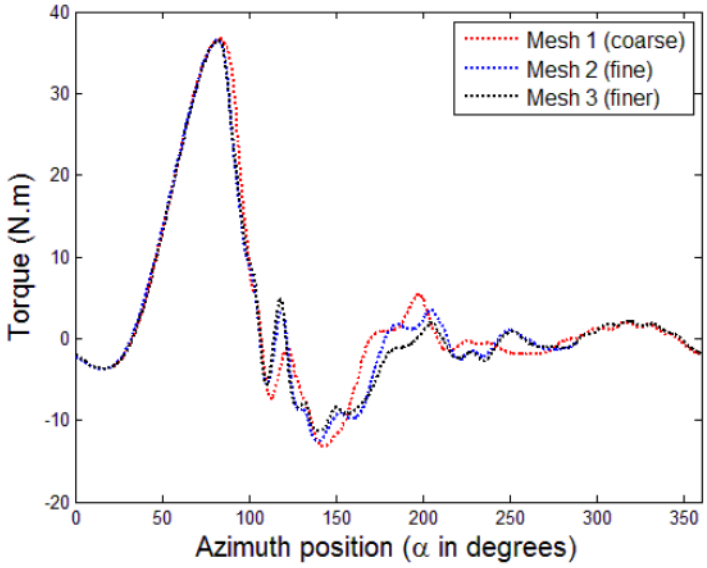

Figure 4.8: Mesh independence study for a velocity $V_0 = 1$ m/s and tip-speed ratio $\lambda = 2$

	Cells in each overset region	Cells in background region
Mesh 1	26902	284046
Mesh 2	29657	320985
Mesh 3	33235	361083

Table 4.4: Statistics of different meshes

4.7 Benchmarking

The importance of benchmarking studies in CFD analysis and validation was identified by Iaccarino (2001). In the present study, a classical Darrieus turbine with fixed blades is examined using moving meshes. These results are later compared

Tip-speed ratio (λ)	Free-stream velocity (V_0)
1.5	1.0, 1.5, 2.0, 2.5, 3.0
2.0	1.0, 1.5, 2.0, 2.5, 3.0
2.5	1.0, 1.5, 2.0, 2.5, 3.0
3.0	1.0, 1.5, 2.0, 2.5, 3.0
3.5	1.0, 1.5, 2.0, 2.5, 3.0

Table 4.5: CFD test matrix for benchmarking studies

with pitching blades for global quantitative results as well as flow fields across the turbine for different azimuth positions. Table 4.5 provides the analysis matrix of operating conditions for which the benchmarking studies were performed. The baseline case consists of tip-speed ratio λ=2 and free-stream velocity $V_0 = 1$ m/s.

CFD predictions of the torque evolution of a single blade as it travels around the azimuth for a free stream velocity of 1 m/s over a range of tip-speed ratios are shown in Figure 4.9(a). The blade kinematics provides the information about the blade's local incidence with respect to the incident velocity which is the key in calculating the torque. Positive torque represents the power extraction resulting in propulsion from the flow and negative results in power loss. If the blade's motion and the tangential hydrodynamic force experienced by the blade are in the same direction, then the torque will be positive, otherwise torque will be negative which will lead to power lost to the flow. It is interesting to notice that most propulsive and power loss features are attributed to the front half of the blade's rotation ($0^o < \alpha < 180^o$) while the rear half is comparatively silent in torque fluctuations. One can see the decreasing trend in torque evolution in the rear half of the cycle as the tip-speed ratio λ increases. The product of instantaneous torque T acting on the blade and rotational velocity of the device ω gives the power P produced by the blade at a given instant. With swept area A of the device and fluid density ρ being known, the Coefficient of Power COP is then calculated using the Equation 2.11.

4.7.1 Effect of tip-speed ratio λ

One of the most influential parameters in designing any rotating machine is the tip-speed ratio λ whose effect is critical in identifying the optimal operating conditions to obtain the maximum performance. Recalling the illustration of power output of the turbine in a confined flow as presented in section 2.5, the corrected COPs here are calculated from

$$COP_{corrected} = (1 - b)^2.COP_{calculated} \tag{4.29}$$

where b is the blockage ratio. Since all of the CFD studies are performed in a 2D domain with a width of 1.6m, the corresponding blockage ratio b is equal to

0.375. Figure 4.9(b) shows the corrected COP plots of the device for different velocities. The optimal value for tip-speed ratio λ_{opt} was found to be 2.5 beyond which the performance characteristics deteriorate. The mean torque proportionally increases with tip-speed ratio λ and reaches the maximum at $\lambda = 2.5$ and then falls down. In the limiting cases (vanishing or infinite λ), the turbine will rotate just neutrally without producing energy. The COP curve on the left side of the peak is controlled by the blade stall, which is associated with low values of λ and high values of relative incidence. These results are consistent with the studies of Ionescu (2014), Malaul and Dumitrescu (2014), Gosselin et al. (2013) and Samaraweera (2010). On the other hand, relative incidence decreases on the right side of the peak which leads to lower power output. Reynolds effect is not very significant for the classical Darrieus case. The shape of the COP-λ curve is mainly dependent on the hydrofoil's design and solidity σ of the turbine (Bryden et al., 1998). These results are consistent with the turbines of similar σ studied by Ionescu et al. (2014).

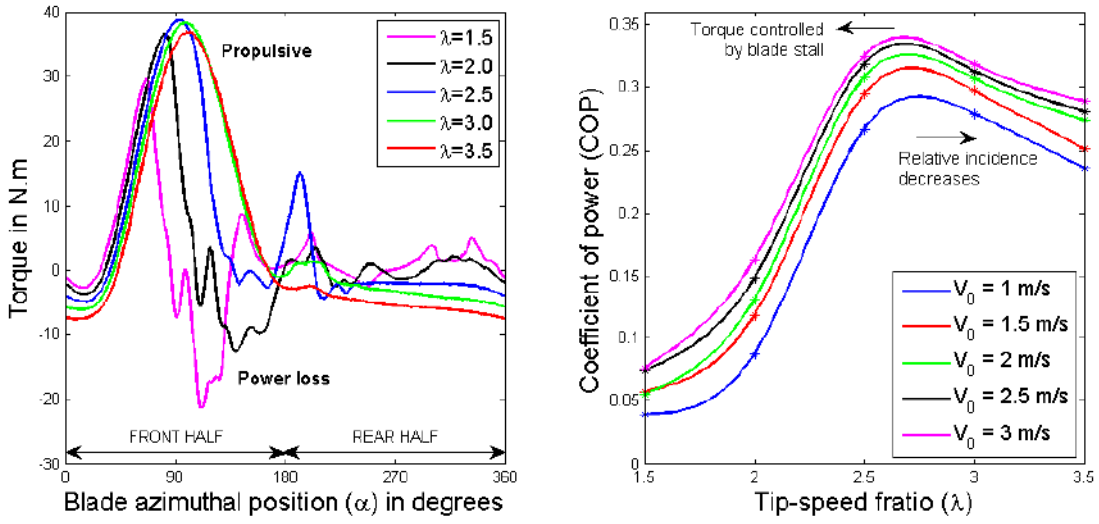

(a) (b)

Figure 4.9: CFD analysis of classical Darrieus turbine with fixed blades. Instantaneous torque plot for a single blade for a complete cycle (left), and Corrected COP vs tip speed ratio λ (right)

4.7.2 Flow field visualization

Before understanding the complete picture of the hydrodynamic forces experienced by the blades at different azimuth position, it is necessary to observe the velocity fields around the blades. This is conveniently obtained from CFD computations. For the sake of understanding, the blade azimuth position α is discriminated from the global azimuth position of the turbine Ψ. Figure 4.10 shows the difference

between these two variables. α is related to the location of an individual blade with respect to the reference axes while Ψ describes the angular positioning of the turbine as a whole relative to the reference axes.

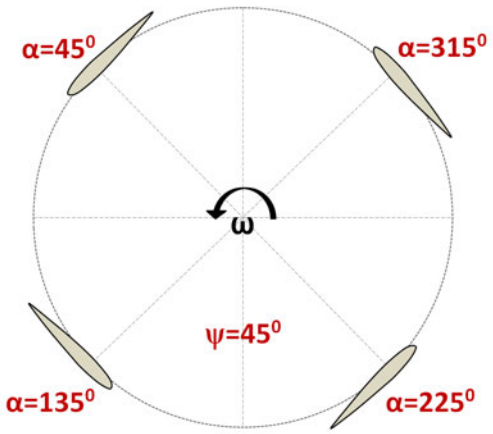

Figure 4.10: Illustration of blade azimuth position α and global azimuth position of turbine Ψ

Figure 4.11 portrays the computationally predicted instantaneous velocity vectors across the turbine when the global azimuth position Ψ corresponds to 0^o. Momentum loss due to power extraction downstream of the turbine is evident. Figure 4.12 shows the instantaneous normalized velocity components plotted at different horizontal distances, both upstream and downstream, from the turbine's centre. While the velocity profile is flat at 2R (=0.6 m) ahead of the turbine, considerable fluctuations are observed within the rotor and downstream. Variation in the velocity components is not observed at a distance 2R ahead of the turbine, while the Y-range of [-2R, 2R] is critical with considerable fluctuations. It means that a large portion of velocity variations is concentrated within 1 m diameter around the turbine's centre, for a given diameter of 0.6 m and a tip-speed ratio $\lambda = 2$ and free-stream velocity $V_0 = 1$ m/s. There is a serious drop in X-velocity as the flow enters and progresses the turbine's region. This results in a very low impact velocity in X-direction of the flow onto the blade at $\alpha = 270^o$ for $X = R$. From Figures 4.11 and 4.12, it is concluded that the X-velocity almost remains unchanged as the flow passes from the centre to the rear half of the turbine, which is consistent with the torque extraction depicted in Figure 4.9(a). On the other hand, the turbine's angular motion in counter-clockwise rotation attempts to deviate the flow upwards which contributes to a more pulsating Y-velocity component.

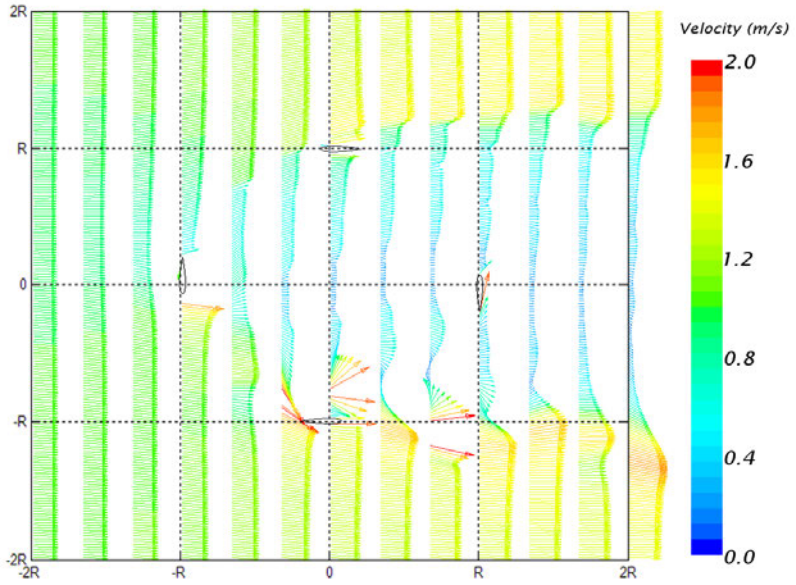

Figure 4.11: Instantaneous velocity vectors around a 2D Darrieus turbine with fixed blades for a tip-speed ratio λ=2 and free-stream velocity V_0=1 m/s

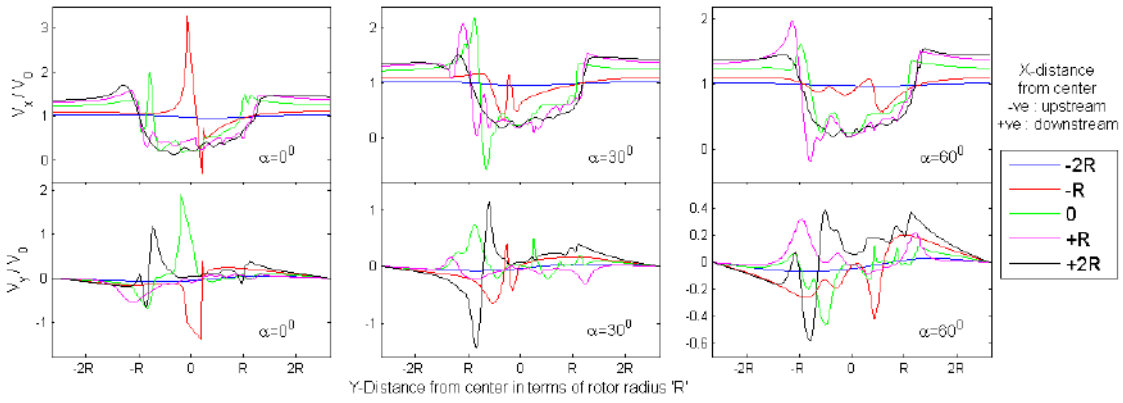

Figure 4.12: Normalized velocity components in X (top) and Y (bottom) directions across the turbine at various azimuth positions of the blade

4.7.3 Torque extraction

With the information available from the velocity fields, the forces experienced by the blade can be scrutinized as the blade positioning during the turbine rotation is associated with varying angles of attack. Figure 4.13 assists with pressure coefficient contour plot, superimposed by streamlines at a global azimuth position Ψ of 0^o. For $\lambda = 2$ and $V_0 = 1$ m/s, the actual apparent velocity deviates from the theoretical kinematics, resulting in low values of both lift and drag, and slightly negative torque. Power output increases as the blade passes through the frontal half of turbine's cycle. Most interestingly, 90^o azimuth location of the blade corresponding to half way down the frontal half is associated with the maximum power

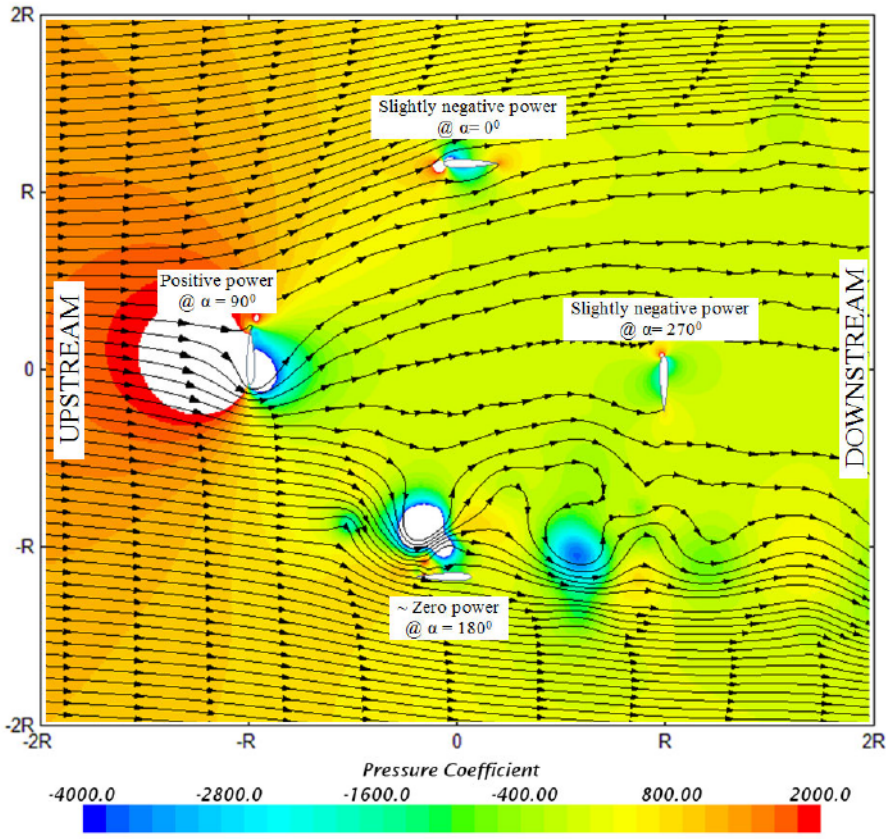

Figure 4.13: Hydrodynamic analysis of torque extraction from the turbine using the computational pressure field with streamlines superimposed when the turbine is at an azimuth position Ψ equal to 0^o

output due to its large apparent incidence. The blade profile at quarter cycle location experiences a huge pressure differential between both of its sides; high pressure region on left and low pressure zone on right side. Further moving down, the blade at $\alpha = 180^o$ provides almost no power and this trend continues through the rear half of the cycle with negligible jumps. The flow fields across the turbine when Ψ is equal to 30^o and 60^o is presented in Figure 4.14 allowing to complete the observations made at $\Psi = 0^o$. The consistent increase in the streamtube expansion over this area is materialized by a distributed pattern of streamlines, associated with inherent power loss.

4.7.4 Vorticity field around the blade

One of the objectives of this study is to understand the vorticity distribution and reduce the vortex shedding from the blade. A careful examination is carried out to characterize the vorticity fields around the blade and possible blade-vortex interaction (BVI). Since the vorticity field around the blade is insignificant for $\alpha \in$

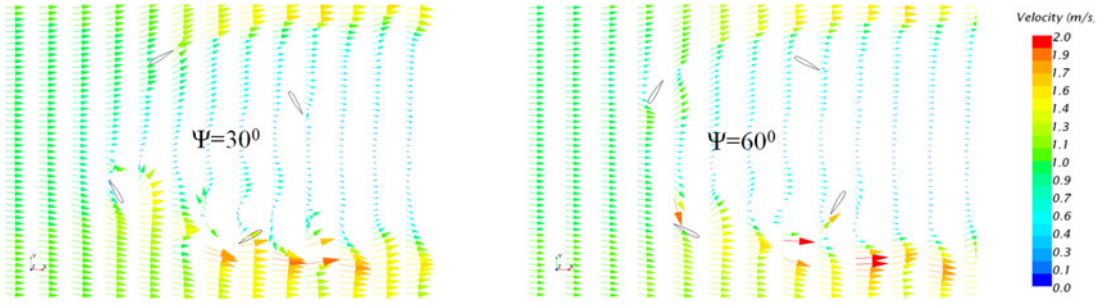

a b

Instantaneous velocity vectors across the turbine

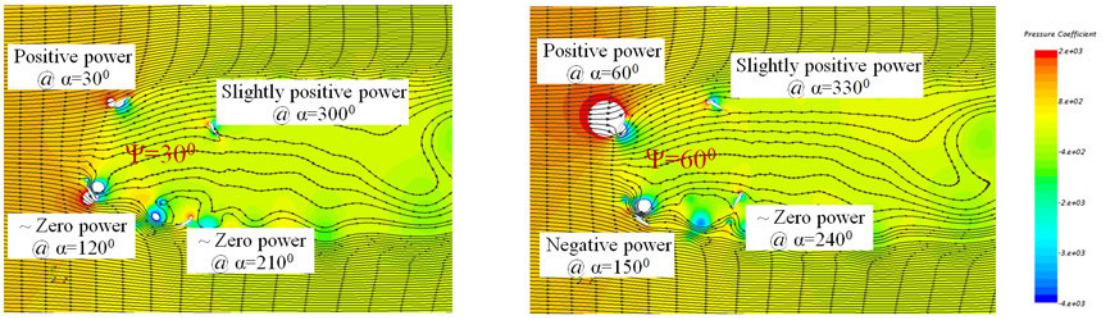

a b

Instantaneous velocity vectors across the turbine

Figure 4.14: CFD predictions of flow patterns during the turbine's operation with a tip-speed ratio $\lambda = 2$ and free-stream velocity $V_0 = 1$ m/s at different global azimuthal positions Ψ

[270, 90], the present discussion is confined to $\alpha = 90^o - 270^o$. The complete vortex shedding process and interaction between the blade and vortex are manifested in Figure 4.15 for a tip-speed ratio λ of 2 and free-stream velocity V_0 =1.5 m/s. The BVI is not necessarily to be with either leading edge vortex or trailing edge vortex. For instance, in the present case, the leading edge vortex is released at about $\alpha = 154^o$ and is later interacted by the same blade in the following rotation whereas the trailing edge vortex released half a cycle earlier is interacted by the following blade. When the turbine rotates at higher speeds, corresponding to larger values of tip-speed ratio λ, the wake developed by the blade convects downstream relatively slowly while the following blade can quickly catch-up these flow structures and therefore strong blade-vortex interaction will be more likely to generate unsteady vortices. There is a possible impact of blade-vortex interaction on the strength of the vortex developed in the next portion of cycle and on the global fluid dynamic loading on the blade. The fluid interaction with the vortex shedding from the blade can lead to localized flow perturbations in the blade incidence due to influenced hydrodynamic loading on it.

Azimuth position	Vorticity contour	Comments
$\alpha = 93.4^o$		Flow is attached to the profile, although a small vortex is started on the low-pressure side. No vortex is shed from the blade.
$\alpha = 123.5^o$		Vortex grows bigger and is about to detach from the profile.
$\alpha = 153.5^o$	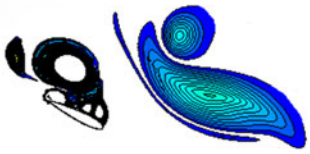	Vortex expansion on the low pressure zone takes place as the blade heads to hit the vortex released by the preceding blade.
$\alpha = 183.6^o$	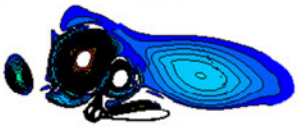	Complexity in the flow characteristics due to large turbulence scales increases as there is a vortex-vortex interaction. At higher tip-speed ratios, these strong unsteady vortex structures diffuse slowly compared to the turbine's rotation and catch up the following blade.
$\alpha = 213.7^o$		Blade penetrates into the vortex which results in an impulsive change in the hydrodynamic loading of the blade.
$\alpha = 243.8^o$		Blade-vortex interaction is ending, resulting vortex is left behind the blade. Progressive reattachment of the flow over the blade is evident. Another weak vortex detaches from leading edge, which does not survive for a long time.
$\alpha = 273.9^o$		Flow is completely reattached with negligible perturbations.
		

Figure 4.15: Vortex shedding and blade-vortex interaction in case of Darrieus turbine with fixed blades at λ=2 and V_0=1.5 m/s

4.8 Parametric analysis

4.8.1 Effect of free-stream velocity V_0

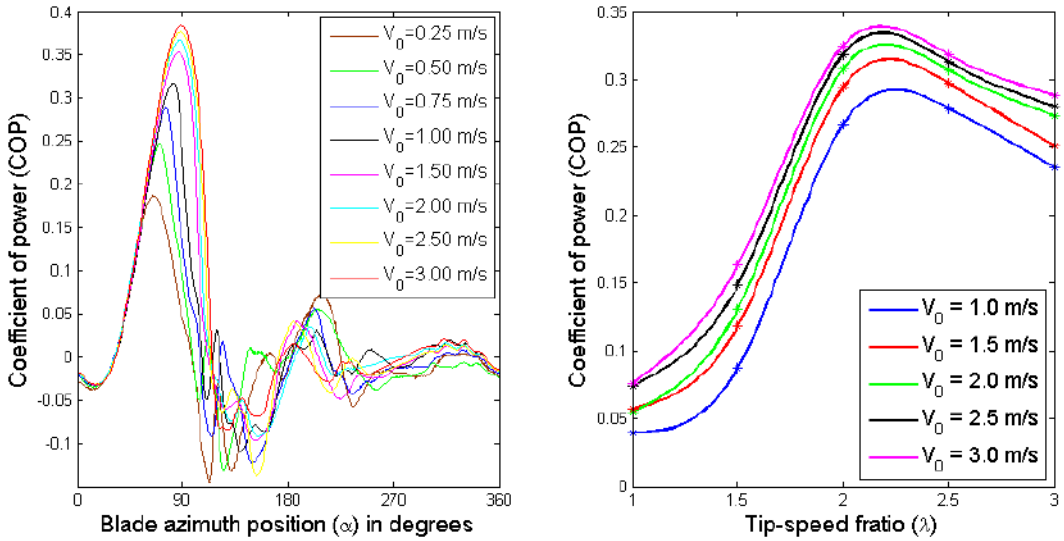

(a) Azimuthal variation of COP with V_0 for a single blade

(b) COP as a function of λ and V_0

Figure 4.16: Effect of free-stream velocity V_0 on the turbine's coefficient of power COP

Figure 4.16 (a) shows the azimuthal variation of power coefficient COP with the free-stream velocity V_0 for a single blade for one complete cycle. Although the global trend of torque throughout the azimuth seems invariable, the peaks of the COP curve explicitly change with respect to V_0. It is obvious that the power extraction capacity during the front half of the cycle proportionally increases with V_0 due to higher relative incidence of the blade while no significant effect on the rear half of cycle is evident because low relative incidence of the blade. It is observed from Figure 4.16 (b) that the maximum achievable coefficient of power increases with increasing V_0. It is interesting to notice that the rate of increase in coefficient of power decreases with the increase in V_0.

Effect of free-stream velocity V_0 on the flow pattern around the turbine rotor is presented in Figure 4.17 through the CFD predicted pressure contours with streamlines. All of the images correspond to the rotor's position at a global azimuth position $\Psi = 0^o$. Three major observations are made. The first observation is concerned about the local flow field around the blade. Although the rotational motion of the turbine is reflected in the flow field through the slight deviation of streamlines, the blade at the azimuth position $\alpha = 0^o$ seems well-aligned with the incoming flow. Dissimilarity in the pressure contours are highlighted at $\alpha = 90^o$ where the pressure on the upper surface of the blade boosts-up as V_0 increases.

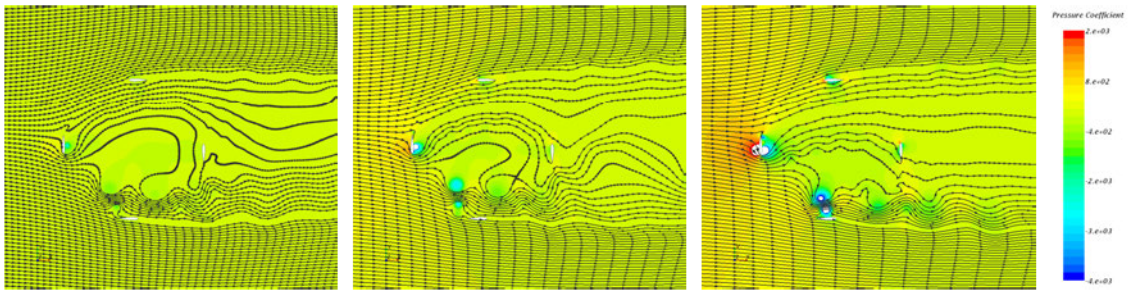

(a) $\lambda = 2, V_0 = 0.25m/s$ (b) $\lambda = 2, V_0 = 0.50m/s$ (c) $\lambda = 2, V_0 = 0.75m/s$

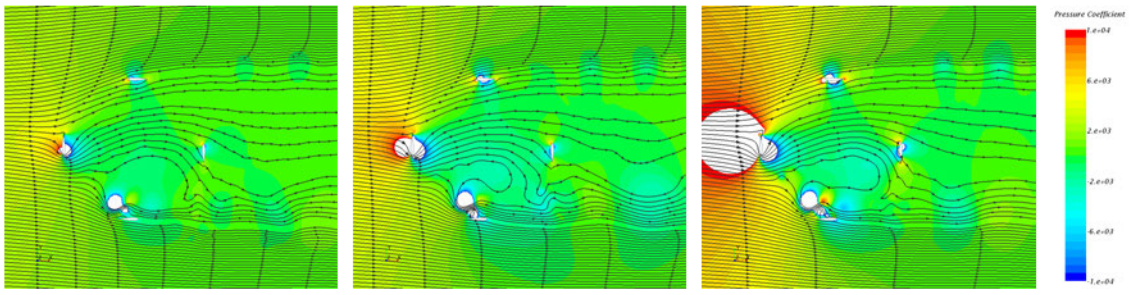

(d) $\lambda = 2, V_0 = 1.5m/s$ (e) $\lambda = 2, V_0 = 2.0m/s$ (f) $\lambda = 2, V_0 = 2.5m/s$

Figure 4.17: Effect of Reynolds number on the flow across the turbine

This means that the blade at this location is capable of producing higher lift force. This is also the reason for extracting the largest amount of power during the front-half of the cycle. At $\alpha = 180^o$, the pressure variations on the blade's upper surface keep increasing with local Reynolds number while no significant effects are observed at $\alpha = 270^o$.

Looking at the streamline orientation within the rotor, it is clearly affected by the changes in V_0. The streamlines downstream of the rotor are largely influenced for V_0 less than 1 m/s (i.e. for the first three cases), while little impact is seen for V_0 greater than 1 m/s. Finally, as expected, there is a clear magnification of scalar contours. Also, the marker distance on the streamlines is proportionally increased with V_0. Apart from these expected and consistent changes in the flow field across the rotor with free-stream velocity, there is no fundamental disparity in the flow physics which concludes that it is possible to scale the experimental results of low Reynolds number flows around the turbine to full-scale analysis.

4.8.2 Effect of solidity σ

One of the major operational problems with the Darrieus turbines, weather it is in wind or tidal applications, is the vibration of the device due to cyclic loading on the blades exerted by the fluid flow. Although the vibrations due to imbalanced designing can be fixed during the manufacturing process, the loading behaviour of tangential and radial forces on the blades is difficult to control. When the

rotational speed of the turbine is controlled to exploit the maximum power, the device gets excited. Generally, the normal force component plays the major role in this phenomenon. As shown in Figure 4.18, helical blades can distribute the cyclic loading to some extent. But the penalty is higher manufacturing costs.

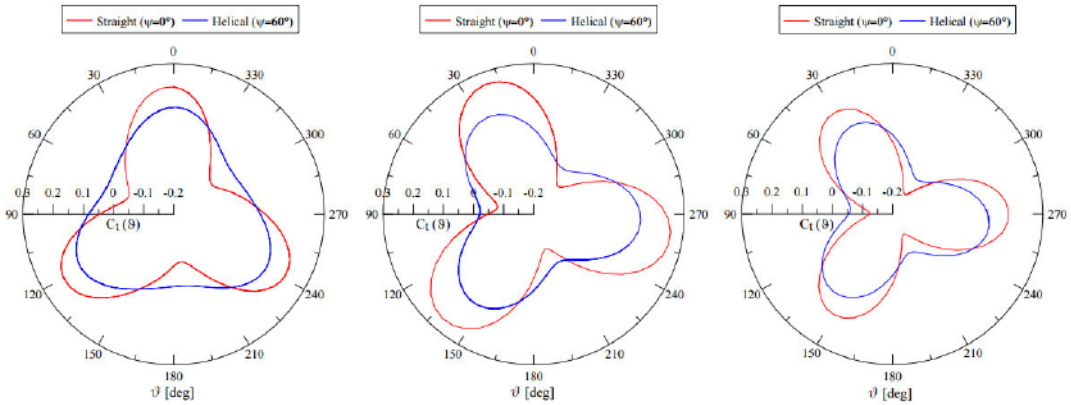

(a) @60RPM (b) @90RPM (b) @120RPM

Figure 4.18: Instantaneous torque coefficient with straight and helical blades (Alaimo et al., 2015)

The role of solidity σ of the turbine is noteworthy regarding the vibrations as well as the overall performance. High solidities would result in relatively lower rotational speeds, hence there would a chuck on the device excitation. However, there is a penalty in the power characteristics of the turbine with higher solidities because of decreased hydrodynamic efficiency of the blade. High solidity designs are known for larger chord-to-radius ratio L/R, higher rate of pitching motions and possible blade-vortex interactions, which make the flow physics different and more complex than the low solidity models (Sheldahl et al., 1980; McLaren et al., 2012a, 2012b). This made the motivation to study the effect of solidity on the flow field development across the turbine, although the improvement of device efficiency is out of the scope of present research. The studies about the solidity effects using streamtube models by Paraschivoiu (1988), Sheldahl et al. (1980) and South and Rangi (1975) lack the detailed information about the vorticity distributions. To this end, URANS modeling has become captious for field analysis as well as performance evaluation.

Model no.	Chord (L)	Radius (R)	Solidity (σ)	L/R	Rotational velocity ω for $\lambda = 2$
1	0.08 m	0.20 m	0.800	0.40	10 rad/s
2	0.08 m	0.25 m	0.640	0.32	8 rad/s
3 (base)	0.08 m	0.30 m	0.533	0.27	6.67 rad/s
4	0.08 m	0.35 m	0.457	0.23	5.71 rad/s

Table 4.6: Turbine models under study on the basis of solidity σ

To study the effects of turbine solidity on the flow development and overall performance, four cases with different rotor radius were tested. The design details of these four models are presented in Table 4.6. Solidity σ has an inverse relationship with the rotor diameter; lowest solidity indicates the largest size of the rotor. The results presented in this section correspond to the same operating conditions of tip-speed ratio $\lambda = 2$ and free-stream velocity $V_0 = 1m/s$.

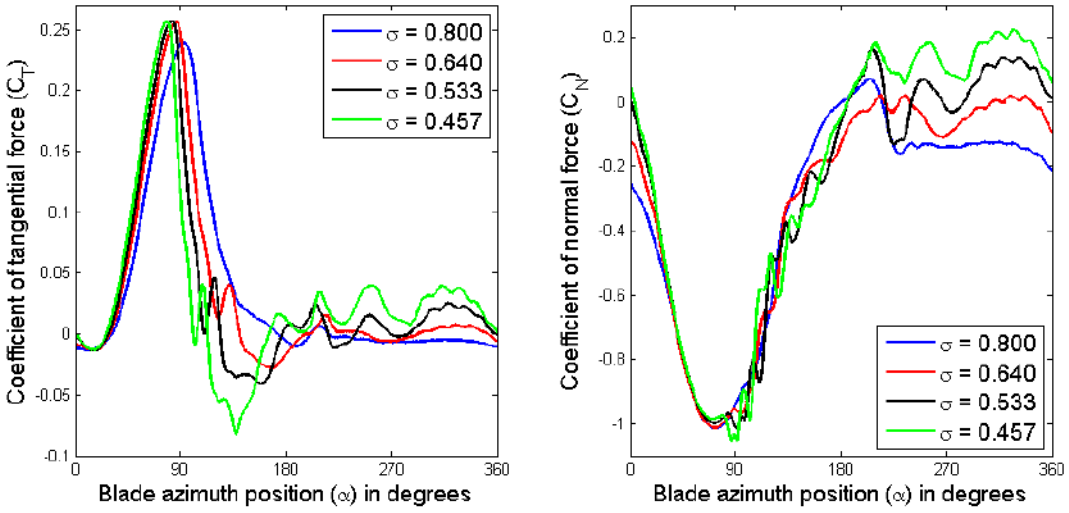

(a) (b)

Figure 4.19: Effect of solidity on the distribution of force coefficients

The computational findings of force coefficients through the azimuth in Figure 4.19 shows the instantaneous impact of solidity σ on the blade loading. Most of the loading is concentrated during the front half of the cycle between the azimuth angle $0^o < \Psi < 180^o$ and least loading is witnessed during the rear half of the cycle of $180^o < \Psi < 360^o$. The fluctuations in the normal force distribution which leads to turbine's vibrations decrease with the solidity σ. The difference in the tangential force distribution with solidity which contributes to the thrust is articulated in the Figure 4.20(a) through the variation of torque. The global effect of solidity σ on the turbine's performance is quantified in terms of the COP plots which are shown in Figure 4.20(b). It is shown that larger solidity models produce lower power due to reduced area swept by the turbine. At higher solidity σ, the initial part of the COP curve is bumpy, which becomes straight as the solidity σ decreases. Although the optimum tip-speed ratio λ_{opt} remains identical for all of the models, the maximum value of COP is attained with the lowest solidity model.

Figure 4.21 shows the contour plots of COP on the dimensions of operational conditions for Model 1 ($\sigma = 0.8$) and Model 3 ($\sigma = 0.533$). For a given operating range of $1 < V_0 < 3$, the comparison between the two plots demonstrate that the

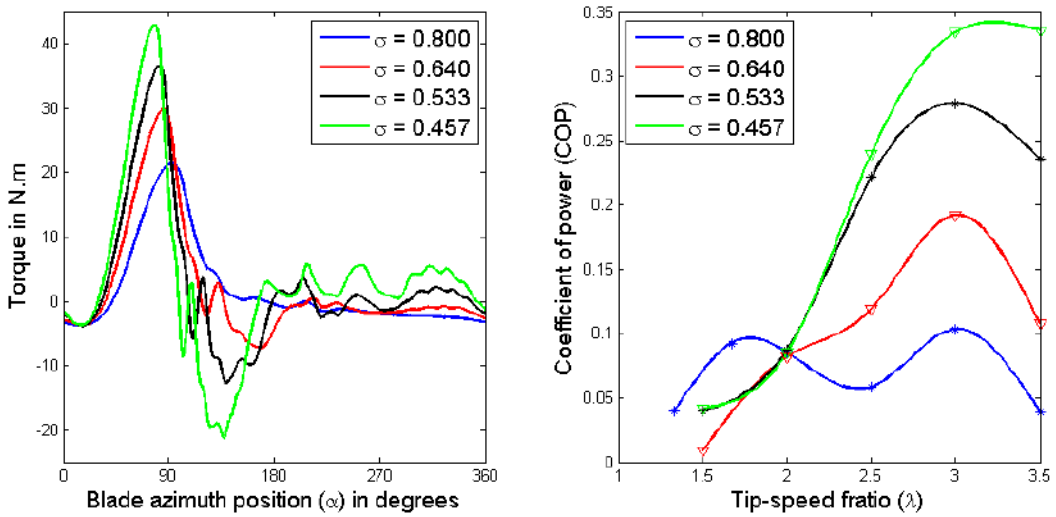

(a) (b)

Figure 4.20: Effect of solidity on the turbine's torque characteristics

model with higher solidity has the maximum COP of 0.16 (27% of the Betz limit) whereas the model with lower solidity has the peak COP of 0.33 (56% of the Betz limit), which corresponds to a difference of more than 100% in the performance. Another observation is about the operating range which is wider for lower solidity model compared to the higher σ due to the reasons mentioned in section 2.5.

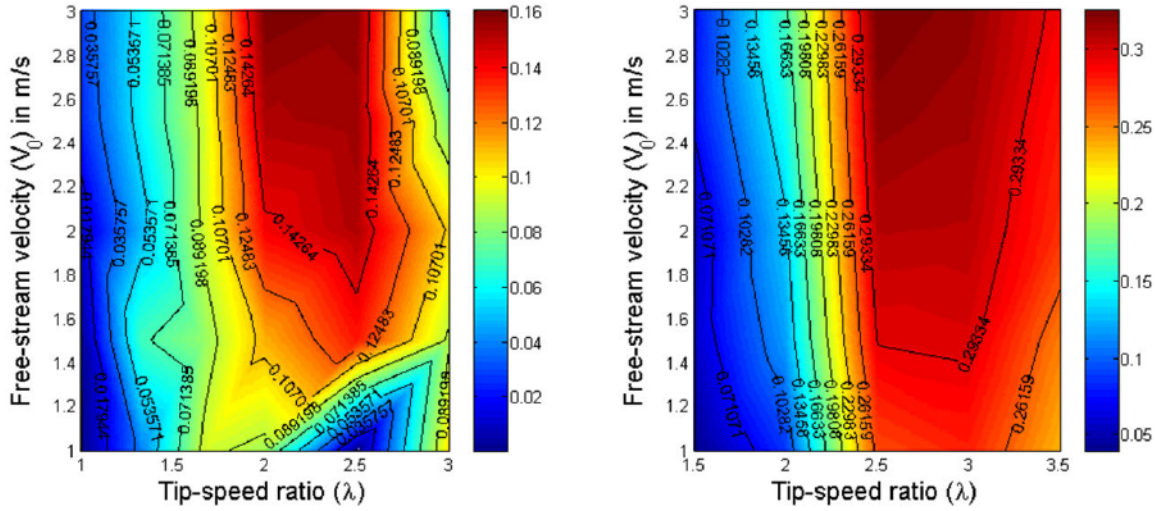

(a) $\sigma = 0.8$ (Model 1) (b) $\sigma = 0.533$ (Model 3)

Figure 4.21: Effect of solidity σ on COP distribution under different operating conditions

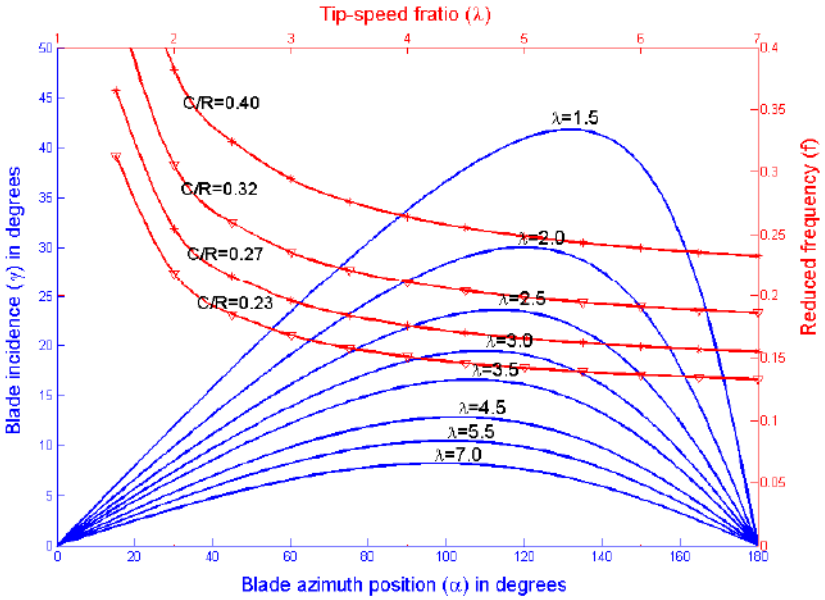

Figure 4.22: Relationship between effective angle of attack γ, reduced frequency F, and tip-speed ratio λ

The ratio of blade chord to the rotor radius gives the chord-to-radius ratio (L/R), which makes an important design criterion from dynamics standpoint. Since the chord of the blade is kept constant throughout the studies, the changes in local Reynolds number and hence the stall angle do not exist. On the other hand, larger sizes of the rotor definitely increase the power output with increasing loads on the blades. Also, there are serious cost implications with the higher rotor diameters. The reason for examining the ratio L/R is that it determines how prone the turbine is to dynamic stall once the blade incidence exceeds the static stall angle (Amet et al., 2009). Recalling the Equation, which relates the blade incidence γ, azimuth position α and tip-speed ratio λ, the reduced frequency as given by Amet et al. (2009) is defined by

$$F = \frac{L}{R} \cdot \frac{1}{2(\lambda - 1)\theta_{max}} \tag{4.30}$$

Figure 4.22 shows the composite plots of $\gamma - \alpha$ relationship and reduced frequencies for the selected turbines models. Considering the static stall angle of NACA 0015 to be 14^o, the occurrence of stall is strongly predicted for all of the models. It is also revealed by Migliore et al. (2012) that the models with larger L/R values generally exhibit enhanced flow curvature effects and hence affect the blade efficiency. Since the efficiency measurements are not covered in this research, further evaluations were not performed at this point of time.

Figure 4.23 shows the vorticity contours on the left, and integrated pressure-velocity distributions on the right for the four models listed in Table 4.6. The

complexity of the flow field is relatively higher for the highest solidity design (Model 1) and following the decreasing trend as the solidity decreases. This is mainly due to the rapidly pitching blades which are more likely to shed vortices. As all of the pictures correspond to an azimuth position $\Psi = 0^o$, there is a clear distinction between the solidity models in terms of the distance d between the blade at bottom of the cycle and the strong vortex ahead of it. As the solidity σ increases, the distance d decreases, and therefore the models with sufficiently large solidity may not experience the blade-vortex interaction. Also, the size of the wake region downstream of the rotor obviously decreases with the solidity σ.

4.9 Conclusion

While explaining the CFD methodology adapted in this research, this chapter provided the turbine model specifications and spatial discretization and appropriate boundary conditions. The processing details mainly illustrated the turbulence modeling techniques with temporal discretization and computing considerations to meet the time and resource constraints. The fidelity and adequacy of the chosen computational models was discussed which highlighted that the SST $k-\omega$ viscous model is the most suitable for the flow across a low speed Darrieus turbine. The reference test case of tip-speed ratio λ=2 is discussed. In addition to the effect of tip-speed ratio λ, the torque extraction mechanism, flow field development around the blade as well as the turbine were detailed. The turbulence modeling exercise was extended to parametric studies to investigate the effect of free-stream velocity V_0. For λ=2, the maximum COP attained by the base turbine model with the solidity σ=0.533 yielded a COP of 56% of Betz limit. The optimum tip-speed ratio λ_{opt} was found to be approximately 2.5. In order to validate the CFD results, the experimental investigation for the flow across the Darrieus turbine should be available. Next chapter illustrates the details of experimental campaign, the results of performance and flow fields which would complement to the numerical analysis.

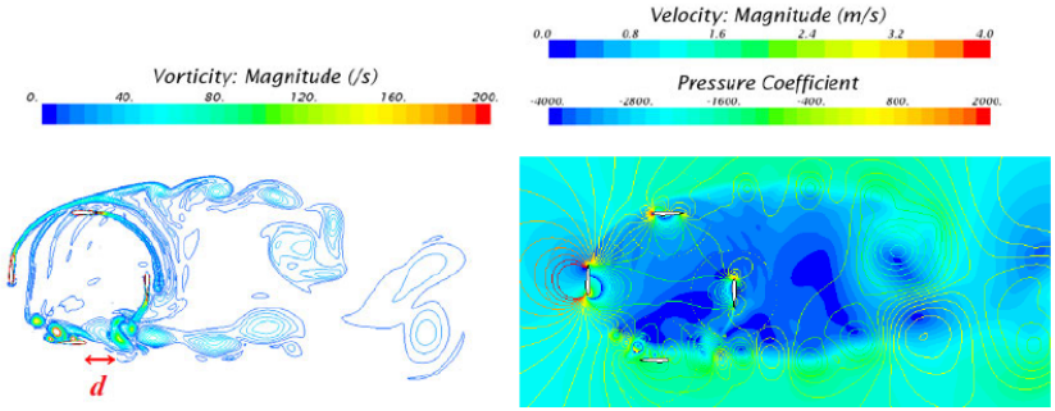

Model 1 ($\sigma = 0.8$)

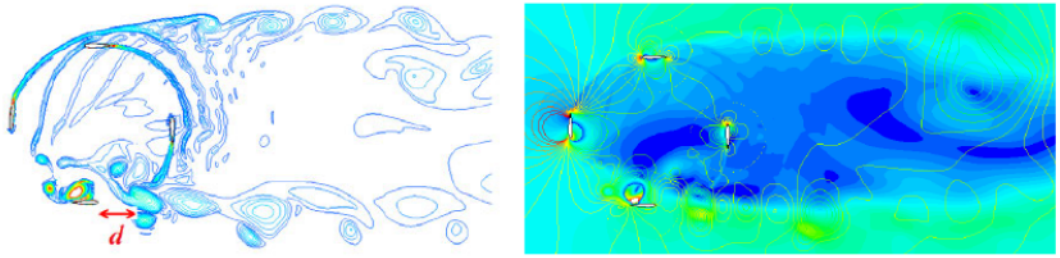

Model 2 ($\sigma = 0.64$)

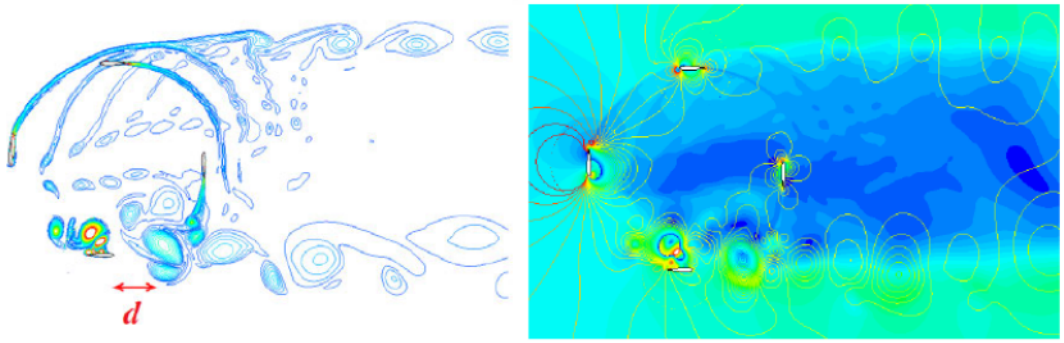

Model 3 (base design with $\sigma = 0.533$)

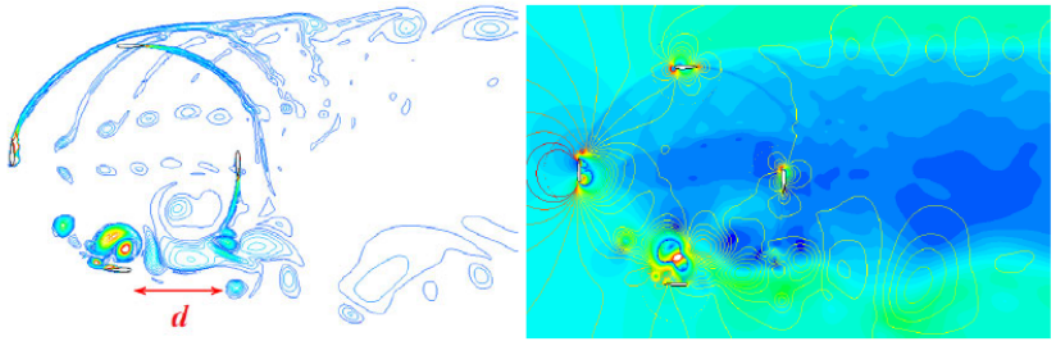

Model 4 ($\sigma = 0.457$)

Figure 4.23: Effect of solidity σ on the flow-field

CHAPTER 5

FIXED BLADE MODEL: EXPERIMENTAL ANALYSIS

Contents

5.1 Introduction

Experimental campaigns that were carried out during this research project targeted to acquire quantitative measurements of the Darrieus turbine in terms of power characteristics as well as the relevant analysis of the flow around the blades and across the turbine at various azimuth positions under different operating conditions. This chapter presents the details of the experimental facility and the

procedures used to acquire full-range power characteristics of the turbine. Following this, complete set-up of the PIV system used for flow measurements and processing steps are discussed. Finally, the performance and flow field visualizations of various parameters obtained from CFD studies are validated using the PIV results.

The experimental facility at Institute Pprime for towing tank tests had been adapted to the study of cross-flow turbine at the beginning of this project (Bardwell, 2013). Since the standard set-up and operational procedure for turbine testing was already put in place which was adapted for present study, the Author's contribution to the experimental campaign was mainly in generating the low velocity flow environment, instantaneous data acquisition and post-processing. Starting with the fundamentals of PIV experimental equipment, this chapter provides the explanations about each procedure and presents the measurement results.

5.2 Two-dimensional two-component Particle Image Velocimetry (2-D 2-C PIV)

In this research, the experimental investigation of flow across the Darrieus turbine used Two-dimensional two-component Particle Image Velocimetry (2-D 2-C PIV) system. The fundamental idea of PIV in fluid mechanics experiments is to capture the image doublet of the flow with certain time gap between them. Appropriate seeding in the flow domain of interest is necessary to scatter the light which is captured in these images. This light is generated from a source of laser illumination which creates a plane of seeding particles. The apparent motion of the particles in successive images provides the displacement vector. The velocity vectors are constructed by dividing the particle displacement by the time step between the images. A typical 2-D 2-C PIV set-up comprises a number of components which mainly include:

1. Neutrally buoyant, light reflective particles
2. A laser generator to create a sheet of illumination to locate the particles
3. A camera to capture the light scattered by the particles
4. A PIV software for image acquisition and data processing

Taking these major components into consideration, the following sections describe the instruments as well as methods used for PIV study in this research.

5.2.1 Tracer particles

PIV measurement of velocity vectors within the flow field is basically performed through the cross-correlation of successive images of tracer particles. In this regard,

the particle's response in attaining the motion equilibrium with the fluid flow is very important. This can be quantified by using Stoke's number S_k, defined as

$$S_k = \frac{\tau V_0}{L_c} \tag{5.1}$$

where τ is the particle response time, calculated from

$$\tau = \frac{\rho_p d^2}{18\mu} \tag{5.2}$$

Here, V_0 is the flow velocity, L_c is the characteristic dimension which is the chord length of the blade in present study, ρ_p is the tracer particle density, d is the particle diameter and μ is the dynamic viscosity of the fluid. Lower S_k (say, <0.1) would yield a tracing error of less than 1%. For the motion equilibrium between the flow and tracer particles, the particle response time τ must be less than the smallest time scale of the flow. These considerations allowed the tracer particles to follow the flow without noticeable deviation.

Apart from particle's response time, the size of the particles matters to trace them clearly. On one hand, too small particles, although being good flow tracers, cannot scatter the laser light adequately due to size limitation. On the other hand, too large particles pose the mass inertia issues. Light scatters at Mie regime with the particles of the order of micro-metric size which is greater than the laser wavelength. The strongest scattering happens in-line of incident light while the weakest scattering occurs perpendicular to the camera view. Since scattering intensity plays an important role in the quality of PIV images, possibly maximum sized particles are always sought of.

5.2.2 Integration window

Cross-correlation process is used to obtain the mean particle displacement in the observation window. The tracer particle density should be within suitable range; under-seeding would miss the statistical accuracy while over-seeding would cause multiphase flow. Literature shows that the desirable range of particle density is $10^9 - 10^{12}$ particles/m^3 which confirms a minimum of 10 particles per integration window (Cruz, 2008). The window size is however difficult to determine due to the occurrence of huge velocity changes within the domain. Too small window may lose the particles while too large window unavoidably yields mean flow conditions. Multi-pass approach plots the solution for this problem where the process commences with the larger window and pre-shifts small sized windows of next passes by means of the distance measured at current pass. This continues until the smallest feasible window size is achieved. Such multi-pass technique is combined with the window deformation techniques based on the spatial gradients. In order to enhance the utilization of measurement data, it is advised to overlap the

neighbouring observation windows.

5.2.3 PIV processing software

The complete PIV measurement system involves various interdependent sub-systems such as laser illuminators, cameras, torque measurements etc... Various PIV hardware and software are available in the market that could meet the modern engineering and research requirements. The current experimental study used RD Vision EG and Hiris for synchronous images, sensors for data acquisition and LaVision Davis 8 for PIV image processing.

5.2.4 Image reconstruction

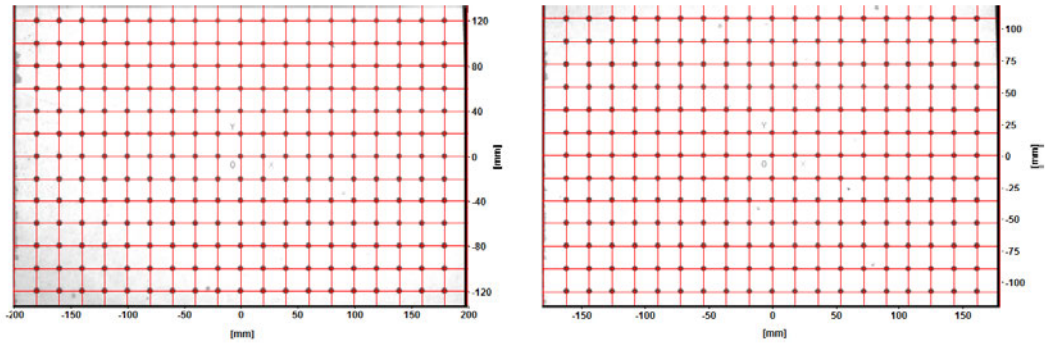

(a) For camera 1 (b) For camera 2

Figure 5.1: Calibration target

Image reconstruction is the process of acquiring the displacement vectors in the plane of particles by projecting the raw data from the image plane back to the object plane through a mapping function. The calibration based reconstruction procedure uses a typical mapping function, defined as

$$q = g(Q) \tag{5.3}$$

where g is generally a polynomial function consisting of unknown coefficients. These coefficients are determined by least-square methods because the number of calibration points on the target is usually more than the number of polynomial coefficients. The calibration target used in PIV experiments is normally a metal plate with predefined grid points on it. For the present experimental set-up, two images of calibration plate are necessary, as shown in Figure 5.1, to calibrate the two cameras used for image capturing.

5.3 Experimental apparatus and procedure

5.3.1 Turbine model

The turbine model consists of 4 straight and fixed blades of length 0.4 m with NACA 0015 cross-section. The rotor diameter is 0.6 m and the blade chord length is 8 cm. The top flange is made of stainless steel. Polymethylmethacrylate (PMMA) used for the bottom flange allows the cameras to capture the flow around the blades. Figure 5.2 shows the turbine model used in the experimental studies.

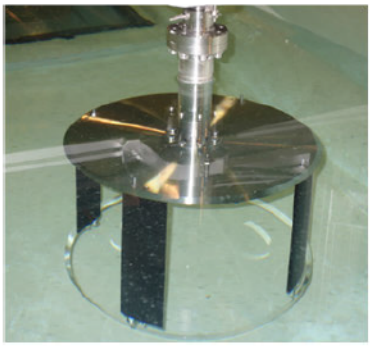

Figure 5.2: Turbine model used in experimental studies

5.3.2 Towing tank facility

In this study, the experiments were performed in the towing tank, which was 20 m in length, 1.5 m wide and 1.3 m deep with optically transparent side and bottom walls to allow laser beam and PIV image capture respectively, as shown in Figure 5.3 (a). The towing tank provided a turbulence-free environment and could host the water-turbine, with a blockage ratio b as defined in section 2.5, equal to 0.1231. This ensures some blockage effects to the flow passage. A Leroy Somer Compabloc reversible generator (CB3135 SB3) with 5.65 reduction ratio was used to rotate the turbine whose nominal power is 3.4 kW at 2400 RPM. An NCTE Series 2200-75 rotary torque sensor was fitted to generator shaft along with an angular index in order to measure the hydrodynamic loads acting on the model. Since the experiments were conducted for various tip-speed ratios ranging from 0.5 - 5 and different flow velocities from 0.5m/s - 1.5m/s, the duration for data acquisition and hence the sample rate were different from case to case for a given distance of turbine's linear motion.

5.3.3 Flow diagnostics

In addition to the torque measurements, a high-resolution Particle Image Velocimetry (PIV) system was employed to realize comprehensive flow field measurements to quantify major characteristics of the unsteady flow around the model. For the

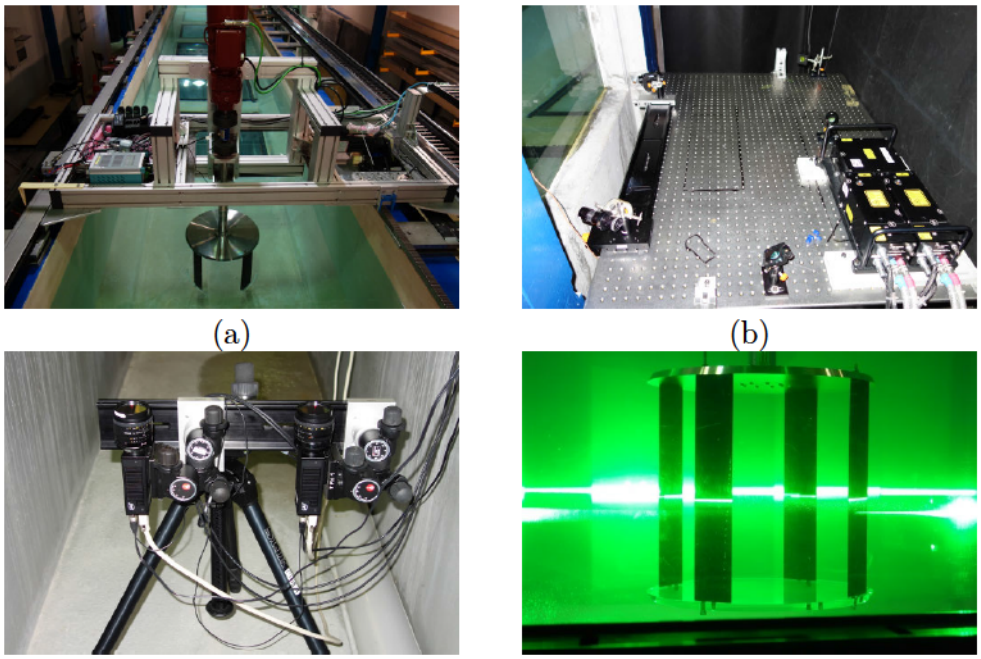

(a) (b)

(c) (d)

(a) Turbine model in the starting zone of the towing tank; (b) Optical arrangement for laser beam separation (c) CCD cameras; (d) Instantaneous laser sheet on the mid-plane of the turbine

Figure 5.3: Experimental facility and instruments

PIV measurements, a 532nm wavelength & 200mJ pulse dual-head Nd:YAG laser (Quantel Big Sky) was used to supply illumination, which was separated into two horizontal sheets on an optic table and entering the towing tank diagonally from a side window as shown in Figure 5.3 (b). The thickness of the laser sheet in measurement region was about 1.5 mm. Figure 5.3 (c) shows two Jai CV-M2 dual-frame CCD cameras (1600x1200 pixels, 15 fps max.) situated below the towing tank capture the PIV images on a 1000 mm x 700 mm area, through the tank windows and transparent bottom flange of the turbine. Seeding was comprised of 20μm mean diameter Polyamide particles. The CCD cameras and the laser were connected to the host computer through a Digital Delay Generator (RD-Vision EG), which controlled the timing of the laser illumination and the image acquisition. The PIV system synchronized with the torque acquisition and the angular index yields phase-locked sequences of image sets. Figure 5.4 shows the schematic of the PIV system used in the present study. The towing motion was initiated so that one of the turbine's blades enters the PIV window at zero azimuth position. This phase control between the carriage and the turbine was achieved by using the angular index as a start-up signal to the carriage drive. RD Vision EG digital delay generator was used for this purpose which delayed the arbitrary initial angular position to achieve a final 10^o resolution for entire cycle. This led to a

number of experiments n_{max} for each flow configuration as shown in Table 5.1. The PIV timing loop was adjusted in such a way that the successive velocity fields for 10-multiplied angular displacements were obtained.

Free stream velocity (V_0) in m/s	Tip-speed ratio (λ)	Phase difference between consecutive frames (ϕ)	Reconstructed phase angles with $\Delta\phi = 10^o$
0.25	2.0	10	
0.50	2.0	20	0, 10 ($n_{max} = 2$)
0.75	2.0	30	0, 10, 20 ($n_{max} = 3$)
1.00	1.5	20	0, 10 ($n_{max} = 2$)
1.00	2.0	30	0, 10, 20 ($n_{max} = 3$)
1.00	2.5	40	0, 10, 20, 30 ($n_{max} = 4$)
1.5	2	40	0, 10, 20, 30 ($n_{max} = 4$)

Table 5.1: The maximum number of runs n_{max} required for each flow configuration to obtain a 10^o angular resolution of blade positioning

Once the turbine crosses the laser trigger, the illumination starts and images are captured. This provides the flow information of 0.3 m upstream of the turbine. Laser and cameras continue to operate even after the turbine passes the field of view, which gives the downstream flow information corresponding to 1.4 m.

Apart from the nature of flow and boundary conditions, the quantification of flow variables around the blade at any position during its operation is usually in negotiation with the laser light in the measurement plane as well as its reflection on blade's surface, and the applied features for PIV post-processing. In this study, instantaneous PIV measurements were obtained by dual-frame FFT cross-correlation using DaVis 8 Imaging Software developed by La Vision. Velocity maps were post-processed using 4-step multipass algorithm of 64x64 and 32x32 pixels respectively and iterative image deformation, in order to overcome in-plane pair loss limitation. An effective overlap of 50% was used in image processing to further increase the spatial resolution. The velocity vectors are formed by the velocity components (Vx and Vy) and the vorticity was derived from the curl of velocity vectors. The number of frames and hence the image set size varied along with the flow configuration since the PIV window is stationary and fixed in size, and camera frame rate was limited.

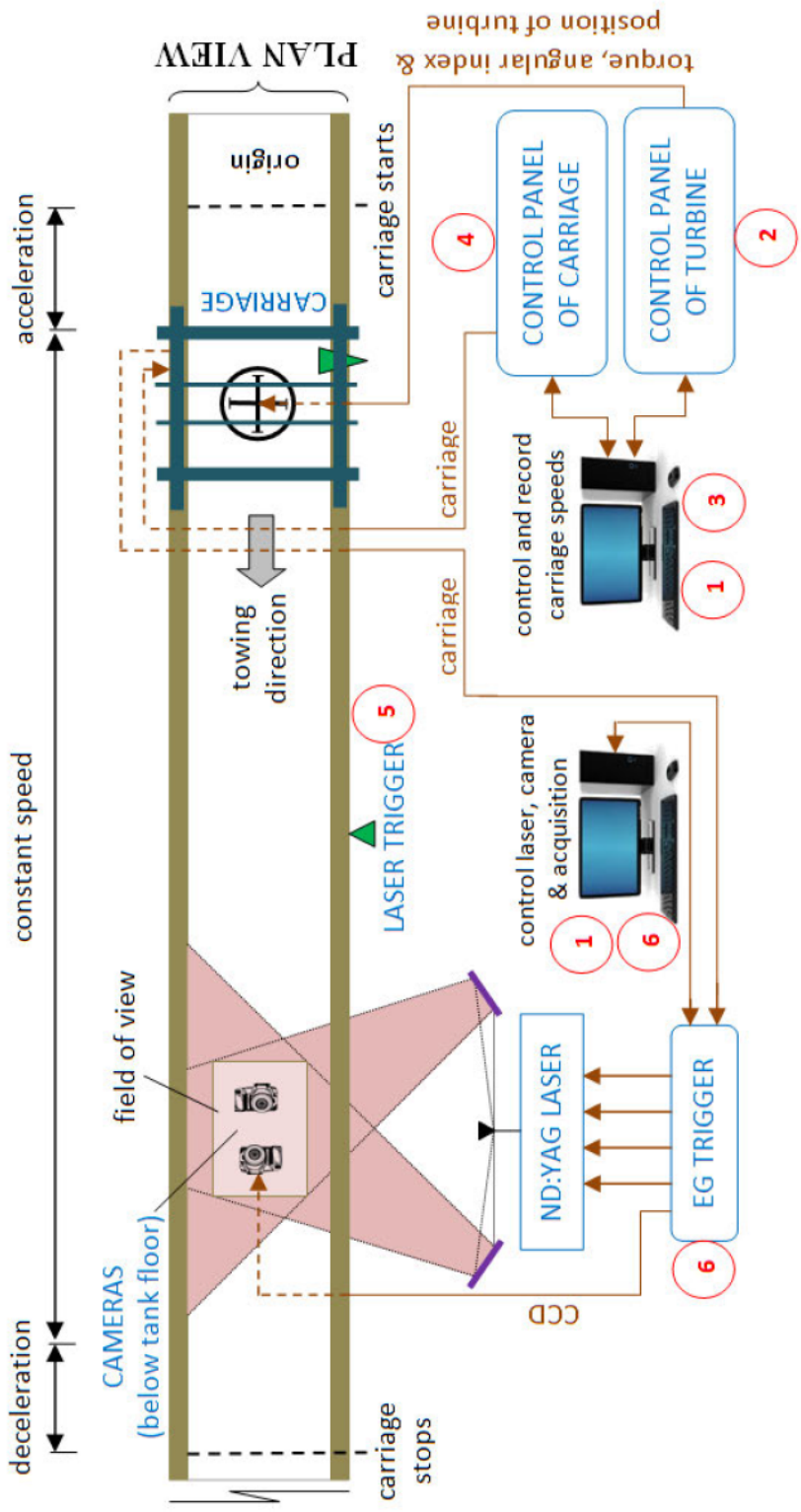

① Set up PIV parameters: length, Δt, acquisition frequency, number of images, recording of images etc.
② Set up the turbine's rotational speed
③ Set up carriage speed, towing length, time delay and torque measurement
④ Start the carriage
⑤ Trigger the laser
⑥ EG trigger receives message from the carriage, pass to laser, CCD camera and PC to start lighting, picture shooting and image recording

Figure 5.4: Schematic diagram of the experimental setup and data acquisition procedure

5.4 Time-dependent torque acquisition

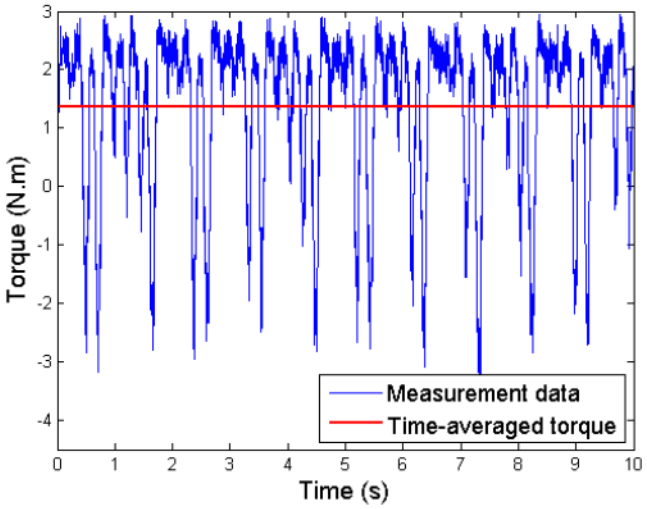

Figure 5.5: Time sequence of torque measurement

Torque measurements were carried out using the load cell connected to LabView software through a 16-bit resolution digital acquisition system. In order to increase the reliability of the results obtained from experimental studies, each experiment was repeated three times. Typical performance results of a turbine model consist of the measurements of hydrodynamic forces acting on the water turbine and the torque characteristics. Figure 5.5 shows the filtered sample result of torque measurement of the turbine model at a tip-speed ratio $\lambda = 2$ and free-stream velocity $V_0 = 1m/s$ and Figure 5.6 show the corresponding histogram of the measured torque. It is noted that the instantaneous loads acting on the turbine were highly unsteady in nature. The mean and standard deviation of the measured torque were found to be 1.3702 Nm and 1.4007 Nm respectively.

Noticing the importance of tip-speed ratio λ in the conceptual design of wind and water turbines, several scholars performed parametric studies to find the optimum tip-speed ratio beyond which the performance characteristics of the device deteriorate. This optimum value of tip-speed ratio is the key in determining the range of favourable operating conditions. Hu et al. (2012) studied the influence of tip-speed ratio on the dynamic wind loads and wake characteristics in terms of thrust and moment coefficients of the wind turbine model. Chaitep et al. (2011) and Biadgo et al. (2013) conducted similar studies using experiments and CFD tools respectively to evaluate the turbine's rotation, torque and power output with respect to operating conditions. To this end, the effect of λ on the model's propulsive performance was examined systematically. For a given free stream velocity V_0, the rotational speed of the turbine was adjusted to have a desired value of λ to see the performance characteristics of the turbine at various values of λ ranging from 0.5 to 5. This process was repeated for different free stream velocities,

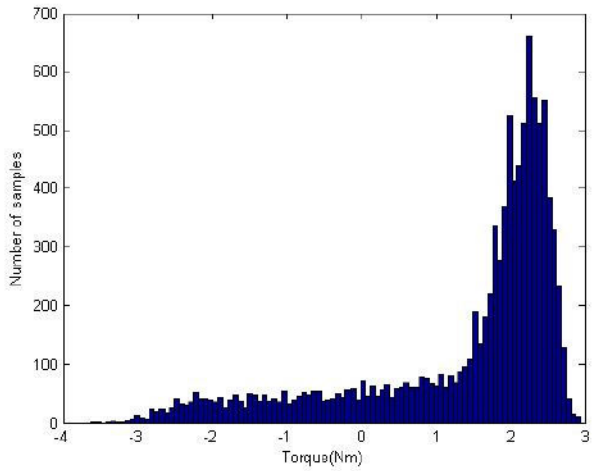

Figure 5.6: Histogram of torque measurement

from 0.5m/s to 1.5m/s. Figure 5.7 compares the histogram plots of instantaneous torque measurement data sets for considered set of tip-speed ratio λ values.

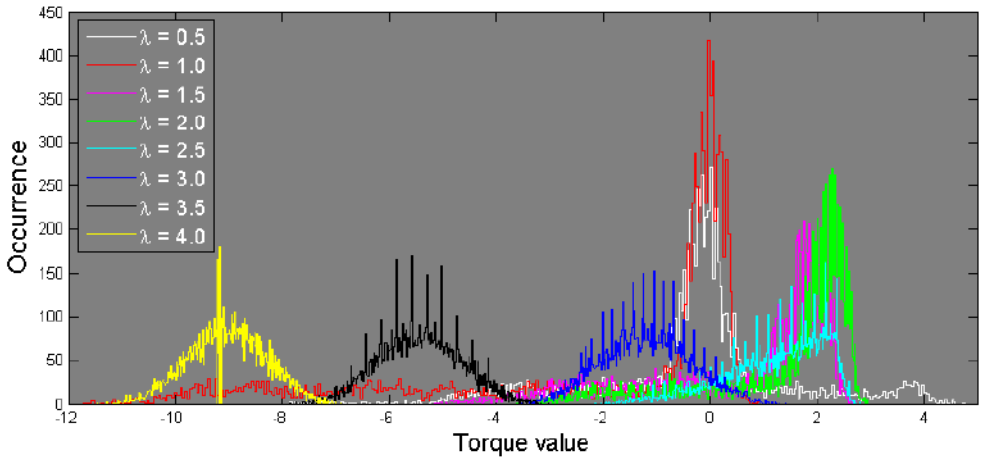

Figure 5.7: Histograms of torque measurements for λ ranging from 0.5 to 4

While the histogram of $\lambda = 1$ achieved the maximum of all the plots, it is evident that the mean value of torque increases as λ increases from 0.5 and reaches the maximum at tip-speed ratio $\lambda = 2$. Beyond this optimal value of tip-speed ratio, the mean torque diminishes. In the limiting case of higher λ, the turbine will rotate just neutrally without producing energy. The evolution of torque profiles for different values of λ and V_0 is shown in Figure 5.8. Each of these curves shows the instantaneous torque developed by the turbine for a complete cycle. The average of each curve gives the amount of torque T generated by the device. The variation of mean torque T with the operating conditions is shown in Figure 5.9. Refer to

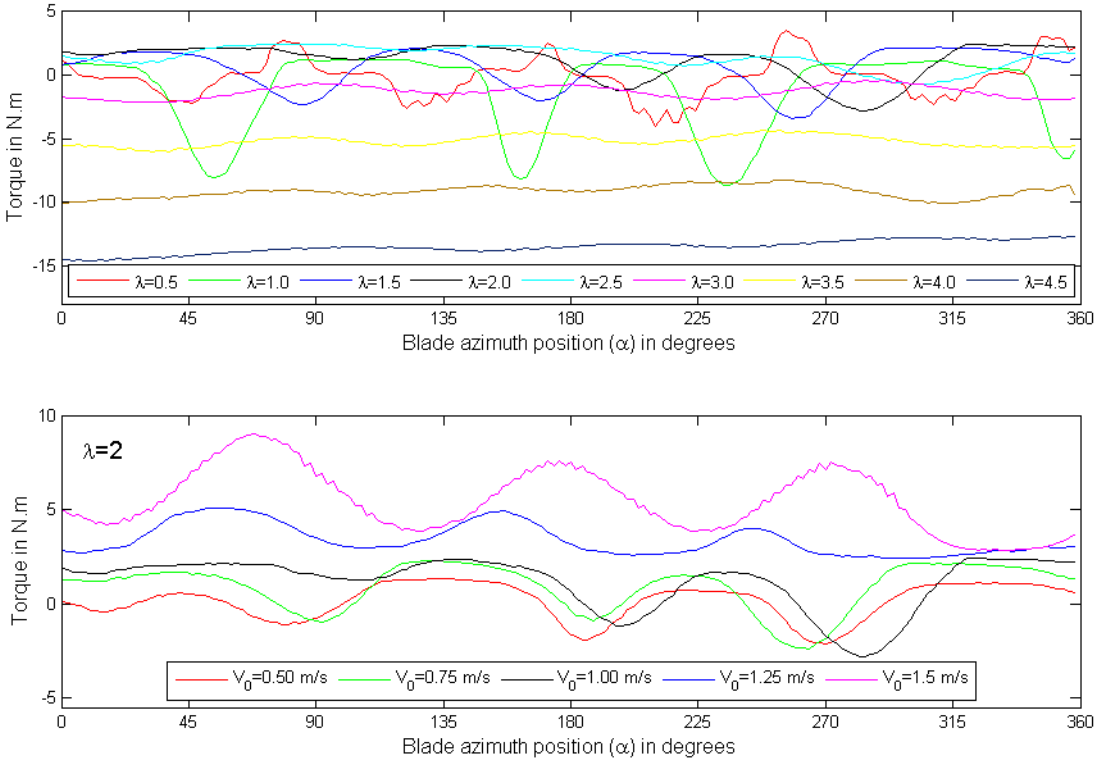

Figure 5.8: Experimental measurements of instantaneous torque for a complete cycle for different values of λ and V_0

Figure 5.9 (a), as noted by Spera (1994), blade stall controls the portion of the curve lying on the left side of the peak, where tip-speed ratio λ is relatively lower. When the turbine spins at lower RPM, the relative incidence of the blade is larger. As the angle of attack increases beyond the stall angle, flow separation behind the blade occurs. At higher RPM, the blade experiences the flow with higher relative velocity. Desired flow characteristics can be obtained when an optimal blade incidence allows larger relative velocity. With higher tip-speed-ratio, the relative incidence of the blade decreases considerably and results in lower values of the torque. Figure 5.9 (b) shows that the maximum torque was achieved at a tip-speed ratio $\lambda = 2$ for free stream velocities V_0 larger than 1m/s.

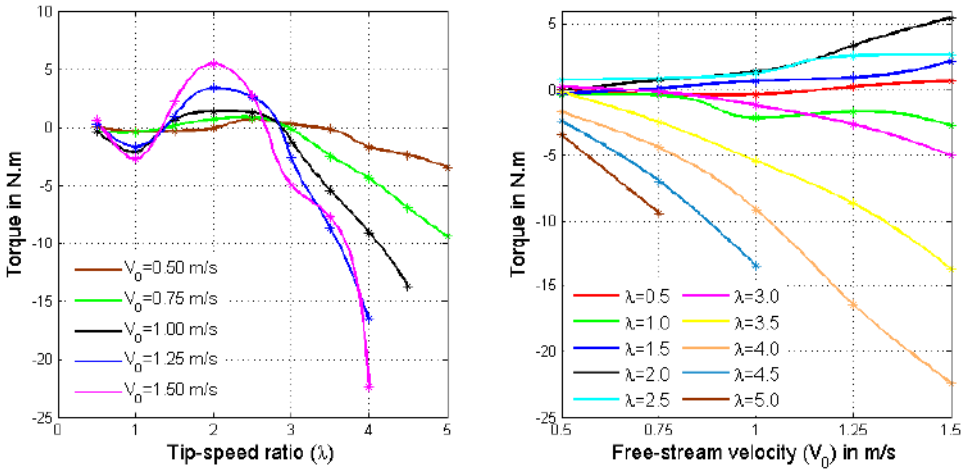

Figure 5.9: Experimental results of the variation of torque with λ and V_0

5.5 Validation of CFD results

This section presents the validation of computationally calculated power coefficients under different operating conditions against experimental measurements. In both approaches, the flow confinement is taken into consideration and therefore corrected COP values for blockage effects in 2D flow for CFD and 3D flow for experiments are plotted. The 0.6m x 0.4m sized turbine when placed in the flow channel of 1.3m x 1.5m produces a blockage ratio of b= 0.1231. Therefore, the 3D flow conditions in experimental studies produced one third of blockage effect developed in 2D CFD environment. Equation 4.29 is therefore used to consider the blockage effects in both of the investigation methods. Figure 5.10 presents the uncorrected and corrected COP curves obtained from both numerical and experimental studies. Consideration of blockage effects thus creates a comparison between the 2D and 3D flow environments.

Looking at the physics of power extraction, since the turbine's rotational velocity corrections were not performed, the effect of bearing and windage losses in the experimental studies were expected to appear in the final results, which would lead to over-predictions of computational results. This is evident particularly at higher rotational speeds. The power curve plots reveal several observations, which are presented here. Firstly, there is a close match between the computational and experimental results at tip-speed ratio $\lambda \leq 2$. Thereafter, spanwise flow variations are reflected in the experimental results, which were missing in the 2D computational studies. With CFD, the maximum value of power coefficient is obtained at a tip-speed ratio λ_{opt} is close to 2.5. From this value of λ, huge difference between the computational and experimental COP values is observed. The blade span of

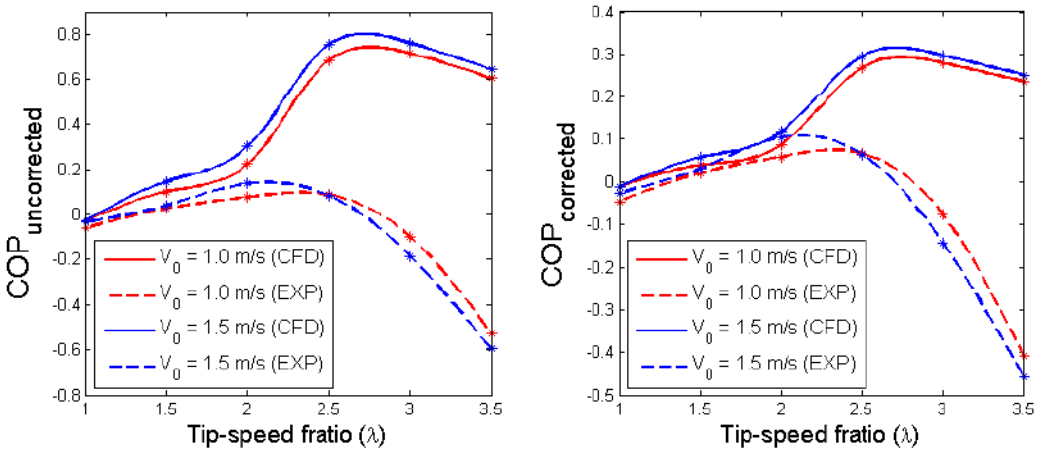

Figure 5.10: Comparison of computational and experimental calculations of uncorrected COP (left) and corrected COP (right)

0.4m which was completely immersed in the fluid during the experiments produce the realistic 3D flow, where the numerical studies clearly missed the 3D relieving effects. In addition, the numerical studies did not consider the energy losses due to the friction. The shape of the COP curves and the difference between the numerical and experimental values are consistent with the observations of Howell et al. (2010). Table 5.2 shows the entire series of experiments and corresponding uncorrected and corrected COP values. Further investigations are necessary to validate the flow field observations of CFD against PIV, which are presented in the following sections.

Free-stream velocity (V_0) in m/s	Tip-speed ratio (λ) in m/s	Turbine RPS	Power (P) in W	COP	Corrected COP
0.50	0.5	0.133	0.042	0,0028	0,0022
	1.0	0.265	-0.642	-0,0429	-0,0330
	1.5	0.398	-0.800	-0,0535	-0,0412
	2.0	0.531	-0.240	-0,0160	-0,0124
	2.5	0.663	3.105	0,2075	0,1598
	3.0	0.796	1.265	0,0845	0,0651
	3.5	0.928	-1.108	-0,0740	-0,0570
	4.0	1.061	-11.160	-0,7458	-0,5743
	4.5	1.194	-17.740	-1,1856	-0,9129
	5.0	1.326	-28.070	-1,8759	-1,4444
0.75	0.5	0.199	-0.490	-0,0097	-0,0075
	1.0	0.398	-1.040	-0,0206	-0,0159
	1.5	0.597	0.435	0,0086	0,0066
	2.0	0.796	3.525	0,0698	0,0537
	2.5	0.995	5.434	0,1076	0,0829
	3.0	1.194	-1.348	-0,0267	-0,0206
	3.5	1.393	-21.480	-0,4253	-0,3275
	4.0	1.592	-44.070	-0,8726	-0,6719
	4.5	1.790	-78.190	-1,5483	-1,1922
	5.0	1.989	-117.200	-2,3207	-1,7870
1.00	0.5	0.265	-0.600	-0,0050	-0,0039
	1.0	0.531	-7.110	-0,0594	-0,0457
	1.5	0.796	3.210	0,0268	0,0206
	2.0	1.061	9.125	0,6098	0,4696
	2.5	1.326	10.420	0,0870	0,0670
	3.0	1.592	-11.920	-0,0996	-0,0767
	3.5	1.857	-63.260	-0,5285	-0,4069
	4.0	2.122	-120.600	-1,0075	-0,7757
	4.5	2.387	-206.000	-1,7209	-1,3251
1.25	0.5	0.332	0.499	0,0021	0,0016
	1.0	0.663	-7.010	-0,0300	-0,0231
	1.5	0.995	5.828	0,0249	0,0192
	2.0	1.326	27.999	0,1198	0,0922
	2.5	1.658	27.068	0,1158	0,0891
	3.0	1.989	-32.920	-0,1408	-0,1084
	3.5	2.321	-126.199	-0,5398	-0,4156
	4.0	2.653	-274.459	-1,1739	-0,9039
1.5	0.5	0.398	1.678	0,0042	0,0032
	1.0	0.796	-13.641	-0,0338	-0,0260
	1.5	1.194	16.326	0,0404	0,0311
	2.0	1.592	54.772	0,1356	0,1044
	2.5	1.989	33.632	0,0832	0,0641
	3.0	2.387	-74.858	-0,1853	-0,1427
	3.5	2.785	-240.119	-0,5943	-0,4576
	4.0	3.183	-448.032	-1,1090	-0,8539

Table 5.2: Consolidation of the experimental measurements of turbine performance

5.6 PIV measurements

The purpose of using two large fields of view was to capture at least one complete rotation of the turbine at any given linear speed. This provided access to observing sufficiently large amount of data in the observation plane. Along with a careful experimental setup, this procedure needs the data to be merged without any spatial and phase offset. As reported by Lemaire et al. (2002), a dual camera PIV setup is always complex due to strict requirement of camera alignment and timing. A scaling factor of 0.40625 mm/pixel in both x- and y- directions was applied to fit the cameras' view planes of 0.65x0.4875 m^2 in size with its resolution. Since the two cameras constituted two isolated systems, the vector fields were computed independently. The velocity fields were then stitched using an appropriate scheme with an overlapping region of 46 pixels as shown in the Figure 5.11. The images in this figure correspond to a tip-speed ratio $\lambda = 2$ and free-stream velocity $V_0 = 0.5m/s$.

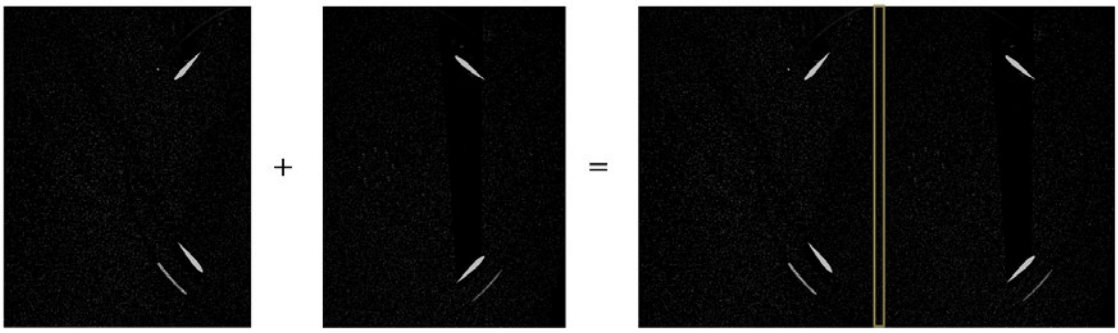

Figure 5.11: Process of merging the raw images taken by 2 cameras

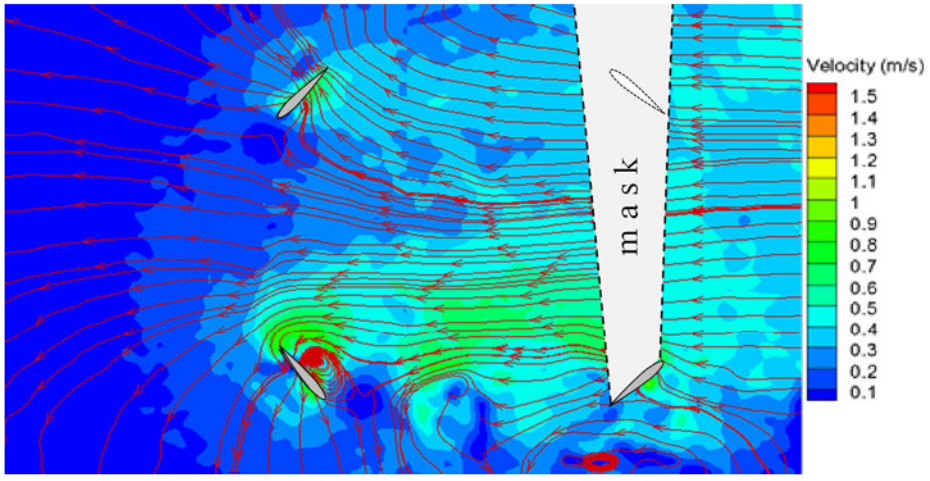

Figure 5.12: Streamlines plot from the resultant image for $\lambda = 2$ and $V_0 = 0.5m/s$

Dependence of PIV process on the Lagrangian approach seeks the particle motion to exactly follow the fluid's motion. The time lag between successive frames was so chosen that the particles were traced with sufficient resolution while the errors due to out-of-plane particles were reduced. Another challenge in the PIV post-processing was to identify the blade's position with reference to the vector mapping. Figure 5.12 shows the velocity magnitude distribution with streamline pattern at global azimuth position $\Psi = 50^o$ approximately for $\lambda = 2$ and $V_0 = 0.5m/s$.

5.7 Phase-locked PIV measurements

Phased-locked PIV measurements are critical to obtain more detailed observation and interpretation of flow physics with respect to the blade's azimuth position. The phasing between the towing carriage and the rotating turbine was provided by using the turbine's angular index as a start-up signal to the carriage drive. Suitable delays then allowed phase-locked measurements to be carried out to arbitrary initial angular position (0^o, 10^o, 20^o, 30^o) and angular resolution (10^o) with a level of uncertainty of a few milliseconds. The PIV timing loop was also adjusted so that successive velocity fields correspond to angular displacements that were multiples of 10^o, ensuring the full rotation cycle to be covered. An optical sensor situated on the towing rail was used to generate a pulse as input to the Digital Delay Generator to prompt the PIV system for the phased-locked PIV measurements. Depending on the defined tip-speed ratio, correct time delay was calculated for each velocity configuration which was added to the input signal from tachometer in order to acquire the images at every 10^o of blade's azimuth position with negligible error in angular measurement.

More detailed experimental analysis of the flow around the turbine model could be obtained from phase-locked PIV measurements, by accounting for the azimuth position of the blade. Combined flow field of phase-locked measurement and random one provides the instantaneous flow. Wernert et al. (1999) considered a much larger sample size in their investigation of phase-averaging of velocity vectors in order to realize a reasonable mean. As noted Ferreira et al. (2009), evaluation of complex vortical structures is critical due to their randomness in both strength and position. Such analysis can quantify the magnitude and distribution of random components. Despite the interest in such studies, higher degree of unsteadiness in the fluid dynamics and random disturbances challenge the success of accomplishing well-resoled phase-lock PIV measurements (Ramasamy and Leishman, 2006; Massouh and Dobrev, 2008).

Phase angle represents the angle between the measurement plane and the predefined position of the turbine's blade. Ferreira et al. (2009) studied the flow around the wind turbine blade at its azimuth position at 113^o and Yang et al.

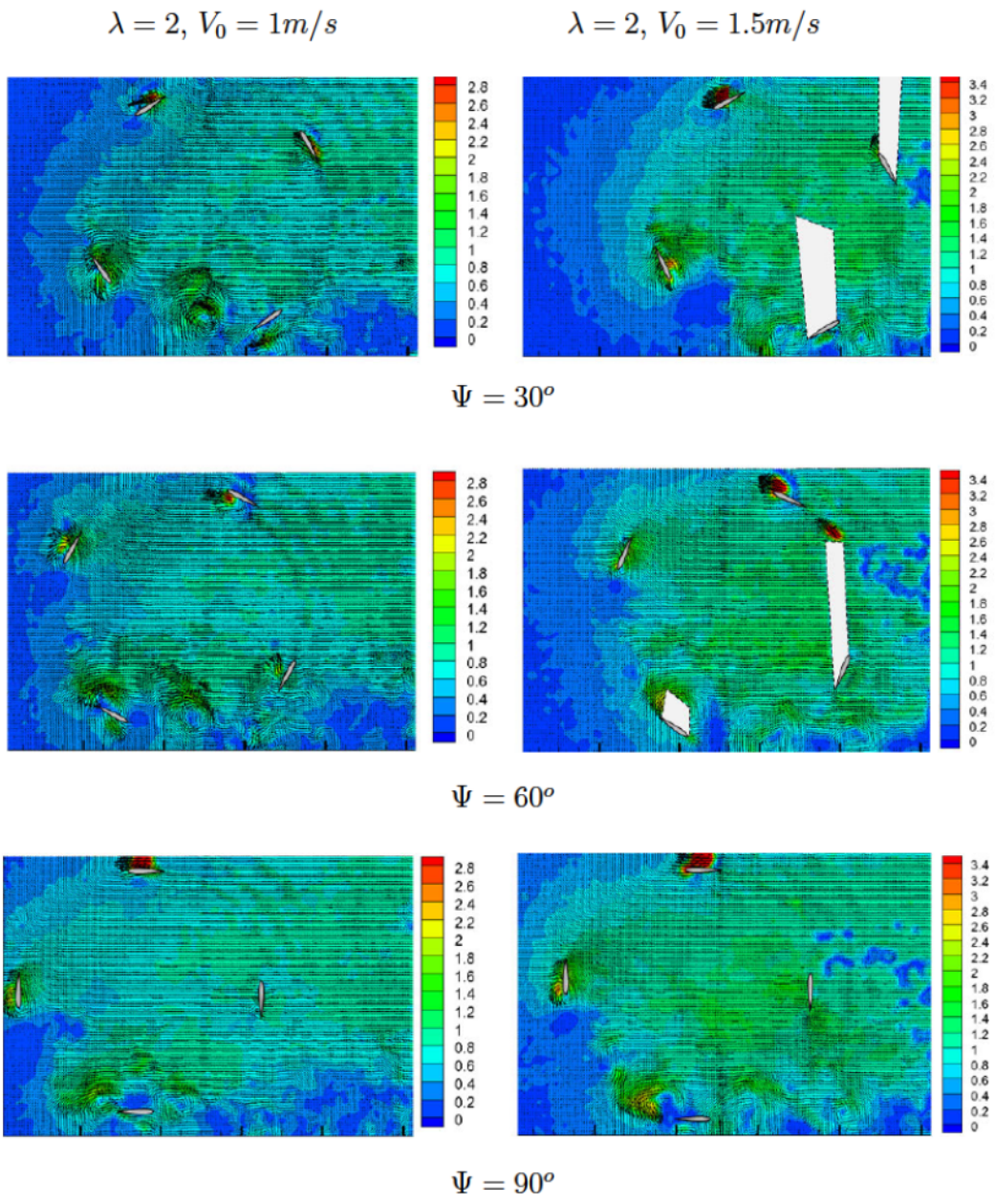

Figure 5.13: Velocity fields at various azimuth positions

(2011) did with a phase angle of 15^o. Green et al. (2012) examined the turbulence characteristics of unsteady wake in case of a horizontal axis wind turbine by catching ten consecutive downstream locations through a length of six rotor diameters. With the aim of resolving the lowest possible phase angle, the present study captured the complete cycle of the turbine with a phase angle of 10^o so that 35 azimuth positions were covered for one rotation. Although the phase-locked measurements were performed at all of the flow configurations, the results presented here mainly focus on the optimum tip-speed ratio $\lambda = 2$ for the model

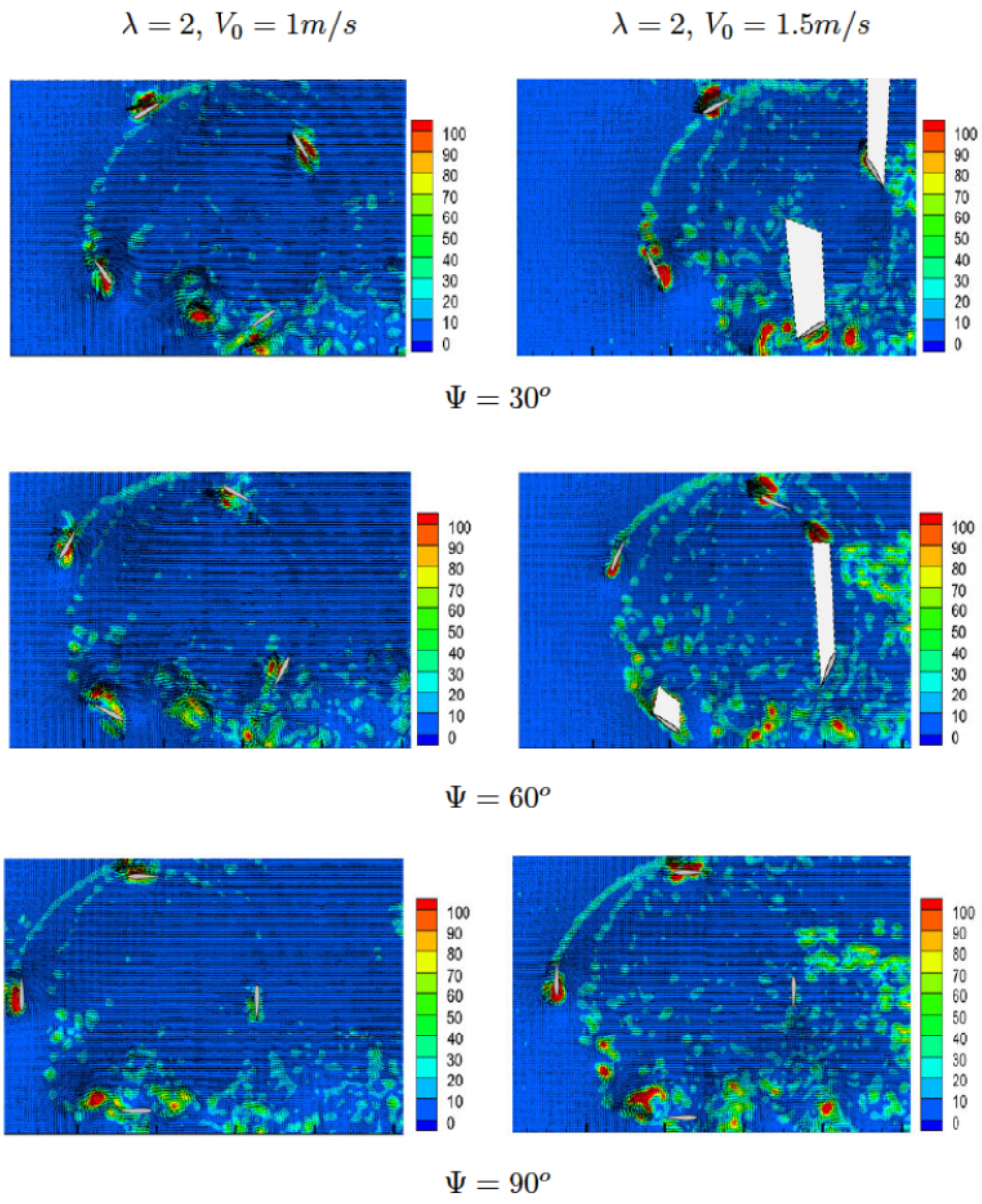

Figure 5.14: Vorticity fields at various azimuth positions

under study. Common fluid dynamic characteristics such as accelerated flow in red colour contour are observed over the suction side of the blade during the analysis of velocity field distribution as seen in Figure 5.13. The size of this accelerated region is governed by the strength of local vortex. Counter-clockwise rotation of the turbine attempts to shift the stream-wise velocity field upwards as the turbine moves forward. This is the reason why relatively lower velocity scales prevailed at the bottom.

Productive characteristics of the device can be assessed with appropriate knowledge about the flow patterns inside and downstream of the rotor system. Paraschivoiu

(2002) and Islam et al. (2008) presented theoretical models to forecast the torque using the information of velocity field around the rotor. Based on the concept of momentum model, Templin (1974) and Paraschivoiu and Declaux (1983) proposed streamtube models for vertical axis wind turbine. As reported by Strickland et al. (1979), this study used the velocity field in the measurement plane to calculate the vorticity distribution. Figure 5.14 shows the vorticity distribution with considerable degree of its interaction with following blades. The instantaneous location of this interaction depends on the flow parameters. The vortex sheet spreads wider and making a faster skewed-trajectory downstream of the rotor due to the self-induction of the unsteady vortices. As explained by Scheurich (2011), this would result in unsteady torsional and bending loads on the rotor shaft. Complexity in the vortex shedding mechanism constitutes the formation of strong vortex in the initial stage which breaks down swiftly. This dismantle is caused by the self-induced velocity components of blade vorticity that warps and muddles the shed vortex into multiple structures.

5.7.1 Velocity gradients

Accuracy in capturing the velocity gradients is very important as they are the major components of turbulence generation term in the flow conservation equations. In complex flow situations, it is always difficult to capture the exact gradients of any flow variable (Freeborn, 2008). Figure 5.15 shows the streamwise velocity gradient measured using CFD (left) and PIV (right) for a tip speed ratio $\lambda = 2$ and free-stream velocity $V_0 = 1m/s$. In the PIV investigation, the velocity gradient was measured from the spatial differentiation of the velocity field. This process intensifies the noise in the global velocity fields. A limitation from the second order approximation in CFD analysis and particle lag in PIV studies might be expected particularly in complex scenarios such as vortex formation and its interaction with the blade. When calculating the velocity gradients particularly around the blade, amplified levels of noise in the global fieldview. Nguyen and Wells (2006) explained several reasons for this. Some of them are smaller displacements of tracer particles, laser reflections, uncertainties in the velocity vector locations etc...

5.7.2 Vorticity measurements

A lot of information available in the existing literature about the wake formation, vortex dynamics and blade-vortex interaction in the context of Darrieus turbine highlights the importance of unsteady flow physics as the blade travels through the azimuth. The complex wake dynamics resulting from the real flow conditions are not only due to the leading or trailing edge vortex releases from the blade but also their interaction with the blades during their downstream passage. This section presents more details on the observations of vorticity fields around the blade at

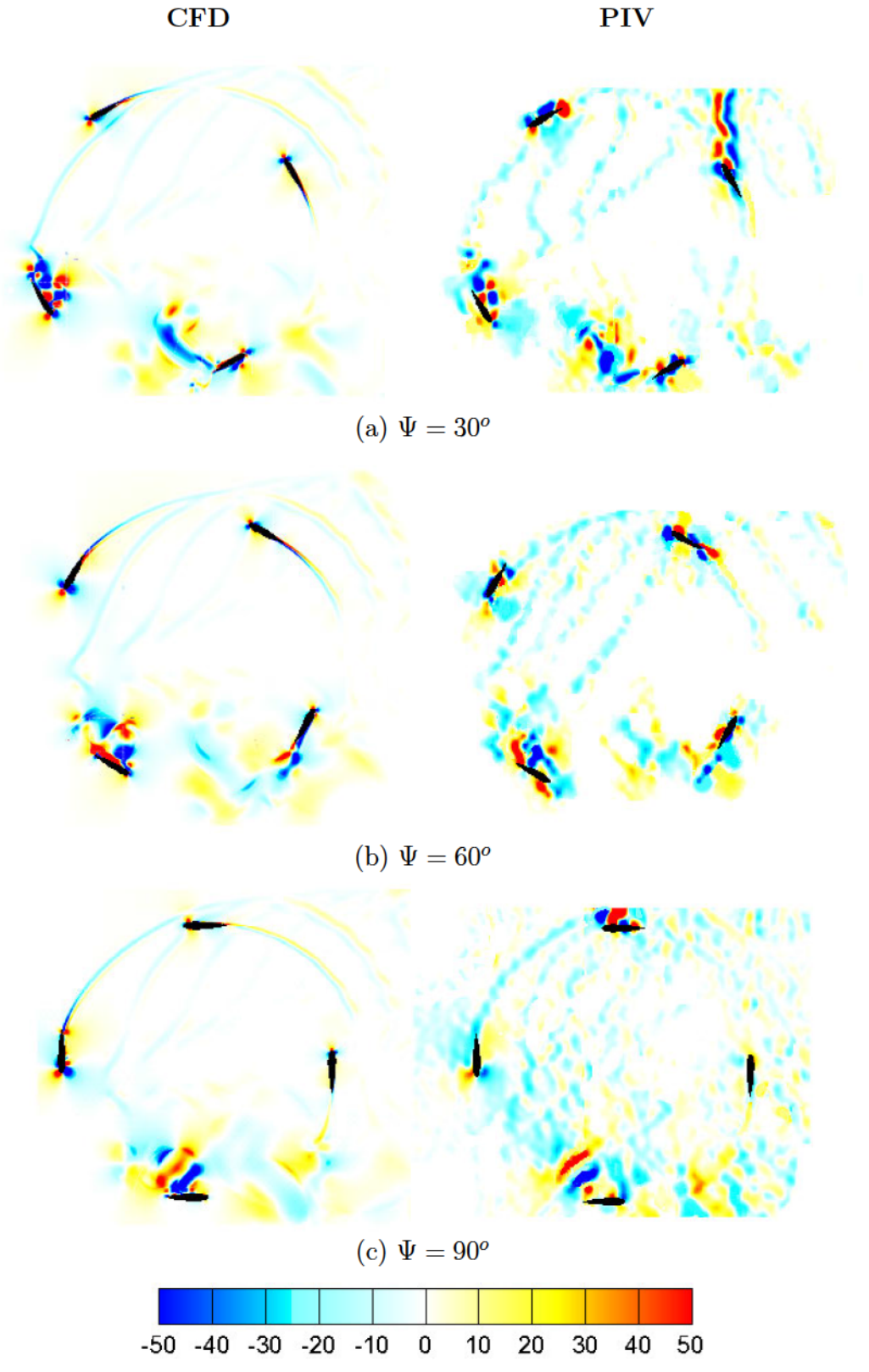

(a) $\Psi = 30^o$

(b) $\Psi = 60^o$

(c) $\Psi = 90^o$

Figure 5.15: CFD and PIV predictions of velocity gradients in flow direction (left to right) at successive azimuth positions for $\lambda = 2$ and $V_0 = 1$ m/s

periodic azimuth positions under different operating conditions.

Figure 5.16 depicts the phase-locked PIV measurements of vorticity magnitude on a concentrated scale (for better visualization) at phase angles of 20-multiples corresponding to respective azimuth positions of the blade through one complete operation cycle at a tip-speed ratio $\lambda = 2$ and free-stream velocity $V_0 = 1m/s$. The flow remains attached to the blade for the azimuth position between 60^o and 100^o. At $\alpha = 120^o$, vortex gets detached from the blade surface on its pressure side, and developed and expanded until $\alpha = 220^o$. Unsteady vortex structures, separation regions and blade-vortex interactions were clearly visualized in the PIV results. During this phase, a relatively low-strength trailing edge vortex was shed at $\alpha = 180^o$. Beyond $\alpha = 240^o$, a progressive reattachment is observed with leading and trailing edge vortices following the downstream fluid motion. Presence of another vortex was found between $\alpha = 0^o$ and $\alpha = 40^o$ that disappeared during $\alpha = 40^o$ to $\alpha = 60^o$. These observations are in comparison with the studies of Nobile et al. (2011), Wang et al. (2010) and Ferreira et al. (2009).

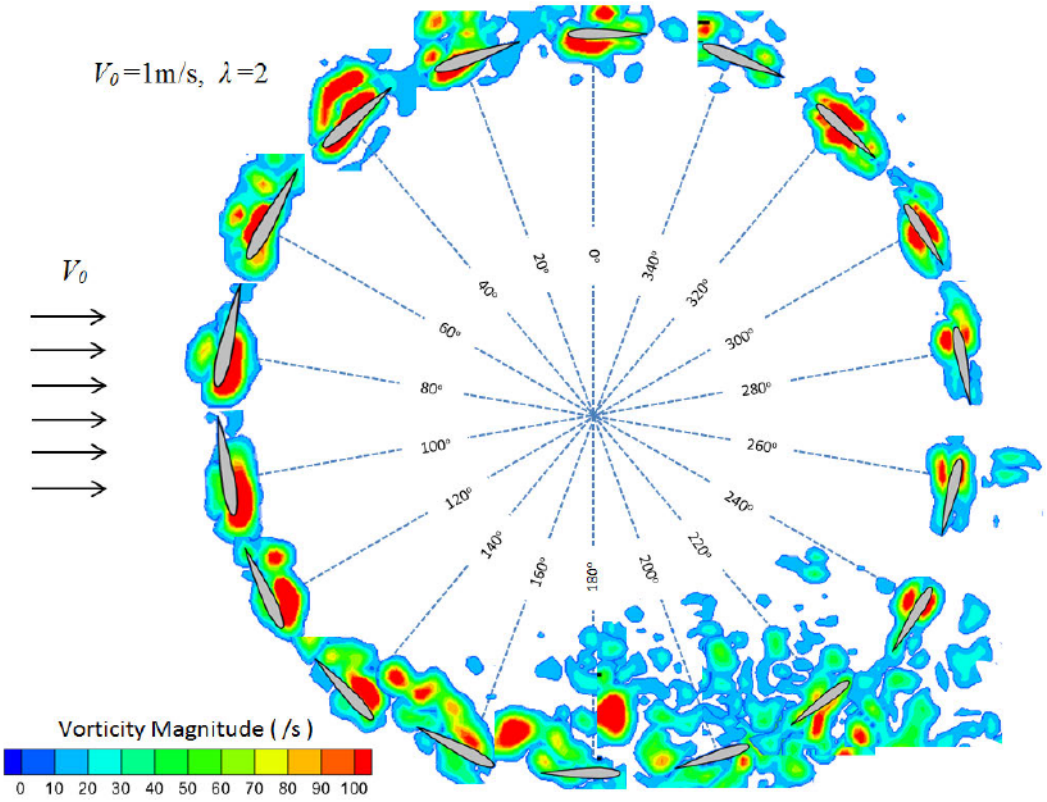

Figure 5.16: Phase-locked measurements of vorticity field around the blade for a complete cycle

Apart from the mechanism of vortex shedding, the present study throws light on another serious consideration, which is blade-vortex interaction. The distur-

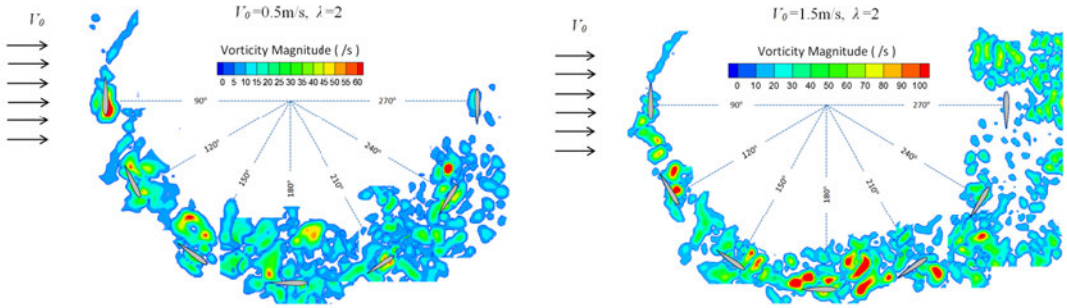

(a) $\lambda = 2$, $V_0 = 0.5m/s$ (b) $\lambda = 2$, $V_0 = 1.5m/s$

Figure 5.17: Vorticity fields around the blade during $\alpha \in [90^o,\ 270^o]$

bances released from the blade during its passage through $\alpha \in [150^o,\ 240^o]$ interact with the following blade as identified in Figure 5.16 for a tip-speed ratio $\lambda = 2$ and $V_0 = 1m/s$. The effect of free-stream velocity V_0 on the formation of vortical structures in terms of their strength, location and motion is illustrated in Figure 5.17. This interaction is not necessarily to be with either leading edge vortex or trailing edge vortex. For instance, in the base case of $V_0 = 1m/s$, the leading edge vortex released at $\alpha = 150^o$ is later interacted by the following blade whereas the trailing edge vortex released in the half past cycle participates in a similar phenomenon. When the turbine rotates at higher speeds, corresponding to larger values of λ, the wake developed by the blade convects downstream relatively slowly while the following blade can quickly catch-up these flow structures and therefore strong blade-vortex interaction will be more likely to generate unsteady vortices. There is a possible impact of blade-vortex interaction on the strength of the vortex developed in the next portion of the cycle and on the global fluid dynamic loading on the blade. The fluid interaction with the vortex shedding from the blade can lead to localized flow perturbations in the blade incidence due to influenced hydrodynamic loading on it. Scheurich et al. (2011) highlighted the disagreement between the experimental and numerical results in the existing literature on rotating devices, which was caused by the insufficient fidelity in modeling the blade-vortex interaction in CFD studies.

Figure 5.18 shows the comparison between computational and experimental predictions of vorticity contours around the blade at every 30^o of azimuth position α, integrated with the torque evolution for one complete cycle when the turbine runs at a tip-speed ratio $\lambda = 2$ and free-stream velocity $V_0 = 0.5m/s$. Roosenboom et al. (2009) experienced the under-prediction of URANS computations compared to PIV studies for the analysis of propeller slipstream due to the relaxed mesh size as well as simplification of flow problem. Unlike this, the present study shows a good comparison between the numerical and computational results. URANS seems to be capable of capturing the larger, but smoother, vortex shedding from

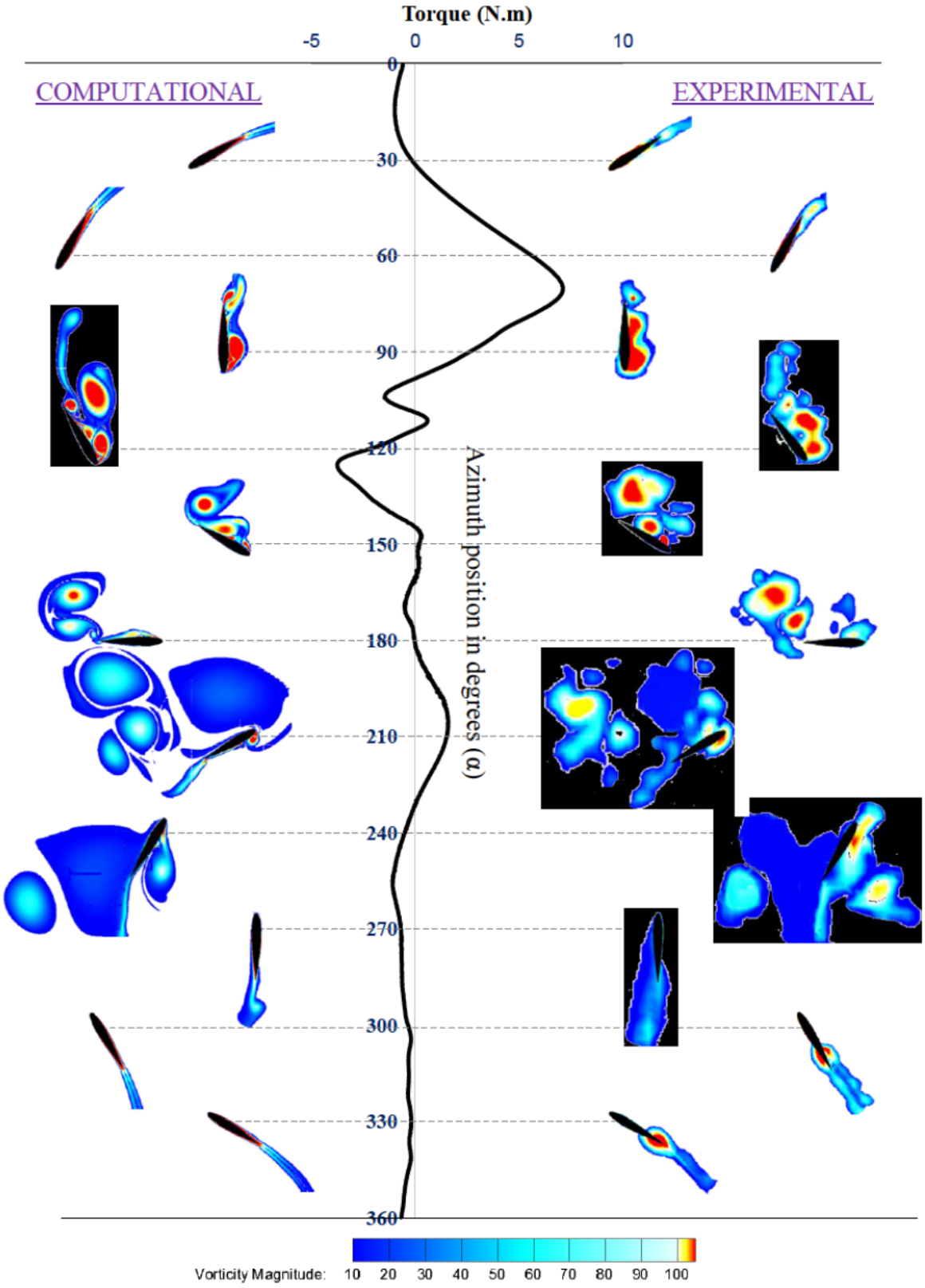

Figure 5.18: CFD and PIV predictions of vorticity fields around the blade at successive azimuth positions, superimposed on torque curve for λ=2 and V_0=0.5m/s

the blade at $\alpha = 120^o$, its downstream motion, and diffusion with time as shown at $\alpha = 210^o$. These observations are consistent with the studies of Sorensen and Michelsen (2004).

It is important to ascertain that, through fluid viscosity, the diffusion process of the vortex generated from the solid boundaries is typically a three-dimensional phenomenon. Since the CFD computations are limited to single-plane studies, the vortex diffusion takes place only in two dimensions. This generally leads to huge and concentrated vorticity structures. URANS modeling however targets not to resolve the Reynolds stress tensor, but to model it. In addition, the strong non-linearities associated with the vortex dynamics during $\alpha \in [120^o,\ 240^o]$ are reflected through small discrepancies between the CFD and PIV results during this interval.

5.7.3 Q-criterion

In order to locate the coherent vorticity patterns in the flow field, The velocity gradient tensor can be used to manifest advanced vortex identification methods. Jeong and Hussain (1995) identified the ways to express the vorticity fields in terms of certain criterion methods such as Q and λ_2, a penetrating insight is provided by Kolar (2007) about using these criteria to describe the location of vortex structures particularly around the solid boundaries and their convection. Such criteria are better than a simple representation of vorticity fields since they are able to differentiate the effects of swirling motion and pure shear in the context of vortex creation. Although the 2D nature of the flow field data generated by PIV studies pose a limitation on the application of Q-criterion, literature supports its relevance for planar calculations. More details about Q-criterion are available in the study of Haller (2005).

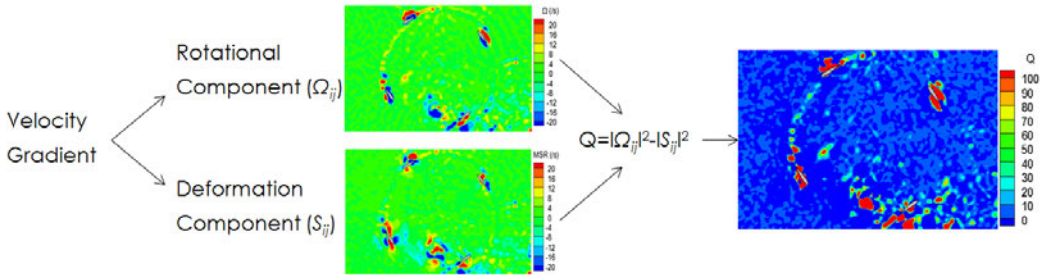

Figure 5.19: Experimental evaluation of Q-criterion for $\lambda = 2$ and $V_0 = 1$ m/s

Mathematically, Q-criterion is the second invariant of the velocity curl (∇V) across the flow field. The pictorial description is provided in the Figure 5.19. When the magnitude of vorticity is larger than that of fluid element strain rate, Q attains the positive values. In that case, if the local pressure is less than the

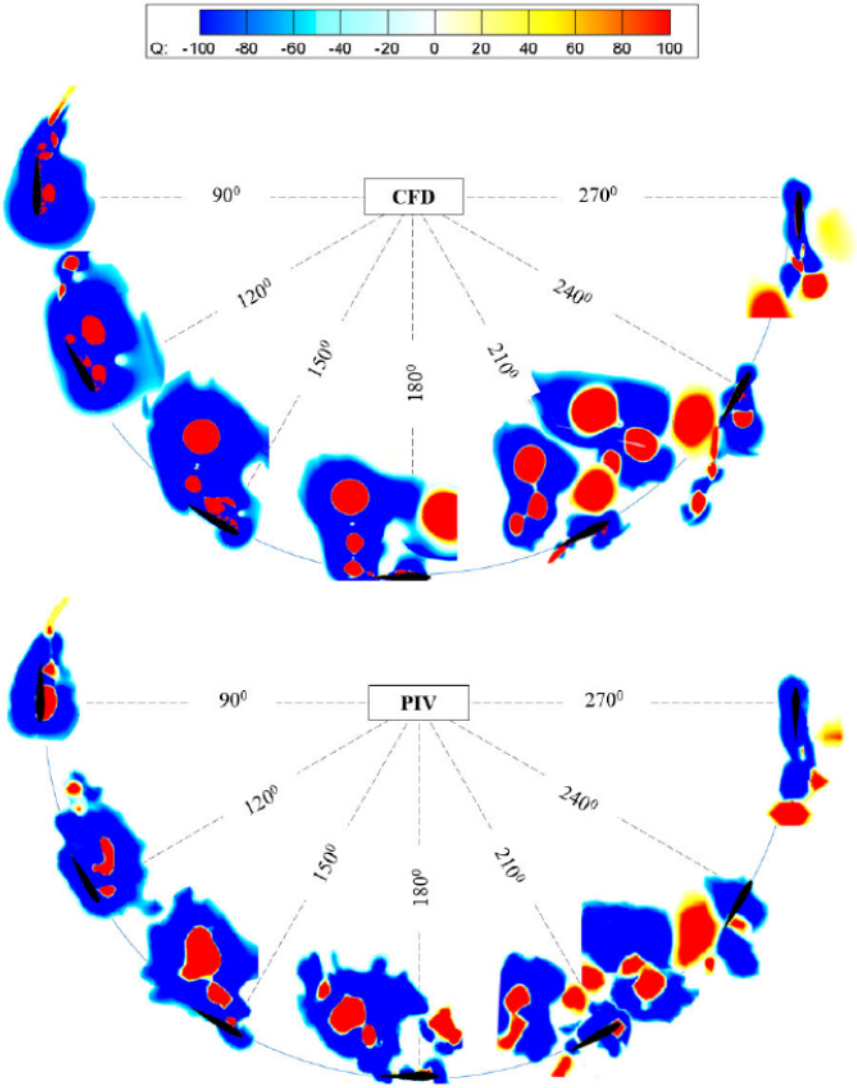

Figure 5.20: Computation of Q-criterion around the blade using CFD (URANS) and PIV (phase-locked) methods for $\lambda = 2$ and $V_0 = 0.5$ m/s

ambient pressure, Q-criterion is said to be satisfied. To illustrate the vorticity distribution in near-blade region, the azimuthal variation of Q-criterion is visualized in Figure 5.20. Good validation of computational results against PIV measurements is achieved. Since the flow dynamics during the bottom half of the cycle are paramount with vortex generation and convection, the discussion here is limited to the blade azimuth position $\alpha \in [90^o,\ 270^o]$. The vortex formed near the upper leading edge of the blade after passing half upstream cycle rolls up and detached from the blade due to stall effect. There is some over-prediction of tip-vortices by CFD, which are comparatively weaker than the leading edge vortices. Also, the computational results missed the skewness attained by the vortex peaks after being detached from the blades and convected downstream. The tip vortices formed

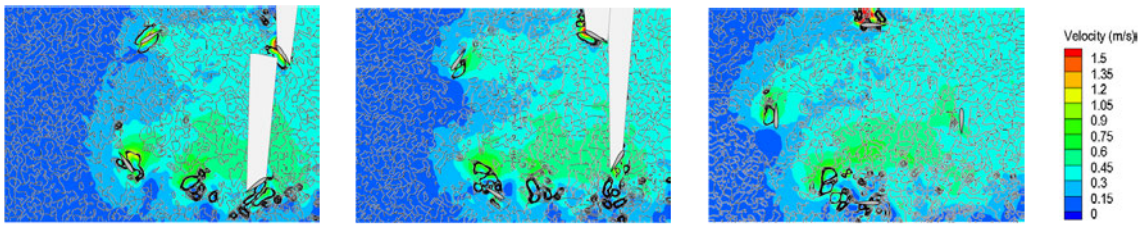

(a) $\Psi = 30^o$ (b) $\Psi = 60^o$ (c) $\Psi = 90^o$

$\lambda = 2$, $V_0 = 0.5m/s$

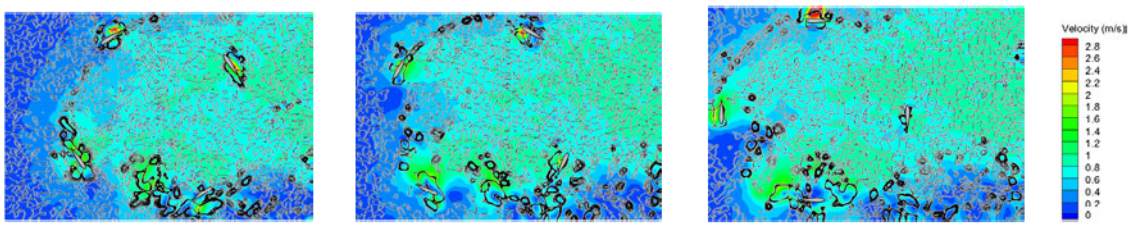

(a) $\Psi = 30^o$ (b) $\Psi = 60^o$ (c) $\Psi = 90^o$

$\lambda = 2$, $V_0 = 1.0m/s$

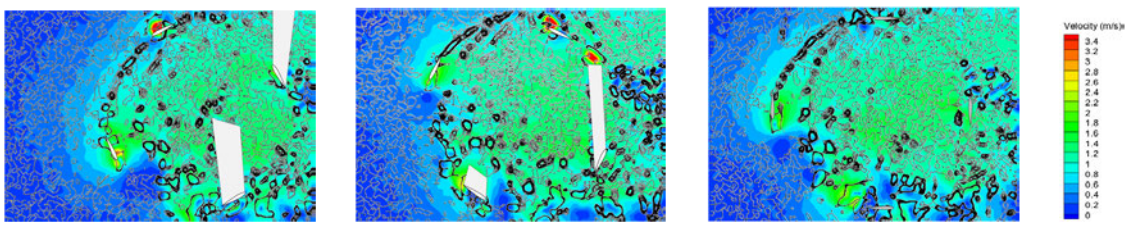

(a) $\Psi = 30^o$ (b) $\Psi = 60^o$ (c) $\Psi = 90^o$

$\lambda = 2$, $V_0 = 1.5m/s$

Figure 5.21: Influence of free-stream velocity on the flow field development. Vorticity isolines for Q=2 are superimposed on velocity contours

at $\alpha = 90^o$ and $\alpha = 270^o$ are relatively weak due to the thrust force at these locations is very small. The Q-criterion reveals that the vortices generated at both leading and trailing edges of the blade seem to be stable within the turbine since no breakdown is observed which imply that the Reynolds stresses inside the blade trajectory are also stable.

Extending these local observations to entire flow field, Figure 5.21 presents the full cycle of turbine's rotation with 30^o phase difference at a tip-speed ratio $\lambda = 2$ and different free-stream velocity V_0. The pictures show the velocity magnitude contours with constant isolines of Q-criterion (=2). Obviously, the complexity in the flow field in terms of unsteadiness increases with increasing V_0. The vorticity

streaks leaving the trailing edge of the blade confer the exact trajectory of the blade during the early portion of the upstream cycle whereas the streaks during the lower portion of the cycle are disturbed and form local peaks. The vortices shed unsteadily are likely to follow the free-stream and convect downstream.

5.8 Conclusion

This chapter has presented the experimental methodology involving apparatus and processes to characterize the low Reynolds number flow around the Darrieus water turbine. The complexity of the entire set-up due to the incorporation of synchronization between different mechanical and PIV systems was discussed in detail. In a nut-shell, advanced methods were used in the standard PIV technique to enhance the fidelity. This experimental study mainly contributes to the present research in two ways.

- *The performance investigation in terms of quantitative measurements such as torque and coefficient of power COP:* These parameters largely dependent on the operation conditions, which was seen in Chapter 4, a parametric experimental study was performed to validate the numerical results. The 2D CFD results and 3D experimental finds of power characteristics were compared by taking the blockage effects into account. The operating region of a low-velocity and high-solidity Darrieus turbine as explored through numerical study is thus compared with the experimental results in this chapter. As COP curve is concerned, there is a good comparison between the two investigation methods at lower λ. The inconsistency however arises at $\lambda > 2$ and the reasons were explained.

- *The qualitative analysis of Darrieus turbine through the flow field observation around the blade as well as across the turbine using PIV set-up:* The experimental evaluation flow field was committed to precise characterization of the whole system to realize anticipated instantaneous phase-locked measurements for every 10^o of turbine's phase angle without compromising on the usual errors that occur in the PIV studies. Starting with the general field observations of velocity and vorticity contours across the turbine at different azimuth positions, the importance of measuring the velocity gradients was identified. The velocity gradient was calculated from the spatial differentiation of velocity field. In order to achieve the global objective of vortex control in this research, a close examination of vorticity distribution is required, which was realized by the instantaneous measurements of vorticity magnitude. The coherent vortex structures within the flow field were identified using the Q-criterion, which was calculated from the 2nd invariant of velocity curl.

There achieved a good comparison between the computational and experimental studies for all of the flow field parameters mentioned above. This draws a conclusion that the numerical methodology adapted in this research can be safely applied to investigate the effectiveness of pitching. Also, the conceptual knowledge gained through the evaluation of vortex dynamics in the present and previous chapters allow assessing if the application of Couchet theory would be efficient in controlling the vortex shedding from the blades. Inclusive investigation in this regard is presented in Chapter 6.

CHAPTER 6

PITCHING BLADE MODEL: COMPUTATIONAL ANALYSIS

Contents

6.1 Introduction

In addition to conventional studies about the vertical axis water turbine of Darrieus type using CFD and PIV methods, a systematic set of computational studies were carried out to investigate the influence of dynamically pitching blades on the turbine's performance. The kinematics of the blade pitching motion, which was discussed in Chapter 3, were numerically applied and tested on classical turbine

model. Before illustrating these results, the computational methodology adapted to serve the analysis of the pitching motion of the blades is detailed in the next section. The effectiveness of the pitching blades under constant circulation framework was assessed in both quantitative and qualitative terms, and compared with the performance of the classical Darrieus turbine. The benefits and disadvantages of the formulation of constant circulation were identified which led to improvement in the system by subjecting the blades to variable circulation. Not only the base work of this formulation and its influence on the device performance is described, but the sensitivity of the pitching regime transition is quantified in this chapter. These discussions form the basis to develop a VAWT prototype with pitching blades for the first demonstrator and its kinematics are provided at the end of this chapter.

6.2 Constant circulation imparted to the blades

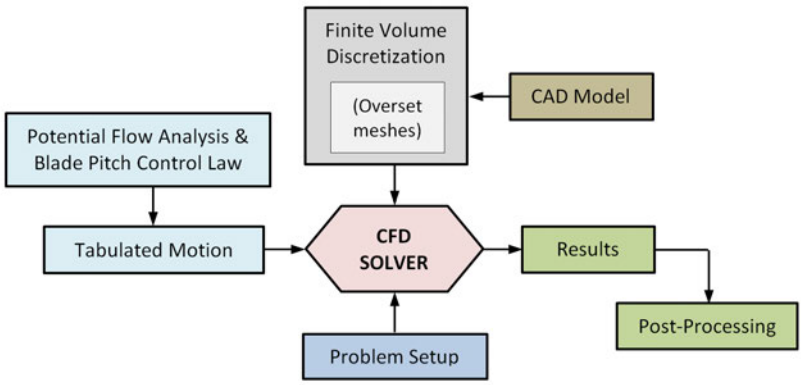

Figure 6.1: Process flow chart of CFD simulations for multiple motions in the computational domain

Desired evolution of flow structures around the blade during the turbine's rotation is possible by imposing a pitch to the profile with respect to free-stream flow direction by means of the control law given in Equation 3.7. This section presents the application of various equivalent angles of the blade's relative incidence. This differential equation is used to tabulate the blade's incidence at discrete azimuth positions for a complete rotation of the turbine. The motion data is then applied to each blade during the simulation. The schematic process flow chart of the numerical computations is presented in Figure 6.1.

For a tip-speed ratio λ ranging from 1.5 to 3.5, Figure 6.2 shows the blade orientation and corresponding variation of blade incidence θ at different azimuth angles α for β values of $+10^o$, $+5^o$ and -5^o in the first and second rows respectively. The third row shows the corresponding torque evolution of one blade through a single rotation for the studied values of λ.

6.2.1 Torque extraction

Recalling the Equation 3.49, for $\lambda \to \infty$ the blades get a fixed pitching orientation. A further quantitative analysis based on the torque measurements is shown in Figure 6.2, which shows the instantaneous torque T produced by a single blade as it moves through the azimuth. The effect of imposing a constant circulation to the blades is strongly demonstrated by the smooth and even-fashioned evolution of the instantaneous torque compared to the classical Darrieus case with fixed blades. It is important to notice that the blade provides a positive torque and hence becomes propulsive during the first half of the cycle for positive values of β, but loses power to the flow during the second half of the cycle as it operates in the reverse position and larger incidence. Since the circulation is preserved throughout the cycle, the resulting tangential force acts only in one direction, i.e. downwards, throughout the cycle. This makes the front half of the cycle propulsive and rear half of the cycle losing power to flow. The viscous drag on top of this phenomenon causes additional power loss. The overall effect of constant circulation around the blades is therefore that the power loss during one complete rotation is either equal or more than the extracted power. This leads to negative power coefficients that would not be of any practical interest. This goes much worse as the tip-speed ratio λ increases. For negative β (here -5^o), power is lost during the first half of the cycle, but not recovered in the second half as dynamic stall is observed. However, the blade's performance during the second half of the cycle is comparatively better than for positive β values.

6.2.2 Flow field evolution

Compared to Figure 4.12 corresponding to the fixed-blade design, the fluctuations in the normalized velocity components in X- and Y-directions have shrunk when the blade is given a certain pitching, which are presented in Figure 6.3. Except at $X = \pm R$ away from the rotor centre on horizontal line, these velocity components remain almost quiet. Particularly with positive values of β, the linearity in the velocity has greatly increased in the downstream region which was highly jagged with fixed blades. This implies a more uniform flow structure in the domain. On the other hand, in the case of $\beta = -5^o$, there is a little extra oscillation which is still less than the fixed blade model. In addition to this information, it is pointed out that $\beta = +5^o$ provides a much more stable flow, while $+10^o$ and -5^o impose the feasible extreme values for β. This analysis is supplemented by the characteristic streamlines superimposed on the pressure coefficient as shown in Figure 6.4. Unlike the disturbed streamline pattern around the turbine with fixed blades, depicted in Figure 4.14, the streamlines orient themselves around the blades in an orderly manner. Also, it is observed that the time integrated markers in case of fixed blades are quite irregular, while the pitching blades are

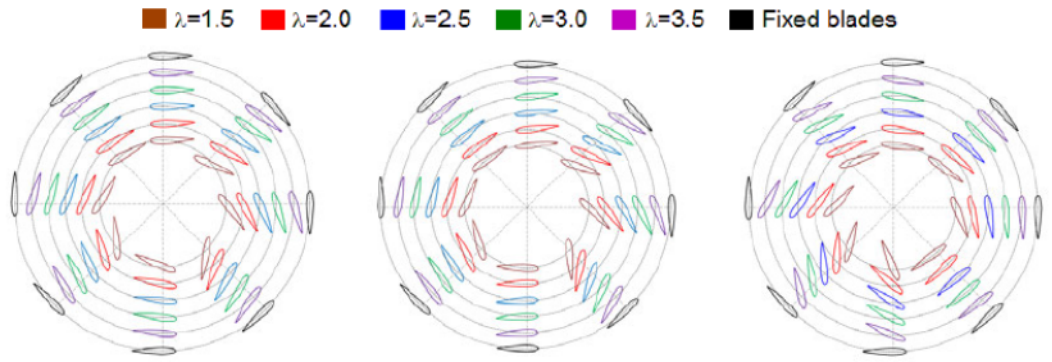

(a) $\beta = +10^o$ (b) $\beta = +5^o$ (c) $\beta = -5^o$

Blade orientation with the free-stream coming from left for different pitch-control regimes in comparison with classical Darrieus blade

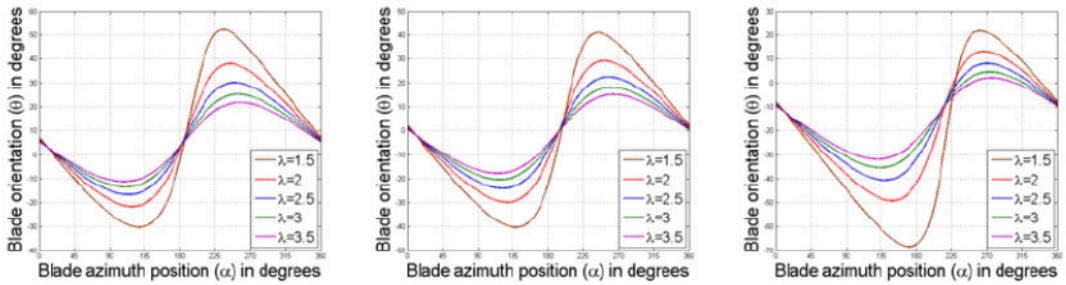

(a) $\beta = +10^o$ (b) $\beta = +5^o$ (c) $\beta = -5^o$

Local incidence of the blade θ as a function of its azimuth position α

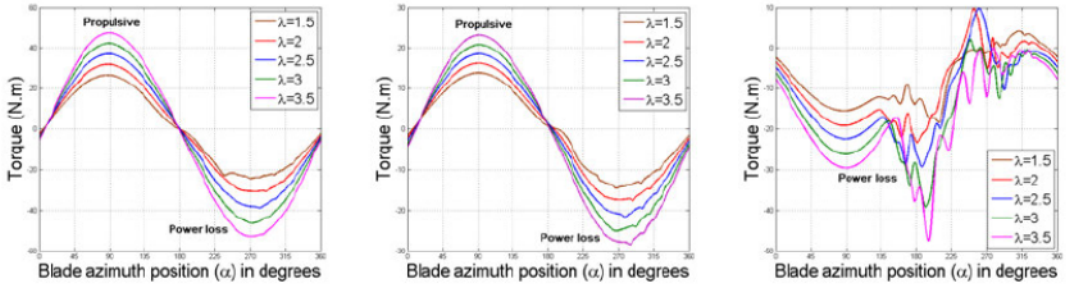

(a) $\beta = +10^o$ (b) $\beta = +5^o$ (c) $\beta = -5^o$

Torque evolution of one blade over a cycle

Figure 6.2: Comparison of different blade pitch regimes in terms of blade orientation (top row), blade incidence (2nd row) and calculated torque for one cycle (3rd row)

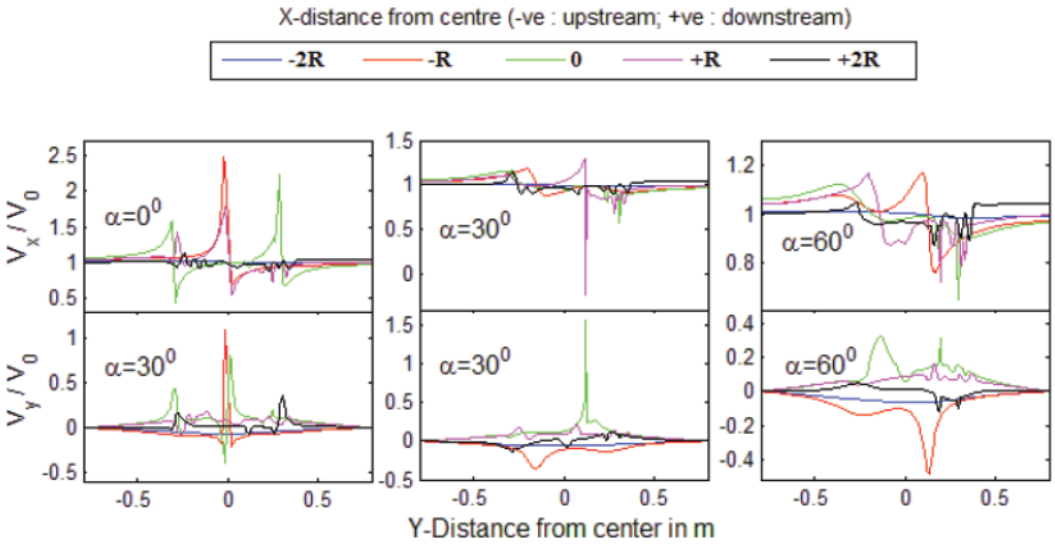

$\beta = +10^o$

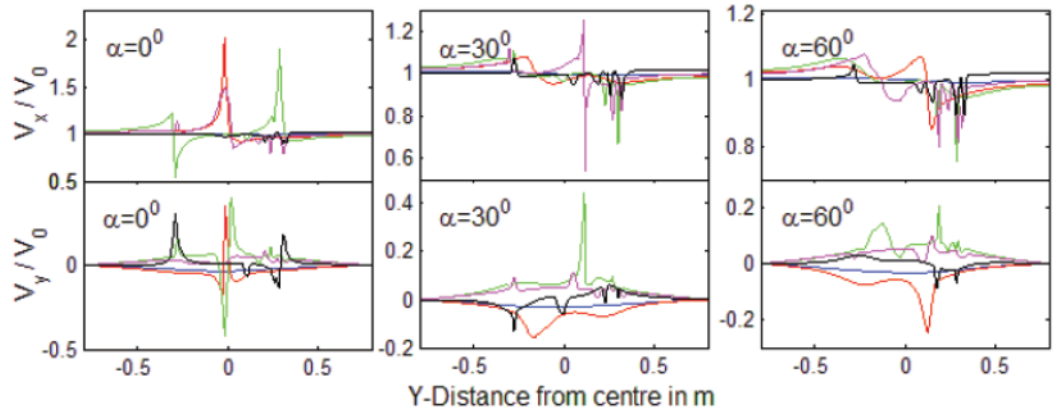

$\beta = +5^o$

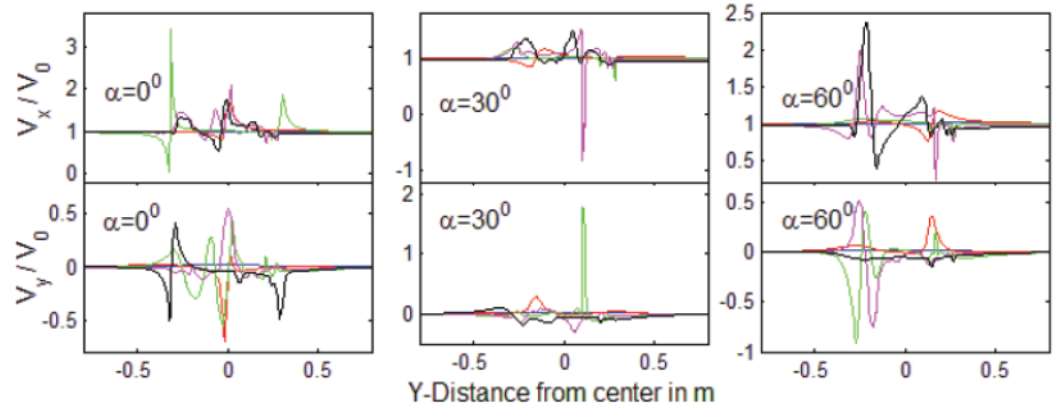

$\beta = -5^o$

Figure 6.3: Velocity components in their normal directions at various distances from the rotor's centre with different blade pitching laws

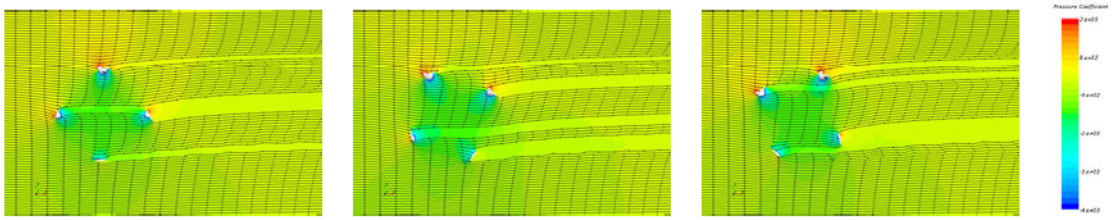

(a) $\Psi = 0^o$ (b) $\Psi = 30^o$ (c) $\Psi = 60^o$

Pitching blades corresponding to $\beta = +10^o$

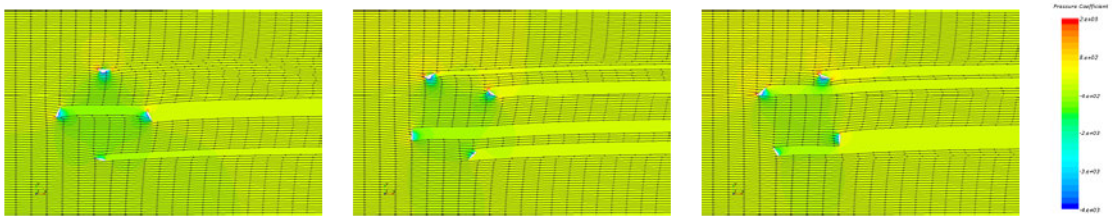

(a) $\Psi = 0^o$ (b) $\Psi = 30^o$ (c) $\Psi = 60^o$

Pitching blades corresponding to $\beta = +5^o$

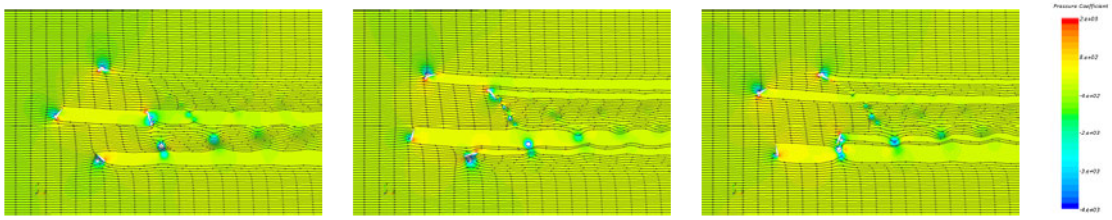

(a) $\Psi = 0^o$ (b) $\Psi = 30^o$ (c) $\Psi = 60^o$

Pitching blades corresponding to $\beta = -5^o$

Figure 6.4: Flow fields presented by pressure coefficient with superimposed streamlines across the Darrieus turbine with pitching blades at same operating conditions of λ=2 and V_0=1m/s at different global azimuth positions Ψ

characterized by evenly spaced markers. Such systematic patterns of streamlines attract to employ multiple turbines in arrays due to the absence of chaotic wake.

6.2.3 Vorticity field around the pitching blade

The vorticity contours in Figure 6.5 correspond to the tip-speed ratio $\lambda = 2$ and similar trends were observed for other values of λ for a given circulation (or β). When $\beta = +5^o$, even for large values of α, the angle of incidence is comparatively lower and therefore the flow is completely attached to the blade and the flow field remains vorticity free. On the other hand, the limiting cases of β equal to $+10^o$ and -5^o slightly missed the credibility of completely arresting the vortex shedding from the blades. Particularly, a turbine operating with a constant blade circulation

with $\beta = -5^o$ produces comparatively stronger vortices shed from each blade as they follow a streamwise motion. In this case, the vortex zone begins to appear for α approaching 150^o and shedding occurs around $\alpha = 200^o$. It is also observed that the extension of the wake zone strongly depends on the angle of incidence of the blade. Interestingly, there is no noticeable interaction between the blades and the vortices shed by preceding blades in any of these 3 cases.

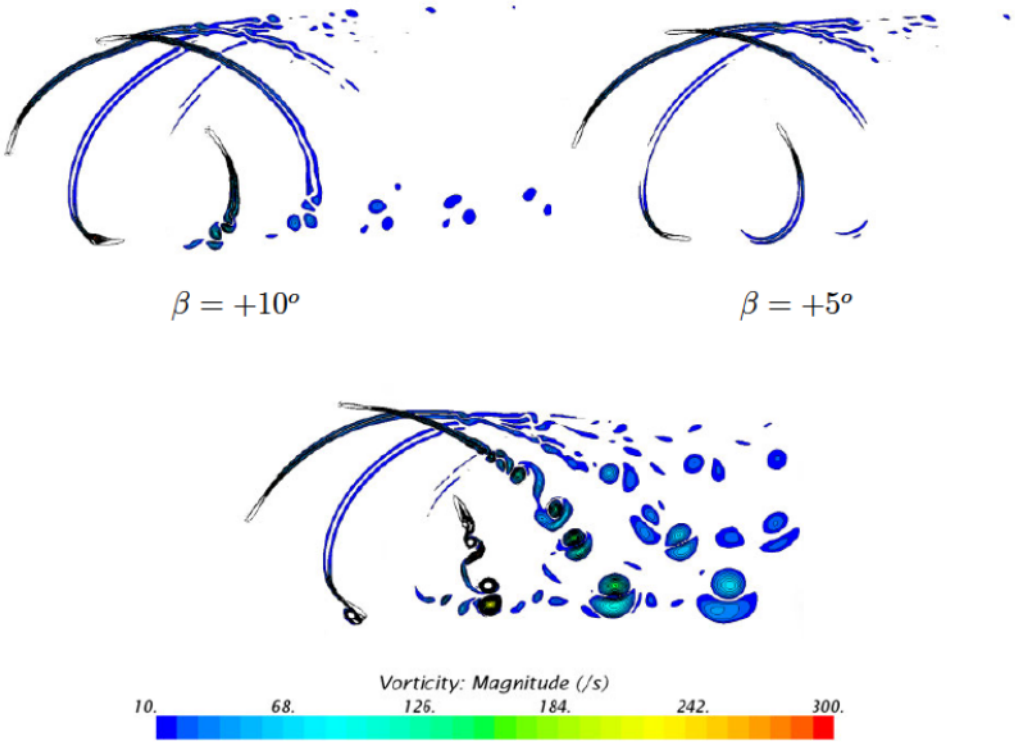

Figure 6.5: Vorticity fields obtained for $\beta = +10^o$, $+5^o$ and -5^o, illustrating the efficiency and limits of the associated vortex shedding control

6.2.4 Comparison between analytical and computational results

Figure 6.6 shows the comparison of analytical results against the CFD computations for the histories of tangential and normal forces acting on the blade throughout its azimuthal travel. When looking at them as functions of the tip-speed ratio λ, the quantified differences between both the approaches are justified by the application of viscous effects and no-slip boundary conditions. From these plots, three points are made clear: firstly, the discrepancy between the two approaches for the tangential force is more evident during the front half of the blade's rotation. This is partly because the drag is not taken into account in the potential flow formulation. Next, the evolution of the tangential force using CFD is such

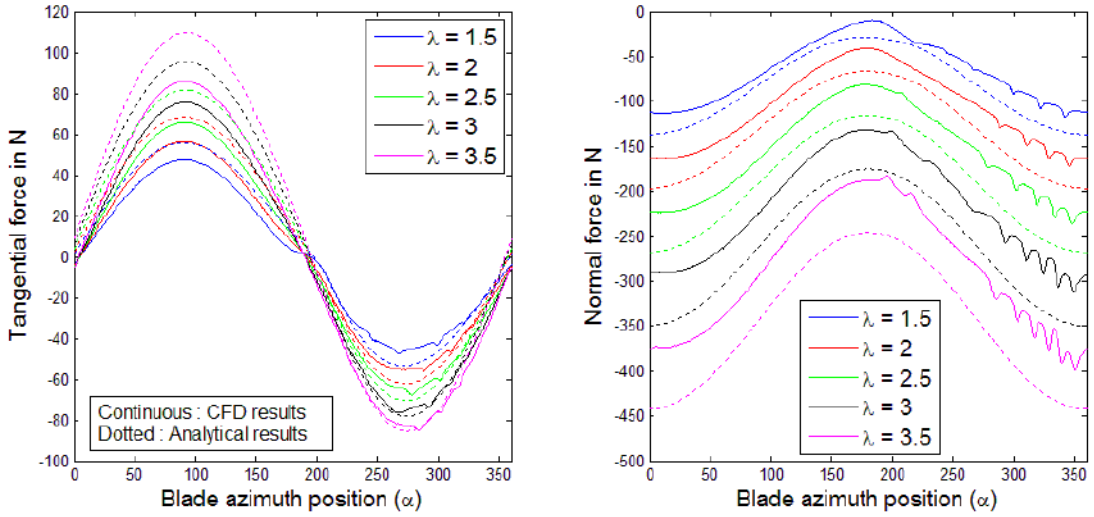

(a) (b)

Dependence of tangential (left) and normal (right) forces on the tip-speed ratio λ for a pitching blade following the control law with $\beta = +5^o$

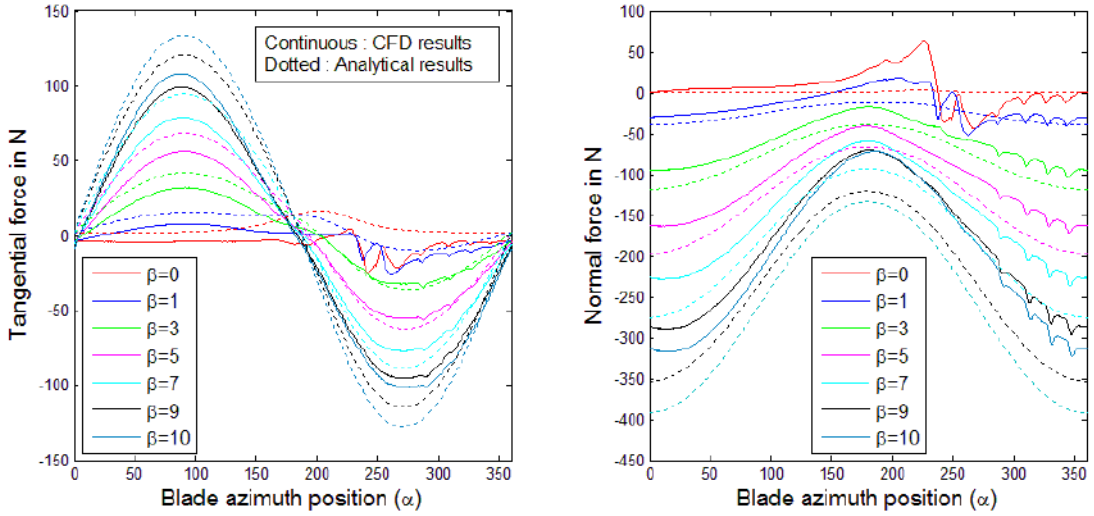

(c) (d)

Dependence of tangential (left) and normal (right) forces on the circulation around the pitching blade for λ=2

Figure 6.6: Comparison of the analytical results (dotted lines) and CFD predictions (continuous) for force coefficients acting on the pitching blade following the control law with $\beta = +5^o$ for a free-stream velocity $V_0 = 1$ m/s

that the curve becomes more anti-symmetrical as the tip-speed ratio λ increases. Finally, the discrepancy between CFD and theory is exacerbated by the increased

tip-speed ratio λ for tangential as well as normal force evolution.

On the other hand, there is a considerable influence of imposed circulation Γ (or β) to the blade on the evolution of tangential and normal forces. Good comparison between the theoretical and computational results are observed for $\beta = +10^o$ and $+5^o$ while there is a discrepancy between the two approaches for $\beta = 0^o$ or less. Although the tangential force calculation is very much similar by both the approaches approximately until $\alpha = 150^o$ for $\beta = -5^o$, the stalling phenomenon and vortex shedding process deviate the CFD solution from theoretical analysis thereafter. From the tangential force curves, it is clear that $\beta = +10^o$ is the most beneficial for the front half of the cycle while $\beta = -5^o$ for the rear half. Although $\beta = 0^o$ is a consideration for rear half of the cycle, this study proceeds further with $\beta = -5^o$. Therefore, within the stringent limitations on the imposed circulation, the idea is to combine the solutions of the best performance for the front half of the cycle and least detrimental for the rear half.

6.2.5 Fixed blade vesrus pitching blade

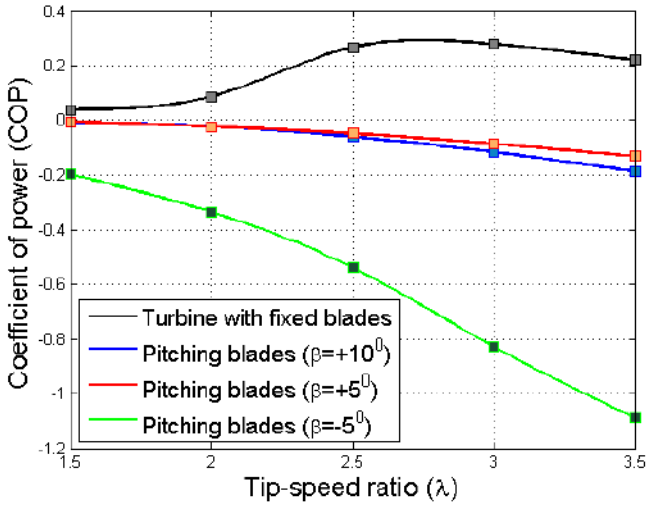

Figure 6.7: Comparison between fixed and pitching blades for COP

Having understood the operating principle of a pitching VAWT, it would be interesting to compare it to a fixed-blade VAWT and also try to quantify the differences in performance characteristics. Although the idea of blade pitching is successful in suppressing the vortex shedding, blade-vortex interaction, and creating a smoother flow across the turbine, the power characteristics are however deteriorated compared to the fixed-blade design. Figure 6.7 shows the difference between the corrected coefficient of power COP (refer Equation to 4.29) obtained from pitching blades and that from fixed blades. Even though the torque measurements from experimental studies of classical Darrieus turbine with fixed blades

are consistent with the CFD results, the present study is confined to only the numerical analysis for the purpose of validating the analytical methods developed in Chapter 3.

6.3 Variable circulation imparted to the blades

As understood so far, the success of controlling the vortex shedding from the Darrieus turbine with pitching blades at any given tip-speed ratio λ results in power lost to the fluid flow due to the blades subject to large negative incidences for more than half of the operation cycle. One way to improve the propulsive characteristics of the device without losing the emphasis on the vorticity distribution is to apply a blade pitching based on two different values of the circulation during the cycle. As noticed in Figure 6.2, the first half of the cycle is propulsive while the rear half is equally losing the power for β equal to $+5^o$ and $+10^o$. On the other hand, the rear half of the cycle for $\beta = -5^o$ is losing less power when compared to positive values of β. An efficient merge of the blade's incidence corresponding to β equal to $+10^o$ or $+5^o$ in the front half of the cycle and -5^o in the rear half of the cycle can result in a fully propulsive cycle. The key issues here are:

- The optimal location of the transition points on the $\theta - \alpha$ profile, in order to maximize the power output. These points were identified by careful examination of instantaneous torque plots in Figure 6.2. The transition is needed between the point where the torque profile switches from positive to negative or vice versa. Therefore, each cycle is normally subject to appropriate transition twice.

- Transition scheme used to switch from one value of β to the other must avoid massive vortex shedding. Various transition methods including sinusoidal, horizontal, polynomial fit etc ... were checked. Figure 6.8 depicts the horizontal and polynomial transition schemes.

The three transition laws analysed in this study are,

Law 1 β equal to $+10^o$ for the front half of the cycle followed by β equal to -5 for the rear half with a set of transition points P_1 for λ=[1.5, 3.5]

Law 2 β equal to $+5^o$ for the front half of the cycle followed by β equal to -5^o for the rear half with a set of transition points P_2 for λ=[1.5, 3.5]

Law 3 β equal to $+5^o$ for the front half of the cycle followed by β equal to -5^o for the rear half with a set of transition points P_1 for λ =[1.5, 3.5]

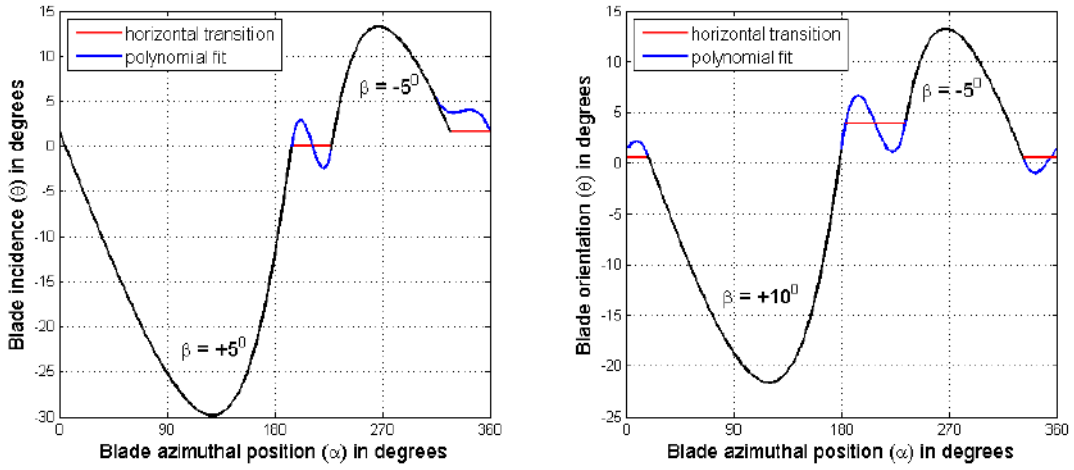

(a) (b)

Figure 6.8: $\theta - \alpha$ relationship for horizontal and polynomial transition schemes

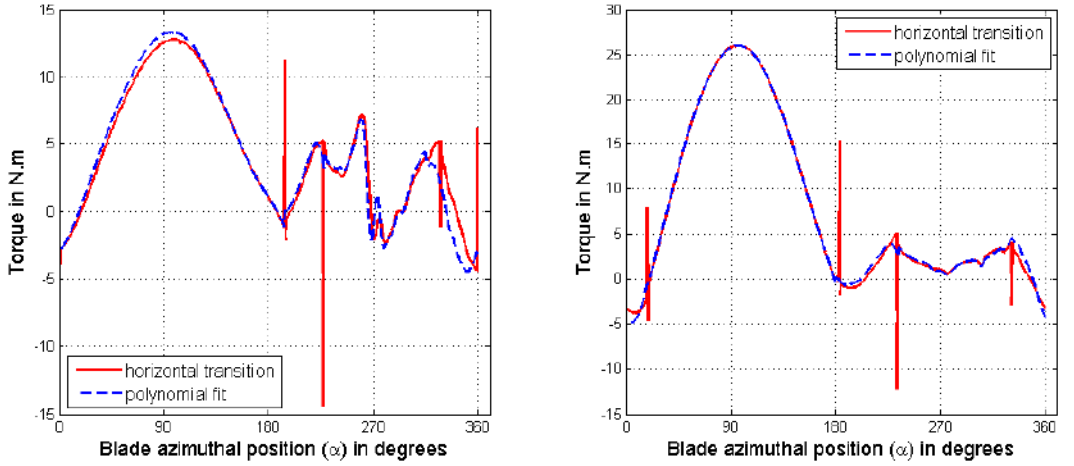

(a) (b)

Figure 6.9: Comparison of horizontal and polynomial transition fit for torque evolution

Figure 6.9 shows the numerical instability and resulting peaks in the torque curves when the horizontal connection between the two pitching regimes is made. For a smooth transition, a polynomial interpolation fitted on the slopes of $\theta - \alpha$ profiles is used.

6.3.1 Torque enhancement

The blade orientation, corresponding plots of blade incidence θ against azimuth position α highlighting the transition part, and instantaneous torque measurements using CFD analysis are furnished in Figure 6.10. It is clear from the torque

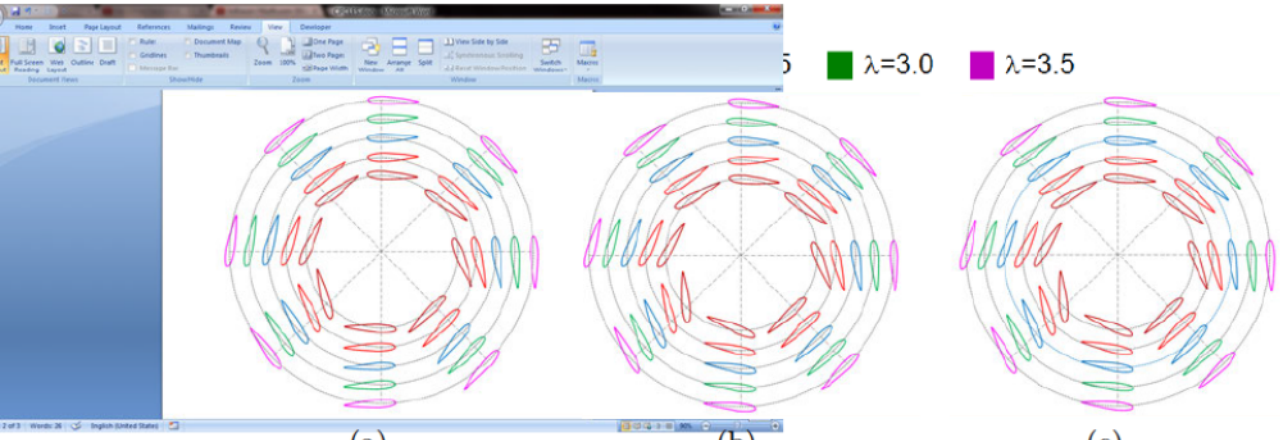

(a) (b) (c)

Blade orientation with the free-stream coming from left to right for different pitch-control regimes.

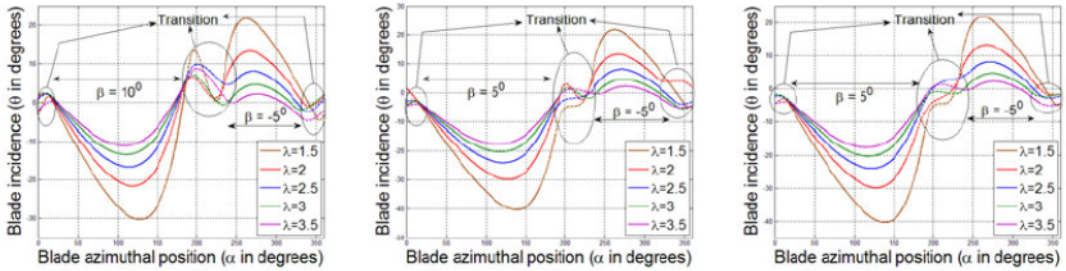

(a) (b) (c)

Local incidence of the blade (θ) as a function of its azimuth position (α)

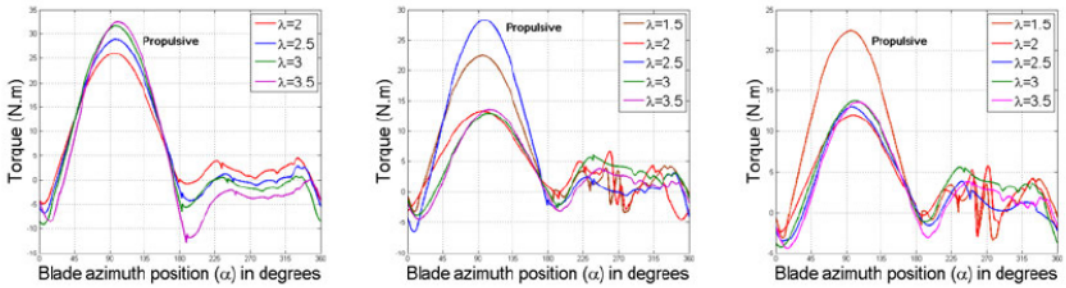

(a) (b) (c)

Torque evolution of one blade over a cycle

Figure 6.10: Comparison of different blade pitch regimes in terms of blade orientation (top row), corresponding plot for a complete rotation (2nd row) and calculated torque for one cycle (3rd row). (a) $\beta = +10^o \rightarrow -5^o$ (b) $\beta = +5^o \rightarrow -5^o$ and (c) $\beta = +5^o \rightarrow -5^o$ with transition points of $\beta = +10^o \rightarrow -5^o$

evolution plots that the blade pitching with variable circulation has successfully improved the overall power output by eliminating the blade stall in the rear part of the cycle thereby reducing the amount of power lost to the fluid flow. In addition, the second transition ($\beta = +5^o \rightarrow -5^o$) has a small adverse effect on the front part of the cycle where the peak of propulsive characteristic has slightly fallen down compared to that of the classical Darrieus turbine with fixed blades.

6.3.2 Flow field analysis

Typical velocity deficit profiles at different horizontal locations for the turbine with variable circulation imparted to the blades are shown in Figure 6.11. Comparing to similar plots as shown in Figures 4.12 and 6.3 for fixed blade model and pitching blade turbine with constant circulation around the blades respectively, the rather vivid impact of variable circulation framework on the distributions of the normalized velocity components is clearly seen. The distribution of normalized velocity components V_x/V_0 and V_y/V_0 is relatively invariant at $2R$ upstream. Compared to the fixed blade design, there is a clear reduction in the streamwise as well as lateral velocity perturbations with the blades subject to variable circulation. Besides the increased overall uniformity in the velocity component distribution compared to the case of flow across a conventional Drarieus turbine, the key difference lies in the location of peak velocities. For instance, at $\Psi = 30^o$, the peak of streamwise velocity component V_x/V_0 was at the centre of the turbine in case of fixed blade model, whereas it is at R downstream in case of variable circulation framework. The largest variations in the velocity components are mostly located at R downstream. Another key observation is the lateral perturbation velocity distribution which is quite variable with $\beta = +5^o \rightarrow -5^o$ compared to any other design. These variations cyclically vary, increasing from $\Psi = 0^o$ to $\Psi = 60^o$ and then decreasing. Compared to the two β formulations, the distribution of V_x/V_0 in the case of $\beta = +10^o \rightarrow -5^o$ is lower than that in the case of $\beta = +5^o \rightarrow -5^o$.

Figure 6.12 shows the entire flow fields for the Darrieus turbine with pitching blades subjected to variable circulation. The stream tube expansion is not significant here, when compared to that with fixed blades. It is important to note that the flow remains essentially unperturbed compared to the fixed blades case.

6.3.3 Vorticity field around the variable pitching blades

The effectiveness of the proposed transition laws is compared through the vorticity contours at the same scale in Figure 6.13 for a tip-speed ratio $\lambda = 2$ and free-stream velocity $V_0 = 1$ m/s in suppressing the severe vortex shedding from the blades and thus avoiding any possible blade-vortex interaction. Although the transition of β from $+10^o$ to -5^o is comparatively better than that from $+5^o$ to -5^o, both laws perform similarly well in controlling the drastic sheds of vortex observed with the

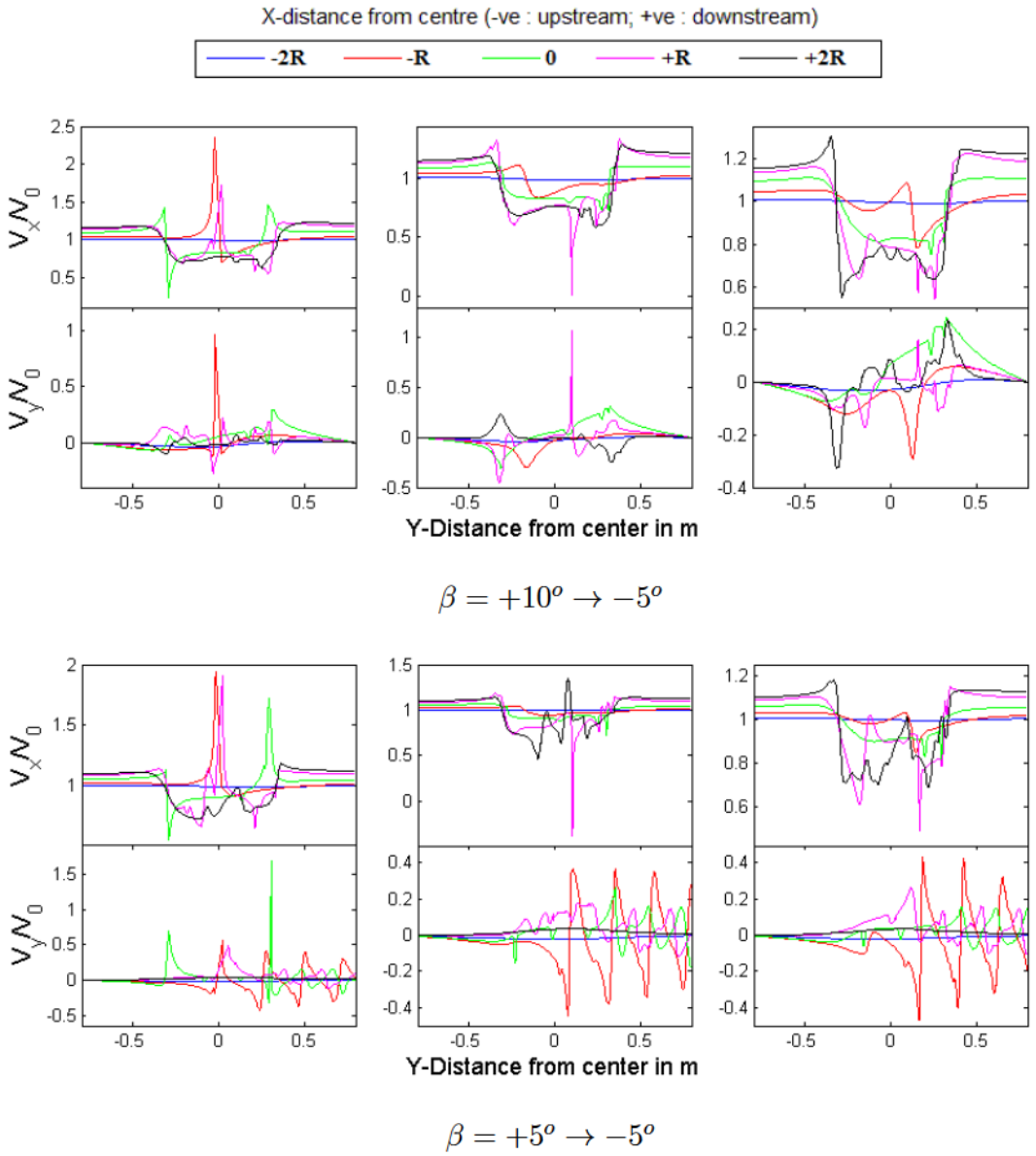

Figure 6.11: Velocity components in their normal directions at various distances from the rotor's centre with different blade pitching laws

fixed blades. In spite of localized vortex shedding that generate little spots of vorticity from the variable pitching blades due to the transition from one regime to the other, there is no blade-vortex interaction as only two regular vortex alleys are shed.

6.3.4 Analysis of Coefficient of Power COP

In order to assess the overall effect of the variable blade pitching concept, the corrected coefficient of power is plotted in Figure 6.14 for all of the transition

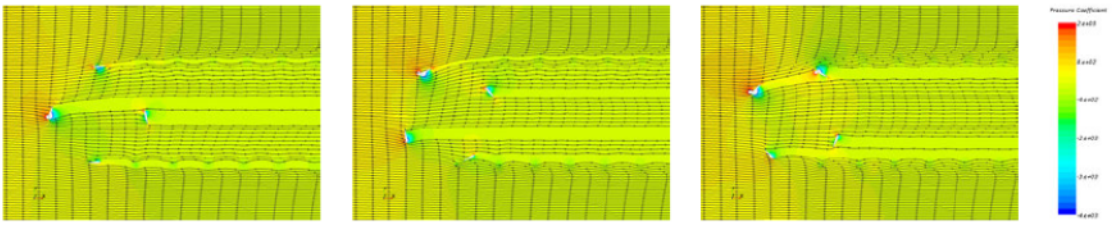

(a) $\Psi = 0^o$ (b) $\Psi = 30^o$ (c) $\Psi = 60^o$

Turbine with pitching blades following $\beta = +10^o \rightarrow -5^o$

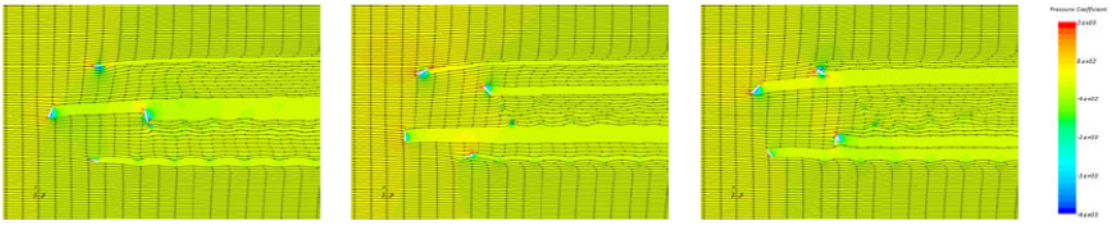

(a) $\Psi = 0^o$ (b) $\Psi = 30^o$ (c) $\Psi = 60^o$

Turbine with pitching blades following $\beta = +5^o \rightarrow -5^o$

Figure 6.12: Pressure coefficient distribution with streamlines superimposed of variable pitching blades at operating conditions of $\lambda = 2$ and $V_0 = 1$ m/s at different azimuth positions Ψ

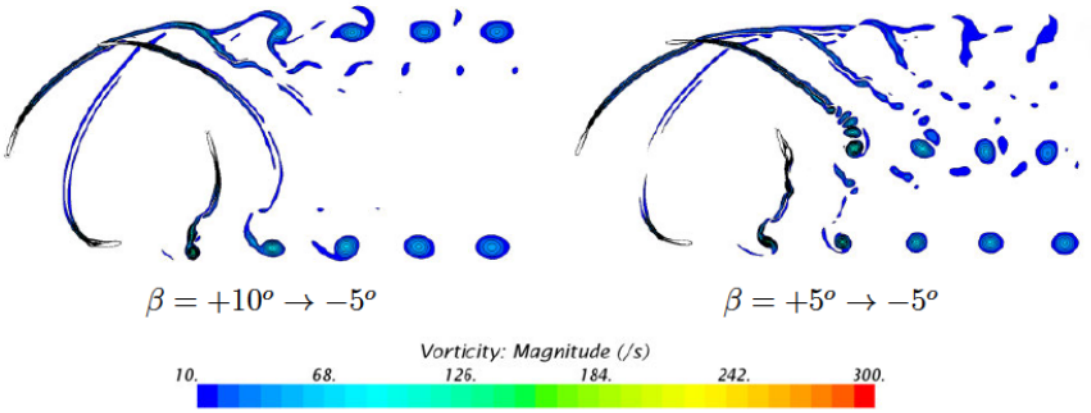

$\beta = +10^o \rightarrow -5^o$ $\beta = +5^o \rightarrow -5^o$

Figure 6.13: Vorticity fields of the turbine with variable blade pitching

cases. Compared to the classical Darrieus turbine with fixed blades shown in Figure 4.9(b), more than 100% gain in the performance for tip-speed ratios λ=1.5 and λ=2 is evident with the transition $\beta = +10^o \rightarrow -5^o$. Another important conclusion is that the optimal tip-speed ratio λ_{opt} with this transition is 3 while the case of fixed blades provides $\lambda_{opt} = 2.5$.

With the transition $\beta = +5^o \rightarrow -5^o$, the COP is increased for more than 250% compared to the fixed blade design for a tip speed ratio $\lambda = 1.5$. Thereafter, both

the designs follow the same trend until the optimum tip speed ratio λ_{opt}= 2.5 is reached. The performance of this transition for λ beyond the optimum value is inferior to the classical case with fixed blades. Comparatively, the transition case of β from $+5^o$ to -5^o using the same transition points of Law 1 i.e. the transition of β from $+10^o$ to -5^o, results in lower performances and is of no interest.

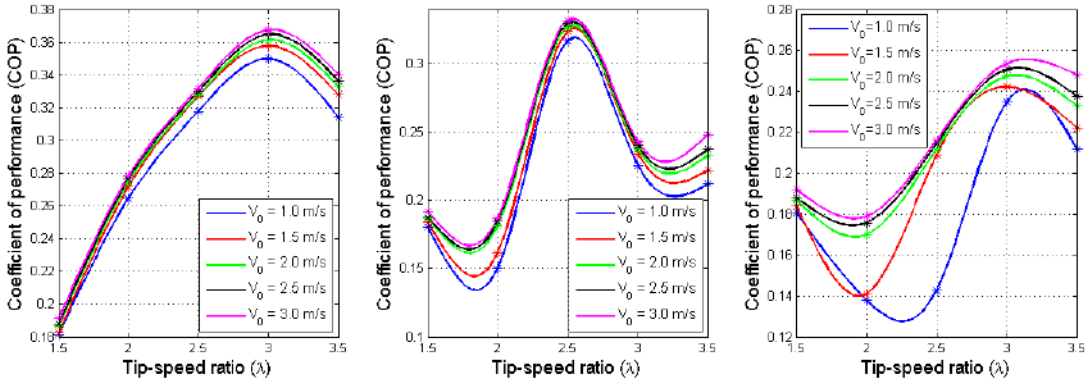

Figure 6.14: Comparison of COPs for different blade pitch regimes. (a) $\beta = +10^o \rightarrow -5^o$ (b) $\beta = +5^o \rightarrow -5^o$ and (c) $\beta = +5^o \rightarrow -5^o$ with transition points of $\beta = +10^o \rightarrow -5^o$

6.3.5 Comparison between fixed blades and variable pitching blades

The effect of blade pitching on the turbine's performance is plotted in Figure 6.15 for a fixed free-stream velocity V_0=1 m/s. With reference to the classical Darrieus turbine with fixed blades, the quantitative difference in COP can be measured in three different locations; before, on and after the peak at λ=2.5. At lower rotational speeds, the performance with pitching blades is much better than that with the fixed blades. Pitch control laws, as proposed in section 6.2, exhibit different behaviours. Law 1 is steadily producing better COP with tip-speed ratio λ until it reaches the optimal value for $\lambda = 3$, while Law 2 delivers oscillating COP values, which is however better than fixed blades up to $\lambda = 2.5$. After this, Law 1 is still better than fixed blade model but Law 2 has deteriorated the performance. Another important observation is that the optimal value of tip-speed ratio with Law 1 has shifted from 2.5 to 3, which means that the operational range of the turbine is improved. Law 3 on the other hand produces a comparable power at lower tip-speed ratios and becomes very inferior than fixed blade model at medium or higher values of λ.

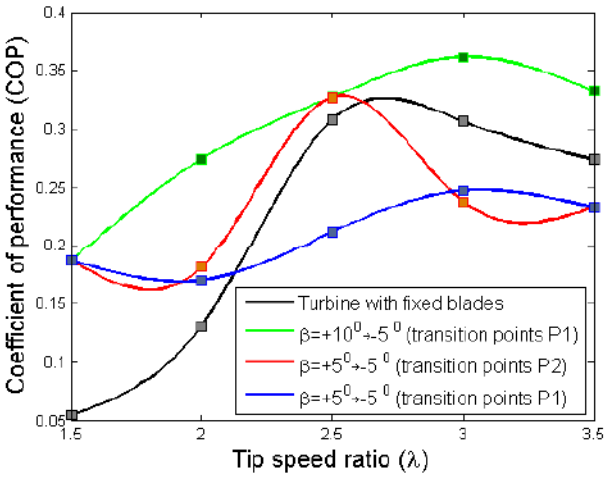

Figure 6.15: Comparison between the fixed and pitching blades for coefficient of power COP

6.4 Effect of solidity σ

With the aim of assessing the application of proposed blade pitching technique to different sizes of rotor, simulations were performed to the four solidity models, as presented in Table 4.6. These computations were carried at a constant free-stream velocity $V_0 = 1m/s$ with a variable rotor angular velocity ω. The resulting power curves for the chosen solidity models in comparison with those of classical Darrieus turbine with fixed blades are plotted in Figure 6.16. From the section 4.7.2, it is understood that the higher solidity models should operate at lower angular velocities to achieve the maximum power output. This is valid for the pitching blade models too, which can be observed from the peak of COP curve shifting towards higher values of λ as σ decreases. This shows that the λ_{opt} is a function of σ.

Model 1, the highest solidity model with σ=0.8, exhibits similar performance at tip-speed ratio λ close to 1.5 for both fixed and pitching blade models. Dramatic jump in the COP is then observed with 94% increase in the peak COP with pitching blades. Also, the oscillating nature of COP evolution is vanished which can provide a better operating range. Model 2 for which σ=0.64 experiences a consistent increase in COP values with 47% rise in the maximum COP value at $\lambda = 3$. The trends of COP curves are quite similar for the base model with $\sigma = 0.533$ and the lowest solidity model with $\sigma = 0.457$. The increase in the maximum COP values for Model 3 and Model 4 are 25% and 17% respectively. It is therefore noted that the maximum COP value evolved inversely with σ. This probably means that, for lesser solidities, the blades are more independent from each other, which favours the applicability of Couchet theory on each single blade.

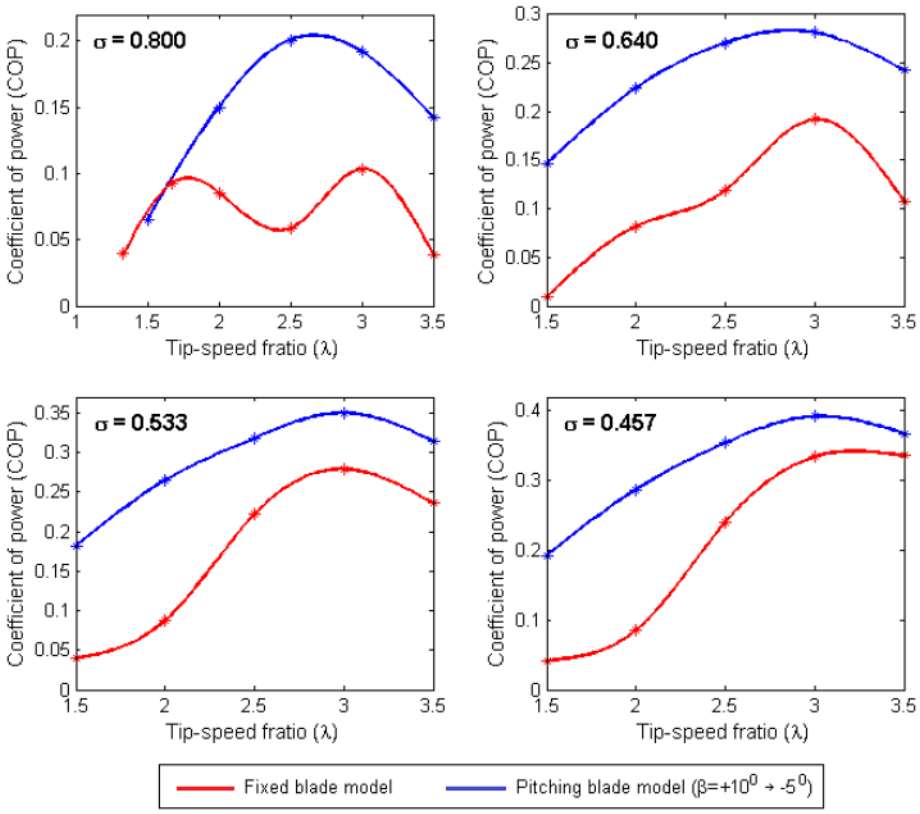

Figure 6.16: Effect of solidity σ on pitching blade model

6.5 Sensitivity analysis of transition points

The performance augmentation and efficiency improvement is significantly sensitive to the turbine to off-design conditions (Hau, 2013; Fuglsang and Bak, 2004). In the same way, it is definitive that identification of right locations for the transition is as important as the transition scheme, because the pitching control law is very sensitive to the azimuthal location where the blade changes its incidence regime, as shown in Figure 6.14. Therefore, further analysis was made to measure the effect of transition points on the device performance. Figure 6.17 quantifies the sensitivity of turbine's performance on choosing the transition location. Here, the sensitivity of pitch regime transition from $\beta = +10^o$ to $\beta = -5^o$ is tested for a tip-speed ratio $\lambda = 2.5$ and free-stream velocity $V_0 = 1$ m/s. It is important to notice that, out of 4 transition locations as shown, only one point at the 3rd spot is shifted to right by 3% as the profile embraces the pitching regime of $\beta = -5^o$. The corresponding drop in the turbine's output is over 4%.

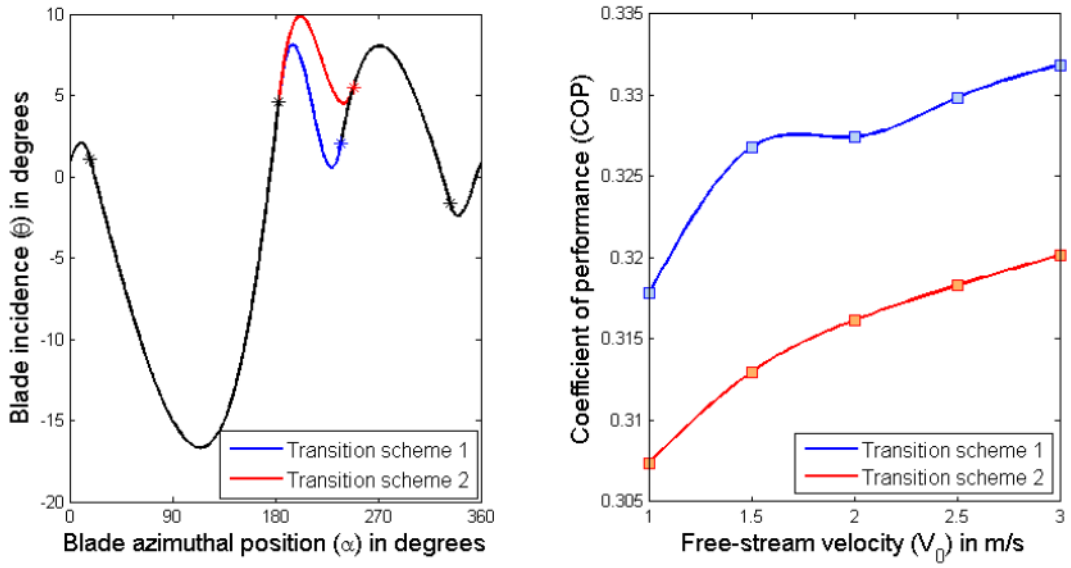

Figure 6.17: Sensitivity of turbine's performance to the transition location for pitch control law $\beta = +10^o \rightarrow -5^o$

6.6 Conclusion

The objective of this chapter was to examine whether potential flow conditions could be applied to real flow situations in order to gain the advantage on ideal flow behaviour with constant circulation. The analytical construction of the irrotational flow over an arbitrary profile formulated in Chapter 3 and prospective potential flow application on the basis of Couchet theory yielded the control law that decides the blade pitching. This chapter computationally analysed the application of this control law in real flows. The complexity in handling both constant circulation paradigm and punctual circulation changes for better performance is highlighted. The use of the SST $k-\omega$ turbulence model for performing numerical analysis of pitching blade performance after validating against classical Darrieus case provided satisfactory results. Beyond the kinematic or dynamic laws suggested by various scholars, the development of more sophisticated, physics-based, control laws were analysed. A precise characterization of the circulation to be applied to the blades not only to prevent the vortex shedding but also to improve the propulsive features has been undertaken in order to identify the most appropriate blade pitch regimes. Considering the real conditions of fluid flow and assumptions in replicating the practical device operation in 2D CFD computations, a feasible range of blade pitching control laws have been identified. The constant circulation paradigm was successfully applied within these limits, resulting in the suppression of most of the vortex shedding and in a quasi unperturbed wake. The design of transition laws between two fixed values of circulation allowed maximizing the coefficient of power

COP while ensuring that vortices are shed at the transition locations only. These results may allow the use of multiple turbines in a denser network which cannot be achieved using conventional devices, with a limited impact on the surroundings. In order to test the effectiveness of the proposed pitching laws in the laboratory, two experimental demonstrators, one with the blades following the control law $\beta = 5^o$ and second with $\beta = +10^o \rightarrow -5^o$ are developed. The former is to suppress the vortex shedding from a conventional machine, while the latter is to optimize the machine's performance. Appendix II shows the pitching mechanism and related kinematics of the prototype.

CHAPTER 7

CONCLUSION AND RECOMMENDATIONS

Contents

7.1 Overview

Considering the scope of this research project, the literature survey as presented in Chapter 2 concluded that better understanding would be needed in the following areas of the study to progress in the research.

⇒ *Hydrodynamic analysis of the Darrieus turbine by understanding the design and functional parameters*: key knowledge was developed from this about the velocity and force vectors around the blade, and power characteristics of the device.

⇒ *Performance analysis of the Darrieus turbine by considering the fundamental blade designing and solidity σ of the turbine*: most of the scholars chose the profiles for Darrieus turbine on the basis of two-dimensional static studies. This discussion led to choose NACA 0015 profile to build the blade model for computational and experimental studies. Apart from the solidity σ of 0.533 for the base turbine model, three other models with different solidity were taken into consideration for CFD studies.

⇒ *Turbine investigation methods including CFD and PIV techniques for detailed examination of the flow across the turbine*: while focusing on the advantages of each of the techniques, the drawbacks were also addressed through existing case details supplied by different scholars.

⇒ *Effect of flow confinement on the turbine's performance*: The Lanchester-Betz theory revisited by Garrett and Cummins (2007), and blockage effects were considered as the turbine occupies considerable space in the flow passage.

⇒ *Performance improvement of Darrieus turbine*: a constant circulation framework was identified as a concept to enhance the power output of the turbine where the blade was subject to instantaneous pitching motion throughout its azimuthal travel.

With this comprehensive knowledge, this study proceeded in a coherent way from concept phase (mathematical approach) to CFD study of the Darrieus turbine (numerical assessment), and torque and PIV measurements of the device (experimental analysis). Finally, the design was improved in terms of power characteristics and vortex shedding by the application of pitching blades. This study therefore contributes to the current research area in three main ways:

1. Unlike the existing blade pitch control methods which were proposed by various scholars based on a simple rules such as sinusoidal or crank-type mechanism, the present pitch control mechanism considered the formulation of constant circulation around the blade. The detailed mathematical construct and force & moment calculations were presented in Chapter 3.

2. Exhaustive computational investigation of the flow across the Darrieus turbine model with fixed blades and their validation against experimental studies were presented in Chapter 4 and 5 respectively. These techniques including the methodology, and rationale for choosing corresponding approaches and apparatus were documented. The results comprised the power curves, flow field visualizations, vortex shedding and blade-vortex interaction. Furthermore, the parametric studies were performed to assess the effect of free-

stream velocity V_0 and turbine's solidity σ. The uncertainties in the experimental studies were quantified using probabilistic collocation method and statistics of blade's force evolution were extracted. Appendix I presents the details and results of this study.

3. The pitch control laws developed in Chapter 3 were tested using new CFD methodology whose details were presented in Chapter 6. Based on the power output of blades under constant circulation, new pitch control laws for the blades with variable circulation were developed and tested. These interrogations revealed that the performance of Darrieus turbine increases with variable circulation imposed on the blades with definite vortex patterns released from the blades.

The summary of these results and discussions can be extended to present the concluding remarks about the new research activities performed on the low-velocity vertical axis water turbine. The following sections describe these points.

7.2 Advancements of VAWT research techniques

In spite of exhaustive studies on the Darrieus turbines in wind as well as tidal applications, the mathematical models, although they may satisfactorily match with experimental results, cannot be used for understanding the detailed flow physics. There is a clear need for computational investigation with sufficient verification and validation to accomplish this. Besides adding the general observations about the flow field development and power output, this study used some advanced techniques in a number of ways for more detailed evaluations. Table 7.1 outlines the tools and techniques used throughout the project.

7.2.1 Performance testing of Darrieus turbine

The force and moment measurements constitute the fundamental means to test the Darrieus turbine. For the fixed-blade turbine model, the full curves of the coefficient of power COP for different free-stream velocities and tip-speed ratios were constructed using CFD and experimental methods. Also, the effect of solidity on the power curve evolution is critically analyzed under different operating conditions. For the pitching-blade turbine model, these investigations were based on the theoretical and computational studies. This cross-validation provided a close comparison between all of the three investigation methods and the results were consistent with the existing literature. In addition, the torque extraction methodology presented in section 5.4 can be used by other researchers to carry out towing tank experiments of Darrieus turbine with pitching blades to obtain the performance measurements.

Investigation method	Techniques used
Analytical	1. Conformal transformation and Couchet theory 2. Blade pitch control under constant circulation 3. Blade pitch control under variable circulation
Computational	1. Overset meshes 2. Validation of analytical results against CFD findings for tangential & normal forces 3. Velocity fields and pressure profiles 4. Vorticity and Q-criterion contours 5. Identification of uncertainties in the experiments and their quantification using stochastic collocation
Experimental	1. Dual camera system to capture larger flow area and velocity field merging 2. PIV system synchronized with torque acquisition system 3. Phase-locked measurements to acquire the flow around the blade for every 10^o azimuth position 4. Validation of CFD results against PIV findings for power curves, velocity gradients, vorticity and Q
Tools used	1. Star CCM+ for CFD 2. RD Vision Hiris, EG and LaVision Davis 3. LabVIEW for data acquisition 4. Tecplot for post-processing 5. Matlab for analytical analysis and post-processing

Table 7.1: Tools and techniques used in this research

7.2.2 Computational modeling

Emerging techniques in handling the heavy geometries and meshes, adaptive methods and high-end computing capabilities made the CFD studies of flow across a VAWT more feasible and economical than ever before. The key challenges are however stay in capturing the non-linearities in the flow physics such as flow separation & reattachment, vortex shedding and blade-vortex interaction etc. Due to the strong dependence of turbine's performance on these phenomena, accurate prediction of flow physics is necessary for quality results. The relative motion between different regions of the geometries such as turbine rotation and blade pitching pose another defiance by lacking the interface conservation. Multiblock dynamic meshing, proposed by Ding et al. (2014), combines the radial basis functions and transfinite interpolation which is expected to have better accuracy. Another choice may be spring analogy which is robust although computationally expensive (Schmidt and Stoevesandt, 2014). With appropriate turbulence solution strategy and controls, the CFD studies produced results on the pressure coefficient, streamlines, velocity magnitude, plots of force components and Q-criterion. Since one of the objectives of this study is to control the vortex shedding from the blades, the vorticity contours including its development, detachment from the blade and its interaction with the blade under different operating conditions were produced by the CFD studies. Multiple motions (fluid flow, turbine's rotation and blade pitching

during the operation) were incorporated within the computational domain without missing any quality in the output. This allowed comparing the performance of Darrieus turbine with fixed and pitching blades to optimize the blade's orientation with respect to incoming flow for the betterment of performance.

7.2.3 Experimental studies

A number of studies on the PIV analysis of VAWT flows were available in the literature. The experimental investigation in the present research not only added the fundamental analyzes of the flow past the Darrieus turbine, but presented detailed information about the velocity gradients, vorticity contours, and Q-criterion which were used to validate the computational approach. The PIV system was completely synchronized with torque acquisition apparatus. The extended qualitative measurements for every 10^o of blade azimuth provided more information about the instantaneous changes and development of the flow field. The size of the measurement window was increased by incorporating two cameras to capture the complete turbine which necessitated precise merging of two raw images. The results obtained from such experimental campaign are meant to contribute to scientific research with the field measurements for a complete turbine cycle with different tip-speed ratios. The specific experimental set-up can be used to transfer the knowledge and allow researchers to perform the enhanced performance tests of full-scale or more complex turbine models in the laboratory.

7.3 Understanding the flow physics of fixed-blade turbine model

7.3.1 Reference case: tip-speed ratio $\lambda = 2$

For the sake of simplicity, inclusive flow physics is understood by considering the near-blade flow field (local) and full-sized flow field (global). As explained in section 2.2, the operation of a Darrieus turbine is characterized by large variations of effective blade incidence. Both numerical and experimental studies in this research identified the azimuthwise evolution of flow parameters and vortex shedding. The cyclic observations of flow field for every rotation of the turbine was noticed as a feature of the repetitiveness of complex processes such as vortex release and blade-vortex interaction.

At a tip-speed ratio λ=2, the flow field images showed that the leading edge vortex was found at early azimuth position (60^0) of the blade during the front half of the cycle. This vortex rolled-up to over the suction side of the blade and thus increase the lift force before it was shed from the blade. A series of vortical structures were released from leading and trailing edges and the process becomes quite erratic as the blade passes $\alpha = 180^0$. Beyond this point where the

blade positioning aligns with the effective flow direction, the flow reattachment was possible. The vortex formation, its strength and release from the bade depends on the free-stream velocity V_0. When $V_0 = 0.5$m/s, a weaker vortex was formed near the blade leading edge which was shed at about $\alpha = 160^0$. When V_0 is increased to 1m/s and 1.5m/s, the vortex was relatively stronger and shed early during the front half of the cycle. Also, higher values of V_0 were observed to cause severe blade-vortex interactions which were likely to impact the entire flow pattern of the cycle.

The vorticity and Q-criterion contours obtained from CFD and PIV studies showed the accuracy of capturing the flow physics under different operating conditions. Next section takes on these comparisons in detail by considering more flow parameters.

7.3.2 Velocity gradients

Good comparison between the CFD-simulated flow field and PIV visualisations was witnessed through the measurements of the velocity gradients for a tip-speed ratio $\lambda = 2$. The velocity gradient of in the direction of uniform flow across the turbine for a complete cycle was calculated. Although there is a good match between the major flow variations on a whole, CFD was found to be over-predicting the peak values. A slight delay in major flow interactions was identified in the numerical results. Also, there is some discrepancy between the computational and experimental results at the onset of vortex shedding and its interaction with the blade.

7.4 Blade pitching

Based on the seminal work of Couchet (1976), the blade pitch control laws as a function of azimuth position were developed, which were expected to ensure the suppression of vortex shedding from the blades. This was possible by imposing a constant circulation to the blade. The mathematical construct of this work in Chapter 3 also provided the analytical calculation of the blade operated in this formulation. 2D CFD studies were performed to assess the influence of blade pitching kinematics on the turbine's performance at different tip-speed ratios. Good comparison between these analytical results and CFD analysis for tangential and normal force components was achieved, which was presented in Chapter 6. This CFD model was used to foster the knowledge obtained from the analytical analysis in terms of power extraction, flowfield development and vortex control. The specific remarks of this investigation are outlined below.

1. Both analytical and CFD studies revealed that the performance of the turbine with constant circulation imposed to the blades varies with the pitching

amplitude, defined by the angle β. A series of β values from -5^0 to $+10^0$ was tested at different tip-speed ratios using CFD to compare the analytical results.

2. For all the positive values of β considered in this study, it was found that the blade extracts the power only during the front half of the cycle and loses the same or even more power during the rear half of the cycle. This caused the coefficient of power COP to evolve as a sinusoidal curve. This is because of larger virtual camber and flow induced incidence during the front half which increases the power extraction. When these models are compared with the classical Darrieus turbine, the fixed blade model produces better power than the pitching blades. However, the constant circulation based pitch control formulation produced almost no power, which was circumvented by subjecting the blades to variable circulation.

3. For the turbine model with variable circulation imposed to blades, increasing the tip speed ratio λ improved the power extraction features throughout the cycle. The practical operating range of these models is better than that of the fixed blade model as the optimal tip-speed ratio λ_{opt} is increased for the turbine with pitching blade. This means that λ_{opt} is certainly dependent on the blade kinematics.

4. The numerical study showed that there is a slight increment in the coefficient of power COP with the free-stream velocity V_0. This improvement reflects the increase of power extracted from the flow during the front half of the cycle with higher free-stream velocities, which was caused by increased lift-to-drag ratio. The rate of increase in COP was however found decreasing with increasing V_0. The power in the rear half remained relatively unchanged with increasing Reynolds number for the pitching kinematics investigated in the present study.

5. The active blade pitching mechanism by means of cam system was developed to model a Darrieus turbine prototype, where the pitching motion of the blade is kinematically coupled to rotor's rotation. This mechanism of changing the blade's orientation with respect to incoming flow is instantaneous and predefined which is expected to offer better performance in terms of power output as well as vortex control. The corresponding demonstrator was built and future experimental investigations are planned.

7.5 Further work

Even though a large number of studies were performed on the design and development of Darrieus turbines for wind and tidal applications for past three

decades, there are still several gaps in the published material as fundamental issues are concerned. These must be properly considered to develop better designs and techniques. One such attempt is made through this thesis work. Despite the appreciable progress achieved by the present research on the marine turbine and its performance improvement, realization of the developed methodologies and proposed techniques in real applications are yet to be made. The mathematical models of constant circulation framework, theoretical concepts of pitching blades are plentifully supplied by the literature. This substantial information along with the knowledge obtained during the present research unravelled that the pitching blade models are very difficult to develop. In addition, the additional complexity in understanding the kinematics and flow physics associated with the pitching blade models pose serious challenges at the development end. The scarcity of fully-adequate computational and experimental models is another cause to fail in addressing the design issues of advanced techniques. For a conclusive study to be conducted, these aspects should be taken into account. It is therefore imperative to recognise the key areas where additional efforts are needed. Starting with a discussion on the continuation of current project, this section is dedicated to provide the following recommendations from practical application view point.

7.5.1 Blade-wise force measurements

The present research offered the base knowledge of experimental and measurement methods which is used to provide constructive recommendations for further improvement in the turbine's performance, which are outlined here.

1. Use of lighter materials and blades not only allow the weight reduction, but permit the smaller bearing and simple supporting elements. Such facility leads to reduced form drag of the set-up. Also, the lighter blades can be spun at higher RPM without any damage which enables to test the operations of higher tip-speed ratios and blade Reynolds numbers.

2. The blade-wise force and moment variations as the turbine rotates, which was missed in the present research. This data is vital for validating the theoretical and computational models. The lighter blades are less prone to errors in this process of obtaining accurate force measurements.

7.5.2 Flow analysis

In the present study, the PIV computation of local flow fields around the blade at different azimuth positions and global flow fields across the turbine were found immensely helpful in understanding the variations of pressure, velocity and circulation. New explorations may be interesting to have additional information about the flow criticalities, which are outlined here.

1. The effect of adverse pressure gradients in defining the behaviour of flow separation and reattachment is necessary to be quantified for comparing with the CFD results as well as possible design improvements.

2. The PIV measurements in the present study were limited to the two-dimensional and two-component flow system. The visualization along the blade span, particularly at the blade tips and supporting structures are important for better understanding of flow dynamics. A stereo PIV or Tomo PIV study can provide the three-dimensional and three-component analysis.

3. With the PIV facility, fully synchronized with force measurement system, this possibility needs further investigation from the tidal turbine standpoint.

7.5.3 Experimental analysis of pitching blade design

Starting from understanding the kinematics and hydrodynamics of a Darrieus turbine, this thesis work provides the preliminary studies on the application of the blade pitch control laws which were tested and compared with classical turbine using CFD. The experimental campaign for PIV studies of the fixed blade model was successfully conducted and full range results were obtained, analyzed and presented. The design and development of the turbine with pitching blades and supporting cam system was completed by the end of the study. The CAD design of the pitching blade model was developed, which is shown in Figure 7.1. See Appendix II for the complete cam mechanism design. The 2D model was parametrically analyzed using CFD to assess its performance under a wide range of operating conditions and with different solidities. In furtherance, the experimental studies of pitching blade model are needed in order to have a consolidated information about the device performance in different flow conditions.

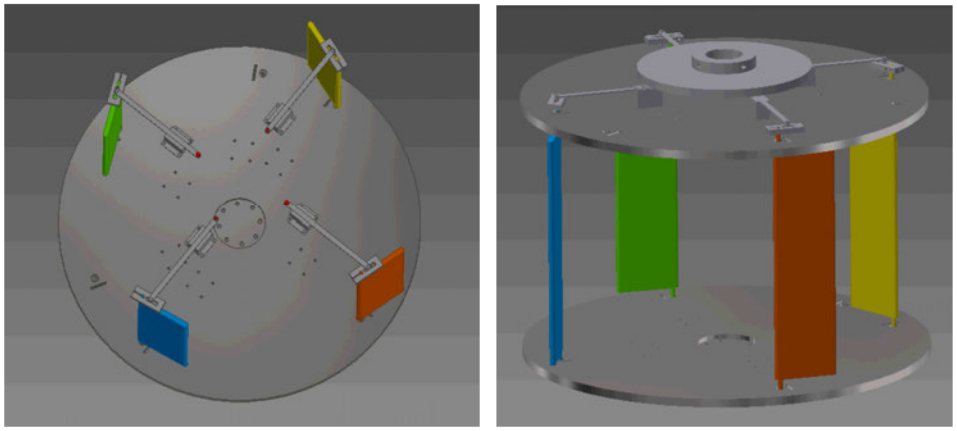

(a) Top view (b) Isometric view

Figure 7.1: Computational model of Darrieus turbine with pitching blades

7.5.4 Vertical axis tidal turbines at larger scale

This work provided the tests and new concepts for conventional turbine models and new designs with pitching blades. It is interesting to transfer these ideas and findings to a larger scale to check if the assessments made in this study would hold their stand and similar performance trends could be accomplished. One of the key notifications is that the rotor geometry was neglected and the blade Reynolds number is in the order of 10^5, which may be feasible for real applications. Literature survey shows that higher Reynolds number models at larger scales were computationally modelled where the inlet turbulence levels were increased. Such tests yielded considerable changes in the power characteristics of the turbine (Edwards, 2012). Therefore, careful testing strategies should be ensured for prospective future studies. On the other hand, the funding limitations and schedule barriers oblige an appropriate assessment of development possibilities for large scale deployment.

7.5.5 Vertical axis tidal turbines in real situations

One significant difference between the investigations made in this study and those in real situations is the flow confinement. Although majority of research articles attempted to replicate the real flow environment in their investigations, the present research included significant blockage effects in both computational and experimental studies. In order to transfer the performance measurements to real flow conditions, these blockage effects should be nullified. Also, the flow confinement imposes additional wall effects on the flow domain which considerably change the physics and therefore should be quantified. The approximate match between the experimental and computational flow conditions did not answer the adequacy of assessment procedure. Therefore, a clear requirement for large domain and 3D CFD models is identified which would dramatically increase the computational cost.

7.5.6 Alternative design configurations

It is obvious that the geometrical design parameters of Darrieus turbines greatly influence the overall performance. The studies of Tirkey et al. (2014) and Gosselin et al. (2013) quantified the changes in the turbine's power curves when the different design parameters such as blade profile, number of blades, aspect ratio, solidity etc... were tested. With the general information provided by such parametric studies, it is interesting to optimize the geometrical shape for improved performance. An adjoint solver in the CFD framework can be used to derive the best possible geometry while the boundary conditions can be optimized by using the statistical techniques such as Design of Experiments (DOE), response surface etc... Commercial CFD software Ansys Fluent has these techniques built in the project workbench while Star CCM+ can be coupled with external tool boxes

such as CAESES and modeFRONTIER for multi-objective optimization process. Numerous possible studies can be conducted using these coupled solvers for improved designs to emerge. Detailed CFD studies of optimized geometries can allow revisiting the mathematical models. Corresponding observations of flow physics using experimental studies will therefore be a new area of interest for prospective researchers.

REFERENCES

[1] Achard JL, Maître T (2006) "Hydraulic turbomachine", Patent No. EP1718863 (A1).

[2] Ahmadi SA, Sharif S, Jamshidi R (2009) "A numerical investigation on the dynamic stall of a wind turbine section using different turbulent Models", World Academy of Science, Engineering and Technology 34, pp. 290 296.

[3] Alaimo A, Esposito A, Messineo A, Orlando C, Tumino D (2015) "3D CFD analysis of a vertical axis wind turbine", Energies 8(4), pp. 3013-3033.

[4] Almohammadi KM, Ingham DB, Ma L, Pourkashanian (2015) "2D CFD analysis of the effect of trailing edge shape on the performance of a straight blade vertical axis wind turbine", IEEE Transactions on Sustainable Energy 6(1), pp. 228-235.

[5] Amet E, Maitre T, Pellone C, Achard JL (2009) "2D numerical simulations of blade-vortex interaction in a Darrieus turbine", Journal of Fluids Engineering 131(11), pp.111103-111115.

[6] Anderson JD (1995) "Computational Fluid Dynamics-basics with applications", McGraw Hill Inc, USA.

[7] Antheaume S, Maitre T, Achard JL (2008) "Hydraulic Darrieus turbines efficiency for free fluid flow conditions versus power farms condition", Renewable Energy 33(10), pp. 2186 2198.

[8] Armstrong S (2011) "Power performance, flow behaviour and excitation response of canted blades for a vertical axis wind turbine", MSc Thesis, McMaster University, Canada.

[9] Ashwill TD, Sutherland HJ, Veers PS (1990) "Fatigue analysis of the sandia 34-meter vertical axis wind turbine", 9th ASME Wind Energy Symposium.

[10] Asim T, Mishra R, Ubbi K, Zala K (2013) "Computational fluid dynamics based optimal design of vertical axis marine current turbines", 2nd International Through-life Engineering Services Conference, Cranfield, UK.

[11] Baker JR (1983)"Features to aid or enable self-starting of fixed pitch low solidity vertical axis wind turbines", Journal of Wind Engineering and Industrial Aerodynamics 15, pp. 369-380.

[12] Baker RA, Semin, Ismail AR (2007) "Development of intake and exhaust stroke flow simulation in an engine cylinder using CFD model", National Conference on Software Engineering & Computer Systems 2007, Malaysia.

[13] Baker TJ (2005) "Mesh generation: Art of science?" Progress in Aerospace Sciences, pp. 29-63.

[14] Bavanish B, Thyagarajan K (2013) "Optimization of power coefficient on a horizontal axis wind turbine using bem theory", Renewable and Sustainable Energy Reviews 26, pp. 169 186.

[15] Bedon G, Castelli MC, Benini E (2013) "Optimization of a Darrieus vertical-axis wind turbine using blade element e momentum theory and evolutionary algorithm", Renewable Energy 59, pp. 184-192.

[16] Belhache M, Guillou S, Grangeret P, Mouaze D, Santa-Cruz A (2014) "Wake numerical study of a vertical marine current turbine", La Houille Blanche 6, pp. 74 78.

[17] Benedict M, Lakshminarayan V, Pino J, Chopra I (2013) "Fundamental understanding of the physics of a small-scale vertical axis wind turbine with dynamic blade pitching: an experimental and computational approach", AIAA Paper 2013-1553.

[18] Beri H, Yao Y (2011) "Effect of Camber Airfoil on Self-Starting of Vertical Axis Wind Turbines", Journal of Environmental Sciene and Technology 4, pp.302-312.

[19] Bhatta P, Paluszek MA, Mueller JB (2008) "Individual blade pitch and camber control for vertical axis wind turbines", 7th World Wind Energy Conference.

[20] Biadgo AM, Simonovic A, Komarov D, Stupar S (2013) "Numerical and analytical investigation of vertical axis wind turbine", FME Transactions 41, pp. 49-58.

[21] Bryden IG, Naik S, Fraenkel P, Bullen CR (1998) "Matching tidal current plants to local flow conditions", Energy 23(9), pp. 699 709.

[22] Carrigan TJ, Dennis BH, Han ZX, Wang BP (2012) "Aerodynamic shape optimization of a vertical-axis wind turbine using differential evolution", Renewable Energy, Article ID 528418, 16 pages.

[23] Castelli MR, Ardizzon G, Battisti L, Benini E, Pavesi G (2010) "Modelling strategy and numerical validation for a Darrieus vertical axis micro-wind Turbine", ASME Conference Proceedings 2010 (44441), pp.409- 418.

[24] Castelli MR, Englaro A, Benini E (2011) "The Darrieus wind turbine: Proposal for a new performance prediction model based on CFD", Energy 36(8): pp.4919-4934.

[25] Chaitep S, Chaichana T, Watanawanyoo P, Hirahara H (2011) "Performance evaluation of curved blades vertical axis wind turbine", European Journal of Scientific Research 57(3), pp. 435-446.

[26] Chan WM, Kim N, Pandya SA (2012) "Advances in domain connectivity for overset grids using the x-rays approach", 7th International Conference on Computational Fluid Dynamics.

[27] Chang L (2005) "Advanced topics in environmental engineering-wind power", Ch.4, University of New Brunswick.

[28] Cheng JC, Su SJ, Miau JJ (2012) "Application of variable blade pitch control on improving the performance of vertical axis wind turbine", Applied Mechanics and Materials 229-231, pp. 2339-2342.

[29] Chougule P, Nielsen S (2014) "Overview and design of self-acting pitch control mechanism for vertical axis wind turbine using multi body simulation approach", Journal of Physics: Conference Series 524-012055, doi:10.1088/1742-6596/524/1/012055.

[30] Chow R, Dam CP (2011) "Inboard stall and separation mitigation techniques on wind turbine rotors", In proceedings of 49th AIAA Aerospace Sciences Meeting, Orlando, USA.

[31] Consul CA, Willden RHJ (2010) "Influence of flow confinement on the performance of a cross-flow turbine", 3rd International Conference on Ocean Energy, Bilbao, Spain.

[32] Consul CA, Willden RHJ, McIntosh SC (2013) "Blockage effects on the hydrodynamic performance of a marine crossflow turbine", Philosophical Transactions of the Royal Society A 371: 20120299.

[33] Consul CA, Willden RHJ, Ferrer E, McCulloch MD (2009) "Influence of Solidity on the Performance of a Cross-Flow Turbine", Proceedings of 8th European Wave and Tidal Energy Conference, pp. 484 493.

[34] Couch SJ, Bryden IG (2004) "The impact of energy extraction on tidal flow development", 3rd International Conference on Marine Renewable Energy (IMarEST).

[35] Couchet G (1976) "Les profils en aérodynamique instationnaire et la condition de Joukowski avec une note sur la dynamique des profils", In Librairie Scientifique et Technique.

[36] Cruz CA (2008) "Experimental and numerical characterization of turbulent slot film cooling", PhD Thesis, University of Maryland, USA.

[37] Danao LA (2012) "The influence of unsteady wind on the performance and aerodynamics of vertical axis wind turbines", PhD Thesis, University of Sheffield, UK.

[38] Danao LA, Qin N, Howell R (2012), "A numerical study of blade thickness and camber effects on vertical axis wind turbines". Proceedings of the Institution of Mechanical Engineers, Part A: Journal of Power and Energy, Pages 15.

[39] Darrieus GJM (1925) "Turbine à axe de rotation transversal à la direction du courant", Patent No. FR000000604390A.

[40] Darrieus GJM (1925) "Turbine having its rotating shaft transverse to the flow of the current", Patent No. US000001835018A.

[41] Deglaire P, Agren O, Bernhoff H, Leijon M (2008) "Conformal mapping and efficient boundary element method without boundary elements for fast vortex particle simulations", European Journal of Mechanics 27, pp.150 176.

[42] Deshpande P, Li X (2013) "Numerical study of Giromill-type wind turbines with symmetrical and non-symmetrical airfoils", European International Journal of Science and Technology 2(8), pp.195-208.

[43] Ding L, Lu Z, Guo T (2014) "An efficient dynamic mesh generation method for complex multiblock structured grid", Advances in Applied Mathematics and Mechanics, The Advances in Applied Mathematics and Mechanics 6(1), pp. 120-134.

[44] Doroshenko SA, Doroshenko AV (2014) "Physical modeling of flow around the underwater tidal power", Procedia Engineering 91, pp. 194-199.

[45] Drela M (1998) "Pros & cons of airfoil optimization", In Frontiers of Computational Fluid Dynamics, ed. David AC, Mohammed MH, World Scientific, pp. 363-380.

[46] Duraisamy K, Lakshminarayan V (2014) "Flow physics and performance of vertical axis wind turbine arrays", AIAA Paper 2014-3139.

[47] Eboibi O (2013) "The influence of blade chord on the aerodynamics and performance of vertical axis wind turbines", PhD Thesis, University of Sheffield, UK.

[48] Eboibi O, Danao LA, Howell R, Edwards JM (2013) "A numerical study of the influence of blade profile and solidity on the performances of vertical axis wind turbines", AIAA Paper 2013-1095.

[49] Edwards JM (2012) "The influence of aerodynamic stall on the performance of vertical axis wind turbine", PhD Thesis, University of Sheffield, UK.

[50] Edwards JM, Danao LA, Howell RJ (2012) "Novel experimental power curve determination and computational methods for the performance analysis of vertical axis wind turbines," Journal of Solar Energy Engineering 134(3), pp.11.

[51] Erickson DW, Wallace JJ, Peraire J (2011) "Performance characterization of cyclic blade variation on a vertical axis wind turbine", 49th AIAA Aerospace Sciences Meeting, Orlando, Florida.

[52] European Commission (1996) "The exploitation of tidal marine currents", Technical Report EUR16683EN.

[53] Ferreira CJS (2009) "the near wake of the VAWT: 2D and 3D voews of the VAWT aerodynamics", PhD Thesis, TU Delft.

[54] Ferreira CJS, Bijl H, van Bussel GJW, van Kuik G (2007) "Simulating dynamic stall in a 2D VAWT: Modeling strategy, verification and validation with Particle Image Velocimetry data", Journal of Physics: Conference Series 75(1) 012023

[55] Ferreira CJS, van Brussel GJW, van Kuik G (2007) "2D CFD simulation of dynamic stall on a vertical axis wind turbine: Verification and validation with PIV measurements", 45th AIAA Aerospace Sciences Meeting and Exhibit, AIAA: Reno, Nevada.

[56] Ferreira CJS, van Bussel GJW, Scarano F, van Kuik G (2008) "PIV visualization of dynamic stall VAWT and blade load determination", 46th AIAA Aerospace Sciences Meeting and Exhibit, AIAA: Reno, Nevada.

[57] Ferreira CJS, Kuik GV, Bussel GV, Scarano F (2009) "Visualization by PIV of dynamic stall on a vertical axis wind turbine", Experiments in Fluids 46(1), pp. 97 108.

[58] Fleisinger M, Vesenjak M, Hribersek M (2014) "Flow driven analysis of a Darrieus water turbine", Journal of Mechanical Engineering 60(12), pp. 769-776.

[59] Freeborn AB (2008) "Pylon Effects on a Scramjet Cavity Flameholder Flowfield", PhD Thesis, Air Force Institute of Technology, Ohio, USA.

[60] Fuglsang P, Bak C (2004) "Development of the Riso wind turbine airfoils", Wind Energy 7, pp. 145 162.

[61] Fujisawa N, Shibuya S (2000), "Observations of dynamic stall on Darrieus wind turbine blades", Journal of Wind Engineering and Industrial Aerodynamics 89, pp. 201-214.

[62] Gant S, Stallard T (2008) "Modelling a tidal turbine in unsteady flow", In proceedings of the 18th International Offshore and Polar Engineering Conference, pp. 473-479.

[63] Garrett C, Cummins P (2004) "Generating tidal power from currents", Journal of Waterway, Port, Coastal, and Ocean Engineering 130(3), pp. 114 118.

[64] Garrett C, Cummins P (2007) "The efficiency of a turbine in a tidal channel", Journal of Fluid Mechanics 588, pp. 243 251.

[65] Gazzano R, Marini M, Satta A (2010) "Performance calculation for a vertical axis wind turbine with variable blade pitch", International Journal of Heat and Technology 28(2).

[66] Gerolymo GA, Michon GJ, Neubauer J (2002) "Analysis and application of chorochronic periodicity in turbomachinery rotor/stator computations", Propulsion and Power 18(6).

[67] Gipe P (2009) "Wind energy basics: A guide to home- and community-scale wind energy systems", 2, Chelsea Green Publishing, Vermont, USA.

[68] Glauert H (1948) "The elements of aerofoil and airscrew theory", 2nd Ed., Cambridge, Cambridge University Press.

[69] Good A, Hamill G, Whittaker T, Robinson D (2011) "PIV analysis of the near wake of a tidal turbine", Proceedings of 21st International Offshore and Polar Engineering Conference, Hawaii, USA.

[70] Gorle JMR, Bardwell S, Chatellier L, Pons F, Ba M, Pineau G (2014) "PIV investigation of the flow across a Darrius water turbine", 17th International Symposium on Applications of Laser Techniques to Fluid Mechanics, Lisbon, Portugal.

[71] Gosselin R, Dumas G, Boudreau M (2013) "Parametric study of H-Darrieus vertical-axis turbines using URANS simulations", 21st Annual Conference of the CFD Society of Canada.

[72] Goude A (2012) "Fluid Mechanics of Vertical Axis Turbines: Simulations and Model Development", PhD thesis, Uppsala University, Sweden.

[73] Green DJ, Chamorro LP, Arndt RE, Sotiropoulos F, Sheng J (2012) "Phase-locked PIV measurement in the wake of model wind turbines under various inflow conditions", 13th Symposium on Fluid-Structure Interaction and Flow-Induced Noise in Industrial Applications, ASME Proceedings 44755(1), pp. 1507-1514.

[74] Gupta R, Biswas A (2013) "Flow physics of 3-bladed straight chord H-Darrieus wind turbine", Journal of Urban and Environmental Engineering 7(1), pp. 151-156.

[75] Hadzic, H (2005) "Development and application of finite volume method for the computation of flows around moving bodies on unstructured, overlapping grids", PhD Thesis, Technical University Hamburg, Germany.

[76] Haller G (2005) "An objective definition of a vortex", Journal of Fluid Mechanics 525, pp. 1-26.

[77] Hansen MOL, Sørensen DN (2001) "CFD model for vertical axis wind turbine", Proceedings of 2001 European Energy Conference and Exhibition, Munich, Germany.

[78] Hau E (2013) "Wind turbines: fundamentals, technologies, application, economics", 3rd ed., Springer.

[79] Healy JV (1978a) "The influence of blade camber on the output of vertical axis wind turbines", Wind Engineering 2(3), pp. 146-155.

[80] Healy JV (1978b) "The influence of blade thickness on the output of vertical axis wind turbines", Wind Engineering 2(1), pp. 1-9.

[81] Hill, N., Dominy, R., Ingram, G., and Dominy, J., (2008), "Darrieus turbines: the physics of self-starting", Proceedings of the Institution of Mechanical Engineers, Part A: Journal of Power and Energy 223, pp. 21-29.

[82] Horiuchi K, Ushiyama I, Seki K (2005) "Straight wing vertical axis wind turbines: a flow analysis", Journal of Wind Engineering 29(3), pp. 243-252.

[83] Houzeaux G, Eguzkitza B, Aubry R, Owen H, Vazquez M (2014) "A Chimera method for the incompressible Navier Stokes equations", International Journal for Numerical Methods in Fluids 75(3), pp. 155 183.

[84] Howell R, Qin N, Edwards J, Durrani N (2010) "Wind tunnel and numerical study of a small vertical axis wind turbine" Journal of Renewable Energy 35(2), pp. 412-422.

[85] Hu H, Yang Z, Sarkar P (2012) "Dynamic wind loads and wake characteristics of a wind turbine model in an atmospheric boundary layer wind", Experiments in Fluids 52(5), pp.1277-1294.

[86] Huyse L, Michael LR (2001) "Aerodynamic shape optimization of two-dimensional airfoils under uncertain operating conditions", Tech. Rep. 210648, NASA Tech. Mem.

[87] Hwang IS, Lee YH, Kim SJ (2009) "Optimization of cycloidal water turbine and the performance improvement by individual blade control", Applied Energy 86(9), pp. 1532 1540.

[88] Hwang IS, Min SY, Jeong IO, Lee YH, Kim SJ (2006) "Efficiency improvement of a new vertical axis wind turbine by individual active control of blade motion", In Smart Structures and Materials 2006 : Smart Structures and Integrated Systems (ed. Matsuzaki, Y.), SPIE Proceedings 6173, pp. 316 323.

[89] Hyun BS, Choi DH, Han JS, Jin JY, Roo CH (2010) "Performance analysis and design of vertical axis tidal stream turbine", 3rd International Conference on Ocean Energy, Bilbao

[90] Iaccarino G (2001) "Predictions of a turbulent separated flow using commercial cfd codes", Journal of Fluid Engineering 123, pp. 819 828.

[91] IEA (2008) "Key World Energy Statistics".

[92] Iida A, Mizuno A, Fukudome K (2007) "Numerical simulation of unsteady flow and aerodynamic performance of vertical axis wind turbines with LES", 16th Australasian Fluid Mechanics Conference, Gold Coast, Australia.

[93] Ionescu RD, Szava I, Ivanoiu M (2014) "Preliminary blade loads analysis and performance of an urban small power vertical axis wind turbine", Acta Technica Napocensis-Series: Applied Mathematics, Mechanics, and Engineering 57(3), pp. 435 438.

[94] IPCC (2007) "Climate Change 2007: Synthesis Report", contribution of working groups I, II, and III to the 4th Assessment Report of the Intergovernmental Panel on Climate Change, Geneva, Switzerland.

[95] Islam M, Tinga DSK, Fartaja A (2008) "Aerodynamic models for Darrieus-type straight-bladed vertical axis wind turbines", Renewable and Sustainable Energy Reviews 12, pp. 1087-1109.

[96] Jacobs EN, Sherman A (1937) "Airfoil section characteristics as affected by variations of the Reynolds number".

[97] Jacobs EN, Ward, Pinkerton RM (1933) "The characteristics of 78 related airfoil sections from tests in the variable-density wind tunnel", NACA Report No. 460.

[98] Jeong J, Hussain F (1995) "On the identification of a vortex", Journal of Fluid Mechanics 285, pp. 69-94.

[99] Johnson E, Fontaine AA, Jonson ML, Meyer RS, Straka WA, Young S, van Dam CP, Shiu H, Barone M (2013) "A 1:8.7 scale water turbine test of an axial flow water turbine", Proceedings of the 1st Marine Energy Technology Symposium, Washington D.C.

[100] Khalid SS, Liang Z, Shah N (2013) "Harnessing tidal energy using vertical axis tidal turbine, Engineering and Technology 5(1), pp. 239 252.

[101] Kirke BK (1998) "Evaluation of self-starting vertical axis wind turbines for stand-alone applications", PhD Thesis, Griffith University.

[102] Klaptocz VR, Rawlings GW, Nabavi Y, Alidadi M, Li Y, Calisal SM (2007) "Numerical and experimental investigation of a ducted vertical axis tidal current turbine", Proceedings of the 7th European Wave and Tidal Energy Conference, Porto, Portugal.

[103] Klonowska ME, Prosnak WJ (1996) "On an effective method for conformal mapping of multiply connected domain", Acta Mechanica 119, pp.35 52.

[104] Kok JC (1999) "Resolving the dependence on free values for $k-\omega$ turbulence model". National Aerospace Laboratory NLR, No. NLR-TP-99295.

[105] Kolar V (2007) "Vortex identification: New requirements and limitations", International Journal of Heat and Fluid Flow 28(1), pp. 638-652.

[106] Lain S, Osorio (2010) "Simulation and evaluation of a straight-bladed Darrieus type cross flow marine turbine", Journal of Scientific and Industrial Research 69, pp. 906-912.

[107] Lakshminarayan VK, Baeder JD (2010) "Computational investigation of microscale coaxial-rotor aerodynamics in hover", Journal of Aircraft 47(3), pp. 940 955.

[108] Laneville A, Vittecoq P (1986) "Dynamic stall: the case of the vertical axis wind turbine", Journal of Solar Energy Engineering 108(2), pp. 140-145.

[109] Lazauskas L (1992) "Three pitch control systems for vertical axis wind turbines compared", Wind Energy 16(5), pp. 269 282.

[110] Lee T, Gerontakos P (2004) "Investigation of flow over an oscillating airfoil", Journal of Fluid Mechanics 512, pp. 313-341.

[111] Lemaire A, Meyer TR, Zahringer K, Gord JR, Rolon JC (2002) "PIV/PLIF investigation of two-phase vortex-flame interactions", 11th International Symposium on Applications of Laser Techniques to Fluid Mechanics, Lisbon, Portugal.

[112] Li Y, Paika KJ, Xing T, Carrica PM (2012) "Dynamic overset CFD simulations of wind turbine aerodynamics", Renewable Energy 37, pp. 285 298.

[113] Li-xun Z, Ying-bin L, Xiao-hong L, Jian G (2014) "Effect of blade pitch angle on aerodynamic performance of straight-bladed vertical axis wind turbine", Journal of Central South University 21, pp.1417-1427.

[114] Loland KM (2011) "Wind turbine in yawed operation", Masters Thesis, Norwegian University of Science and Technology, Norway.

[115] Lutum E, Cottier F (2011) "Aerothermal predictions on a highly loaded turbine blade including effects of flow separation",In proceeding of European Turbomachinery Conference 2, pp. 1581-1591.

[116] Malaul I, Dumitrescu H (2014) "Numerical simulation of VAWT flow using Fluent", UPB Scientific Bulletin, Series D 76(1), pp. 109 122.

[117] Malcolm DJ (2003) "Market, cost, and technical analysis of vertical and horizontal axis wind turbines, Task no. 2: VAWT vs. HAWT technology", Global Energy Concepts, Lawrence Berkeley National Laboratory.

[118] Marsh P, Ranmuthugala D, Penesis I, Thomas G (2012) "Three dimensional numerical solutions of a straight-bladed vertical axis tidal turbine", 18th Australasian Fluid Mechanics Conference, Launceston, Australia.

[119] Massouh F, Dobrev IK (2008) "Exploration and numerical simulation of wind turbine wake", International Scientific Journal for Alternative Energy and Ecology 62(6), pp. 163-167.

[120] Masters I, Malki R, Williams AJ, Croft N (2012) "The influence of turbulence model on wake structure of TSTs when used with a coupled BEM-CFD model", Oxford Tidal Energy Workshop, University of Oxford.

[121] Mays I, Holmes BA (1979) "Commercial development of the variable geometry vertical axis windmill", International Power Generation, Surrey, UK.

[122] Maydew RC, Klimas PC (1981) "Aerodynamic performance of vertical and horizontal axis wind turbines", Journal of Energy 5(3), pp. 189 190.

[123] McGowan R, Morillas K, Pendharkar A, Pinder M (2012) "Optimization of a vertical axis micro wind turbine for low tip-speed ratio operation", 10th International Energy Conversion Engineering Conference, Atlanta, Georgia.

[124] McIntosh SC (2009) "Wind energy for the built environment", PhD Thesis, Cambridge University.

[125] McLaren KW, Tullis SW, Ziada S (2012a) "Computational fluid dynamics simulation of the aerodynamics of a high solidity, small-scale vertical axis wind turbine", Wind Energy 15(3), pp.349-361.

[126] McLaren KW, Tullis SW, Ziada S (2012b) "Measurement of high solidity vertical axis wind turbine aerodynamic loads under high vibration response conditions", Journal of Fluids and Structures 32, pp. 12-26.

[127] Mehmood N, Liang Z, Khan J (2012) "CFD study of NACA 0018 for diffuser design of tidal current Turbines", Research Journal of Applied Sciences, Engineering and Technology 21(4), pp. 4552 4560.

[128] Mehmood N, Qihu S, Xiaohang W, Liang Z (2011) "Tidal current turbines", Proceedings of International Conference on Mechanical and Electrical Technology 3, pp. 445 450.

[129] Meneses D, Lopez O, Lain S (2014) "Computational study of the interaction between hydrodynamics and rigid body dynamics of a Darrieus type H-turbine", 11th World Congress on Computational Mechanics, Barcelona, Spain.

[130] Menter FR (1992) "Influence of freestream values on $k-\omega$ turbulence model predictions", AIAA Journal 30(6), pp. 1657 1659.

[131] Menter FR (1993) "Zonal two-equation $k-\omega$ turbulence models for aerodynamic flows", AIAA Paper 93-2906.

[132] Menter FR (1994) "Two-equation eddy-viscosity turbulence models for engineering applications", AIAA Journal 32(8), pp. 1598 1605.

[133] Miau JJ, Liang SY, Yu RM, Hu CC, Leu TS, Cheng JC, Chen SJ (2014) "Design and test of a vertical axis wind turbine with pitch control", Applied Mechanics and Materials 225, pp. 338-343.

[134] Migliore PG, Wolfe WP, Fanucci JB (2012) "Flow curvature effects on Darrieus turbine blade aerodynamics", Journal of Energy 4(2), pp. 49 55.

[135] Miguel AF, Aydin M (2011) "Ocean energy: exergy analysis and conversion", Proceedings of the global conference on global warming, Lisbon, Portugal.

[136] Mohamed MH (2012) "Performance investigation of H-rotor Darrieus Turbine with new airfoil shapes", Energy 47, pp.522-530.

[137] Nguyen CV, Wells JC (2006) "Direct measurement of fluid velocity gradients at a wall by PIV image processing with stereo reconstruction", Journal of Visualization 9(2), pp.199-208.

[138] Noack RW, Boger DA (2009) "Improvements to SUGGAR and DiRTlib for overset store separation simulations", AIAA Paper 2009-340.

[139] Nobile R, Vahdati M, Barlow J, Crook AM (2011) "Dynamic stall for a vertical axis wind turbine in a two dimensional study", World Renewable Energy Congress, Sweden.

[140] Pacala S, Socolow R (2004) "Stabilization wedges: solving the climate problem for the next 50 years with current technologies", Science 305, pp. 968 972.

[141] Pahl G (2007) "The Citizen-Powered Energy Handbook: Community Solutions to a Global Crisis", Vermont: Chelsea Green Publishing Company

[142] Paillard B, Hauville F, Astolfi JA (2013) "A coupled unsteady ONERA-EDLIN model and streamtube model", Renewable Energy 52, pp. 209 217.

[143] Paraschivoiu I (1988) "Double-multiple streamtube model for studying vertical axis wind turbines", AIAA Journal of Propulsion and Power 4, pp.370-378.

[144] Paraschivoiu I (2002) "Wind turbine desig: With emphasis on Darrieus concept", Presses internationales Polytechnique, Canada.

[145] Paraschivoiu I, Delclaux F (1983) "Double multiple streamtube model with recent improvements", Journal of Energy 7, pp. 250-255.

[146] Paraschivoiu I, Trifu O, Saeed F (2009) "H-Darrieus wind turbine with blade pitch control", International Journal of Rotating Machinery, pp. 1 7.

[147] Priegue L, Stoesser T, Runge S. (2015) "Effect of blade parameters on the performance of a cross-flow turbine", Proceedings of the 36th IAHR World Congress, Hague, Netherlands.

[148] Prosnak WJ (1987) "Computation of Fluid Motions in Multiply Connected Domains", Wissenschaft & Tecnik.

[149] QinetiQ (2004) "Cycloidal tidal power generation: Phase II", Technical Report URN 04/1102, DTI.

[150] Quon EW, Smith MJ (2015) "Advanced data transfer strategies for overset computational methods", AIAA Paper 2015-566.

[151] Ramasamy M, Leishman JG (2006) "Phase-locked particle image velocimetry measurements of a flapping wing", Journal of Aircraft 43(6), pp. 1867-1875.

[152] Rathi D (2012) "Performance prediction and dynamic model analysis of vertical axis wind turbine blades with aerodynamically varied blade pitch", MSc thesis, North Carolina State University.

[153] Ravi HC, Madhukeshwara N, Kumarappa S (2013) "Numerical investigation of flow transition for NACA-4412 airfoil using computational fluid dynamics", International Journal of Innovative Research in Science, Engineering and Technology 2(7), pp. 2778-2785.

[154] Richardson K, Steffen W, Schellnhuber HJ, Alcamo J, Barker T, Kammen DM, Leemans R, Liverman D, Munasinghe M, Osman-Elasha B, Stern B, Wæver O (2009) "Synthesis Report", Climate Change, Global Risks, Challenges & Decisions, Copenhagen.

[155] Robelius F (2007) "Giant oil field decline rates and their influence on world oil production", Digital comprehensive summaries of Uppsala dissertations from the faculty of science and technology, Uppsala, Sweden.

[156] Rolland S, Newton W, Williams AJ, Croft TN, Gethin DT, Cross M (2013) "Simulations technique for the Design of vertical axis wind turbine device with experimental validation", Applied Energy 111, pp. 1195 1203.

[157] Roosenboom EWM, Stürmer A, Schröder A (2009) "Comparison of PIV measurements with unsteady RANS calculations in a propeller slipstream", 27th AIAA Applied Aerodynamics Conference, Texas.

[158] Saad Y (1996) "Iterative methods for sparse linear systems", PWS Publishing Company.

[159] Samaraweera KKMNP, Pathirathna KAB, De Silva HED, Sugathapala AGT (2010) "Development of Darrieus-type vertical axis wind turbine for standalone applications", International Conference on Sustainable Built Environment, pp. 421 430.

[160] Samsonov V, Baklushin P (1992) "Comparison of different ways for VAWT aerodynamic control", Journal of Wind Engineering and Industrial Aerodynamics 39, pp. 427 433.

[161] Scheurich F, Fletcher TM, Brown RE (2011) "Simulating the aerodynamic performance and wake dynamics of a vertical-axis wind turbine", Journal of Wind Energy 14(2), pp. 159-177.

[162] Schmidt J, Stoevesandt B (2014) "Dynamic mesh optimization based on the spring analogy", ITM Conferences 2.

[163] Schmidt S, Thiele F (2002) "Comparison of numerical methods applied to the flow over wall-mounted cubes", International Journal of Heat and Fluid Flow 23, pp. 330-339.

[164] Sengupta T (2012) "Instabilities of flows and transition to turbulence", CRC Press, USA.

[165] Sheldahl RE, Klimas PC, Feltz LV (1980) "Aerodynamic performance of a 5m diameter Darrieus turbine with extruded Aluminium NACA0015 blades", Technical Report SAND80-0179, Sandia National Laboratories.

[166] Shiono M, Suzuki K, Kiho S (2000) "Experimental study of the characteristics of a Darrieus turbine for tidal power generation", Electrical Engineering in Japan 132(3), pp. 38 47.

[167] Shires A, Kourkoulis V (2013) "Application of circulation controlled blades for vertical axis wind turbines", Energies 6(8), pp. 3744 3763.

[168] Shives M, Crawford C (2014) "Turbulence modelling for accurate wake prediction in tidal turbine arrays", 5th International Conference on Ocean Energy, Halifax.

[169] Singal RK, Singal M, Singal R (2009) "Hydraulic Machines: Fluid Machinery", New Delhi: I.K. International Publishing House.

[170] Soraghan C, Leithead W, Jamieson P (2013) "Influence of lift to drag ratio on optimal aerodynamic performance of straight blade vertical axis wind turbines", EWEA2013, Vienna, Austria.

[171] Sorensen NN, Michelsen JA (2004) "Drag prediction for blades at high angle of attack using CFD", Journal of Solar Energy Engineering 126(4), pp. 1011-1016.

[172] South P, Rangi RS (1975) "An experimental investigation of a 12-ft diameter high-speed vertical axis turbine", National Research Council of Canada, Ottawa, LTRLA-166.

[173] Spera DA (1994) "Wind turbine technology: fundamental concepts of wind turbine engineering", ASME Press, New York.

[174] Steger JL, Dougjerty FC, Benek JA (1983) "A Chimera grid scheme", in Advances in Grid Generation, ed. Ghia KN, Ghia U, ASME FED, 5.

[175] Strickland JH, Webster BT, Nguyen T (1979) "A vortex model of the Darrieus turbine: an analytical and experimental study", Journal of Wind Engineering 101, pp. 500-505.

[176] Sumantraa B, Chandramouli S, Premsai TP, Prithviraj P, Mugundhan V, Velamati RK (2014) "Numerical analysis of effect of pitch angle on a small scale vertical axis wind turbine", International Journal of Renewable Energy Research 4(4), pp. 929 935.

[177] Swidan A, Amin W, Ranmuthugala D, Thomas G, Penesis I (2013) "Numerical prediction of symmetric water impact loads on wedge shaped hull form using CFD", World Journal of Mechanics 4, pp. 311 318.

[178] Templin RJ (1974) "Aerodynamic performance theory for the NRC vertical axis wind turbine", National Research Council of Canada: Ottawa, ON, Canada.

[179] Thompson JE, Warsi ZUA, Mastin CW (1997) "Numerical grid generation-foundations and applications", Elsevier Science Publishing, USA.

[180] Tirkey A, Sarthi Y, Patel K, Sharma R, Sen PK (2014) "Study on the effect of blade profile, number of blade, Reynolds number, aspect ratio on the performance of vertical axis wind turbine", International Journal of Science, Engineering and Technology Research 3(12), pp.3183-3187.

[181] Tran T, Kim D, Song J (2014) "Computational fluid dynamic analysis of a floating offshore wind turbine experiencing platform pitching motion", Energies 7, pp. 5011 5026.

[182] Tu J, Yeoh GH, Liu C (2008) "Computational Fluid Dynamics: A practical approach", Butterworth-Heinemann publication, USA.

[183] Untaroiu A, Wood HG, Allaire PE, Ribando RJ (2011)"Investigation of self-starting capability of vertical axis wind turbines using a computational fluid dynamics approach", Journal of Solar Energy Engineering 133(4), pp.041010-041018.

[184] Vahdati M, Morgan K, Peraire J (1992) "Computation of viscous compressible flows using an upwind algorithm and unstructured meshes", In: Atluri SN (ed.) "Computational Nonlinear Mechanics in Aerospace Engineering", AIAA, pp. 479-505.

[185] Vassberg JC, Gopinath AK, Jameson A (2005) "Revisiting the vertical axis wind turbine design using advanced computational fluid dynamics", 43rd AIAA Aerospace Sciences Meeting and Exhibit, Nevada.

[186] Versteeg HK, Malalasekera W (1995) "An introduction to computational fluid dynamics-The finite volume method", Prentice-Hall publishers, England.

[187] Wang LB, Zhang L, Zeng ND (2007) "A potential flow 2-D vortex panel model: Applications to vertical axis straight blade tidal turbine", Energy Conversion and Management 48(2), pp. 454 461.

[188] Wang S, Ingham DB, Ma L, Pourkashanian M, Tao Z (2012) "Turbulence modeling of deep dynamic stall at relatively low Reynolds number", Journal of Fluids and Structures 33, pp. 191 209.

[189] Wang S, Ingham DB, Pourkashanian M, Tao Z (2010) "Numerical investigations on dynamic stall of low Reynolds number flow around oscillating airfoils", Journal of Computers and Fluids 39, pp. 1529-1541.

[190] Wenlong T, Baowei S, Zhaoyong M (2013) "Conceptual design and numerical simulations of a vertical axis water turbine used for underwater mooring platforms", International Journal of Naval Architecture and Ocean Engineering 5, pp. 625-634.

[191] Wernert P, Favier D (1999) "Considerations about the phase averaging method with application to ELDV and PIV measurements over pitching airfoils", Experiments in Fluids 27(6), pp. 473-483.

[192] Wilcox DC (1988) "Reassessement of the scale-determining equation for advanced turbulence models", AIAA Journal 26(11), pp. 1299 1310.

[193] Wilcox DC (1993) "Comparison of two-equation turbulence models for boundary layers with pressure gradients", AIAA Journal 31(8), pp. 1414 1421.

[194] Wilcox DC (1998) "Turbulence modelling for CFD, DCW industries", 2nd Ed., La Canada, CA, USA.

[195] Wilhelm JP, Nawrocki A, Hard S, Smith J (2010) "Controller design methodology for a circulation controlled vertical axis wind turbine", AIAA Paper 2010-4405.

[196] Wilson RE, McKie WR (1980) "A comparison of aerodynamic analyses for the Darrieus rotor", AIAA Paper 1980-605.

[197] Yang Z, Sarkar P, Hu H (2011) "An experimental investigation on the wake characteristics of a wind turbine in an atmospheric boundary layer wind", 29th AIAA Applied Aerodynamics Conference, Hawaii.

[198] Zagaris G, Bodony DJ, Brandyberry MD, Campbell MT, Shaffer E, Freund JB (2010) "A collision detection approach to chimera grid assembly for high fidelity simulations of turbofan noise", In proceedings of the 48th AIAA Aerospace Sciences Meeting, Orlando, FL.

[199] Zahle F, Sorensen NN, Johansen J (2009) "Wind turbine rotor-tower interaction using an incompressible overset grid method", Wind Energy 12, pp. 594 619.

[200] Zannetti L, Gallizio F, Ottino G (2007) "Vortex capturing vertical axis wind turbine", Journal of Physics 75, pp. 1 10.

[201] Zanon A, Giannattasio P, Ferreira CS (2013) "A vortex panel model for the simulation of the wake flow past a vertical axis wind turbine in a dynamic stall", Journal of Wind Energy 16(5), pp. 661-680.

[202] Zhang X, He GW, Ni SZ (2007) "Computation of flow over a rotating body on unstructured Chimera mesh", 5th International Conference on Fluid Mechanics, Tsinghua University Press & Springer, pp.278 280.

APPENDIX I: UNCERTAINTY ANALYSIS

The concept of stochastic collocation is primarily based on interpolation of function for chosen random variables at specific nodes within the stochastic space. The mathematical implementation of stochastic collocation method in this study follows Xiu (2010).

I.1 Stochastic flow model

For stochastic modeling, two random variables are considered which are free-stream velocity V_0 and rotational velocity ω of the turbine. These two variables are dealt separately in order to discriminate their influence level on the performance characteristics of the turbine. The reason for selecting these four as random parameters to construct the stochastic space is that these are typical characterizing variables of torque evolution and hence the power output. One of the critical concerns in probabilistic collocation is to select an appropriate base to support the random distributions (Ghanem and Spanos, 1991). Considered random variables with mean $\bar{\mu}$ and standard deviation $\bar{\sigma}$ are defined by

$$V_0 = \bar{\mu}_{V_0} + \bar{\sigma}_{V_0}.u$$
$$\omega = \bar{\mu}_{\omega} + \bar{\sigma}_{\omega}.u$$

The so-constructed stochastic space with predefined mean $\bar{\mu}$ and standard deviation $\bar{\sigma}$ of considered random variables is furnished in Table I.1. The standard deviations of free-stream velocity V_0 and the turbine's rotational velocity ω mentioned here are observed in experiments. The stochastic calculations are carried out on a 8x8 Clenshaw-Curtis quadrature based 2D stochastic grid, as shown in Figure I.1.

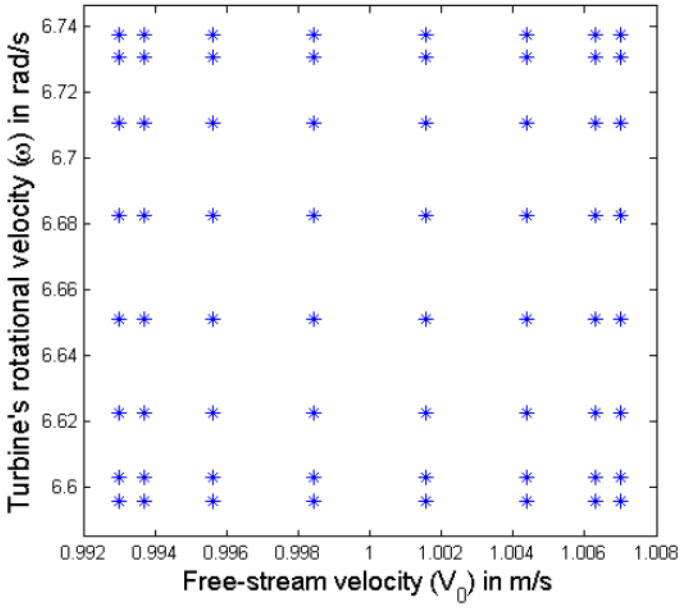

Figure I.1: Clenshaw-Curtis quadrature based stochastic space

	Mean ($\bar{\mu}$)	Std dev ($\bar{\sigma}$)	Support
Free-stream velocity (V_0)	1 m/s	0.007 m/s	[0.993, 1.007]
Rotational velocity (ω)	6.667 rad/s	0.067 rad/s	[6.600, 6.734]

Table I.1: Stochastic space of uncertain variables

I.2 Results

Figures I.2 and I.3 show the plot of statistical moments of the tangential and normal force components for individual random variables. The largest deviations in the force coefficients are observed at the azimuthal locations where the vortex is released from the blade and where the blade-vortex interaction occurs. As the flow non-linearities are reported in the stochastic solution, it is easy to identify the zone of maximum sensitivity, which is $180^o < \alpha < 270^o$. Compared to tangential force, the amount of deviation in the normal force is more. The cumulative effect of both the uncertainties in the flow domain boosts the solution deviation to greater extent, which is shown in Figure I.4. This understanding lays a path to classify the uncertain variables according to their influence on the solution variability.

Figure I.5 shows the interpolated response surface of coefficient of power COP, constructed on the probabilistic space of uncertainty analysis. Red coloured asterisks on the response surface represent the deterministic cubature nodes of uncertain variables. It is clear that the rotational velocity ω is more influential than the free-stream velocity V_0 since the response surface seems sensitive to the changes in ω. While the inverse relationship between free-stream velocity V_0 and COP is evident

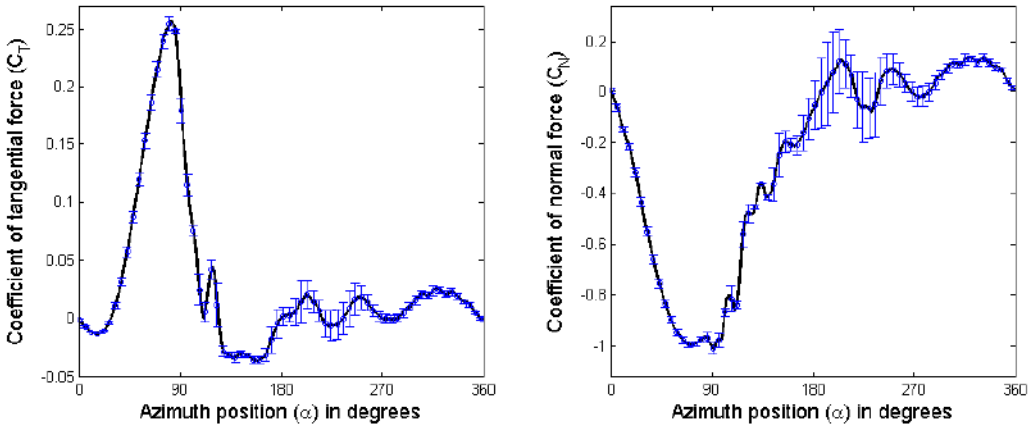

Figure I.2: $\bar{\mu} \pm \bar{\sigma}$ of tangential & normal force coefficients with uncertainty in V_0.

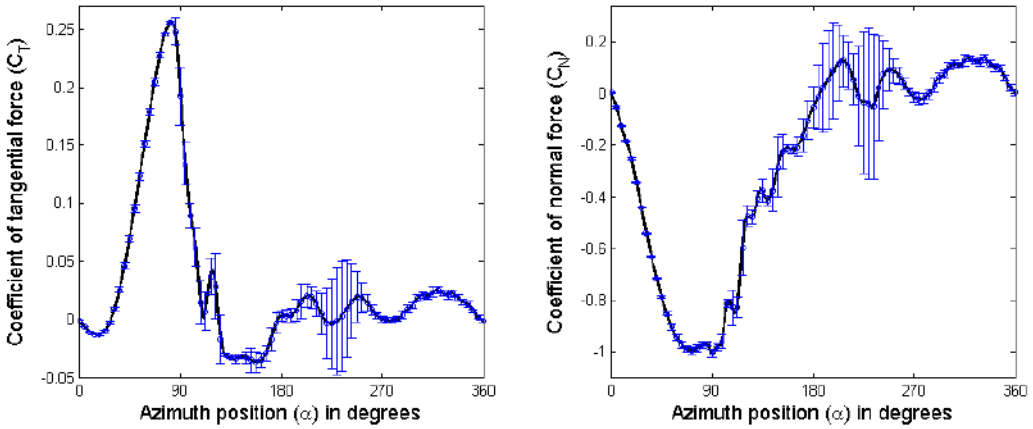

Figure I.3: $\bar{\mu} \pm \bar{\sigma}$ of tangential & normal force coefficients with uncertainty in ω.

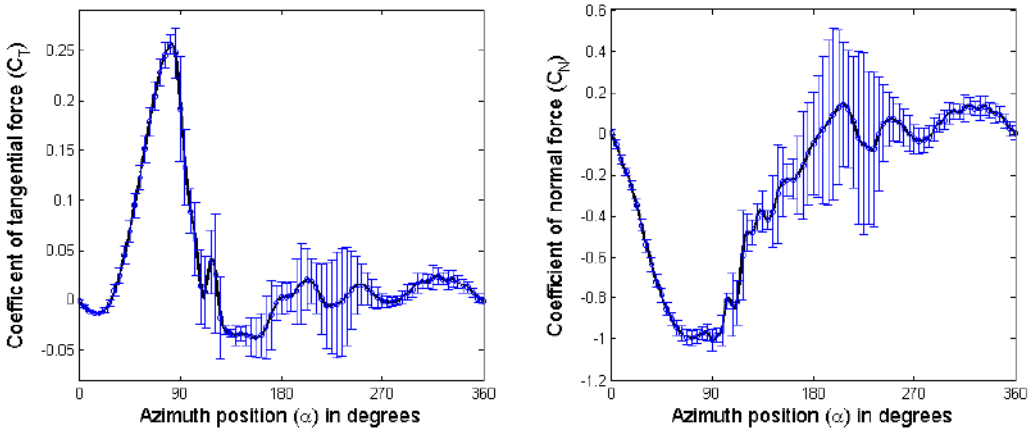

Figure I.4: $\bar{\mu} \pm \bar{\sigma}$ of tangential & normal force coefficients with uncertainties in both V_0 and ω.

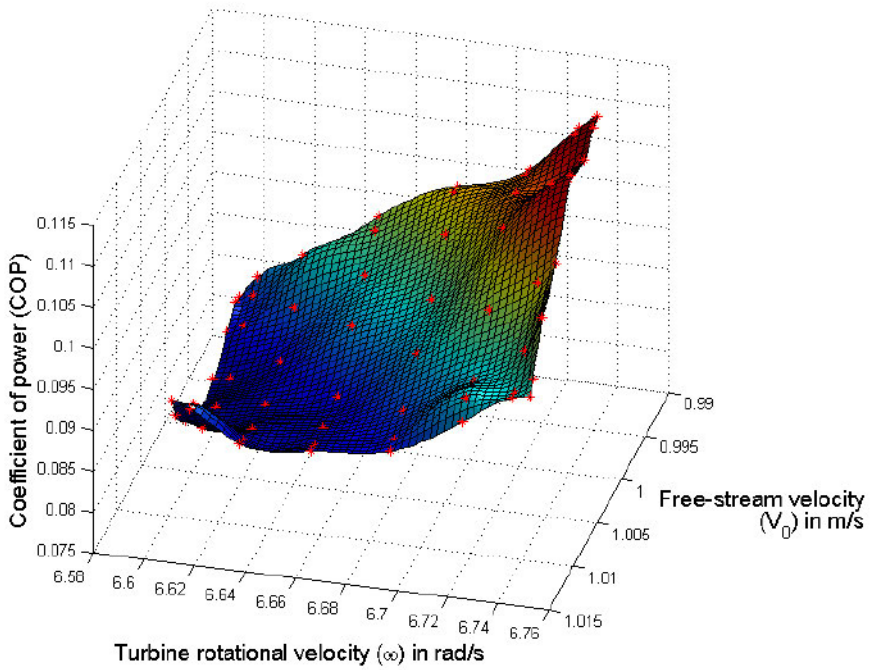

Figure I.5: Response surface of COP on the uncertain dimensions of V_0 and ω.

within the uncertain dimensional space, the surface plot reveals that the performance of the turbine is appreciably influenced by the randomness in the boundary conditions.

APPENDIX II: PITCHING MECHANISM DESIGN

II.1 Model design

In order to develop an instrumented VAWT prototype with the pitching blade, a forced pitch actuation mechanism is used. The objective is to have the blades being subjected to the desired pitch angle defined by the differential Equation 3.49. This mechanism consists of a cam and control rod to geometrically set the pitching dynamics. Refer to Figure II.1, let R_c be the mean radius of the base circle from

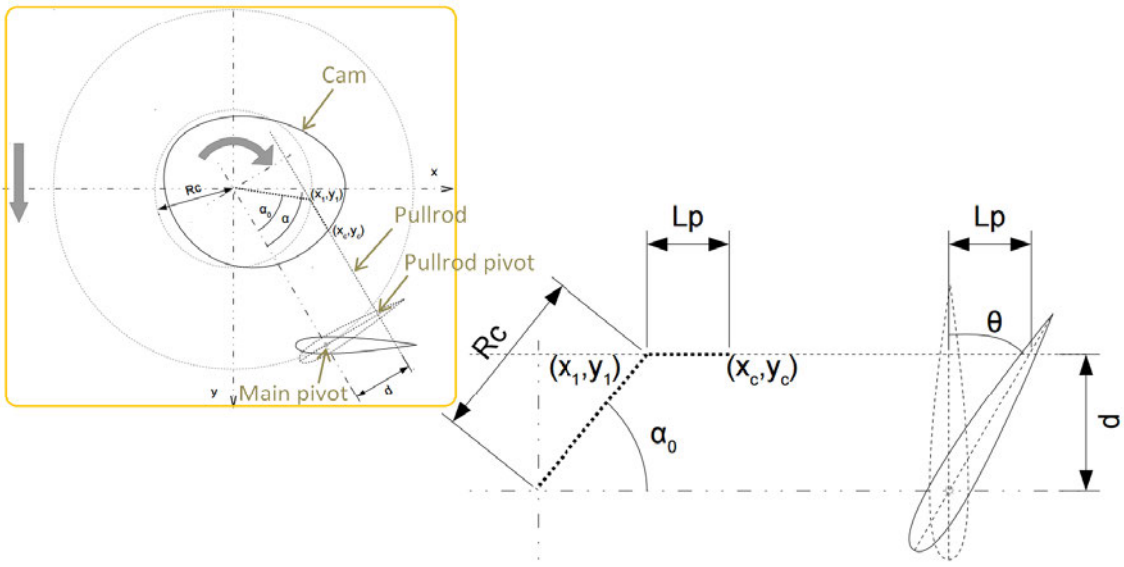

Figure II.1: Blade pitch kinematics and definition of coordinate system on a pitching blade model.

which the cam profile is derived. The coordinates of an arbitrary point on the this circle at a given azimuth position α are calculated from

$$x_1 = R_c \cos(\alpha - \alpha_0) \tag{II.1}$$

$$y_1 = R_c \sin(\alpha - \alpha_0) \tag{II.2}$$

where α_0 is the angle used to position the sliding rod on the cam and to actuate the pivoting blade through a lever of length d. Let L_p be the effective displacement of pullrod pivot of the blade which is also equal to the distance between the $(x_1,\ y_1)$ and the cam coordinates $(x_c,\ y_c)$ at α_0 so that the shape of the cam track is defined by the control law. This relationship defines the cam shape through its profile coordinates, which are given by

$$x_c = x_1 + L_p \cos(\alpha) \tag{II.3}$$

$$y_c = y_1 + L_p \sin(\alpha) \tag{II.4}$$

where $L_p = d.\tan(\theta)$. Figure II.2 shows the plan and side views of the draft of cam and its mount.

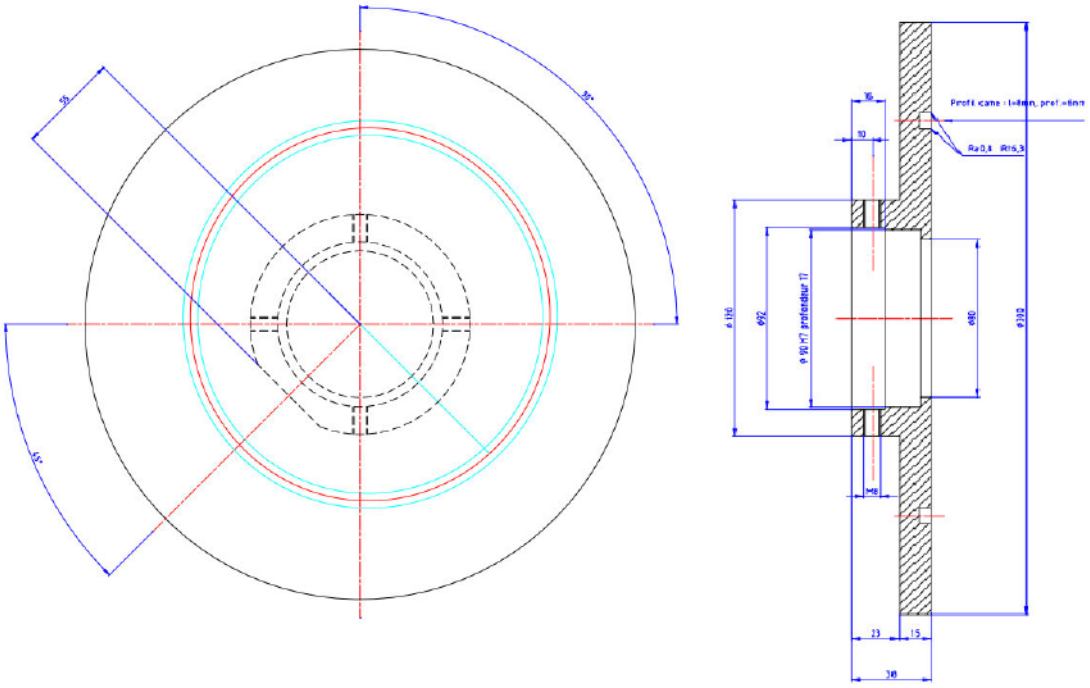

Figure II.2: Plan and side views of cam for $\beta = +5^0$.

II.2 Prototype

The complete mechanism of cam and control rod of the Darrieus turbine model for experimental investigation is shown in Figure II.3. The cam is grooved on the under-face of the cam mount. The cam follower which is attached to the end of the pullrod moves along this cam track. The other end of the rod connects with the pullrod pivot of the blade. A slider assembly fixed to the blade allows a low-friction sliding action to the blade so that the follower's motion through the cam

track is translated into the blade pitching as it travels through the azimuth. The position of the blade pivot is at the hydrodynamic centre of the profile.

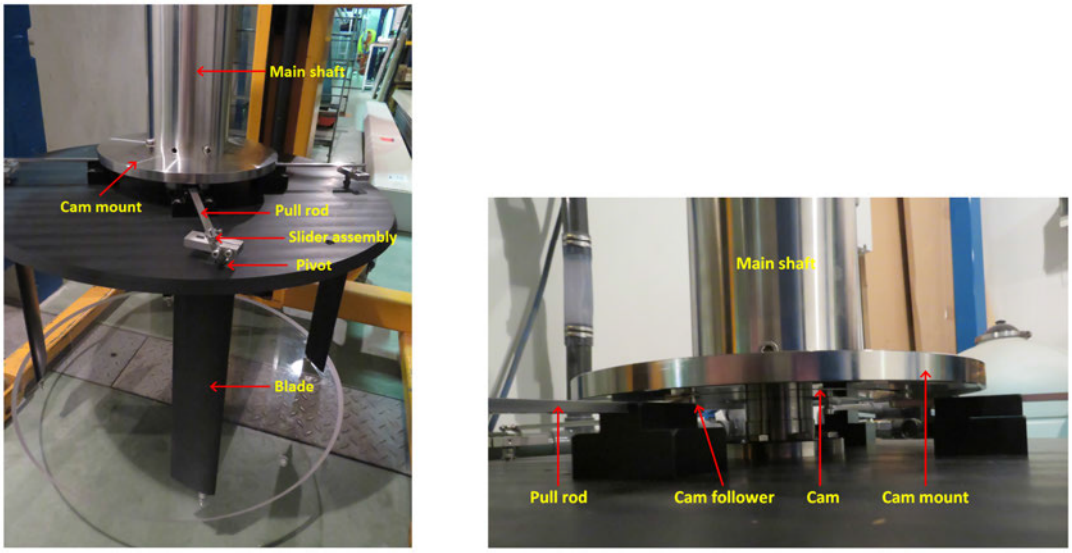

Figure II.3: Forced pitch actuation mechanism.

The location of blade pivot and pullrod pivot, the pullrod motion and slider assembly design were selected without considering their respective inertial moments, centrifugal loads and friction. Therefore, an obvious deviation in the performance measurements using experiments from the numerical results is expected.

Résumé

L'étude développée dans cette thèse concerne le contrôle des performances et des lâchers tourbillonnaires au cours du cycle de rotation d'une hydrolienne à axe vertical de type Darrieus. L'élaboration d'une famille de lois de commande d'incidence de pales exploitant le principe de conservation de la circulation autour de profils en mouvement permet ici le contrôle du fonctionnement de l'hydrolienne ainsi que la maîtrise de son sillage tourbillonnaire afin de préserver l'environnement.

L'écoulement 2D est simulé à l'aide du solveur incompressible de Star CCM+ afin de mettre en évidence l'effet de ce type de contrôle sur le rendement de la turbine pour différents points de fonctionnement. Ce modèle CFD a été utilisé pour améliorer l'analyse analytique en ce qui concerne l'extraction de l'énergie, la compréhension de l'écoulement autour de l'hydrolienne et le contrôle des tourbillons générés. La nouveauté de cette étude est l'élaboration de lois de commande de pales d'hydrolienne, basées sur des valeurs constantes et transitoires de la circulation, afin d'augmenter la puissance de la turbine tout en garantissant un contrôle efficace de la vorticité et ainsi prévenir de l'interaction entre les tourbillons et les pales. Une bonne comparaison est réalisée entre les résultats analytiques et numériques concernant les forces hydrodynamiques.

En outre, une campagne d'essais a été menée afin d'acquérir des mesures quantitatives sur une hydrolienne de type Darrieus à pales fixes en terme de puissance, mais aussi des résultats qualitatifs pertinents comme la visualisation de l'écoulement autour des pales à différentes positions et pour différents points de fonctionnement. La mise en place complète d'un système PIV pour les mesures qualitatives et les étapes de traitement sont discutées et les divers paramètres obtenus à partir des études CFD sont validées en utilisant ces résultats PIV. L'étude expérimentale dans la présente recherche apporte des informations détaillées sur les gradients de pression et de vitesse, les contours de vorticité et le critère Q qui ont servi à valider les visualisations obtenues numériquement.

Mots clefs : Hydrolienne, Contrôle, Circulation, Sillage, PIV, CFD

Abstract

With key applications in marine renewable energy, the vertical axis water turbine can use current or tidal energy in an eco-friendly manner. However, it is difficult to reconcile optimal performance of hydrokinetic turbines and compliance with the aquatic environment as the main drawback of the turbines is the formation of non-linear flow structures caused by the unsteady movement of the blades. Eddies in the flow are advected and can interact with other blades, which leads to a reduction in power output. To limit this phenomenon, the turbines operate at high speeds, which are likely to reduce the shaft power. High speeds of rotation also forbid the passage of aquatic animals, and are the cause of a suction effect on the sediments.

The objective of this thesis work is twofold. First, it aims to develop a blade pitch control to get the flow adjusted around the blade profile at any given flow configuration by incorporating the profile's motion with respect to incident flow. Such a system intends to achieve the objective of operating at reduced speeds without vortical releases, which should allow achieving a high torque without causing damage to the environment.

This thesis work is mainly carried out in three phases. In the first phase, the irrotational flow over an arbitrary profile is formulated using conformal mapping. Prospective potential flow application on the basis of Couchet theory (1976) is involved in the development of a control law that decides the blade pitching in a constant circulation framework. In the second phase, a numerical validation of the developed analytical work is presented using CFD to examine how the theoretical formulation can be effectively applied to Darrieus turbines. In the final phase, two prototypes are developed, one is classical Darrieus turbine with fixed blades, and other is the turbine with pitching blades for experimental measurements of performance as well as flow fields (by PIV) in order to validate the computational results.

Keywords : Water turbine, Control, Circulation, Wake, PIV, CFD